DEVELOPMENT AND ELECTRO-ACOUSTIC PROPERTIES OF BNKLT-BASED

PIEZOELCTRIC CERAMIC

by

ELAHEH TAGHADDOS

A dissertation submitted to the

School of Graduate Studies

Rutgers, The State University of New Jersey

In partial fulfillment of the requirements

For the degree of

Doctor of Philosophy

Graduate Program in Materials Science and Engineering

written under the direction of

Ahmad Safari

And approved by

_____

_____

_____

_____

New Brunswick, New Jersey

May, 2019

ABSTRACT OF THE DISSERTATION

Development and Electro-Acoustic Properties of BNKLT-Based Piezoelectric

Ceramic

By ELAHEH TAGHADDOS

Dissertation Director:

Professor Ahmad Safari

The functionality of piezoelectric materials to interconverting the mechanical and electrical energy leads to a huge market of piezoelectric materials in a wide range of applications from daily use, such as a speaker, musical instrument, humidifier to more specialized applications in military, medical and automotive industries. The market of piezoelectric is dominated by $Pb(Zr_xTi_{1-x})O_3$ compositions with outstanding electromechanical properties. However, it is essential to replace lead-containing piezoelectric materials with non-toxic alternatives.

Bismuth sodium titanate and its solid solution are a promising lead-free candidate for transducer and actuators applications. The ternary solid solution of 0.88BNT-0.08BKT-0.04BLT (BNKLT88) exhibits high coercive field ($E_c \sim 47$ kV.cm^{-1}), mechanical quality factor ($Q_m \sim 420$), depolarization temperature ($T_d \sim 220$ °C), and low dielectric loss (tanδ $\sim 1.2\%$). These desired high power properties make BNT-based composition a potential lead-free candidate to replace for hard commercial PZT.

In this dissertation, an attempt has been made to study the effect of B-site Mn and Fe acceptor dopants on the mechanical quality factor of BNKLT88 ceramics and improve the high power performance. The samples were processed by conventional and flash sintering methods. The effect of sintering parameters on the crystal structure, piezoelectric, dielectric and electrical properties have been comprehensively evaluated. The electromechanical properties were measured by the IEEE-Standard procedures. The impedance spectroscopy technique was used to characterize the electrical conductivity and impedance relaxation of the specimen. The optimum electromechanical properties were obtained at 1.5 mol% of Mn or Fe-doped composition processed by the conventional sintering method. The functionality of the $(BiNa_{0.88} K_{0.08}Li_{0.04})_{0.5}Ti_{0.985}Mn_{0.015}O_3$ ceramic for high power application has been evaluated by prototyping of low frequency transducer. In the conventional sintering method, the effect of both sintering temperature and the particle size on the electromechanical properties showed improved mechanical quality factor up to 1200 in calcined powder with a median particle size of 535 nm. The evaluation of the mechanical quality factor as a function of vibration velocity for high power application showed lower heat generation resulting in stable Q_m at higher vibration velocity of 0.6 m.s^{-1} and reduction of input power by 70-75%. X-ray photoelectron microscopy study of the specimen indicated coexistence of Mn $^{2+}$/Mn^{+3} or Fe^{2+}/Fe^{+3} in Mn or Fe-doped ceramics. In flash sintering (FS), the optimum sintering parameters to fully densify BNKL88-1.5Mn composition were achieved at 1 KHz alternating current, 100 V·cm^{-1} initial electric field and the preset maximum current limit of 1.5 A·cm^{-2}. The uniform distribution of elements was observed via energy-dispersive spectroscopy. Ceramics with finer grain size of 10-15 μm, similar electromechanical properties, more symmetric

butterfly shape strain, and lower resistivity have been achieved by the FS method at a preset furnace temperature of 880 °C. The grain boundary contribution in the conduction mechanism was more pronounced in FS specimen.

Two unfocused single-element transducers with the same center frequency of 3.5 MHz were designed and fabricated based on BNKLT88-1.5 Mn and commercial PZT. The pulse-echo response showed that -6dB bandwidth of 20% and 18% for BNT-based and PZT transducer, respectively. The acoustic pressure of BNT-based and PZT-based transducers was linear up to 105 V and 70 V peak to peak voltage with maximum rarefaction acoustic pressure of 1.1 MPa and 1.01 MPa, respectively. Spatial peak pulse average intensity, spatial peak temporal average intensity, and output power were characterized. The results confirmed that the properties of BNT-based transducer are comparable with lead-based PZT counterpart.

The electrical conductivity and impedance relaxation of BNKLT-based ceramics were systematically explored in the temperature range from 450 to 600 °C via impedance spectroscopy technique. The bulk and grain boundary characteristics were extracted from simulating the impedance spectrum with equivalent circuits. Interestingly, even though Mn and Fe had similar oxidation state with similar dielectric and piezoelectric properties, their electrical behavior was completely different. Considerably higher resistivity in the bulk, a modest increase in the grain boundary activation energy and a decrease in the bulk activation energy were caused by Mn-doping. On the other side, Fe doping resulted in remarkably higher conductivity, lowering the bulk activation energy, and a modest increase in grain boundary activation energy. The conductivity as high as 0.01 S.cm^{-1} was achieved in Fe-doped piezoceramic at 600 °C.

ACKNOWLEDGMENTS

for me and supported me, even now that I am 7200+ miles away from home. The value of hard work, strength, independency is instilled in me by your wisdom and positive discipline. This journey was not possible without your support, if I am successful, it's because of you. Thank you and I LOVE YOU!

PREFACE

This thesis is based on following published and accepted under revision papers:

1- **E. Taghaddos**, M. M. Hejazi, A. Safari, "Electromechanical properties of acceptor-doped lead- free piezoelectric ceramics", J. Am. Ceram. Soc., 1-7(2014).

2- M. Hejazi, **E. Taghaddos**, E. Gurdal, K, Uchino, A. Safari, "High power performance of Manganese-doped BNT-based Pb-free piezoelectric ceramics", J. Am. Ceram. Soc., 97 [10] 3192-3196 (2014).

3- **E. Taghaddos**, T. Ma, H. Zhong, Q. Zhou, M. X. Wan, A. Safari, "Fabrication and Characterization of Single-Aperture 3-MHz BNT-based ultrasonic therapeutic transducer's", IEEE Transactions on Ultrasonics, Ferroelectrics, and Frequency Control, vol. 65, no. 4, pp. 582–588, April. 2018

4- **E. Taghaddos**, H. Charalambous, T Tsakalakos, A. Safari, "Electromechanical properties of flash sintered BNT-based piezoelectric ceramic", J. Eur. Ceram. Soc., doi.org/10.1016/j.jeurceramsoc.2019.03.050

5- **E. Taghaddos**, A. Safari, "Study the electrical properties of acceptor- doped *BNT-based electroceramics by impedance spectroscopy*", under review.

The additional results and discussions are provided where necessary

TABLE OF CONTENTS

LIST OF FIGURES

1   Introduction /Background

1.1   Dielectric Materials

An electric dipole is the separation of positive and negative charge on an atomic or molecule level under application of electric field. The nonmetallic materials that are electrically insulating and are exhibiting an electric dipole under electric field are known as dielectric materials. One of the important electrical properties of dielectric materials is their ability to store the electric charge which is characterized via dielectric constant (K) or relative permittivity (ε_r) and are given by the ratio of the permittivity of a material (ε) to the permittivity of the free space ($\varepsilon_0 = 8.854 \times 10^{-12}$ F.m^{-1}) [1], [2]

$$K = \varepsilon_r = {}^{\varepsilon}\!/_{\varepsilon_0} \tag{1.1}$$

Dielectric constant are unit less and would be affected by the frequency of the alternating electric field, chemical structure, concentration of defects, physical parameters including temperature and pressure [2].

The dielectric polarization led to store more charges in an electroded dielectric material compare to free space between the same electrodes separated by an identical distance, Fig. 1.1(a-b). The capacitance (C_p) in term of stored charges could be computed by

$$C_p = \frac{\varepsilon_r \varepsilon_0 A}{d} \tag{1.2}$$

Where A is the electrode area, and d is the separation between them. Ceramic, paper or polymer film, and electrolytic (aluminum or tantalum) are three main types of capacitors [3]. The sum of the charges stored on the electrode along with those originating from the polarization (P) in C.m^{-2} define the dielectric displacement (D) with SI unite of C.m^{-2}

$$D = \varepsilon_0 E + P \tag{1.3}$$

where E is the applied electric field in V.m^{-1}.
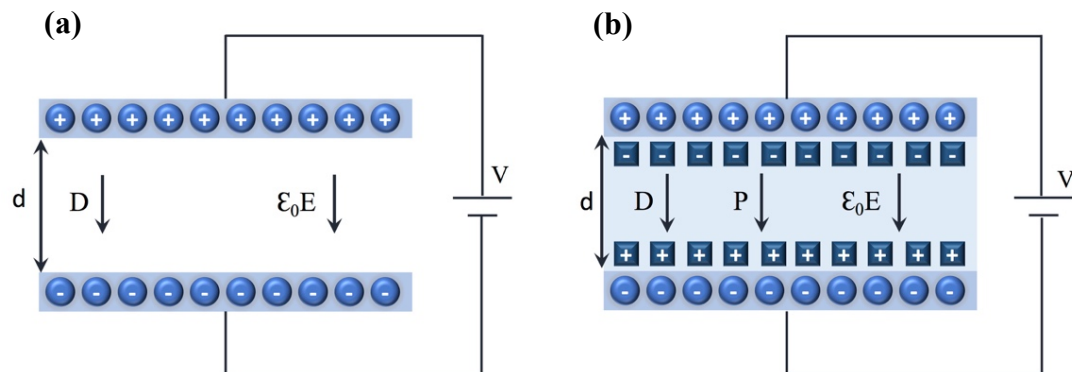
Figure 1. 1. A plate capacitors (a) vacuum separating two electrodes (b) filled with a dielectric material
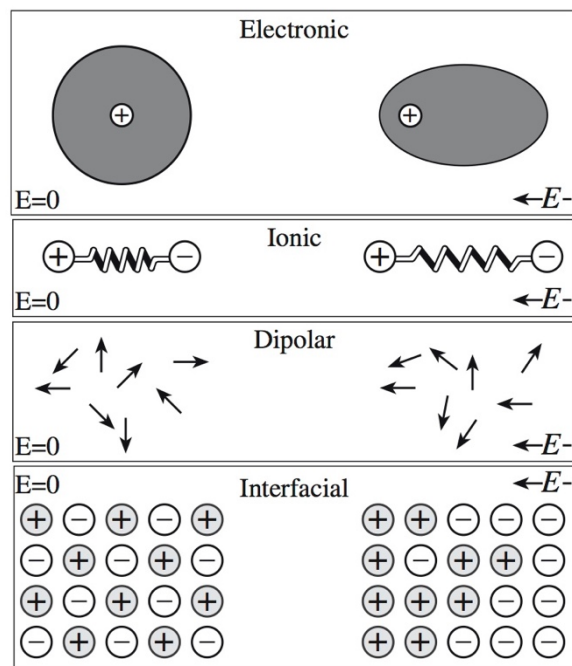
Figure 1. 2. Four major polarization mechanisms resulting in the dielectric displacement/polarization [3] .

Electronic, ionic, dipolar (also called molecular or orientation), and space charge (also called interfacial) are four possible types of polarization mechanisms, as schematically shown in Fig. 1.2, that contribute to the dielectric properties.

Electronic polarization occurs in all materials under application of an external electric field due to the displacement of the electron cloud relative to the nucleus. The concentration of the electron on the side of the nucleus near the positive end is higher which consequently generate temporarily dipole. The ionic polarization initiates in ionic materials via the elastic deformation of the ionic bonds under an electric field. The movement of the cations and anions either closer together or further, depending on the direction of the field, will temporarily create dipoles and may as well change the dimensions of the materials. The dipolar polarization contribution is associated with the reorientation of the permanent molecular dipoles in direction of the electric field. The space charge or interfacial polarization comes from mobile charge carriers in the form of ions or electrons that can migrate considerable distance through dielectric under applied field, but become trapped at an electrode.

The total polarizability (α) will obtain via the sum of all the individual contributions

$$\alpha = \alpha_{electronic} + \alpha_{ionic} + \alpha_{dipolar} + \alpha_{space\ charge} \tag{1.4}$$

The performance of each type of the polarization is time dependent and each mechanism is active up to a specific frequency. As a result, the total degree of polarization would affected by the time variation of the electric field. Permittivity under alternative current consist of real (K' or ε_r') and imaginary part (K″ or ε_r'')

$$\varepsilon_r = \varepsilon_r' - j\varepsilon_r'' \tag{1.5}$$

The finite speed of polarization is the source of time lag with delay angle of δ between the phase angle of the electric flux density and the electric field [3]. The dielectric loss or dissipation factor (tan δ) define as:

$$tan\ \delta = \frac{\varepsilon''}{\varepsilon'}$$ (1. 6)

The frequency dependence of the real and imaginary parts of dielectric constant is shown in Fig. 1.3. Very small mass of electrons makes them capable of following the electric field up to very high frequency. As a result, the only operative polarization and dielectric component at optical frequency is electronic polarization which is proportional to the refractive index (n) of materials ($\varepsilon_r = n^2$). The ions with heavier mass respond to frequency up to infrared range. Permanent dipoles can follow alternating fields up to MHz-GHz and the contribution of space charge is limited to kilohertz range or even lower [2]–[5] .
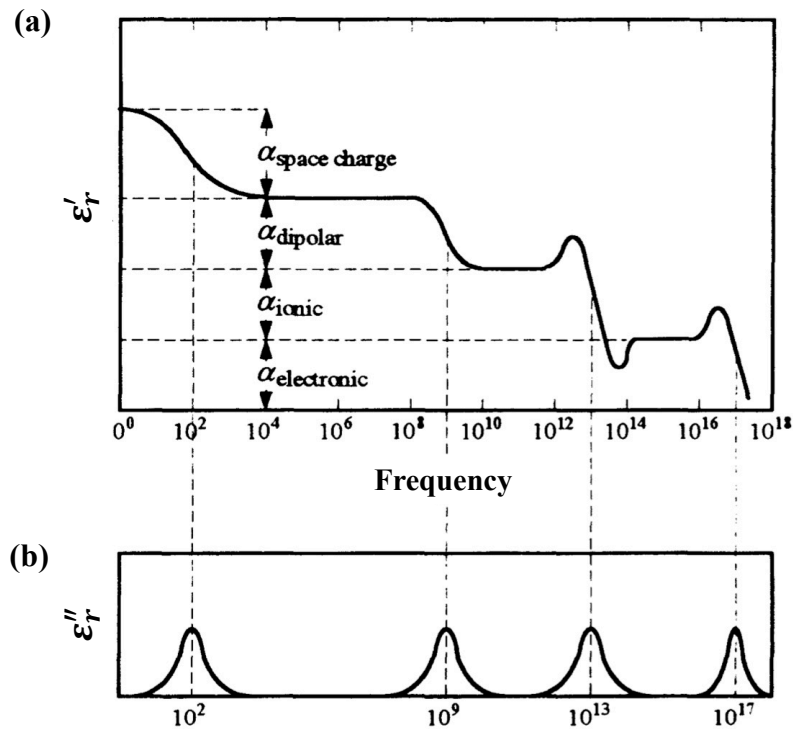
Figure 1. 3. Variation of (a) relative dielectric constant and (b) dielectric loss with frequency [6]

Paraelectric (non-ferroelectrics or normal dielectrics) and ferroelectrics are considered as two major categories of dielectric materials. The non-ferroelectric materials can be classified into three categories depend on the mechanisms of the electric polarization [2]:

(I) Nonpolar materials: For this category, elastic displacement of electron clouds, specifically the valence electron cloud is the only mechanism which will get active under application of electric field. As a result, the total polarizability is electronic polarization

$$\alpha = \alpha_e \tag{1.7}$$

Elemental materials which are made of single kind of atom such as silicon (Si) and diamond (C) belongs to this group.

(II) Polar materials: In this category, besides the elastic displacement of the electron clouds the elastic displacement of the relative positions of the ions also contribute in the polarization. Consequently, the total polarizability contains electronic and ionic component

$$\alpha = \alpha_e + \alpha_i \tag{1.8}$$

This class of materials does not include the permanent dipole moments. Ionic crystals such as alkali halides, some oxide, paraffins belong to this group.

(III) Dipolar materials: This class of materials contain all three fundamental polarizations. Electronic, ionic and dipolar polarization are all exist and total polarizability is

$$\alpha = \alpha_e + \alpha_i + \alpha_o \tag{1.9}$$

The ferroelectric materials will extensively explain in following section (1.3).

1.2 Piezoelectricity

All crystalline system can be described via 32 crystallographic point group which include 11 centrosymmetric and 21 non-centrosymmetric point groups (Table 1.1). The existence of inversion center (center of symmetry) makes the polar properties impossible via inverting any polar vectors. On the other side, 20 out of 21 non-centrosymmetric point groups (except 432) exhibit coupling between mechanical and electrical energies which define as piezoelectricity. The polarization (P) or dielectric displacement (D) of piezoelectric materials will change under application of external mechanical stress (T). Such a phenomenon is recognized as direct piezoelectric effect. On the other side, an electric field (E) leads to a mechanical strain (s) and change of dimensions which is known as the converse piezoelectric effect. The following general formula describe direct and converse piezoelectric effect

$$D_i = d_{ijk} T_{jk} \quad , \text{i,j,k} = 1,2,3 \tag{1.10}$$

$$s_{ij} = d_{kij} E_k \quad , \text{i,j,k} = 1,2,3 \tag{1.11}$$

where d is the piezoelectric coefficient with same value from both formula but two different unite of pC.N^{-1} and pm.V^{-1} for direct and invers effect, respectively. The piezoelectricity could be converted into a polar third rank sensors with $3^3 = 27$ tensor components. However, the stress tensor is symmetric ($T_{ij} = T_{ji}$) and only 18 independent components exist. Therefore, 6 × 3 matrix can be used to describe the piezoelectricity with general formula as following

$$D_i = d_{ji} T_j , \quad \text{i=1,2,3 ; j= 1,2,..,6} \tag{1.12}$$

$$s_i = d_{ji} E_j \tag{1.13}$$

The number of independent components can reduce to lower number, depending on the symmetry and point group. For example, three independent piezoelectric coefficient d_{33}, d_{31} and d_{15} was exist in poled ceramic with point group 4mm [1].

Table 1. 1. Thirty-two point groups in crystallography

Polarity	Symmetry	Crystal System										
		Cubic		Hexagonal		Tetragonal		Rhombohedral		Orthorhombic	Monoclinic	Triclinic
Non-Polar (22)	Centro (10)	m3m	m3	6/mmm	6/m	4/mmm	4/m	$\bar{3}$m	$\bar{3}$	mmm	2/m	$\bar{1}$
Polar Pyroelectric (10)	Non-Centro (21)	432	23	622	$\bar{6}$	422	$\bar{4}$	32		222		
		$\bar{4}$3m		$\bar{6}$m2		$\bar{4}$2m						
Polar Pyroelectric (10)				6mm	6	4mm	4	3m	3	mm2	2 / m	1

 Piezoelectric

 Pyroelectric and ferroelectric

1.3 Ferroelectricity

One of the most fascinating properties of dielectric materials are ferroelectricity that observe in single crystal or polycrystalline materials with nonsymmetrical structure (Table 1.1). Among the twenty polar point groups that exhibit piezoelectricity, 10 groups have one unique direction axis that leads to spontaneous polarization (P_s) on the absence of electric field over certain temperature range. In other words, spontaneous polarization arises from existence of permanent dipole moment in the crystal, which are reversible under application of electric field. Four major classification of the ferroelectric materials based on the unit cell structures are perovskite family or oxygen octahedral group ($BaTiO_3$, $PbTiO_3$), layered structure materials ($Bi_4Ti_3O_{12}$), and tungsten-bronze group ($PbNb_2O_6$, $SrNb_2O_6$). The perovskite structure with general formula of ABO_3 is the widely known

ferroelectric materials that is used in many practical applications. "A" represents the large cations with low valence of 1+, 2+, and 3+ sitting at the corner of the unit cell (e.g. Pb^{2+}, Ba^{2+}, Bi^{3+}, Na^{1+}). "B" represents the smaller cation with large valence of 3+, 4+, and 5+ which occupy the center of the unit cell (e.g. Ti^{4+}, Zr^{4+}, Nb^{5+}). "O" represents the oxygen atoms which occupied the face of the unit cell and create oxygen octahedron. The perovskite crystal structure of lead titanate ($PbTiO_3$) with cubic and tetragonal structure illustrated in Fig. 1.4.
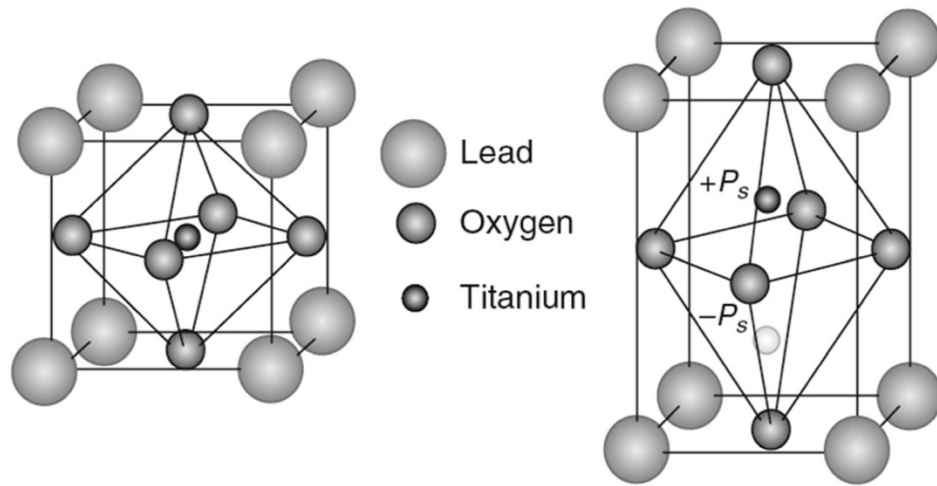
Figure 1. 4. The perovskite crystal structure of $PbTiO_3$ with (a) paraelectric cubic phase above Curie temperature (T_c,), and (b) tetragonal phase structure below T_c which demonstrate off-center displacement of Ti ions along [001] directions [7].

The ferroelectric properties delimit by Curie temperature (T_c) which is transition point from paraelectric cubic phase to ferroelectric tetragonal phase. At temperature higher than T_c, thermal disorder eradicates the spontaneous polarization; as a result, the ferroelectric materials behave as nonpolar dielectrics and dielectric susceptibility (χ) follows Curie-Weiss law

$$\chi \cong \frac{\varepsilon'}{\varepsilon_0} = \frac{C}{T-\theta} \qquad (1.14)$$

where C is the Curie constant, θ is the Curie-Weiss temperature, ε' real part of the dielectric permittivity, and ε_0 is the permittivity of the free-space.

On the other hand, at temperature lower than T_c the inter-ferroelectric transition accompany with re-orientation of the polarization directions may occur. Phase transition can be recognized via sharp anomaly in temperature dependence of the dielectric constant. Fig. 1.5 illustrate the ferroelectric phase transition in BaTiO$_3$. This composition undergoes a sequence of three distinct phase transition when cooled from T_c (120 °C) at ambient pressure: Cubic (Pm$\bar{3}$m) $\xrightarrow{\sim 120°C}$ tetragonal (P4mm) $\xrightarrow{\sim 0°C}$ orthorhombic (Amm2) $\xrightarrow{\sim -90\,°C}$ rhombohedral (R3m). The value of T_c depends on the structure and the grain size and the range of 120 °C-131°C has been reported.
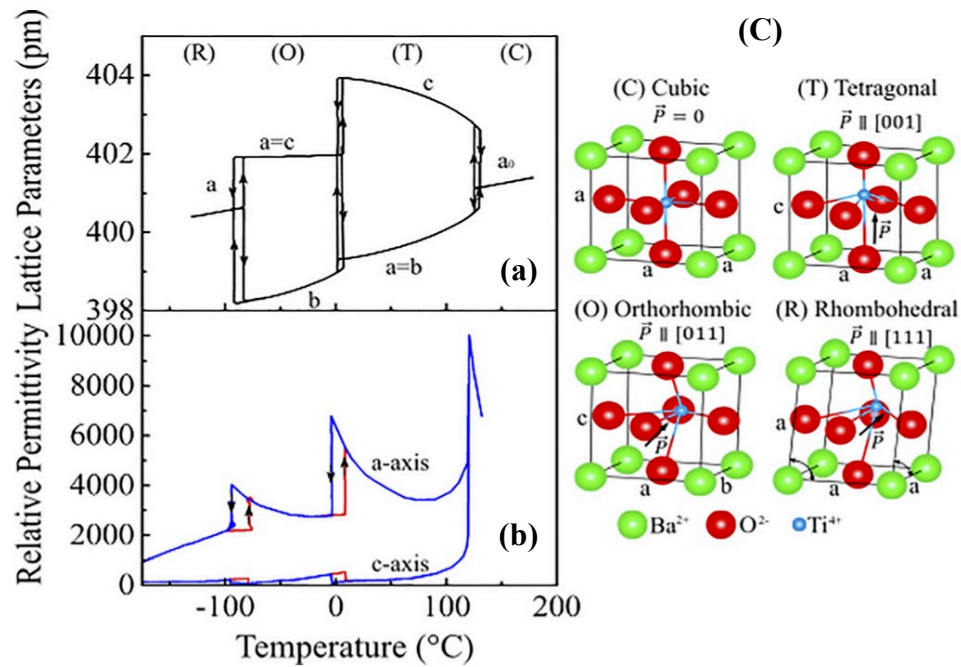
Figure 1. 5. BaTiO$_3$ phase transition at temperature below T_c.(a) Temperature dependence of the dielectric constant (b) Temperature dependence of lattice parameter (C) [8], [9]

The phase transition from high-temperature paraelectric symmetric phase to low-temperature ferroelectric phase with lower symmetry is accompanied by formation of domains structure to minimize the free energy, the elastic energy and the electrostatic energy of system [9], [10] . Within each domain, the dipoles are aligned in the same direction. The boundary between two adjacent domains is described as domain wall which has been categorized into two main groups of 180° and non-180°.

180° domains walls sperate domains consist of the parallel polar vector with opposite polarization directions, whereas non-180° domains walls sperate domains consist of two different polar vectors oriented at given angle to one another. Based on the crystal structure the permitted domains are varying. For instance, in barium titanate (BT), both 90° and 180° domains are initiate and contribute to reduction of the energy, while, 90° domains are considered as the only contributor to the minimization of elastic energy. 60°, 90°, 120°, and 180° are permitted domains for orthorhombic symmetry of BT, while rhombohedral symmetry possesses 71°, 109°, and 180° domains. Fig. 1.6 schematically illustrate the pattern domains with 180° and 90° domain walls.
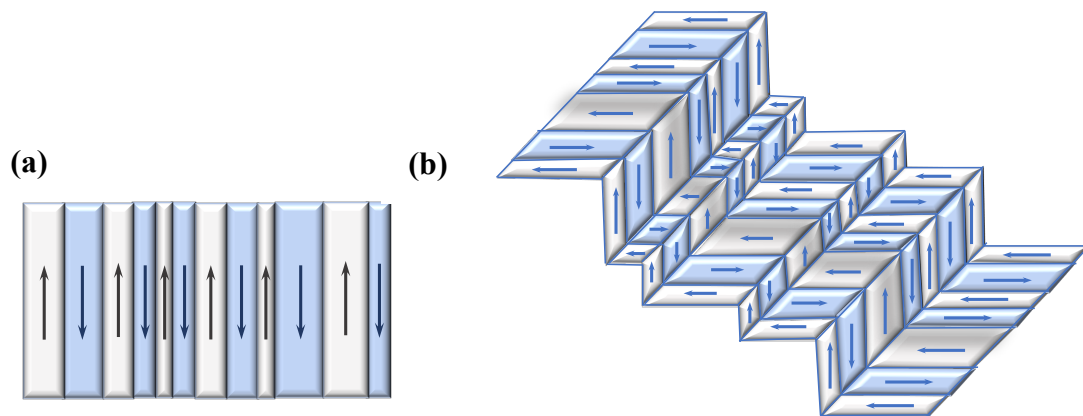
Figure 1. 6. Schematic domain pattern (a) antiparallel domains with 180° walls (b) domains with combination 180° and 90° walls [2]

It is important to study the effect of temperature, electric field, stress, chemical forces and other external factors on the ferroelectric domains and their responses. One of the most accepted method to understand and identify the ferroelectric materials is the polarization and strain hysteresis upon application of an electric field. Ferroelectricity could be directly characterized via hysteresis loops as each ferroic martial has its own unique hysteresis loop. The typical polarization-electric field and strain-electric field for ferroelectric materials are shown in Fig. 1.7. A random polydomain configuration of as-sintered ferroelectric materials leads to zero net polarization vector in macroscopic scale (point "a" in Fig. 1.7). When external electric field applied, the dipoles orientations are switching to align with polar axis which is closest to the direction of the applied field. At the condition that the field is small, dipoles are not able to switch, and there is a linear relationship between polarization and electric field. However, by increasing the applied field and passing the low-field region, domains are able to switch and align toward the electric field. Consequently, the polarization increases nonlinearly and reach to the saturation polarization, P_s, (point 'b'). Due to the presence of the internal stress some of the domains may return to their original positions by lowering the electric field. However, the majority of domains keep their alignment and result in nonzero net polarization on zero electric field (Point 'c') which known as remnant polarization (P_r). In order to get zero polarization (Point 'd'), it is required to apply a certain amount of electric field in opposite direction, which describe by the coercive field (E_c). The internal friction opposing the motion of domain wall is evaluated by the magnitude of E_c. Similar rearrangement of the domains and the polarization in opposite direction will be occurred by increasing the negative applied field (Point 'e') [9], [10].
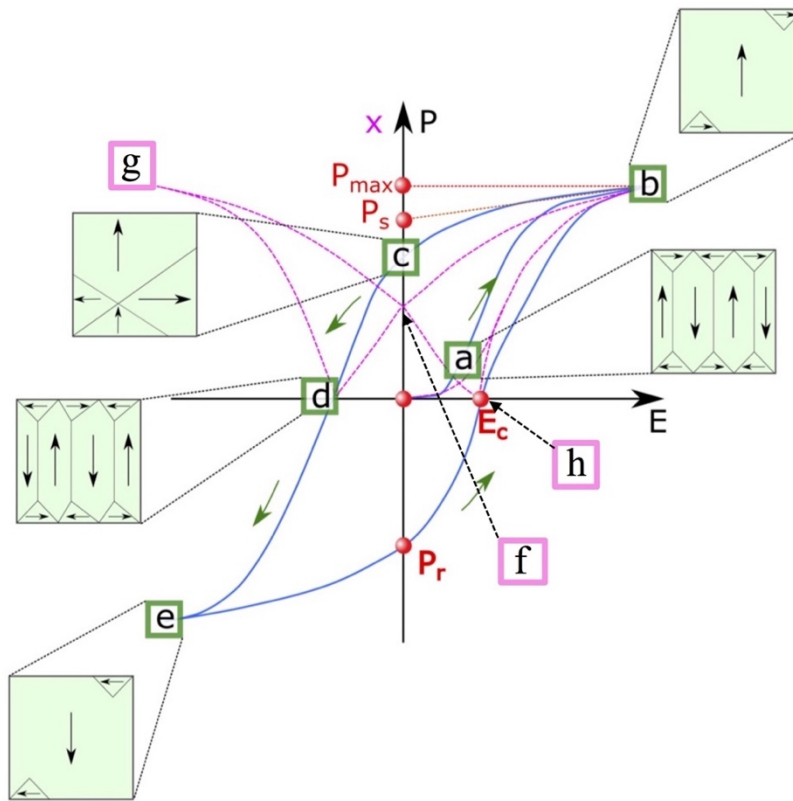
Figure 1. 7. P-E hysteresis loop for ferroelectric sample [9]

The strain-electric field hysteresis loop can be obtained simultaneously as polarization if the strain gets monitored during cycled electric field. Reorientation of 180° domains wall does not have any contribution in macroscopic strain. On the other side, the extrinsic reversible and irreversible displacement of non-180 domain walls significantly contribute on the macroscopic strain of ferroelectrics [10], [11]. The intrinsic converse piezoelectric effect and the intrinsic electrostriction are two other mains contributor in the evolution of strain developed by electric field or phase transition. On the absence of the electric field, the strain is zero (point "f" in Fig. 1.7). Applying the electric field in the direction same as spontaneous polarization lead to crystal expansion to point "b". The

lattice continuously expands and reaches to the maximum value at the highest applied-filed (point "b"). When the electric field decreases, the magnitude of strain drops to zero. Then, the direction of applied-field is changed and become antiparallel to P_s which cause lattice contraction. When the applied-field reach to coercive field ($-E_c$), the electric field is large enough to switch the polarization direction and the ferroelectric domain direction (point "d"). After reorientation of domain in parallel to the field, the strain becomes positive again and reach to maximum point "g". Then as the field reduces, the strain drops to zero at point "f". The alteration of the polarization, domains direction, and sudden change of the strain occurs once more time at point "h".

Piezoelectricity and ferroelectricity are affected by grain size, phase transition, dopants, thickness frequency, amplitude of electric field, temperature, and frequency. Four typical kinds of P-E, and their corresponding bipolar and unipolar S-E curves summarized in Fig. 1.8. Anti-ferroelectric materials show double-loop hysteresis loop feature (Fig. 1.8-b). The asymmetric loop observed in acceptor-doped ferroelectrics due to domain wall pinning effects (Fig. 1.8-c). The ralxor ferroelectrics do not have any macroscopic domains, as a result there is no or very low hysteresis loop (Fig. 1.8-d).
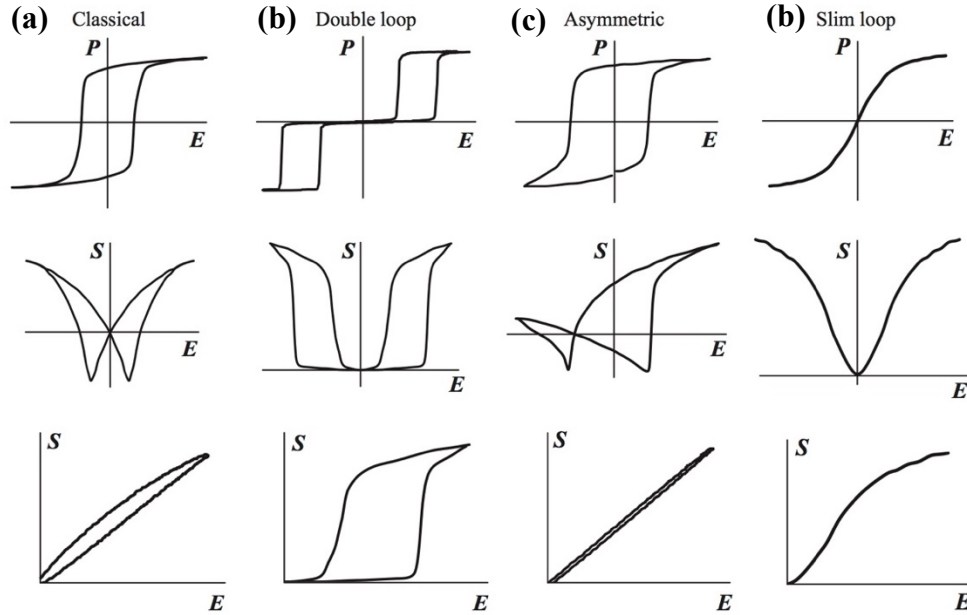
Figure 1. 8. Four typical types of P-E hysteresis loops and their corresponding bipolar and unipolar S-E curves (a) soft ferroelectrics (b) anti-ferroelectrics (c) hard-ferroelectrics (d) relaxor ferroelectrics
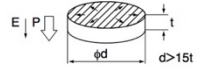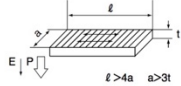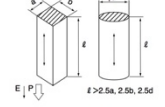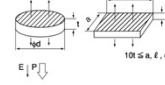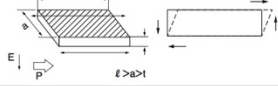
1.4 Applications of piezoelectric and ferroelectric materials

Ferroelectric and piezoelectric materials found hundreds of civil, military, and energy applications, which can be grouped as transducers and generators. Some of the military applications of piezoelectric materials are sound navigation and ranging (Sonars) used in the submarine detection/navigation system. The ferroelectric generators are used in the Army to drive a variety of loads such as high-power microwave and ultra wideband sources for defeating electronics, and lasers for blinding sensors. The energy of soldier's arm and leg motion can be harvested via piezoelectric harvester. Piezoelectric MEMS for Infrared cameras and other devices such small flying robots for unobtrusive surveillance of the battlefield are few other military and defense applications. Piezoelectric materials have other numerous applications in automotive, computer, medical, electronic, and

consumer industries. Tunable high-dielectric materials for high-frequency applications; sensors, actuators, transducers, nonlinear optical devices, ferroelectric memories, vibration damping, artificial muscles, air bag sensor, fuel atomizers, seat belt buzzers, inject printers, disposable patient monitors, heart monitors, and ultrasonic imaging and therapeutic transducers are some of the other applications of piezoelectric materials.

The essential required piezoelectric properties of the materials for specific application determines by the design and the working condition of the devices. Some different fundamental vibration modes can be obtained in the piezoelectric resonator which depend on the geometry, orientation of polarization and direction of the electric field. Five main resonant motions for poled piezoceramic, corresponding resonant frequencies summarized in Table 1.2.

Table 1. 2. Different vibration modes, corresponding resonant frequencies and the piezoelectric properties[12], [13].

Vibration Mode	Shape/Vibration Mode	Resonant Frequency (f_r)	Material Constant Symbol				
			k	d	g	ε^T	N
Radial Mode		$\dfrac{N_p}{d}$	k_p	d_{31}	g_{31}	ε^T_{33}	N_p
Length Mode		$\dfrac{N_{31}}{l}$	k_{31}	d_{31}	g_{31}	ε^T_{33}	N_{31}
Longitudinal Mode		$\dfrac{N_{33}}{l}$	k_{33}	d_{33}	g_{33}	ε^T_{33}	N_p
Thickness Mode		$\dfrac{N_t}{l}$	k_t	d_{33}	g_{33}	ε^T_{33}	N_t
Shear Mode		$\dfrac{N_{15}}{l}$	$k_{24}=k_{15}$	d_{15}	g_{15}	ε^T_{11}	N_{15}

Piezoelectric charge coefficient (d_{ij}), piezoelectric voltage or strain coefficient (g_{ij}), electromechanical coupling coefficient (k_{ij}), mechanical quality factor (Q_m), and acoustic impedance (Z) are five main parameters as a figure of merit for specific applications [1], [14]. Several applications of piezoceramics, required mode of operation (resonance or off-resonance), and figure of merit (FOM) has been summarized in Table 1.3.

The efficiency of the coupling between electrical and mechanical energy of the piezoceramics is defined by the coupling coefficient (k_{ij}). It describes the ratio of the mechanical energy stored caused by piezoelectric effect to the electrical input energy or vice versa. Quality factor generally quantify 'Resistance' to damping of oscillator or resonators. The oscillator with higher quality factor shows more stability of the performance during operation. In the case of mechanical vibrator such as piezoelectric materials the quality factor specifically represents by mechanical quality factor (Q_m) [15]. When the device operates in the resonance mode, the product of mechanical quality factor and square of electromechanical coupling coefficient ($Q_m.k^2$) is the critical evaluation factor.

The actuation performance evaluates via measuring the large signal piezoelectric coefficient (d_{ij}^*) and it consider as a FOM for actuator applications which operates on the resonance mode,

$$d_{ij}^* = \frac{S_{max}}{E_{max}} \tag{1.15}$$

where S_{max} is the maximum achievable strain, E_{max} is the maximum electric field while E is usually unipolar.

The attainable voltage output for given mechanical input signal, or vice versa, a mechanical displacement in reaction to accumulated charge density is defined by

piezoelectric voltage coefficient (g_{ij}). The sensitivity of sensors and the functionality of piezoelectric igniters evaluate by g_{ij}. Additionally, for applications which demand to run under off-resonance mode conditions such as sensing (microphone) and energy harvesting, the FOM is the value of g.d.

Vibration velocity (v_0) is the figure of merit for high power applications:

$$v_0 = \frac{1}{\sqrt{2}}\, \omega\epsilon_m \propto \sqrt{\frac{\varepsilon_{33}^T}{\rho}}\, k_{31} Q_m . E \qquad (1.16)$$

where ω is angular resonance frequency, ϵ_m is the root mean square (rms) of maximum vibration amplitude, ρ is density and E is the driving electric field.

The chemical modification considers as a practical and effective technique to optimize the piezoelectric and ferroelectric properties. Substitution of A-site/B-site in ABO_3 piezoelectric materials with higher valence (donor dopants) possesses an extra electron leading to soft piezoelectric composition with larger electromechanical coupling coefficient, lower coercive field, and smaller mechanical quality factor. On the contrary, substitution of A site/B-site in piezoelectric materials with lower valence (acceptor dopants) resulted in hard piezoelectric composition with high mechanical quality factor (Q_m) as well as coercive field.

Table 1. 3. " Current and future applications and their critical figures of merit" took from reference [14].

Temperature range	Resonant or non-resonant	Applications		FOM	Other
		Well-established	Impending		
Special use T > 500°C	Resonant		Aerospace, Aircraft, Nuclear power plant or geothermal power plant sensors	$k^2.Q_m$	
	Non-resonant			d.g	
SMD T > 250 °C	Resonant	Filter		k	F_r-TC
		Oscillator		Q_m	F_r-TC
		Gyro sensor		$k^2.Q_m$	
	Non-resonant	Acceleration sensor, HDD shock sensor		d.g	
Automotive T=40 to 180 °C	Resonant	Knocking sensor, Back sensor	Energy harvesting (TPMS)	$k^2.Q_m$	
	Non-resonant	Knocking sensor	Energy harvesting (TPMS)	d.g	
		Fuel injection		S_{max}/E_{max}	
Consumer T= −20 to 80 °C	Resonant	Fish sonar, Flowmeter Medical probe	Energy harvesting (Burglar alarm), Ultrasonic transducer (data entry device), Non-destructive testing	$k^2.Q_m$	
		Ultrasonic cleaner, Ultrasonic machining tool,[a] Camera lens autofocus (motor), Power window (motor), Backlight inverter, High-voltage supply transformer	Wind blower, Air ionizer	$k^2.Q_m$	v_{max}
			Micro-mass sensor	Q_m	
	Non-resonant	Microphone	Energy harvesting (Burglar alarm)	d.g	
		Stove burner, Lighter, Buzzer, Vibration damping (sports equipment)		d	
		Ink jet, Loud speaker, Camera lens module	HDD tracking, Pump	S_{max}/E_{max}	

[a] High power langevin transducers are often used for ultrasonic machining tools. In this case large d_{33} values under a pre-stress are important.

1.5   Ferroelectric and Piezoelectric Materials

Lead-based piezoceramics with outstanding piezoelectric and ferroelectric properties can be produced without any difficulty. As illustrated in Fig. 1.9, they have superior figure of merit compare to lead-free compositions. Consequently, ferroelectric materials which used for those mentioned applications mostly based on lead containing materials such as lead zirconate titanate $PbZr_{0.5}Ti_{0.5}O_3$ (PZT), lead titanate (PT), and lead magnesium niobate-lead titanate $(1-x)[Pb(Mg_{1/3}Nb_{2/3})O_3]-x[PbTiO_3]$ (PMN-PT). However, lead is a toxic element causing multiple side effects on children and adults. Lead is a volatile element with a low vapor pressure which can enter to the atmosphere during high temperature processing the piezoelectric ceramics. It can directly (through inhalation) or indirectly (contaminated food, rain, etc) cause various side effects on human body. Lead-based materials also require a special handling, storage, disposal and recycling system due to their hazardous nature. Unfortunately, Lead poisoning has no obvious signs, and most children do not report any abnormal symptoms. People with lead poisoning might report stomachaches, decreased appetite, hyperactivity, sleeping problems or irritability. Because these symptoms appear to mimic other childhood problems, lead poisoning is sometimes mistaken for a cold or the flu. European Union and Some of Asian countries such as Japan have banned usage of lead-based materials in different applications including electronic devices.

Therefore, to protect the environment and public health, it is essential to find new lead-free piezoelectric ceramics which can be used as alternatives for lead-based materials such as PZT. During last decades, noticeable amount of research has been carried out on lead-free piezoelectrics and the numbers of publications in this field have been remarkably

increasing. Although, currently lead-free piezoelectrics show inferior electromechanical properties compared to Pb-based materials, for some applications promising lead-free compositions have been identified. In general, there has been a remarkable progress on the development of lead-free piezoelectric ceramics with improved electromechanical property. As an example, two different FOMs of d_{33}^* and d.g as a function of depolarization/Curie temperature for PZT and lead-free piezoceramic has been show in Fig. 1.9. Soft lead-free piezoelectrics with high piezoelectric coefficient and low Curie temperature have been introduced for actuator applications. On the other hand, BNT-based and KNN-based hard lead-free piezoelectric with a high mechanical quality factor and low piezoelectric constant have been developed for high power applications where minimal heat dissipation and power consumption is needed [15]–[18].
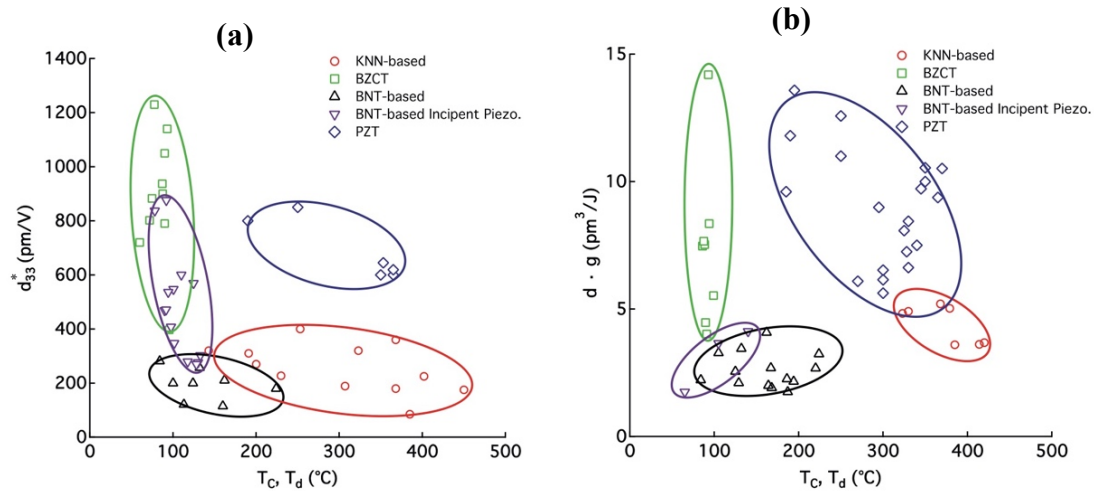
Figure 1. 9. The large signal piezoelectric coefficient (d_{33}^*) vs. depolarization/Curie temperature (a) d.g vs. depolarization/Curie temperature (b) and d$_{33}$ for PZT and lead-free based piezoceramic took from ref. [14]

1.6   BNT-Based Ceramic

Discovered by Smolenskii et al., $(Bi_{0.5}Na_{0.5})TiO_3$ (BNT) is one of the most prominent lead-free piezoelectric materials with perovskite structure, large remnant polarization ($P_r \sim 38$ $\mu C/cm^2$), and high Curie temperature ($T_c \sim 540$) [19], [20]. BNT is relaxor-type ferroelectrics with rhombohedral structure at room temperature, which shows diffuse phase transition to tetragonal ($T_{R-T} \sim 300$ °C) and then goes to cubic phase at T~540 °C. The maximum dielectric temperature (T_m) of BNT is ~ 320-340°C and the depolarization temperature is around 185 °C (Fig. 1.10) [21]–[24]. Depolarization temperature is the ferroelectric to antiferroelectric transition and characterize by the maximum dielectric loss (tan δ) in temperature dependence dielectric plot [25]. The antiferroelectric phase can changed to ferroelectric under application of electric field.

The half of the Curie temperature usually defines as the working temperature of ferroelectric materials in which the performance of the device does not affect by temperature. However, in the case of BNT-based composition, even though it shows high T_c, working temperate restricted by lower temperature of T_d.
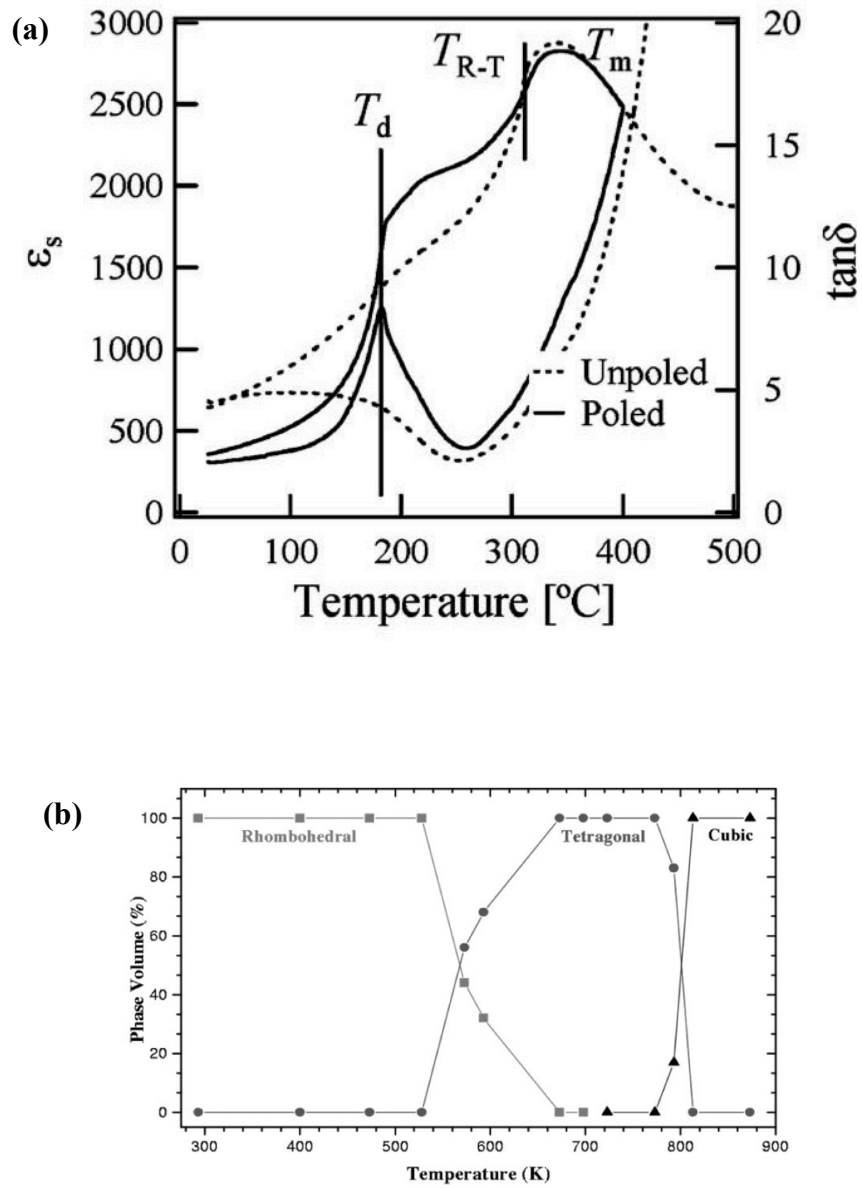
Figure 1. 10. Phase transition and temperature dependence of dielectric constant and dielectric loss of BNT (a)took from Ref. [25] and phase volume (%) as a function of temperature (b) took from Ref [23]

In order to obtain dense BNT ceramics, a sintering temperature higher than 1200 °C is required. Thermograph (TG, weight loss) measurements reveal that vaporization of Bi occurred over 1130 °C, which results in low resistivity and poor poling conditions [20]. A very high coercive field ($E_c > 7$ kV/mm) of pure BNT makes the poling conditions even more difficult. This inherent restrictions on synthesizing of BNT piezoceramic was a driving force to find BNT-based ceramic with lower sintering temperature, smaller coercive, and enhanced piezoelectricity. Consequently, different binary and ternary solid solution of BNT have been developed which are reported as a potential candidate for lead-based counterpart [26]–[33].

Binary system of $(1-x)(Bi_{0.5}Na_{0.5})TiO–x(Bi_{0.5}K_{0.5})TiO_3$ (abbreviated to BNTK–100x) [34], [35] and ternary system of $x(Bi_{0.5}Na_{0.5})TiO–y(Bi_{0.5}Li_{0.5})TiO_3–z(Bi_{0.5}K_{0.5})TiO_3$ xBNT-yBLT-zBKT (x+y+z=1) (abbreviated to BNLKT100y-100z) [36]–[38] possess morphotropic phase boundary (MPB) between rhombohedral and tetragonal structure. The phase relation of BNT-BKT and BNT-BKT-BLT has been demonstrated in Fig. 1.11. The coercive filed decreased effectively by the substitution of K^+ and Li^+ for Na^+, while the remnant polarization remained high. Furthermore, the piezoelectric constant increases by increasing the value of K^+/Li^+ ratio. Table 1.4 summarized the overall achieved properties for some of the BNT-BKT and BNT-BKT-BLT compositions.

The ternary system of 0.88BNT-0.08 BKT-0.04BLT (abbreviated to BNKLT88) shows rhombohedral structure with higher mechanical quality factor of 392 and lower dielectric loss of 1.23%, compare to MPB and tetragonal structure. Reported by Y. Hiruma et al. that the mechanical quality factor and vibration velocity could be enhanced via Mn doping [38].

(a)

(b)
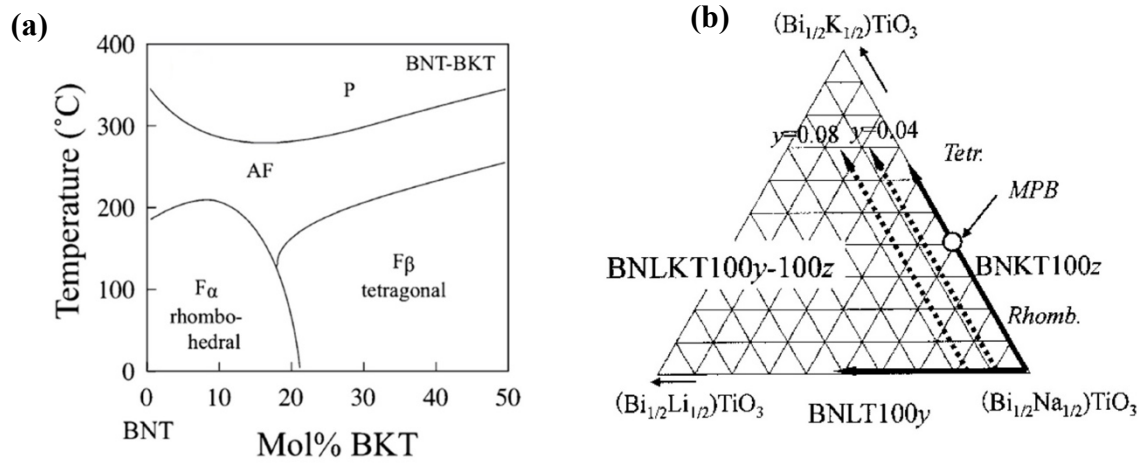
Figure 1. 11.Phase diagram of BNT-BKT system (a) and BNT-BKT-BLT system

Table 1. 4. The overall achieved properties for some of the BNT-BKT and BNT-BKT-BLT compositions

	d_{33} (pC/N)	Tan δ (%)	ε_r	k_p	k_t	$Q_{m\text{-planar}}$	Ref
BNTK16	42.2 (d_{31})	---	635	0.314	0.423	195	[35]
BNTK20	46.9 (d_{31})	---	1030	0.270	0.418	109	[35]
BNKLT 68	138	4	1220	0.193	0.465	67	[39]
BNKLT78	174	3.13	925	0.367	0.522	97	[39]
BNKLT88	96	1.23	379	0.262	0.499	392	[39]

1.7   Sintering

In addition to chemical modification, the microstructure, piezoelctrisity and electromechanical properties are directly affected by sintering methods including two step sintering, spark plasma sintering, and flash sintering. Similarly, other effective parameters are sintering temperature and atmosphere as well as polling conditions.

Sintering (or firing) define as a processing technique to densify the green body from metal or/and ceramic powders component via applying thermal energy [40]. The sintering method can be divided in four categories of solid-state sintering, liquid phase sintering, vitrification and viscous sintering [41].

In solid state sintering, the formed or pressed powder is heated to temperature typically up to 0.5-0.9 of the melting point. The densification occurs in the absence of any liquid phase via atomic diffusion in the solid state.

By contrast, in liquid phase sintering, the presence of small amount of liquid at sintering temperature facilitate densification. The amount of liquid phase is less than a few volume percent of the original solid mixture. Compared to solid state sintering, densification can take place at lower temperature. The softening temperature of the solidified liquid phase delimit the maximum working temperature of the materials.

Vitrification sintering occurs in the presence of relatively large volume of liquid (~25% of the original solid volume) which is sufficient to fill the volume of the remaining pores. The liquid phase flow to the pores then during cooling either crystalize or vitrify (form glass).

Viscous sintering is basically for densification of the glasses via heat treatment of the consolidate mass of glass particles near to /or above the softening temperature. [41].

The application of an external pressure during sintering, such as hot pressing (HP) and hot isostatic pressing can enhance the densification and the electrotechnical properties. Temperature and pressure considered as two traditional parameters to control and modify the microstructure of ceramic. Beside the traditional method, densification can be improved via electric current activated/assisted sintering technique (ECAS) and field assisted sintering technique (FAST) in which the electric current or electromagnetic field facilitate the consolidation [42], [43]. Spark plasma sintering (SPS), microwave sintering (MW), and flash sintering are three types of FAST.

1.7.1   Flash Sintering

The flash sintering (FS) method originally was developed by Cologne et al. while they were working in university of Colorado Boulder with Professor Rishi Raj [44]. In flash sintering the green shaped powder is expose simultaneously to an electric field and to the heat, such that the material is densified [43]. The applied electric field is between 7.5 $V.cm^{-1}$ and 1000 $V.cm^{-1}$. Non-linear increase in the conductivity of the material and power dissipation between 10 to 1000 $mWmm^{-3}$ take place at the beginning of flash sintering. The total time; the time between the start of sintering and the completion of sintering, is less than one minute. In order to get almost instantaneous full densification in few seconds, the critical combination of electric field and temperature (T_{onset}) is required, wherein a 'flash event' and power surge occurs [43], [45]–[47]. FS experiment can be conducted under either isothermal or non-isothermal conditions. If an electric field is applied while the furnace is heated, it is considered as non-isothermal experiments. The conductivity of specimen increases as a function of rising the furnace temperature until a nonlinear rise in

current occur. In contrast, in isothermal experiments the electric filed is applied after the furnace temperature is reached to the predefined temperature, in which is held constant until completion of process. The non-linear rise in temperature happens if the electric field is sufficiently high. In general, in both isothermal and non-isothermal FS experiments, three distinct stages exist. The correlation between electric field (E), current density (J), power density (P), and relative density for isothermal condition schematically demonstrated in Fig. 1.12.
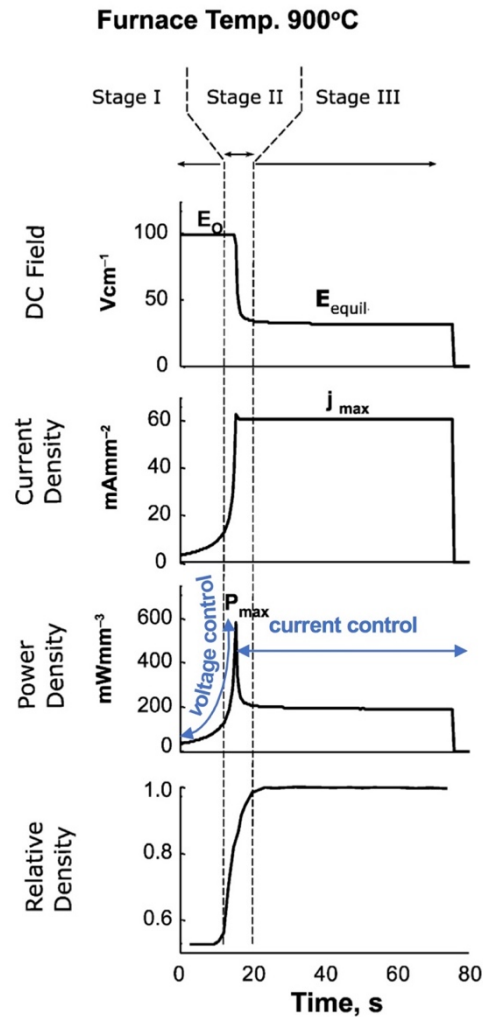
Figure 1. 12. Relation of electric field (E), current density (J), and power density (P) to densification in isothermal condition [48]

In stage I, which is known as incubation time, the current flowing through the specimen gradually increases as a function of time. Even though the current density is not too high, it is enough to initiate necking between powders particles. The necking leads to conduction path for current and modest dimension shrinkage in specimen [49]. The power (P) follows the equation 2.16 and increases as a result of raising the applied field. Nerveless to say that, it considers as a voltage control stage and specimen heated via joule heating.

$$P = \frac{E^2}{R} \qquad\qquad (1.\ 17)$$

In stage II, which is known as the onset time, the current rises nonlinearly until it reaches the current limit set at the power supply [50]. To protect the sample from melting via catastrophic runaway of the current, the current limit set to the suitable value, which depends on the composition and its melting point. Reaching to current limit coincide with the onset of current-control-mode, wherein the electric field reduces to maintain the constant current. This stage accompanied by rise and drop in power which result in power spike through the sample. The densification mostly take place during stage II which may go with modest grain growth. End of the power spike usually define as the completion of this stage.

In stage III, which is known as the steady state, the electric field and power density ($P = E\ J = J^2.R$) reach to a constant value. Densification enhances via closer of the pores and the grain growth may occur depending on the time allowed fore stage III. Contingent on the desired microstructure, the electric field can be turned off at any time.

Table 1. 5. Summary of different stages during flash sintering under isothermal condition [48]

Stage	Furnace Temperature	Voltage/Current	Time Duration	Mechanism	Initial state: Powder	Initial State: Presintered Polycrystal	Electro-luminescence	Far from Equilibrium Phenomena*
I	Isothermal	Voltage control	Incubation time can vary from one second to several hours	Joule Heating	Porous	dense polycrystal	No	No
II	Isothermal	Switch from voltage to current control	1-5 s	Sintering rate is four or more orders of magnitude faster than conventional	Sintering completed in about 2 s	dense polycrystal; grain growth?	Yes	?
III	Furnace can be turned off	Current control	The excited state of flash can be maintained indefinitely	Intense Electroluminescence suggests electron hole pair formation, and electronic conductivity. Emission is NOT black body radiation	Sample in the sintered state.	Accelerated grain growth.	Yes	Yes

*Including phase transformation, changes in the crystal structure and chemical reactions.

Some of the most pronounced advantageous of flash sintering are: lowering of time and temperature required for ceramic consolidation, non-equilibrium process, comparable properties with specimens prepared via conventional sintering, and absence of constrain sintering. In spite of the strong dependency of flash sintering behavior on the electrical properties of materials, FS is quite adaptable/adjustable technique. Different types of ceramic such as, ionic conductor, semiconductor, protonic conductors, Li-ion conductors, and electronic conductors have been synthesizde via this method.

The required time and temperature for ceramic densification is reduced significantly with the aid of flash sintering which leads to energy saving. This also effects on the microstructure. The flash sintered ceramic with fine grain has been observed in different materials such as 3YSZ [44], $BaTiO_3$ [51], $BiFeO_3$ [52], Al_2O_3-$MgAl_2O_4$-8YSZ [53], hydroxyapatite [54]. Other researchers, however, reported acceleration of grain coarsening, in some cases (such as ZnO) under application of electric field [55].

In FS, extremely high heating rate accompany with fast processing lead to non-equilibrium process. As a result, the consolidation of metastable materials is possible due out of equilibrium conditions. Similarly, the undesirable phase transition can be avoided [52], [56], [57]

On the other side, like all the other methods, flash sintering has some draw backs. Formation of "autocatalytic" or hot spot as a result of electrical concentration along preferential path is the main limitation of FS. The other restriction is local contamination of the component due to application of conductive past on the surface of the specimen. Fig. 1.13 schematically demonstrate the process parameter which can influence on the consolidation, flash sintering process and final properties.
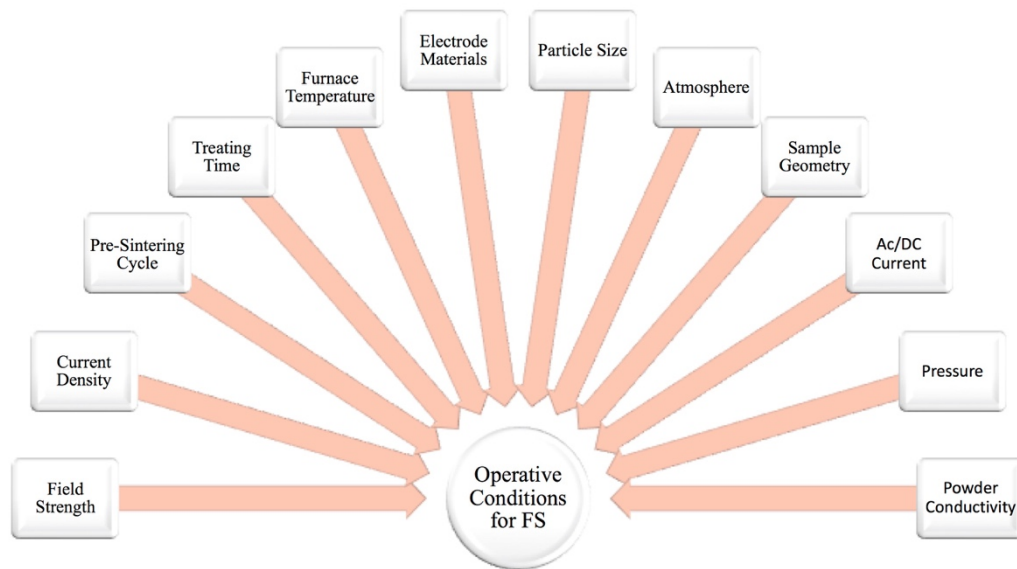
Figure 1. 13. Effective parameters on flash sintering

1.7.1.1 Proposed Mechanisms for FS

It has been tried to find and describe the mechanisms of the ultra-rapid densification in FS, either based on experimental evidence or hypothesis mechanisms. In this purpose, several theories have been proposed which can categorized in three different types:

(i)   on the macroscopic scale, extraordinarily rapid Joule heating materializing with likely heat localization on the lattice scale.

(ii)   The nucleation of the Ferenkel pairs which lead to formation of vacancies.

(iii)   Electrochemical reduction.

1.7.1.1.1 Joule Heating

Following an electric current through the ceramic specimen with some level of resistance lead to power dissipation, initiation of Joule heating, and increasing the temperature, wherein both electric conduction and diffusion are amplified. This theory is considered as the simplest physical mechanism to explain FS [46]. However, due to extremely high heating rate (heating rate can reach to order of 10^4 °C.min^{-1} [58]) , it is challenging to accurately measure the specimen temperature during peak power dissipation, and even more difficult and complicated to measure the gradient temperature inside the specimen during sintering. The rapid densification may describe by rapid heating to the high temperature which is several hundred degrees higher than conventional sintering. This has been proved in variety of materilas via different methods such as simulation, black body radiation model and experimentally measuring the temperature (thermometry) [57]–[63].

1.7.1.1.2 Formation of Frenkel Defect Pairs

It is controversial that if the heat produce via thermal runaway Joule heating is sufficient for rapid densification or not. Thus far, a number of studies have been reported that the temperature rise by Joule heating is too low to provide the required thermal energy for sintering in few second. Even it is inclined to be lower than conventional sintering which has much slower kinetics [64]–[67]. Infrared pyrometry, a blackbody radiation model, and in situ XRD calibration using synchrotron radiation are considered as three pieces of evidences which is reported by Raj's group. As a result, it is suggested that another mechanism should occur to accommodate the observed phenomena of rapid densification.

The field-induced formation of Frenkel pairs within the ceramic grain is another proposed mechanism for enhanced sintering kinetics of FS [44], [64], [68], [69]. During flash sintering process, the formation of lattice disorder both for an ions and cations is elevated under application of electric field. Consequently, the interstitials and vacancies population are increasing and lead to origination of Frenkel disorder in an oxide according to following reactions [46]:

$$M_M^x \longrightarrow M_i^{\bullet\bullet} + V_M'' \tag{1.18}$$

$$O_O^x \longrightarrow O_i'' + V_O^{\bullet\bullet} \tag{1.19}$$

The lattice defect can be discharged via ionization of defects and creation of electronic disorder [46] :

$$M_i^{\bullet\bullet} \longleftrightarrow M_i^{\bullet} + h^{\bullet} \longleftrightarrow M_i + 2h^{\bullet} \tag{1.20}$$

$$O_i'' \longleftrightarrow O_i' + 2e' \longleftrightarrow O_i + 2e' \tag{1.21}$$

$$V_M'' \longleftrightarrow V_M' + e' \longleftrightarrow V_M + 2e' \tag{1.22}$$

$$V_O^{\bullet\bullet} \longleftrightarrow V_O^{\bullet} + h^{\bullet} \longleftrightarrow V_O + 2h^{\bullet} \tag{1.23}$$
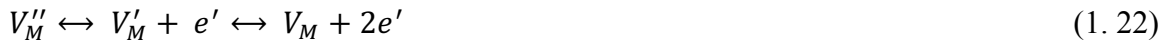
The electron and holes dispart from the Frenkel pair due to the forces caused by applied field and travel along the direction of electric field. The charge neutrality of the interstitials and the vacancies lead to higher mobility of defects. The interstitials travel toward pores and the vacancies accommodate at the grain boundaries due to the sintering pressure which result in the enhancement of sintering kinetics and rapid densification [50]. On the other side, electronic conductivity increases and electrical resistivity decreases due to the origination of free electrons and holes. The initiation of strong and bright emission which is known as electroluminescence attributed to the recombination of free electrons and holes [48], [70]–[72].

1.7.1.1.3 Grain Boundary Over Heating

Preferential and superior Joule heating at the grain boundary consider as a basis for another possible flash sintering mechanism [73]–[79]. It is widely known that the grain boundary has different characteristic; such as higher diffusion coefficient and higher formation of space charge in compare to the bulk. Higher formation of space charge in the grain boundary leads to increasing the local power dissipation via providing an extra-contribution to the grain boundary resistivity, which cause higher temperature and local melting in the grain boundary.

Narayan (2013) [73] proposed that at high electric field the defect segregation is responsible for selective Joule heating of dislocation and grain boundaries, initiation of avalanche, and selective melting of grain boundaries. Higher diffusivity of liquid phase (10^{-4}-10^{-5} cm^2 s^{-1}) leads to rapid densification within a second and flash phenomena.

As noted by Chaim (2016) [74], higher current concentration at the particles contact result in local melting followed by origination of capillary forces, spread the liquid phase

along the grain boundaries, and particles wetting. Consequently, the particles rearrange under capillary forces, and lead to the densification. Corapicioglu et al. [76] reports core/shell structure in $K_{0.5}Na_{0.5}NbO_3$ piezoceramic prepared via flash sintering, while the surface of particles is richer in potassium. It has been claimed that the core-shell structure can be considered as an indirect evidence for grain boundary overheating/ melting. Similarly, Uehashi et al. [78] report the presence of secondary phase of $BaTi_4O_9$ at the grain boundary of flash sintered $BaTiO_3$ powder. The formation of barium-deficient secondary phase is attributed to the preferential heating of the grain boundary, localize melting and consequently evaporation of barium. The phase segregation and secondary phases in flash sintered specimen have been reported in other materials as well references.

1.7.1.1.4 Electrochemical Effect

Origination of partially electrochemically reduced structure consider as another theory to describe the flash phenomena, mostly in covalent material and ionic conductors under DC or low frequency (~1 Hz) AC test conditions.

If the applied voltage in fuel cells is increased up to more than electrochemical reduction potential, the ionic conductivity is deteriorated while the electrical conductivity is enhanced. Similarly, the effect of electrochemical reduction during flash sintering lead to transition from ionic to electronic conductivity. Based on this theory, the sequence of steps to occur flash events is following:

(i)   Origination of the electrochemical reduction take place from the cathode to the anode, wherein the release of oxygen ions is significant at the anode.

(ii)   During the incubation stage, the electrochemical reduction progresses from the anode toward the cathode and the conductivity of the sample continuously increases because of electrochemical reduction.

(iii)   As soon as materials became adequately conductive accompanied with transition from ionic to electronic conductivity a flash event occurs.

The electrochemical reduction during flash sintering usually goes with the blackening effect (Fig. 1.14).
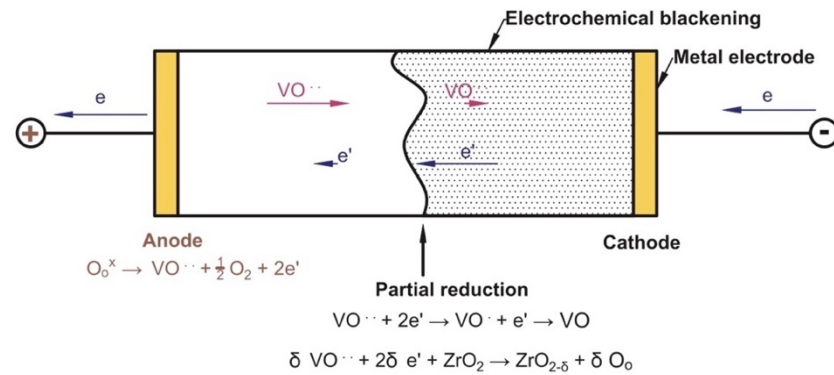
Figure 1. 14. Electrochemical effect in YSZ under direct current. Adapted from Janek and Korte [46], [80]

1.7.1.2   Flash Sintering of Piezoceramic

A large and growing body of literature has investigated the effect of flash sintering on different types of polycrystalline ceramics such as ionic conductors, insulators, semiconductors, and metallic-like conductors. There are few articles reported flash sintered $BaTiO_3$ [51], [77], [78], [81], $SrTiO_3$ [72], [82], [83], $KNbO_3$ [56], $BiFeO_3$ [52], [84], [85], $K_{0.5}Na_{0.5}NbO_3$ [76], $Pb(Zr_{0.52}Ti_{0.48})O_3$ PZT [86]. Table 1.6 summarized the experimental procedure on these materials.

Table 1. 6. Summary of experimental flash sintered procedure on piezoceramics

Composition	Shape of the Sample	E (V.cm⁻¹)	Current Density (mA.mm⁻²)	Current (mA)	Time (s)	Waveform	Heating condition	T$_F$ (°C)	Relative Density (%)	Average grain size (μ m)	Ref.
SrTiO$_3$	Dog bone	150-1000		60	---	DC	Non-isothermal	740-900	70-95	1	[82]
BaTiO$_3$	Dog bone	150-500	9.3	60	1min-15min	DC	Both	612-900	91.6-97.1	1.1-0.3	[51]
BaTiO$_3$	Rectangular	100	---	---	60	DC	Non-isothermal	1020	90-95	---	[77]
K$_{0.5}$Na$_{0.5}$NbO$_3$	Dog bone	100-500	7-40	---	10-60	DC	Non-isothermal	900-1090	79-94	---	[76]
KNbO$_3$	Rectangular	600	---	100	---	DC	Non-isothermal	750	95	1-3	[56]
BiFeO$_3$	Dog bone	15-150			869-941	DC	Non-isothermal	400-600		20 (nm)	[52]
BiFeO$_3$ (Bi$_2$O$_3$ & Fe$_2$O$_3$)	Dog bone	25-100	20-50	---	60	DC	Non-isothermal	???	???	???	[84]
BiFeO$_3$	Dog bone	100	25	---	75	DC	Isothermal	350	90	---	[85]
PZT	Dog bone	300-600	37	10-100	30	DC	Non-isothermal	538-860	83.7-94.3 Fully density	0.269-2.13	[86]

J. C. M'Peko et al. [51] consolidate the dogbone-shape BaTiO$_3$ ceramic under DC electric filed. They reported comparable permittivity, dielectric loss, and Curie temperature of flash sintered BaTiO$_3$ comparing to conventional method (Table 1.7). The flash sintering conditions accompany with dielectric properties is summarized in the Table 1.7. The optimum FS was achieved at 500 V.cm^{-1} while the current density was 9.3 mA. mm^{-2}. The abnormal grain growth of BaTiO$_3$ which occurs during conventional sintering can be eliminated with the aim of FS (Fig. 1.15) [51]. However, A. Uehashi et al. observed the secondary phase of BaTi$_4$O$_9$ at grain boundary region which is attributed to grain boundary over heating mechanism (Fig. 1.16) [78].
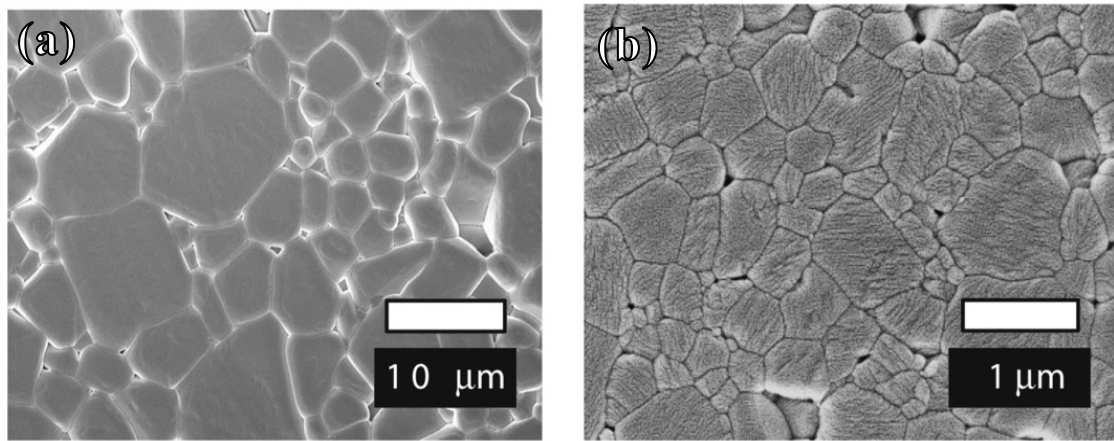
Figure 1. 15. Microstructure of BaTiO$_3$ (a) CSed at 1300°C for 5 min (b) FSed at electric field of 250 V.cm^{-1} and current density of 9.3 mA.mm^{-1} [51]

Table 1. 7.Grain size and dielectric properties of BaTiO$_3$ prepared via flash sintering and conventional sintering [51]

Sintering Condition	D (μm)	ε' (35°C)	tan δ (%) (35°C)	T$_c$ (°C)	ε'_m	tanδ$_m$(%)
1350 °C/1h	15.0	1930	3.2	132	9050	5.8
1300/5 min	5.2	2290	3.2	132	10160	6.6
150 V.cm^{-1}– 15 min	1.1	3540	2.7	127	6050	2.2
250 V.cm^{-1}– 3min	0.6	3320	3.0	128	5990	2.8
375 V.cm^{-1}– 2 min	0.4	2620	3.9	129	5330	4.1
500 V.cm^{-1}– 5 min	0.3-0.4	2150	2.6	128	3620	2.4
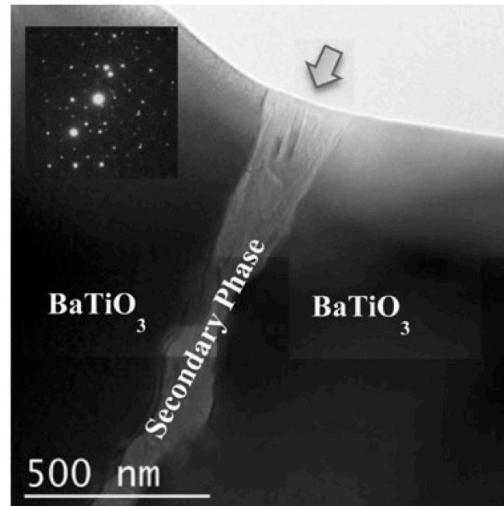
Figure 1. 16. TEM bright field image and the electron diffraction pattern from secondary phase in BaTiO$_3$ flash sintered at temperature (T$_F$) of 1020 °C, and applied electric field of 100 V.cm^{-1} (DC) for 60s,

N. Shomrat et al. developed stochiometric KNbO$_3$ with 95% TD via FS at electric field of 600 V.cm^{-1} while the furnace temperature was 750 °C. Corapcioglu et al. was one of the first group working on the flash sintering of potassium sodium niobate. The single phase KNN ceramic with relative density of 94% obtained at electric field of 250 V.cm^{-1}, current density of 20 mA.mm^{-2}, and furnace temperature of 990 °C. However, the chemical analysis via EDX accompany with high resolution transmission electron microscopy (HR-STEM) and STEM-EDX showed core-shell structure which has been attributed to localize the heat at grain boundary and melting those area (Fig. 1.17). Recrystallization of melted grain boundaries during the cooling result in chemical gradiant and non-uniform distribution of elements; specifically, K and Na, in FSed specimen. On the other side, it has been reported that heat treatment at 1000 °C for 4h successfully aim to obtain equilibrium composition [76].
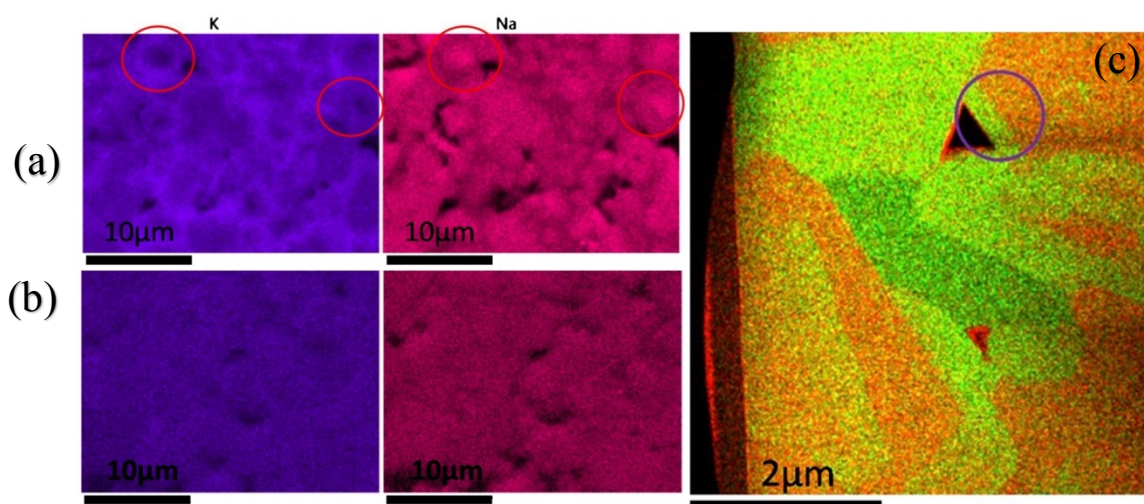
Figure 1. 17. Elemental mapping from EDX for K and Na after flash sintering show potassium and sodium rich regions(a), elemental mapping from EDX for K and N after heat treatment revealed compositional equilibrium (b) HR-STEM of flash sintered KNN (c)

The first attempt to flash sinter Bismuth ferrite (BFO) has been accomplished by L. A. Perez-Maqueda et al. in 2017. BFO with perovskite structure, grain size of 20 nm and low porosity has been achieved under 100 V.cm^{-1} electric field and maximum current density of 20 mA.mm^{-2} [52]. Later on, Gil-González et al. developed phase-pure BFO by reaction between Bi_2O_3 and Fe_2O_3 powders via flash sintering at 625 °C, electric field of 50 V.$^{cm-1}$, and current limit of 35 mA.mm^{-2} [84]. L. A. Perez-Maqueda et al. (2018) subsequently, studied the BFO flash mechanism via in-situ energy dispersive X-ray diffraction (ED-XRD) where the FS performed at 350 °C, under application of DC protentional of 100 V.cm^{-1}, and current limit of 25A.mm^{-2}.

X. Su et al studied flash sintering of lead zirconate titanate with chemical composition of undoped PZT, $Pb(Zr_{0.52}Ti_{0.48})O_3$, at morphotropic phase boundary (MPB). They have reported the effect of electric field and current limit on the microstructure, density and piezoelectric coefficient which are summarized in Table 1.8 and 1.9.

Table 1. 8. Effect of electric field, at constant current limit of 100 mA, and 30 s holding time30 s holding time

Electric field (v.cm^{-1})	300	400	500	600
Power dissipation at steady state (mW/mm^3)	387	401	492	502
Furnace temperature (°C)	860	782	583	538
Sample temperature (°C)	1135-1184	1105-1158	1089-1156	1084-1153
Average Grain Size (μm)	3.97	2.83	1.89	1.62
Piezoelectric Coefficient (pC/N)	228	225	220	217

Table 1. 9. Effect of current limit at constant electric field of 500 V.cm^{-1}, and

Current limit (mA)	10	20	30	40
Power dissipation at steady state (mW/mm^3)	60	81	145	340
Furnace temperature (ºC)	583	583	583	583
Sample temperature (ºC)	698-722	731-759	813-853	990-1048
Average Grain Size (μm)	0.269	0.371	0.69	1.25
Relative density	83.7	88.9	92.3	94.03

1.8   Summary

This chapter provides the basics theories and concepts studied in this investigation including dielectrics, piezoelectricity, and ferroelectricity. A general overview of the most important applications on piezoelectric materials and required figure of merit has been reported. The new field assisted technique known as flash sintering has been introduced. In addition, the possible flash mechanism, such as joule heating, Frenkel defects pair, grain boundary overheating and electrochemical effect has been briefly described. Finally, a general overview on the flash sintered piezoelectric ceramics accompany with reported properties and processing conditions has been presented.

1.9 References

[1] R. E. Newnham, *Properties of materials: anisotropy, symmetry, structure*. Oxford ; New York: Oxford University Press, 2005.

[2] K.-C. Kao, *Dielectric phenomena in solids : with emphasis on physical concepts of electronic processes /*. Amsterdam ; Academic Press, c2004.

[3] C. B. Carter and M. G. Norton, *Ceramic Materials: Science and Engineering*, 2nd ed. New York: Springer-Verlag, 2013.

[4] K. Uchino, *Ferroelectric Devices*, 1 edition. New York: CRC Press, 2000.

[5] W. D. Callister, *Materials science and engineering: an introduction*. New York: John Wiley & Sons, 2007.

[6] M. Barsoum, *Fundamentals of Ceramics*, 1 edition. Place of publication not identified: CRC Press, 2017.

[7] A. Safari and E. K. Akdogan, Eds., *Piezoelectric and Acoustic Materials for Transducer Applications*. Springer US, 2008.

[8] F. Jona and G. Shirane, *Ferroelectric Crystals*, Unabridged, Reprint edition. New York: Dover Pubns, 1993.

[9] M. Acosta *et al.*, "BaTiO3-based piezoelectrics: Fundamentals, current status, and perspectives," *Appl. Phys. Rev.*, vol. 4, no. 4, p. 041305, Dec. 2017.

[10] L. Jin, F. Li, and S. Zhang, "Decoding the Fingerprint of Ferroelectric Loops: Comprehension of the Material Properties and Structures," *J. Am. Ceram. Soc.*, vol. 97, no. 1, pp. 1–27, 2014.

[11] D. Damjanovic, "Ferroelectric, dielectric and piezoelectric properties of ferroelectric thin films and ceramics," *Rep. Prog. Phys.*, vol. 61, no. 9, pp. 1267–1324, Sep. 1998.

[12] "p19e6.pdf." .

[13] K. Uchino, "Chapter 17 - High-Power Piezoelectrics and Loss Mechanisms," in *Advanced Piezoelectric Materials (Second Edition)*, K. Uchino, Ed. Woodhead Publishing, 2017, pp. 647–754.

[14] J. Rödel, K. G. Webber, R. Dittmer, W. Jo, M. Kimura, and D. Damjanovic, "Transferring lead-free piezoelectric ceramics into application," *J. Eur. Ceram. Soc.*, vol. 35, no. 6, pp. 1659–1681, Jun. 2015.

[15] C.-H. Hong *et al.*, "Lead-free piezoceramics – Where to move on?," *J. Materiomics*, vol. 2, no. 1, pp. 1–24, Mar. 2016.

[16] P. Ditas, E. Hennig, and A. Kynast, "Lead-Free Piezoceramic Materials for Ultrasonic Applications," in *Sensors and Measuring Systems 2014; 17. ITG/GMA Symposium*, 2014, pp. 1–4.

[17] C.-H. Hong *et al.*, "Ring-Type Rotary Ultrasonic Motor Using Lead-free Ceramics," *J. Sens. Sci. Technol.*, vol. 24, no. 4, pp. 228–231, Jul. 2015.

[18] T. Tou, Y. Hamaguti, Y. Maida, H. Yamamori, K. Takahashi, and Y. Terashima, "Properties of $(Bi_{0.5} Na_{0.5})TiO_3 -BaTiO_3 -(Bi_{0.5} Na_{0.5})(Mn_{1/3} Nb_{2/3})O_3$ Lead-Free Piezoelectric Ceramics and Its Application to Ultrasonic Cleaner," *Jpn. J. Appl. Phys.*, vol. 48, no. 7, p. 07GM03, Jul. 2009.

[19] G. A. Smolensky, V. A. Isupov, A. I. Agranovskaya, and N. N. Krainik, "New ferroelectrics of complex composition," *Sov. Phys. Solid State*, vol. 2, pp. 2651–2654, 1961.

[20]   T. Takenaka and H. Nagata, "Current status and prospects of lead-free piezoelectric ceramics," *J. Eur. Ceram. Soc.*, vol. 25, no. 12, pp. 2693–2700, 2005.

[21]   "Phase transition temperature and electrical properties of (Bi1/2Na1/2)TiO3–(Bi1/2A1/2)TiO3 (A=Li and K) lead-free ferroelectric ceramics - ResearchGate." .

[22]   J. Suchanicz, K. Roleder, A. Kania, and J. Hańaderek, "Electrostrictive strain and pyroeffect in the region of phase coexistence in Na0.5Bi0.5TiO3," *Ferroelectrics*, vol. 77, no. 1, pp. 107–110, Jan. 1988.

[23]   G. O. Jones and P. A. Thomas, "Investigation of the structure and phase transitions in the novel A-site substituted distorted perovskite compound Na $_{0.5}$ Bi $_{0.5}$ TiO $_3$," *Acta Crystallogr. B*, vol. 58, no. 2, pp. 168–178, Apr. 2002.

[24]   K. Roleder, J. Suchanicz, and A. Kania, "Time dependence of electric permittivity in na0.5Bi0.5TiO3 single crystals," *Ferroelectrics*, vol. 89, no. 1, pp. 1–5, Jan. 1989.

[25]   K. Y. Yuji Hiruma, "Phase transition temperature and electrical properties of (Bi1/2Na1/2)TiO3–(Bi1/2A1/2)TiO3 (A=Li and K) lead-free ferroelectric ceramics," *J. Appl. Phys.*, no. 8, pp. 084121-084121–7, 2008.

[26]   H. Nagata, M. Yoshida, Y. Makiuchi, and T. Takenaka, "Large Piezoelectric Constant and High Curie Temperature of Lead-Free Piezoelectric Ceramic Ternary System Based on Bismuth Sodium Titanate-Bismuth Potassium Titanate-Barium Titanate near the Morphotropic Phase Boundary," *Jpn. J. Appl. Phys.*, vol. 42, no. Part 1, No. 12, pp. 7401–7403, Dec. 2003.

[27]   D. Q. Xiao, D. M. Lin, J. G. Zhu, and P. Yu, "Investigation on the design and synthesis of new systems of BNT-based lead-free piezoelectric ceramics," *J. Electroceramics*, vol. 16, no. 4, pp. 271–275, Jul. 2006.

[28]   S. H. Choy, X. X. Wang, H. L. W. Chan, and C. L. Choy, "Electromechanical and ferroelectric properties of (Bi1/2Na1/2)TiO3-(Bi1/2K1/2)TiO3- (Bi1/2Li1/2)TiO3-BaTiO3 lead-free piezoelectric ceramics for accelerometer application," *Appl. Phys. A*, vol. 89, no. 3, pp. 775–781, Sep. 2007.

[29]   T. Takenaka, K. Maruyama, and K. Sakata, "(Bi1/2Na1/2)TiO3-BaTiO3 System for Lead-Free Piezoelectric Ceramics," *Jpn. J. Appl. Phys.*, vol. 30, no. 9S, p. 2236, Sep. 1991.

[30]   M. Gröting, S. Hayn, and K. Albe, "Chemical order and local structure of the lead-free relaxor ferroelectric Na1/2Bi1/2TiO3," *J. Solid State Chem.*, vol. 184, no. 8, pp. 2041–2046, Aug. 2011.

[31]   N. Lei *et al.*, "Effect of lattice occupation behavior of Li $^+$ cations on microstructure and electrical properties of (Bi $_{1/2}$ Na $_{1/2}$)TiO $_3$ -based lead-free piezoceramics," *J. Appl. Phys.*, vol. 109, no. 5, p. 054102, Mar. 2011.

[32]   R. Sun *et al.*, "Growth and orientation dependence of electrical properties of 0.92Na0.5Bi0.5TiO3-0.08 K0.5Bi0.5TiO3 lead-free piezoelectric single crystal," *J. Appl. Phys.*, vol. 109, no. 12, p. 124113, Jun. 2011.

[33]   J. Kreisel, A. M. Glazer, P. Bouvier, and G. Lucazeau, "High-pressure Raman study of a relaxor ferroelectric: The Na $_{0.5}$ Bi $_{0.5}$ TiO $_3$ perovskite," *Phys. Rev. B*, vol. 63, no. 17, Apr. 2001.

[34]   O. Elkechai, M. Manier, and J. P. Mercurio, "Na0.5Bi0.5TiO3–K0.5Bi0.5TiO3 (NBT-KBT) system: A structural and electrical study," *Phys. Status Solidi A*, vol. 157, no. 2, pp. 499–506, 1996.

[35]   A. Sasaki, T. Chiba, Y. Mamiya, and E. Otsuki, "Dielectric and Piezoelectric Properties of (Bi0.5Na0.5)TiO3?(Bi0.5K0.5)TiO3 Systems," *Jpn. J. Appl. Phys.*, vol. 38, no. 9S, p. 5564, Sep. 1999.

[36]   Y. Hiruma, H. Nagata, and T. Takenaka, "Phase-transition temperatures and piezoelectric properties of (Bi1/2Na1/2)TiO3- (Bi1/2Li1/2)TiO3-(Bi1/2K1/2)TiO3 lead-free ferroelectric ceramics," *IEEE Trans. Ultrason. Ferroelectr. Freq. Control*, vol. 54, no. 12, pp. 2493–2499, Dec. 2007.

[37]   D. Lin, D. Xiao, J. Zhu, and P. Yu, "Piezoelectric and ferroelectric properties of [Bi0.5(Na1−x−yKxLiy)0.5]TiO3 lead-free piezoelectric ceramics," *Appl. Phys. Lett.*, vol. 88, no. 6, p. 062901, Feb. 2006.

[38]   Y. Hiruma, T. Watanabe, H. Nagata, and T. Takenaka, "Piezoelectric Properties of (Bi1/2Na1/2)TiO3-Based Solid Solution for Lead-Free High-Power Applications," *Jpn. J. Appl. Phys.*, vol. 47, no. 9S, p. 7659, Sep. 2008.

[39]   M. M. Hejazi, B. Jadidian, and A. Safari, "Fabrication and evaluation of a single-element Bi0.5Na0.5TiO3-based ultrasonic transducer," *IEEE Trans. Ultrason. Ferroelectr. Freq. Control*, vol. 59, no. 8, pp. 1840–1847, Aug. 2012.

[40]   S.-J. L. Kang, *Sintering: Densification, Grain Growth and Microstructure*. Elsevier, 2004.

[41]   L. C. De Jonghe and M. N. Rahaman, "Chapter 4 - 4.1 Sintering of Ceramics," in *Handbook of Advanced Ceramics*, S. Sōmiya, F. Aldinger, N. Claussen, R. M. Spriggs, K. Uchino, K. Koumoto, and M. Kaneno, Eds. Oxford: Academic Press, 2003, pp. 187–264.

[42]   R. Orrù, R. Licheri, A. M. Locci, A. Cincotti, and G. Cao, "Consolidation/synthesis of materials by electric current activated/assisted sintering," *Mater. Sci. Eng. R Rep.*, vol. 63, no. 4–6, pp. 127–287, Feb. 2009.

[43]   M. Yu, S. Grasso, R. Mckinnon, T. Saunders, and M. J. Reece, "Review of flash sintering: materials, mechanisms and modelling," *Adv. Appl. Ceram.*, vol. 116, no. 1, pp. 24–60, Jan. 2017.

[44]   M. Cologna, B. Rashkova, and R. Raj, "Flash Sintering of Nanograin Zirconia in <5 s at 850°C," *J. Am. Ceram. Soc.*, vol. 93, no. 11, pp. 3556–3559, Nov. 2010.

[45]   R. Raj, M. Cologna, and J. S. FRANCIS, "Methods of flash sintering," US9334194B2, 10-May-2016.

[46]   M. Biesuz and V. M. Sglavo, "Flash sintering of ceramics," *J. Eur. Ceram. Soc.*, vol. 39, no. 2, pp. 115–143, Feb. 2019.

[47]   R. I. Todd, E. Zapata-Solvas, R. S. Bonilla, T. Sneddon, and P. R. Wilshaw, "Electrical characteristics of flash sintering: thermal runaway of Joule heating," *J. Eur. Ceram. Soc.*, vol. 35, no. 6, pp. 1865–1877, Jun. 2015.

[48]   Jha S. K., Terauds K., Lebrun J.-M., and Raj R., "Beyond flash sintering in 3 mol % yttria stabilized zirconia," *J. Ceram. Soc. Jpn.*, vol. 124, no. 4, pp. 283–288, Apr. 2016.

[49]   H. Charalambous, S. K. Jha, H. Wang, X. L. Phuah, H. Wang, and T. Tsakalakos, "Inhomogeneous reduction and its relation to grain growth of titania during flash sintering," *Scr. Mater.*, vol. 155, pp. 37–40, Oct. 2018.

[50]   S. K. Jha and R. Raj, "Electric Fields Obviate Constrained Sintering," *J. Am. Ceram. Soc.*, vol. 97, no. 10, pp. 3103–3109, 2014.

[51]   J.-C. M'Peko, J. S. C. Francis, and R. Raj, "Field-assisted sintering of undoped BaTiO3: Microstructure evolution and dielectric permittivity," *J. Eur. Ceram. Soc.*, vol. 34, no. 15, pp. 3655–3660, Dec. 2014.

[52]   L. A. Perez-Maqueda, E. Gil-Gonzalez, A. Perejon, J.-M. Lebrun, P. E. Sanchez-Jimenez, and R. Raj, "Flash sintering of highly insulating nanostructured phase-pure BiFeO3," *J. Am. Ceram. Soc.*, vol. 100, no. 8, pp. 3365–3369, Aug. 2017.

[53]   D. Kok, S. K. Jha, R. Raj, and M. L. Mecartney, "Flash sintering of a three-phase alumina, spinel, and yttria-stabilized zirconia composite," *J. Am. Ceram. Soc.*, vol. 100, no. 7, pp. 3262–3268, 2017.

[54]   I. Bajpai, Y.-H. Han, J. Yun, J. Francis, S. Kim, and R. Raj, "Preliminary investigation of hydroxyapatite microstructures prepared by flash sintering," *Adv. Appl. Ceram.*, vol. 115, no. 5, pp. 276–281, Jul. 2016.

[55]   C. Schmerbauch, J. Gonzalez-Julian, R. Röder, C. Ronning, and O. Guillon, "Flash Sintering of Nanocrystalline Zinc Oxide and its Influence on Microstructure and Defect Formation," *J. Am. Ceram. Soc.*, vol. 97, no. 6, pp. 1728–1735, 2014.

[56]   N. Shomrat, S. Baltianski, C. A. Randall, and Y. Tsur, "Flash sintering of potassium-niobate," *J. Eur. Ceram. Soc.*, vol. 35, no. 7, pp. 2209–2213, Jul. 2015.

[57]   M. Frasnelli and V. M. Sglavo, "Flash sintering of tricalcium phosphate (TCP) bioceramics," *J. Eur. Ceram. Soc.*, vol. 38, no. 1, pp. 279–285, Jan. 2018.

[58]   S. Grasso *et al.*, "Modeling of the temperature distribution of flash sintered zirconia," *J. Ceram. Soc. Jpn.*, vol. 119, no. 2, pp. 144–146, 2011.

[59]   J. Park and I.-W. Chen, "In Situ Thermometry Measuring Temperature Flashes Exceeding 1,700°C in 8 mol% Y2O3-Stablized Zirconia Under Constant-Voltage Heating," *J. Am. Ceram. Soc.*, vol. 96, no. 3, pp. 697–700, 2013.

[60]   X. Hao, Y. Liu, Z. Wang, J. Qiao, and K. Sun, "A novel sintering method to obtain fully dense gadolinia doped ceria by applying a direct current," *J. Power Sources*, vol. 210, pp. 86–91, Jul. 2012.

[61]   Y. Dong and I.-W. Chen, "Predicting the Onset of Flash Sintering," *J. Am. Ceram. Soc.*, vol. 98, no. 8, pp. 2333–2335, 2015.

[62]   H. Yoshida, P. Biswas, R. Johnson, and M. K. Mohan, "Flash-sintering of magnesium aluminate spinel (MgAl2O4) ceramics," *J. Am. Ceram. Soc.*, vol. 100, no. 2, pp. 554–562, 2017.

[63]   A. Gaur, M. A. Mohiddon, and V. M. Sglavo, "Phenomenological understanding of flash sintering in MnCo2O4," *J. Eur. Ceram. Soc.*, vol. 38, no. 13, pp. 4543–4552, Oct. 2018.

[64]   M. Cologna, J. S. C. Francis, and R. Raj, "Field assisted and flash sintering of alumina and its relationship to conductivity and MgO-doping," *J. Eur. Ceram. Soc.*, vol. 31, no. 15, pp. 2827–2837, Dec. 2011.

[65]   H. Yoshida, Y. Sakka, T. Yamamoto, J.-M. Lebrun, and R. Raj, "Densification behaviour and microstructural development in undoped yttria prepared by flash-sintering," *J. Eur. Ceram. Soc.*, vol. 34, no. 4, pp. 991–1000, Apr. 2014.

[66]   J. S. C. Francis, M. Cologna, and R. Raj, "Particle size effects in flash sintering," *J. Eur. Ceram. Soc.*, vol. 32, no. 12, pp. 3129–3136, Sep. 2012.

[67]   R. Raj, "Joule heating during flash-sintering," *J. Eur. Ceram. Soc.*, vol. 32, no. 10, pp. 2293–2301, Aug. 2012.

[68]   J. S. C. Francis, M. Cologna, D. Montinaro, and R. Raj, "Flash Sintering of Anode–Electrolyte Multilayers for SOFC Applications," *J. Am. Ceram. Soc.*, vol. 96, no. 5, pp. 1352–1354, 2013.

[69]   J. S. C. Francis and R. Raj, "Flash-Sinterforging of Nanograin Zirconia: Field Assisted Sintering and Superplasticity," *J. Am. Ceram. Soc.*, vol. 95, no. 1, pp. 138–146, 2012.

[70]   J.-M. Lebrun and R. Raj, "A First Report of Photoemission in Experiments Related to Flash Sintering," *J. Am. Ceram. Soc.*, vol. 97, no. 8, pp. 2427–2430, 2014.

[71]   K. Terauds *et al.*, "Electroluminescence and the measurement of temperature during Stage III of flash sintering experiments," *J. Eur. Ceram. Soc.*, vol. 35, no. 11, pp. 3195–3199, Oct. 2015.

[72]   K. Naik, S. K. Jha, and R. Raj, "Correlations between conductivity, electroluminescence and flash sintering," *Scr. Mater.*, vol. 118, pp. 1–4, Jun. 2016.

[73]   J. Narayan, "A new mechanism for field-assisted processing and flash sintering of materials," *Scr. Mater.*, vol. 69, no. 2, pp. 107–111, Jul. 2013.

[74]   R. Chaim, "Liquid Film Capillary Mechanism for Densification of Ceramic Powders during Flash Sintering," *Materials*, vol. 9, no. 4, p. 280, Apr. 2016.

[75]   R. Chaim, "Particle Surface Softening as Universal Behaviour during Flash Sintering of Oxide Nano-Powders," *Materials*, vol. 10, no. 2, p. 179, Feb. 2017.

[76]   Corapcioglu G., Gulgun M. A., Kisslinger K., Sturm S., Jha S. K., and Raj R., "Microstructure and microchemistry of flash sintered K0.5Na0.5NbO3," *J. Ceram. Soc. Jpn.*, vol. 124, no. 4, pp. 321–328, Apr. 2016.

[77]   H. Yoshida, A. Uehashi, T. Tokunaga, K. Sasaki, and T. Yamamoto, "Formation of grain boundary second phase in BaTiO$_3$ polycrystal under a high DC electric field at elevated temperatures," *J. Ceram. Soc. Jpn.*, vol. 124, no. 4, pp. 388–392, 2016.

[78]   A. Uehashi, K. Sasaki, T. Tokunaga, H. Yoshida, and T. Yamamoto, "Formation of secondary phase at grain boundary of flash-sintered BaTiO3," *Microscopy*, vol. 63, no. suppl_1, pp. i19–i20, Nov. 2014.

[79]   R. Chaim and C. Estournès, "On thermal runaway and local endothermic/exothermic reactions during flash sintering of ceramic nanoparticles," *J. Mater. Sci.*, vol. 53, no. 9, pp. 6378–6389, May 2018.

[80]   J. Janek and C. Korte, "Electrochemical blackening of yttria-stabilized zirconia – morphological instability of the moving reaction front," *Solid State Ion.*, vol. 116, no. 3, pp. 181–195, Jan. 1999.

[81]   Y. Nakagawa, H. Yoshida, A. Uehashi, T. Tokunaga, K. Sasaki, and T. Yamamoto, "Electric current-controlled synthesis of BaTiO3," *J. Am. Ceram. Soc.*, vol. 100, no. 9, pp. 3843–3850, 2017.

[82]   Karakuscu Aylin *et al.*, "Defect Structure of Flash-Sintered Strontium Titanate," *J. Am. Ceram. Soc.*, vol. 95, no. 8, pp. 2531–2536, May 2012.

[83]   F. Lemke, W. Rheinheimer, and M. J. Hoffmann, "A comparison of power controlled flash sintering and conventional sintering of strontium titanate," *Scr. Mater.*, vol. 130, pp. 187–190, Mar. 2017.

[84]   E. Gil-González, A. Perejón, P. E. Sánchez-Jiménez, M. J. Sayagués, R. Raj, and L. A. Pérez-Maqueda, "Phase-pure BiFeO3 produced by reaction flash-sintering of Bi2O3 and Fe2O3," *J. Mater. Chem. A*, vol. 6, no. 13, pp. 5356–5366, Mar. 2018.

[85] L. A. Perez-Maqueda *et al.*, "Insight into the BiFeO3 flash sintering process by in-situ energy dispersive X-ray diffraction (ED-XRD)," *Ceram. Int.*, Aug. 2018.

[86] X. Su *et al.*, "Flash sintering of lead zirconate titanate (PZT) ceramics: Influence of electrical field and current limit on densification and grain growth," *J. Eur. Ceram. Soc.*, vol. 38, no. 10, pp. 3489–3497, Aug. 2018.

7

2   Research Objectives and Scope of The Dissertation

2.1   Statement of The Problem

Lead based piezoelectric materials are widely used in civil, military and energy applications as a sensors, resonators and transducers. Lead-based compositions such as modified lead zirconate titanate $PbZr_{0.5}Ti_{0.5}O_3$ (PZT), Ca and Sm doped lead titanate (PT), and lead magnesium niobate - lead titanate (1-x) $[Pb(Mg_{1/3}Nb_{2/3})\ O_3]$-x$[PbTiO_3]$ (PMN-PT) have outstanding piezoelectric and electromechanical properties. However, lead (Pb) is a volatile and toxic element which can enter to the atmosphere during high temperature processing of ceramics. It can directly (through inhalation) or indirectly (contaminated food, rain, etc.) cause various side effects on human body. Therefore, to protect the environment and public health, it is essential to develop new lead-free piezoelectric materials which can be used as alternatives for lead-based compositions.

Lead-based powder and ceramic also require a special handling, storage, disposal and recycling system due to their hazardous nature. European Union (EU), the Restriction of Hazardous Substances Directive (RoHS), and some of Asian countries such as Japan and China have banned usage of lead and lead-based materials in different applications including electronic devices. On the other side, the manufacturers have been required to be in charge of recovery and recycling of their waste products by the Waste Electrical and Electronic Equipment Directive (WEED) and the End of Life Vehicle Directive (ELV). These legislations were driving force to find safer materials in piezoelectric industries. During past decade, noticeable research efforts have been carried out on environment friendly, biocompatible and lead-free compositions and numbers of publications in this field have been remarkably increased.

Currently, bismuth sodium titanate (BNT) and sodium potassium niobate (KNN) have been introduced as two main categories of perovskites lead-free materials. Donor and acceptor dopants have been utilized to enhance the electromechanical properties and obtained desire application-specific properties. A major part of the studies has been allocated to develop soft piezoelectrics through A-site substituted with high piezoelectric coefficient for applications including energy harvesting and MEMs. While there is a need to extensively study the effect of B-site dopants on electromechanical properties and develop hard lead-free piezoceramics with minimal heat dissipation and power consumption for high power applications.

Another field of interest for the development of piezoceramic is sintering method and conditions in which have been given a broad range of study worldwide and continue to get attention today. Sintering temperature and dwell time directly affected on the densification, the chemical stoichiometry and the electromechanical properties of piezoceramics. There is a tremendous amount of research on lowering the sintering temperature to control the loss of volatile elements such as Bi, Pb, Na, K, and Li in both Pb and Pb-free based compositions. One of the newest sintering methods which effectively help to reduce the temperature is Flash sintering (FS) introduced by Cologna, et al.in 2010. A wide variety of binary and ternary oxide ceramics such as oxygen-ion conductors, semiconductors, dielectrics, and piezoelectrics has been densified through FS. However, there is a limited study on the flash sintering of complex oxide and ferroelectric materials. There is a lack of information on the effect of the flash sintering parameter on the electromechanical properties. On the other side, high quality ceramic with enhanced electromechanical properties will be achieved by the optimization of the all processing parameter including

particle size, pressing condition, sintering temperature and time. A significant part of the research on lead-free piezoelectric transducers has been devoted to high frequency non-invasive medical ultrasound devices. However, there is a necessity to develop low frequency lead-free transducers with high output energy for therapeutic application. Until now, hard lead-based piezoceramics are the only available materials for therapeutic and high intensity focused ultrasound transducers.

2.2   Research Objective

The primary goal of this thesis work is to develop, optimize the processing conditions and investigate the electromechanical properties of hard lead-free BNT-based ceramics. In addition, high power transducers have been developed and their acoustic pressure and acoustic intensity characterization have been tested.

On the development of the ceramics, the study was focused on the effects of acceptor dopants on the piezoelectric, ferroelectric and electrical properties. A reliable processing conditions has been established with high degree of reproducibility. The details of the research work are:

1- To investigate the effect of acceptor dopants such as Mn and Fe on electromechanical properties.

2- To study the effect of the powder particle size on the sintering temperature, grain size and electromechanical properties.

3- Comprehensive study on the effect of Mn and Fe as acceptor dopants on the electrical properties of grains and grain boundaries in the ceramics by impedance spectroscopy.

4- Investigate the high power performance of hard BNT-based ceramics for high power application purposes.

5- Prototype single element High Intensity Focus Ultrasound (HIFU) transducer to evaluate the functionality of hard BNT-based composition.

6- Characterize the acoustic pressure and acoustic intensity and compared to PZT counterparts.

Another objective of this research was the development of BNT-based ceramic by flash sintering method as outlined below:

7- Optimization of flash sintering parameters to fabricate dense BNT-based ceramic at low temperature

8- Investigate the microstructure, chemical composition, and crystalline phase of densified ceramics.

9- Study the effect of current density and holding time on the piezoelectric and ferroelectric properties

10- Study the effect of flash sintering on electrical properties of grain and grain boundaries by impedance spectroscopy.

3   Preparation and Characterization Methods:

3.1   Powder Synthesize

The ternary system of BNT-BKT-BLT ceramic powder with a chosen formulation and compositions (Table 3.1) were synthesized by the conventional mixed-oxide method. High purity precursor ($\leq$99.9%) including oxides and carbonates powders; K_2CO_3 (Alfa Aesar, 99.997%), Na_2CO_3 (Alfa Aesar, 99.997%), Li_2CO_3 (Sigma-Aldrich, 99.99%), Bi_2O_3 (Alfa Aesar, 99%), TiO_2 (Sigma-Aldrich, 99.9%), $MnCO_3$ (Alfa Aesar, 99.9%), Fe_2O_3 (Alfa Aesar, 99.945%); were dried overnight at 120 °C. Dried powders were then mixed and milled in acetone with yttrium-stabilized zirconium balls for 12 h or 24h. The mixed powder was dried and calcined at 800 °C for 3 h with the heating and the cooling rate of 5 °C.min^{-1}. In order to obtain a uniform homogenous powder, the calcined powder was milled again for 12 h, 24h or 36h.

Table 3. 1. Chemical composition of synthesized powders and ceramics in this study

Chemical Composition	Abbreviation	x%
$(BiNa_{0.88} K_{0.08}Li_{0.04})_{0.5}Ti\, O_3$	BNKLT88	----
$(BiNa_{0.88} K_{0.08}Li_{0.04})_{0.5}Ti_{1-x}Mn_x\, O_3$	BNKLT88-x% Mn	1.0,1.4,1.5,1.6,1.7, 2.0, 2.2
$(BiNa_{0.88} K_{0.08}Li_{0.04})_{0.5}Ti_{1-x}Fe_x\, O_3$	BNKLT88-x% Fe	1.25, 1.5, 1.75

53

3.2   Consolidating and Sintering

The calcined powder sieved by 100-micron mesh to get uniform distribution of powder. In order to create the plastic flow, and optimize the density of green body 8 wt% Poly Vinyl Alcohol solution (10wt%PVA in water) was added to the powder. In addition, uniaxial pressing flaw such as delamination is hinder via binder addition to the powder. Then, another step of sieving was done to break up all the agglomerated powders. The steel die with diameter of 14, 12.9 and 6.35 mm accompany with the hydraulic machine was used to uniaxially press the disk-shape samples under 150 MPa pressure. In order to remove the binder, the samples heat treated at 550 °C for 2 h with heating and cooling rate of 1.5 °C.min^{-1}. Next, the samples sintered via conventional sintering (CS) or flash sintering (FS).

3.2.1   Conventional Sintering

In this study cylindrical pellet with diameter of 14, 12.9 and 6.35 mm was used for conventional sintering. A thin layer of platinum foil was placed between samples and high-alumina crucible in order to prevent any possible reaction between the alumina and the samples. In the purpose of minimizing the possible evaporation of bismuth and alkaline and also to protect the possible contaminations, the samples were covered with another high-alumina dish. The furnace was set at the desired temperature with heating and cooling rate of 5 °C.min^{-1} for 2h.

3.2.2 Flash Sintering

Doegbone, rod and pellet are three most common sample geometries used for flash sintering experiments (Fig. 3.1) [1]. In this study, a cylindrical pellet with 6.35 mm diameter was used for flash sintering experiment.
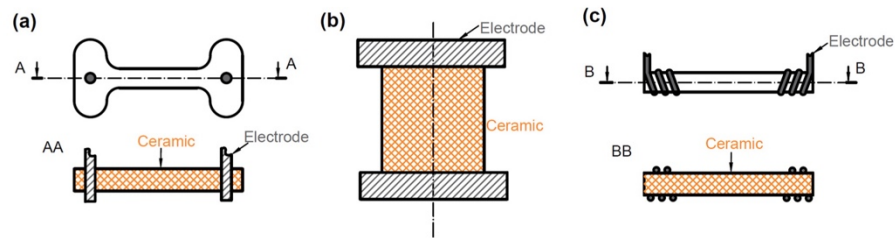
Figure 3. 1. (a) doge bone (b) pellet (c) rod as three common sample geometries in flash sintering experiments [1]

Fig. 3.2 schematically demonstrate the set up for FS study. AC or DC electric field applied across the cylindrical specimen via one of the power supplies mentioned in Table 3.2. The lab view program controls the applied electric field and current limit. It also records the electric field, current density, power density, furnace temperature, and linear displacement output data. Eurotherm 2404 controller and Epack SCR were used to control the temperature. The alumina stage was put inside the custom furnace, after loading the specimen in the purpose-built space. The furnace is capable of reaching to 1200 °C.

Table 3. 2. Power supplied used for flash sintering experiment

	Equipment	Voltage range (V)	Current range (A)	Frequency (Hz)
DC	BK 9115	0-80	0-60	----
AC	Pacific 118ACX	0-150	0-10	45-1200
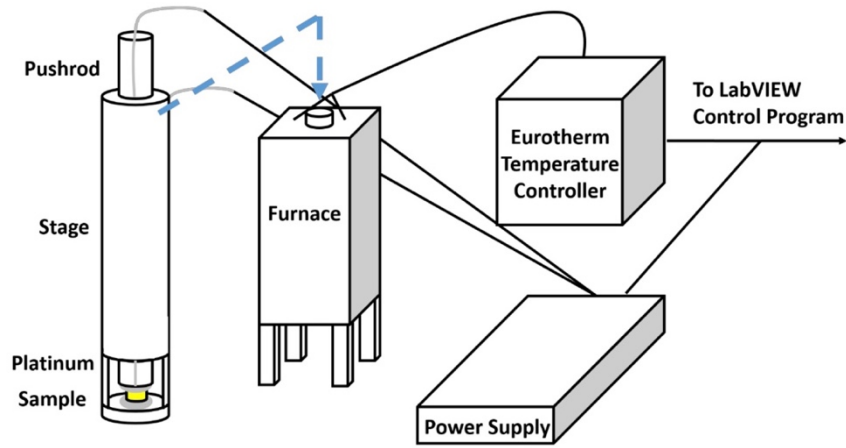
Figure 3. 2. Schematic of flash sintering set up at Rutgers University, Dr. Tsakalakos

3.3 Ferroelectric and Dielectric Characterization

In order to obtain the desired thickness (< 1mm), the ceramics were mechanically polished and then the high temperature silver past (PELCO®, Ted Pella, CA) diluted in n-Butyl Acetate was applied on the surface of the ceramic as the bottom and top electrode. After heat treating at 550 °C for 20 min, the samples were poled under application of electric filed via DC power supply. 24 hours after polling, the electrical properties were evaluated. An impedance analyzer HP4194A with an oscillation level of 1 volt, and set at 1 kHz, was used to measure the dielectric constant ($\varepsilon_r = \varepsilon_{33}^T/\varepsilon_0$) and dielectric loss (tan δ). The longitudinal piezoelectric charge coefficient (d_{33}) was measured at 100 Hz via Berlindourt piezometer (Channel Products Inc., OH). The resonance (series) frequency, f_s, and antiresonance (parallel) frequency, f_p, were used to evaluate the piezoelectric planar and thickness coupling coefficient (k_p and k_t, respectively) [2], [3]

$$\frac{k_p^2}{1-k_p^2} = \frac{\Delta f}{f_s(1+\sigma_p)}\left[(\sigma_p^2)-1+\eta^2\right] \tag{3.1}$$

$$k_t^2 = \frac{\pi}{2}\frac{f_s}{f_p}\tan\left(\frac{\pi.\Delta f}{2f_p}\right) \tag{3.2}$$

where σ_p is the planar Poison's ratio and η is frequency constant of disk resonator.

The thickness and planar coupling coefficient were utilized to calculate the longitudinal coupling coefficient, k33, and clamped dielectric constant ($\varepsilon_{33}^S/\varepsilon_0$) as specified by following equations

$$k_{33} = k_p^2 + k_t^2 - k_p^2 k_t^2 \qquad (3.3)$$

$$\left(\frac{\varepsilon_{33}^S}{\varepsilon_0}\right) = \left(\frac{\varepsilon_{33}^T}{\varepsilon_0}\right)(1 - k_t^2)(1 - k_p^2) \qquad (3.4)$$

Three different methods were used to estimate the planar mechanical quality factor (Q_m) at radial resonance frequency:

I. 3dB up/down technique in admittance spectrum and using following formula

$$Q_A = \frac{\omega_a}{(\omega_{a2} - \omega_{a1})}$$

where Q_A is mechanical quality factor at resonance frequency ω_a is resonance frequency and $(\omega_{a2} - \omega_{a1})$ is equivalent to 3dB bandwidth in the admittance curves around resonance (Fig. 3.3)
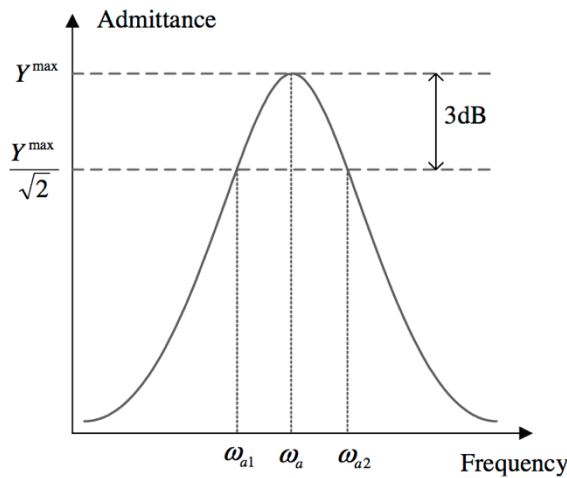
Figure 3. 3. Quantification of mechanical quality factor via 3 dB down/up method in admittance spectrum at resonance frequency [4]

II. Using Van-Dyke equivalent circuit of piezoelectric resonator at the resonance frequency (Fig. 3.4) and equation 3.5

$$Q_m = \frac{1}{R}\sqrt{\frac{L}{C_a}} \tag{3.5}$$

where R is the resistance, L is the inductance, and C_a is the capacitance from the Van-Dyke equivalent circuit.
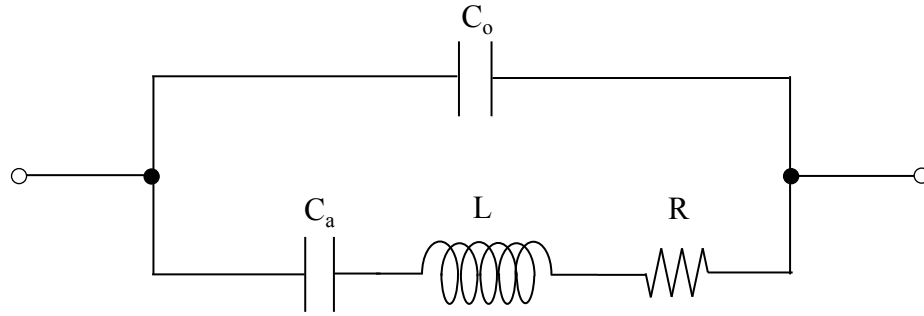
Figure 3. 4. Van-Dyke model for piezoelectric resonator

The Van-Dyke model consists of a parallel connection of a capacitor, C_0, and series LCR. C_0 represents the electrostatic capacitance and LCR represents the mechanical mass, elastic compliance, and damping of the piezoelectric resonator.

III. Based on the IRS and IEEE standard the equation 3.6 can be used to estimate the planar mechanical quality factor

$$Q_m^{-1} = 2\pi f_s |Z_m|(C_0 + C_1)\frac{f_p^2 - f_s^2}{f_p^2} \tag{3.6}$$

where Z_m is the minimum impedance, C_0 is the shunt capacitance, and C_1 is the series capacitance of the sample.

Although the results showed that the value of Q_m obtained by all three methods are very close to each other (5%), the first method seems to be more accurate. In the first method estimation of the equivalent circuit parameters are eliminated and the admittance spectrum is directly obtained via admittance spectrum which result in higher accuracy.

3.4   High Power Characterization

Loss factors and high power characterizations in piezoelectric materials can be evaluated via various methods including thermal analysis, pseudostatic, admittance spectrum, and transient/burst mode methods. Constant voltage, constant current, and constant vibration velocity are known as three categories of the admittance/impedance spectrum method [4], [5]. Although the constant voltage and constant current modes can be used to evaluate the mechanical quality factor (Q_m) at resonance frequency (Q_A) and antiresonance frequency (Q_B), in reality, the current and voltage are not thoroughly constant at these fundamental of frequencies. The non-linear behavior of elastic compliance leads to significant distortion of admittance frequency under constant voltage [4]. In contrast, the vibration velocity mode provides higher accuracy while prevent the distortion of the admittance spectrum. This method also makes possible to measuring the resonance and antiresonance frequency in single set of experiment. Consequently, in this study the constant vibration velocity, which schematically illustrated in Fig 3.5 was selected for evaluation of high power performance of piezoceramics.
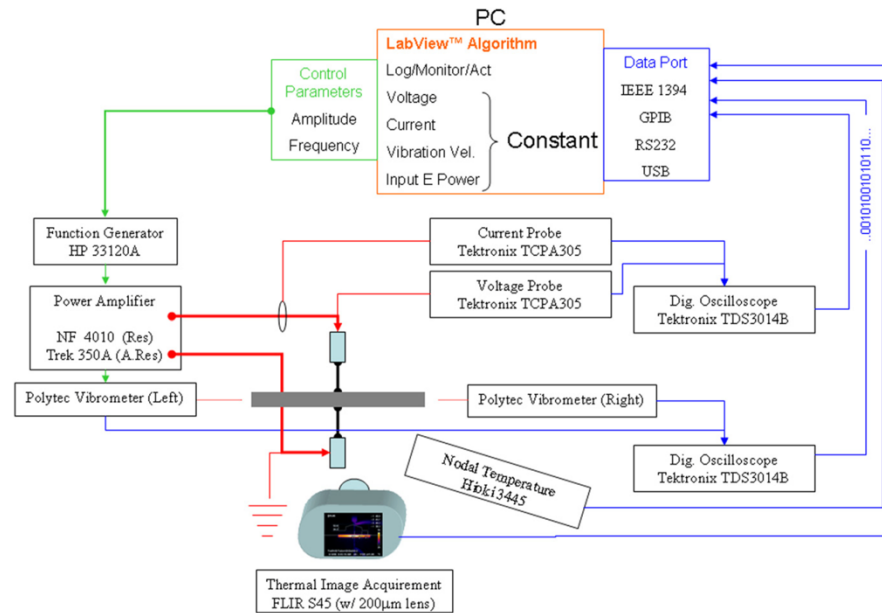
Figure 3. 5. Schematic set up of high power characterization system (HiPoCS), Penn State University [4]

A function generator (HP 331120 Hewlett-Packard, Palo Alto, CA) produced a sinusoidal signal, which was amplified via power amplifier (NF 4010, NF Corporation, Yokohanma, Japan). A clamp-on AC current sensor (TCP 305, Tektronix) detected the sample current. Two digital oscilloscopes (TDS 3014B, Tektronix) were used to monitor the voltage, current and displacement waveforms of the piezoceramic sample while a laser interferometer (Polytec Polytec PI, Model OFV-511, Polytec Inc., Irvine, CA) was utilized to measure the vibration amplitude on the edge of the sample. An infrared spot thermometer (HIOKI 3445, Japan) monitored the temperature on the surface of the specimen nodal point while a thermal camera (FLIR Systems Therma-CAM S40, FLIR Systems, Boston, MA) tooke the thermal images. A Lab VIEW program was used to automatically control the driving voltage and current to maintain constant vibration velocity over the whole range of frequencies.

The mechanical quality factor at the resonance (Q_A) and antiresonance (Q_B) at each vibration velocity were calculated from the admittance/impedance curves and using 3dB up/down technique (Fig. 3.3 and 3.6) and using following formula

$$Q_A = \frac{\omega_a}{(\omega_{a2} - \omega_{a1})} \tag{3.7}$$

$$Q_B = \frac{\omega_b}{(\omega_{b2} - \omega_{b1})} \tag{3.8}$$

where ω_b is antiresonance frequency and $(\omega_{b2} - \omega_{b1})$ is equivalent to 3dB bandwidth in the admittance curves around the antiresonance.
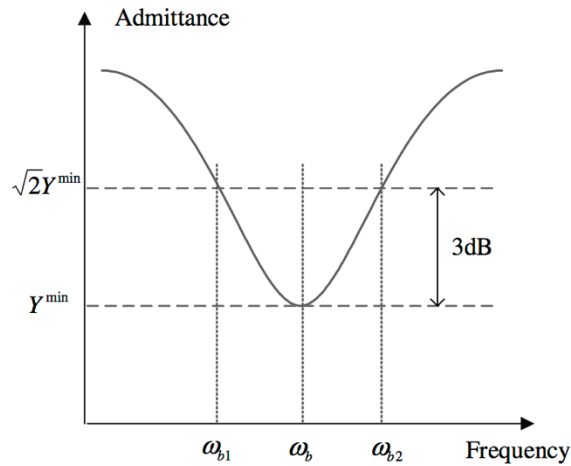
Figure 3. 6. Quantification of mechanical quality factor via 3 dB down/up method in admittance spectrum at antiresonance frequency $Q_B = \omega_b/(\omega_{b2} - \omega_{b1})$ [4]

3.5 Impedance Spectroscopy

The complex impedance spectroscopy is a technique to systematically measure the electrical properties of electroceramics in the wide range of frequencies. The following four basic immittance formalisms of impedance (Z^*), permittivity (ε^*), modulus (M^*), and admittance (Y^*) are interrelated (Table 3.3) and can be used to interpret AC electrical data.

$$Z^* = Z' - jZ'' \tag{3.9}$$

$$\varepsilon^* = \varepsilon' - j\varepsilon'' \tag{3.10}$$

$$M^* = M' + jM'' \tag{3.11}$$

$$Y^* = Y' + jY'' \tag{3.12}$$

where $(Z', \varepsilon', M', Y')$ and $(Z'', \varepsilon'', M'', Y'')$ are the real and imaginary components of the impedance, permittivity, modulus, and admittance, respectively. $j \equiv \sqrt{-1} \equiv \exp(j\pi/2)$, ω is the angular resonance frequency and C_0 is the capacitance of the empty cell.

$$\omega = 2\pi f \tag{3.13}$$

$$C_0 = \frac{\varepsilon_0 A}{L} \tag{3.14}$$

where f is the relaxation frequency, ε_0 is the permittivity of free space, 8.854×10^{-14} F.cm^{-1}, A is the area, and L is the thickness of the material.

Table 3. 3. "Relations between the four basic immittance functions" [6]

	M	Z	Y	ε
M	M	$j\omega C_0 Z$	$j\omega C_0 Y^{-1}$	ε^{-1}
Z	$(j\omega C_0)^{-1}M$	Z	Y^{-1}	$(j\omega C_0)^{-1}\varepsilon^{-1}$
Y	$j\omega C_0 M^{-1}$	Z^{-1}	Y	$(j\omega C_0)\,\varepsilon$
ε	M^{-1}	$(j\omega C_0)^{-1}Z^{-1}$	$(j\omega C_0)^{-1}Y$	ε

The Z* and Y* functions are useful to analyze the resistivity and/or conductivity where the long-range conduction dominates. On the other side, if the localized relaxation dominates, the ε* and M* functions are suitable to use. As a result, it is necessary to plot the data in all terms (impedance, admittance, electrical modulus, and dielectric permittivity) to provide a comprehensive information about the physical process taking place in the materials [7]. These complex functions can be graphically illustrated by using Polar and Cartesian coordinate in a form of Nyquist and Bode plot (Fig 3.7).

The magnitude of the complex impedance defines the impedance modulus, $Z_{mode} = |Z|$, and the phase shift between the applied voltage and the current defines the phase angle, Z_θ, wherein $0 \leq Z_\theta \leq 1$. With the aims of these two quantities, the real and the imaginary part of the impedance can be determined

$$Z' = Re(Z) = Z_{mode}Cos(Z_\theta) \qquad (3.15)$$

$$Z'' = Im(Z) = Z_{mode}Sin(Z_\theta) \qquad (3.16)$$

The plot of imaginary part of the impedance ($-Z''$ or $-ImZ^*$) vs. real part of impedance (Z' or $Re\ Z^*$) on a linear presentation calls Nyquist Plot while Bode-Bode plot is Z^*, Z', Z'' and phase angle $\theta(\omega)$ vs. frequency in logarithmic or in linear coordinates. Each peak or anomaly in Bode-Bode plot and each semi-circle in Nyquist plot associated with a distinct process. In this regard, the relationship between microstructure and electrical properties, and the contributions of grain, grain boundaries and electrode/specimen interface can be obtained from complex impedance plots. The semi-circle at high frequency (I) attributed to bulk and grain interior conduction response, the second semi-circle at intermediate

frequency (II) is attributed to the grain boundary conduction, and at low frequency the semicircle arc (III) is attributed to contribution of the electrode-material interface.
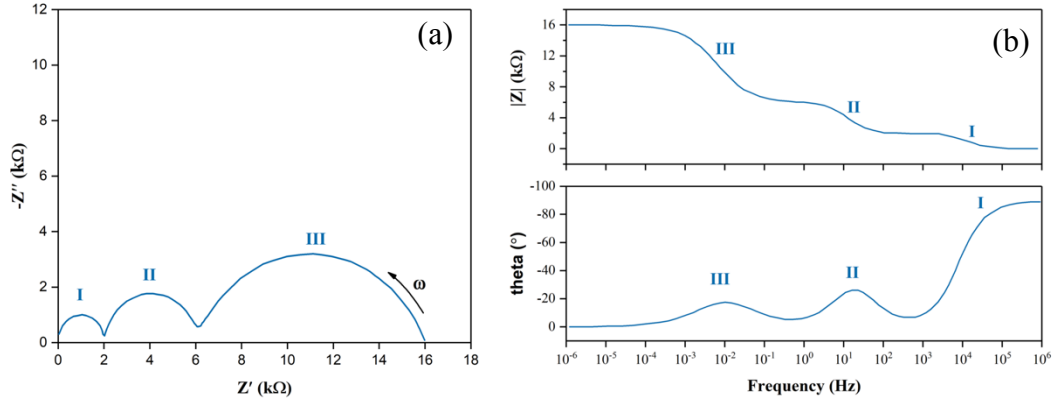
Figure 3. 7. The schematic of (a) Nyquist plot (b) Bode-Bode plot

The equivalent circuit which consist of discrete electrical components usually utilizes to study the behavior of the real system and to analysis the impedance spectroscopy data. The basic circuit elements are resistor, capacitance, inductance, constant phase elements, and Generalized Finite-Length Warburg Element.

In the case of ideal resistor there is no phase delay in the current, and Z_θ is zero. As a result, the impedance consists of only real part ($Z' = R$, $Z'' = 0$)

$$Z^* = Z_R^* = R \tag{3.17}$$

where R is resistance. On the other side, the phase angle of perfect capacitor is -90°, so the impedance consists of only imaginary (complex) part

$$Z^* = Z_C^* = \frac{1}{j\omega C} \tag{3.18}$$

where C is the capacitance. In microscopic scale, the materials properties are often distributed due to non-homogeneity in the system, such as rough or porous surface. The constant phase element (CPE) is a non-intuitive equivalent electrical circuit component that models the behavior of real-world system [8]. The impedance of CPE, mathematically define as

$$Z^* = \frac{1}{(j\omega)^\alpha C_\alpha} = \frac{1}{(j\omega)^\alpha Y_0} \tag{3.19}$$

with two parameters of Y_0 and α ($0 \leq \alpha \leq 1$), which are frequency independent but temperature dependent. The phase angle of impedance CPE has a value of $-(90 \times \alpha)$. Pure resistor and pure capacitor can be obtained at $\alpha=0$ and $\alpha=1$, respectively.

The impedance of inductance defined from equation 3.20

$$Z = j\omega L \tag{3.20}$$

The parallel connection of a resistor, R, and constant phase element, CPE, known as ZARC, which is one of the most important subcircuit to fit the impedance data. The impedance of ZARC is

$$Z^*_{ZARC} = \frac{R}{1 + R Y_0 (j\omega)^\alpha} \tag{3.21}$$

By way of illustration, Fig. 3.2 consists of 3 semicircles which can be fitted to 3 ZARC subcircuit (Fig. 3.8)
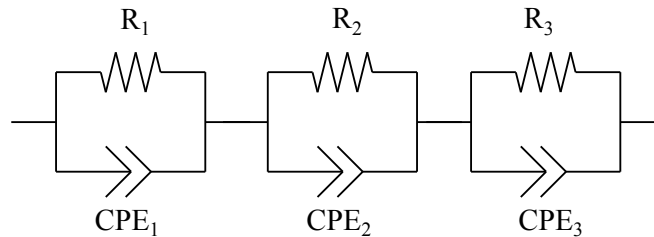
Figure 3. 8. Three R-CPE, ZARC, subcircuit in series

In this study, the impedance measurements performed via a Gammry Reference 600+ potantiostat at temperature range of 450 to 600°C with 25 °C step size, the applied voltage of 1000 mV, and over frequency range from 1 Hz to 1MHz.

3.6 X-Ray Photo Electron Microscopy

X-Ray Photo Electron Microscopy (XPS) [9], [10] or electron spectroscopy for chemical analysis (ESCA) is non-destructive technique which commonly use to estimate the surface chemistry of materials and elemental composition. It also provides information about empirical formula, chemical state, and electronic state of the existing elements within a material. Although in theory XPS supposed to detect all the elements, in practice it can detect the element with atomic number (Z) higher than 3.

In this method, a sample is irritated by a beam of X-rays- Monochromatic or unfiltered Al K_α or Mg K_α under vacuum condition where leads to emission of photo electron from the surface of the sample (Fig 3.9). The emitted electrons and their kinetic energy from the top 1-10 nm of the surface of the material were simultaneously evaluated. The chemical state and quantitative information can be obtained from the position and intensity of the peaks in an energy spectrum. The measured kinetic energy ($E_{kinetic}$) depends on the chemical state of an atoms which also effects on the binding energy of the electron ($E_{binding}$)

$$E_{binding} = E_{photon} - (E_{kinetic} + \phi) \text{ or } BE = vh - KE \tag{3.22}$$

where E_{photon} is the energy of the X-rays photon being used for sample irritation (vh) and ϕ is the work function. The bulk chemistry can be characterized via fracturing, cutting or scraping in air or under ultra-high vacuum (UHV) condition. Mild ion beam etching use

for cleaning the surface while more extensive ion etching use to expose deeper layer and for depth-profiling XPS.
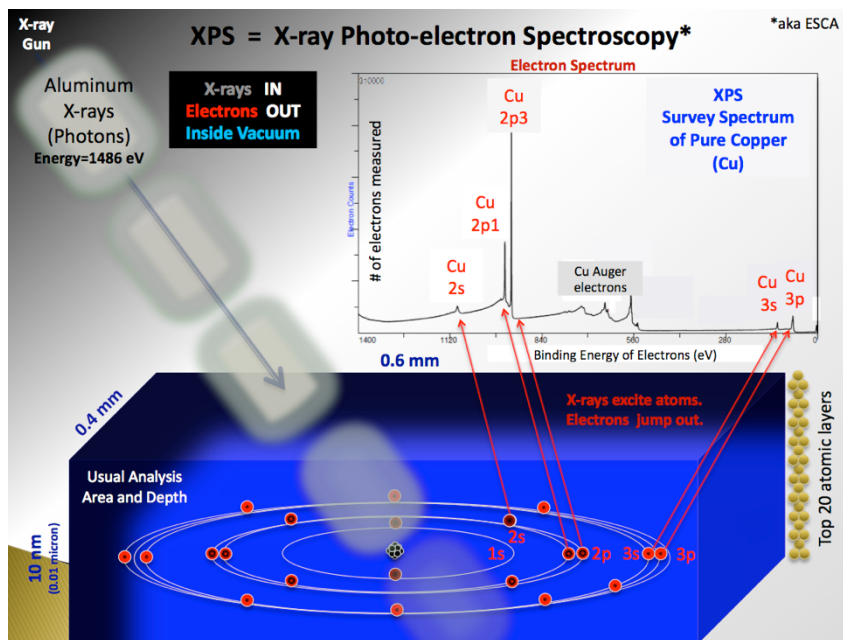
Figure 3. 9. Schematic of photoelectron spectroscopy

In this research study, ThermoFisher K-Alpha E-Ray Photoelectron Spectroscopy with 1486.7 X-ray photon energy and 400 μm spot size utilized for chemical analysis of the samples.

3.7   X-ray Diffraction

The X-ray diffraction (XRD) is non-destructive technique which is used to analyze all types of materials such as crystals, fluids, powder, and amorphous. Strong electric field (20-60 kV) is used to accelerate high velocity electron which is utilized to bombard metal targets. This interaction between high velocity electron and metal target lead to X-rays emitting. Copper (Cu) and molybdenum (Mo) are considered as two most common metal targets while chromium (Cr), cobalt (Co) and iron (Fe) can also use to generate X-ray.

The atomic arrangement of the materials can be studied via analyzing the XRD pattern. The principal of the XRD is based on the Bragg's law (equation 3.23 and Fig. 3.10)

$$n\lambda = 2d_{hkl} \sin\theta \qquad\qquad (3.\,23)$$

where n is a positive integer, taken as 1, λ is the wave length of the beam (radiation), d_{hkl} is the spacing of the crystal lattice planes responsible for particular diffracted beam or d-spacing of the Millar index, hkl, and θ is the incident angle.

The collected XRD pattern analysis to determine the orientation of a single crystal or polycrystalline samples, estimating the grain size, internal stress and small crystallin region. Peak positions provide information about the translation symmetry, size and the unit cell. On the other side, the details about the electron density and location of atoms inside the unit cell can be obtained from the peak intensity. Additionally, the information on deviation from a perfect crystal and grain size are provided via studying the peak shapes and width.
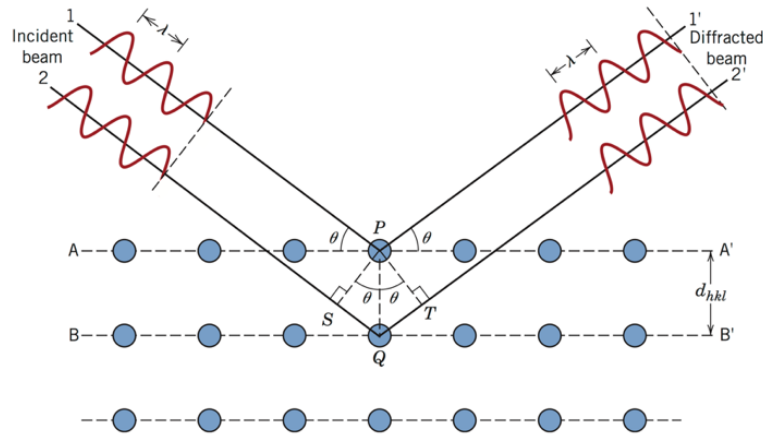
Figure 3. 10. Diffraction of X-ray by planes of atom and schematically illustration of Bragg's law [11]

3.8   Scanning Electron Microscopy

Scanning Electron Microscopy (SEM) uses accelerated electron as the illumination source to get higher resolution power which allows to explore the features of smaller object. The scanning speed must be restricted in order to sequentially collect all the specimen signal for each data point. To avoid the accumulation of charge on the surface of the sample the specimen should be electrically conductive. In this purpose a thin layer of metal electrode such as Au or C should be deposited onto the surface of insulative specimen.

A Zeiss Sigma Field Emission SEM and Phenom Pro SEM were used in the studies. After mirror polishing, thermal etching was done via heat treatment of the samples at 850 °C for 30 min. A 10 nm gold was coated onto the surface to explore the microstructure. However, the samples for energy-dispersive spectroscopy (EDS) did not coated with electrode. The porosity was estimated via using ImageJ softaware.

3.9   Summary

This chapter aimed to provide a general overview on sample preparation used in this investigation including powder processing, conventional sintering and flash sintering. The fundamental principles of characterization techniques which has been used to understand the behavior and properties of bismuth sodium titanate based ceramics are discussed. Electromechanical properties at low drive conditions were evaluated based on IEEE standard. The high power characteristic was measured at constant vibration velocity mode. The crystallography structures are studied with x-ray diffraction pattern. The chemical and composition analysis was determined by x-ray photo electron microscopy

and energy dispersive spectroscopy. The impedance spectroscopy was utilized to study the conductivity behavior of grain and grain boundary.

3.10 References

[1] M. Biesuz and V. M. Sglavo, "Flash sintering of ceramics," *J. Eur. Ceram. Soc.*, vol. 39, no. 2, pp. 115–143, Feb. 2019.

[2] "Publication and Proposed Revision of ANSI/IEEE Standard 176-1987 'ANSI/IEEE Standard on Piezoelectricity,'" *IEEE Trans. Ultrason. Ferroelectr. Freq. Control*, vol. 43, no. 5, pp. 717-, Sep. 1996.

[3] "IRE Standards on Piezoelectric Crystals: Measurements of Piezoelectric Ceramics, 1961," *Proc. IRE*, vol. 49, no. 7, pp. 1161–1169, Jul. 1961.

[4] K. Uchino, Y. Zhuang, and S. O. Ural, "Loss determination methodology for a piezoelectric ceramic: new phenomenological theory and experimental proposals," *J. Adv. Dielectr.*, vol. 01, no. 01, pp. 17–31, Jan. 2011.

[5] K. Uchino, "Chapter 17 - High-Power Piezoelectrics and Loss Mechanisms," in *Advanced Piezoelectric Materials (Second Edition)*, K. Uchino, Ed. Woodhead Publishing, 2017, pp. 647–754.

[6] J. R. Macdonald and W. R. Kenan, *Impedance Spectroscopy: Emphasizing Solid Materials and Systems*. Wiley, 1987.

[7] R. N. P. Choudhary, D. K. Pradhan, C. M. Tirado, G. E. Bonilla, and R. S. Katiyar, "Impedance characteristics of Pb(Fe2/3W1/3)O3–BiFeO3 composites," *Phys. Status Solidi B*, vol. 244, no. 6, pp. 2254–2266, Jun. 2007.

[8] E. Barsoukov and J. R. Macdonald, *Impedance Spectroscopy: Theory, Experiment, and Applications*. Hoboken, UNITED STATES: John Wiley & Sons, Incorporated, 2005.

[9] "X-ray photoelectron spectroscopy," *Wikipedia*. 13-Feb-2019.

[10] "Thermo Scientific XPS: What is XPS." [Online]. Available: https://xpssimplified.com/whatisxps.php. [Accessed: 10-Mar-2019].

[11] W. D. Callister, *Materials science and engineering: an introduction*. New York: John Wiley & Sons, 2007.

Electromechanical Properties of Acceptor-Doped Lead-Free Piezoelectric Ceramics

Elaheh Taghaddos, Mehdi Hejazi, and Ahmad Safari

Glenn Howatt Electroceramics Laboratories, Department of Materials Science and

Engineering, Rutgers, The State University of New Jersey, New Jersey 08854

4   Electromechanical Properties of Acceptor-Doped Lead-Free Piezoelectric Ceramics

Abstract

We have studied the processing and electromechanical properties of Mn and Fe-doped $0.88[Bi_{0.5}Na_{0.5}TiO_3]$-$0.08[Bi_{0.5}K_{0.5}TiO_3]$-$0.04[Bi_{0.5}Li_{0.5}TiO_3]$ piezoelectric ceramics prepared by the mixed oxide route. Different amounts of Mn (0.01, 0.014, 0.015, 0.016, 0.017, 0.02, 0.022) or Fe (0.0125, 0.015, 0.0175) were doped to this lead-free piezoelectric composition. Ceramics were sintered at different temperatures (1075°C–1150°C) to achieve the highest density and mechanical quality factor. Mn or Fe doping resulted in a considerable enhancement of Q_m in both planar and thickness resonance modes. In 1.5 mol% Mn-doped ceramics sintered at 1100°C, a planar Q_m of about 970 and tanδ of 0.88% were obtained. In Fe-doped ceramics, a planar Q_m as high as 900 was achieved. Acceptor dopants also resulted in decreasing the coupling coefficients, the piezoelectric charge coefficient, and the dielectric constant.

4.1   Introduction

For high power applications such as ultrasonic motors, high power sonar, and piezoelectric transformers, minimum heat generation and maximum output power are desired. Hard piezoelectric ceramics with a high mechanical quality factor (Q_m), low dielectric loss, low mechanical loss, and high coercive field are suitable materials for high power applications [1]. The low mechanical and dielectric losses in hard ferroelectrics prevent dissipation of energy in the form of heat and hence, increase the efficiency of the device. The power loss per unit volume is inversely proportional to the mechanical quality factor [2].

In lead-based ceramics such as lead zirconate titanate (PZT), hard compositions with a high Q_m have been commercially developed by partial substitution of Ti with acceptor dopants such as $Mn^{2+,3+}$, $Fe^{2+,3+}$, and Cr^{3+} [3]–[5]. Acceptor dopants with a lower valence than the host cations (e.g., Zr^{4+} and Ti^{4+}) create oxygen vacancies to maintain the charge neutrality. In the perovskite structure, oxygen vacancies are able to diffuse to the domain walls through octahedral sites [5], [6]. The positively charged oxygen vacancies form oriented dipoles with negatively charged acceptor sites (e.g., $V_O^{\bullet\bullet} - Mn_{Ti}''$). The defect dipoles are known to reduce the extrinsic ferroelectric contribution by pinning the domain walls [2], [5]–[7]. The formation of defect dipoles is accompanied by building up of an internal bias field in the direction of the spontaneous polarization [4]–[9]. The internal bias field prohibits the ferroelectric domain wall motion and is recognized by an imprint or a horizontal shift in P–E hysteresis loops [8], [10]. Consequently, the addition of acceptor dopants decreases the piezoelectric activity of the electroceramics, but results in a considerable enhancement of the mechanical quality factor as well as the coercive field.

Donor dopants such as Nb^{5+}, on the other hand, induce soft piezoelectric characteristics by creating A-site vacancies and randomly distributed point defects [5]. In general, materials with a high Q_m, high E_c, low $\tan\delta$, and high coupling coefficients (k_{ij}) are the best candidates for high power applications. The suppression of the domain wall motion is the essential key for decreasing the dielectric, mechanical, and piezoelectric losses under high drive conditions. As indicated, high Q_m can be achieved through the domain wall pinning and development of an internal bias field upon addition of acceptor dopants [5]. Grain boundaries in a polycrystalline ceramic have similar pinning effect as the dipole defects. Therefore, the grain size refinement can be considered to be another method for enhancing the mechanical quality factor [11]. It has been demonstrated that the heat dissipation under high electric field in PZT ceramics can be suppressed by the addition of acceptor dopants Mn and Fe [12]–[14], whereas it is increased through the addition of donor dopants [15].

In lead-free materials such as BNT and KNN ceramics, the mechanical quality factor can be similarly enhanced by the addition of acceptor dopants [16]. In KNN-based ceramics, Q_m values as high as 1500–2000 have been achieved by Cu doping and addition of sintering aids such as $K_{5.4}Cu_{1.3}Ta_{10}O_{29}$ (KCT), $K_4CuNb_8O_{23}$ (KCN), and $K_{1.94}Zn_{1.06}Ta_{5.19}O_{15}$ (KZT). Due to the hygroscopic nature of precursor materials, processing of KNN ceramics are sensitive to the atmosphere conditions, such as humidity. Furthermore, the orthorhombic–tetragonal phase transition which occurs at about 190°C, is a drawback for high power applications [4], [8], [17]. On the other hand, BNT-based ceramics show higher remanent polarization and coercive field than KNN-based materials. It is reported that the modification in BNT ceramics by doping small amount of Li^+ into the A site, increases the depolarization temperature to 220°C [18]. BNT-based

piezoelectrics, therefore, can be potential candidates for high power applications. However, there is limited information published on hard BNT-based ceramics. Tou et al. [19] reported a Q_m of about 500, Curie temperature of 260°C, and a dielectric constant of 520 in a $0.82(Bi_{0.5}Na_{0.5})TiO_3–0.15BaTiO_3–0.03(Bi_{0.5}Na_{0.5})(Mn_{1/3}Nb_{2/3})O_3$ solid solution. This composition was successfully used in the fabrication of ultrasonic cleaners [19]. Nagata et al. [16] and Takenaka et al. [20] showed that the mechanical quality factor in planar mode of $0.88[Bi_{0.5}Na_{0.5}TiO_3]–0.08[Bi_{0.5}K_{0.5}TiO_3]–0.04$ $[Bi_{0.5}Li_{0.5}TiO_3]$ (BNKLT88) ceramics with a depolarization temperature of 220°C [18] was increased to 700 upon Mn addition. However, no detailed explanation on the processing of these ceramics was provided in their article. Furthermore, it was not clear if Mn was incorporated into the lattice as an acceptor dopant or whether it was added as an additive.

In this study, a comprehensive processing–property relationship in hard BNKLT88 ceramics with high mechanical quality factor is reported. Different amounts of Mn^{2+} and Fe^{3+} were doped to ceramics prepared by the mixed oxide route. The dielectric, piezoelectric, and electromechanical properties were measured in ceramics sintered at different temperatures.

4.2 Experimental Procedure

The conventional mixed oxide method was used to prepare $(BiNa_{0.88}K_{0.08}Li_{0.04})_{0.5}Ti_{1-x}Mn_xO_3$ (x = 0, 0.01, 0.014, 0.015, 0.016, 0.017, 0.02, and 0.022) and $(BiNa_{0.88}K_{0.08}Li_{0.04})_{0.5}Ti_{1-x}Fe_xO_3$ (x = 0.0125, 0.015, and 0.0175) ceramics. Raw materials including high-purity oxides and carbonate powders were dried overnight at 120°C in an oven. Then, powders with appropriate molar ratios were milled in acetone with

zirconia balls for 12 h. The mixed powder was dried and calcined at 800°C for 3 h. The calcined powders were ball milled again for 12 h. The particle size of the powders at this stage was measured to be about 600 nm. After binder addition (8 wt% Polyvinyl Alcohol solution), disk-shape samples of 14-mm-diameter were uniaxially pressed at 150 MPa. Upon binder removal at 550°C, pellets were sintered at different temperatures (1075°C–1150°C) for 2 h. Sintered ceramics were lapped down to about 700 μm in thickness and then were electroded using fired-on silver paint (the diameter to thickness ratio of the ceramics used for electrical characterization was higher than 15). The electrode ceramics were poled in a silicone oil bath at 85°C–95°C under an applied electric field of 50 kV/cm for 15 min.

The dielectric constant ($\varepsilon_{33}^T/\varepsilon_0$) and dielectric loss (tanδ) were measured at 1kHz by an impedance analyzer (HP4194a; Hewlett Packard, Tokyo, Japan). A Berlincourt piezometer was used to measure the longitudinal piezoelectric charge coefficient (d_{33}) at 100 Hz. Piezoelectric planar and thickness coupling coefficients (k_p and k_t, respectively) were calculated from the resonance and antiresonance frequencies of the impedance traces, based on the IEEE standards [19], [20] . The longitudinal coupling coefficient, k_{33}, was estimated from the thickness and planar coupling coefficients according to Eq. (4.1) [18]:

$$k_{33} = k_p^2 + k_t^2 - k_p^2 k_t^2 \tag{4. 1}$$

The mechanical quality factors at the resonance frequency for planar and thickness vibration modes were measured by the following equation using the admittance-frequency spectrum [21]

$$Q_\mathrm{m} = \frac{f_\mathrm{r}}{(f_2 - f_1)} \tag{4. 2}$$

$$Q_m = \frac{1}{R}\sqrt{\frac{L}{C_a}} \hspace{6cm} (4.\,3)$$

where R, L, and Ca are the resistance, inductance, and capacitance of the Van dyke equivalent circuit of a piezoelectric resonator at the resonance frequency. It was found that both Eqs. (2) and (3) yielded similar values of Q_m ($\pm 5\%$).

Hysteresis loops were measured using a Sawyer–Tower circuit at a pulse width of 1000 ms (1 Hz frequency) using a triangular wave signal.

4.3   Result and Discussion

4.3.1   Mn-Doped Ceramics

The XRD pattern of an undoped $(BiNa_{0.88}K_{0.08}Li_{0.04})_{0.5}TiO_3$ ceramic sintered at 1125°C is shown in Fig. 4.1. Mn-doped ceramics showed a similar XRD pattern with a perovskite structure, indicating that the Ti^{+4} ions (0.68 Å) were success- fully substituted by Mn cations with similar ionic radii (Mn^{+2} [r ~ 0.67 Å low spin, r ~ 0.83 V high spin], Mn^{+3} [r ~ 0.58 Å low spin, r ~ 0.64 Å high spin] and Mn^{+4} [r ~ 0.53 Å] [14] .The origin of the very low intensity peak close to 29° is not quite clear. However, that peak is close to the sodium main reflection as well as complex oxide of bismuth and titanium. According to the Rietveld refinement, undoped and doped BNKLT88 ceramics possessed a rhombohedral symmetry with an R3c space group. The variation in the lattice parameter and rhombohedrality as a function of Mn concentration is displayed in Fig 4.2. Mn doping resulted in shrinkage of the unit cell. The shrinkage of the unit cell can be attributed to the formation of oxygen vacancies following the occupation of B sites by Mn cations [22] and the substitution of Ti^{4+} by smaller cations (Mn^{4+}).
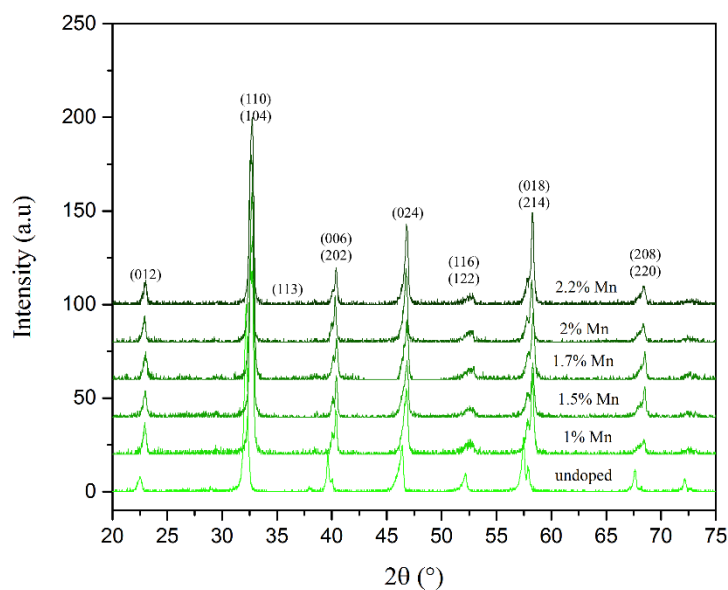
Figure 4. 1. XRD patterns of undoped and Mn-doped BNKLT88 ceramics showing a rhombohedral structure.
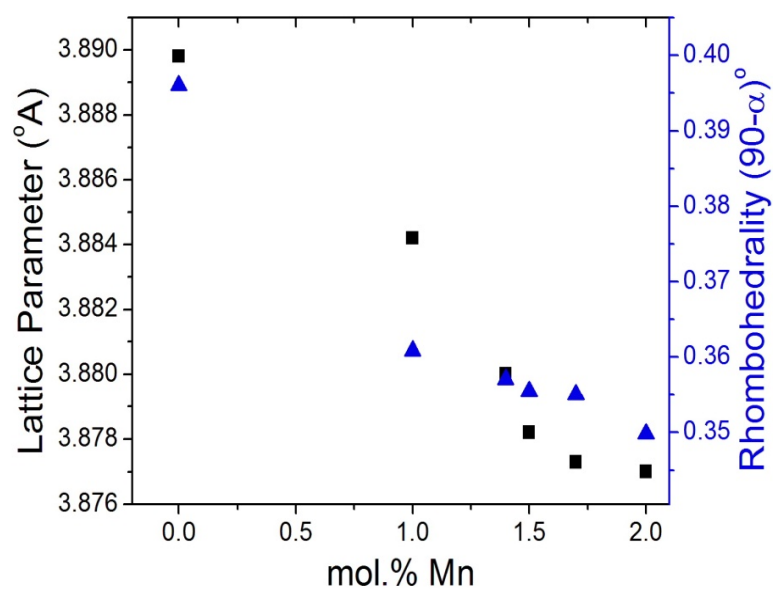
Figure 4. 2. Effect of Mn content on the lattice parameter and rhombohedrality of BNKLT88 ceramics.

Table 4. 1. The Physical and Electromechanical Properties of Undoped and Mn-Doped
BNKLT88 Ceramics Sintered at Different Temperatures

%Mn	Sintering temperature (°C)	Density (g.cm⁻³)	d_{33} (pC.N⁻¹)	ε_r	tanδ (%)	k_p	k_t	Planar Q_m	Thickness Q_m
0	1100	5.78	96	374	1.21	0.260	0.498	402	246
	1125	5.83	97	369	1.15	0.258	0.497	423	259
	1150	5.76	96	379	1.23	0.262	0.499	392	240
1	1100	5.76	89	363	1.48	0.244	0.491	666	282
	1125	5.74	92	354	1.42	0.237	0.479	683	307
	1150	5.71	93	358	1.63	0.231	0.488	618	295
1.4	1100	5.78	88	324	0.97	0.224	0.474	868	402
	1125	5.78	88	306	0.97	0.216	0.476	851	352
1.5	1075	5.83	88	340	1.56	0.235	0.494	904	391
	1100	5.88	85	308	0.89	0.218	0.487	974	437
	1125	5.77	86	327	1.06	0.216	0.483	847	395
	1150	5.72	86	330	1.17	0.212	0.481	801	353
1.6	1075	5.83	88	315	1.14	0.220	0.480	912	383
	1100	5.76	87	320	1.01	0.217	0.479	886	378
1.7	1075	5.92	88	320	1.36	0.221	0.469	935	406
	1100	5.81	87	319	1.10	0.211	0.457	906	387
2	1075	5.87	84	333	1.68	0.214	0.482	820	377
	1100	5.80	85	328	1.66	0.192	0.474	745	345
	1125	5.75	87	338	1.73	0.190	0.471	695	298
	1150	5.73	87	350	1.81	0.190	0.463	645	271
2.2	1075	5.84	84	297	1.71	0.184	0.470	603	302
	1100	5.82	83	307	1.78	0.179	0.459	569	279

*The standard deviation of density, d_{33}, ε_r, and tanδ is ±0.03, ±1, ±5, and±0.03, respectively.

‡The standard deviation of k_p and k_t is ±0.002 and ±0.006, respectively.

§The standard deviation of planar and thickness Q_m is 15 and 30, respectively.

Table 4.1 lists the density and electromechanical properties of the undoped and Mn-doped BNKLT88 ceramics sintered at different temperatures. The sintering shrinkage of the samples was in the range of 14%–17%. The electrical properties of these ceramics were very sensitive to the dopant concentration as well as the sintering temperature as shown in the Table 4.1. A great enhancement in the mechanical quality factor was achieved by optimization of the dopant level and the sintering temperature.

Figures 4.3 (a)–(b) display the impedance-phase (Z- θ) spectra of undoped and 1.5 mol% Mn-doped BNKLT88 ceramics around the resonance (f_r) and antiresonance (f_a) frequencies of the planar vibration mode. The undoped BNKLT88 composition with Q_m of about 400 exhibited a wider bandwidth in the vicinity of f_r and f_a for both impedance and phase angle spectra. Upon Mn doping, the bandwidth of the impedance and phase angle spectra was decreased. This results in concentration of the vibration energy at the resonance and antiresonance frequencies, leading to a high mechanical quality factor (low mechanical loss).
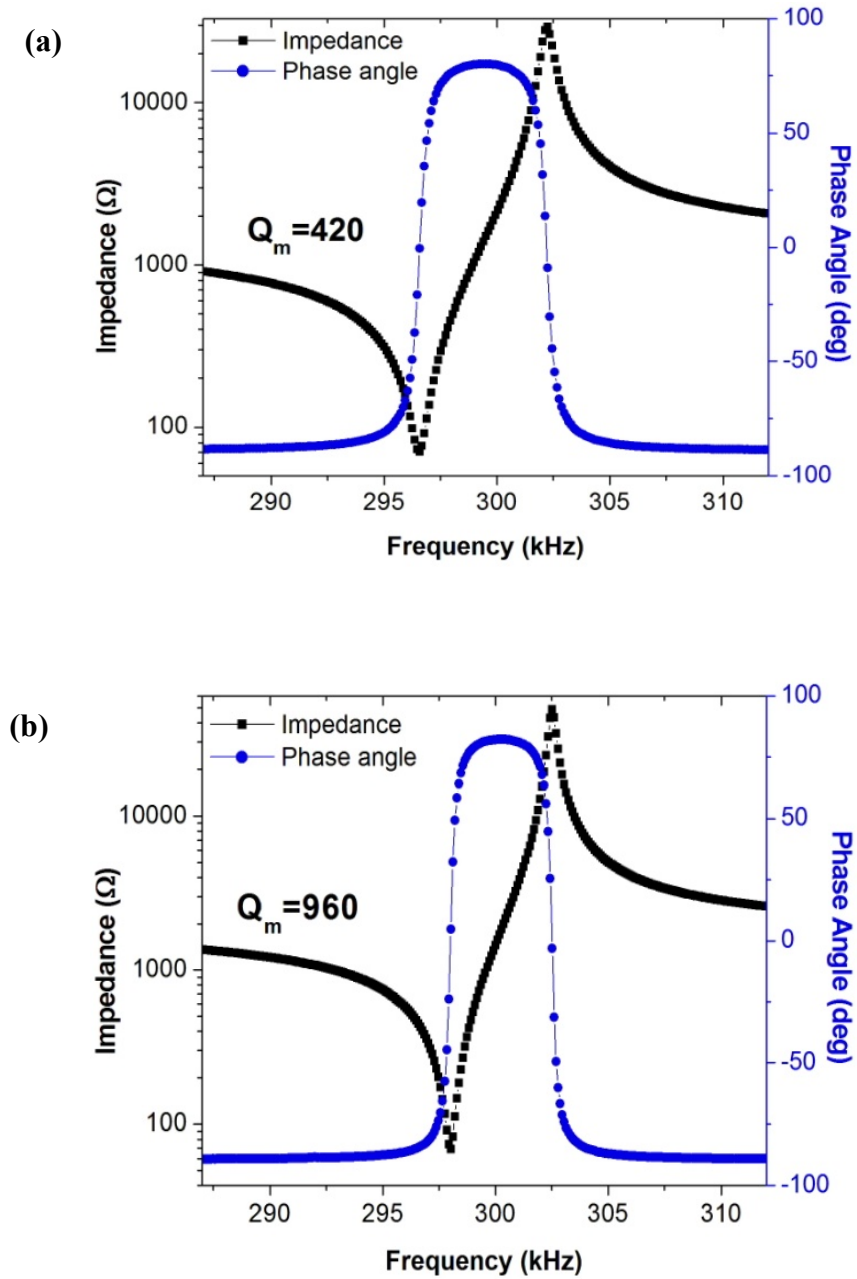
Figure 4. 3. Impedance and phase angle spectra showing the resonance and antiresonance frequencies of planar mode in ceramics sintered at 1100°C: (a) undoped and (b) 1.5 mol% Mn-doped BNKLT88.

Figure 4.4 (a) shows the effect of Mn doping on the mechanical quality factor of BNKLT88 ceramics sintered at 1100°C. Increasing the Mn concentration up to 1.5 mol% remarkably enhanced the planar and thickness Q_m. Further increasing the dopant concentration resulted in a reduction in the Q_m. The maximum planar and thickness Q_m were measured to be about 970 and 435, respectively. The planar quality factor in 1.4% and 1.6% Mn-doped samples was as high as 870 and 915. The Other ceramics sintered at different temperatures showed a similar trend of variations of the Q_m with Mn concentration. The observed decline of Q_m at high dopant concentration is probably caused by Mn accumulation at grain boundaries, formation of secondary phases (in the extent not detectable by XRD), or incorporation of Mn into the A-site [3], [12], [23]–[25]. As explained earlier, the substitution of Ti with Mn results in domain wall pinning which decreases the dielectric, mechanical, and piezoelectric losses [5], [22]. It can be observed in Fig. 4.4 (b) that the minimum dielectric loss (tan$\delta \sim 0.9\%$) was also obtained at 1.5 mol% Mn. Therefore, the optimum concentration of Mn dopant for achieving hard piezoelectric ceramics, that is, the minimum dielectric and mechanical losses, was 1.5 mol%. The dielectric constant for this composition (at 1 kHz) was about 310.
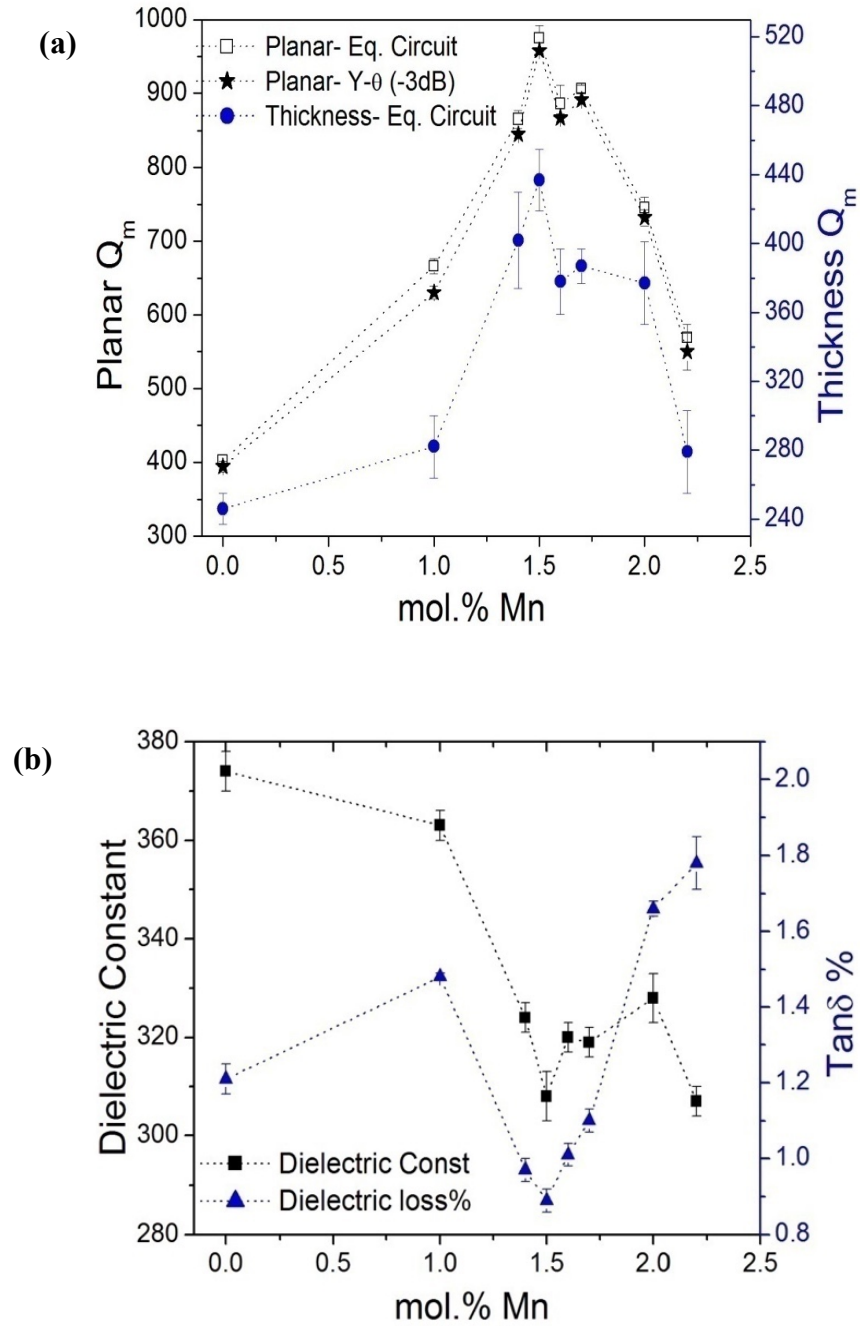
Figure 4. 4. Effect of Mn doping on (a) the planar and thickness mechanical quality factors and (b) the dielectric properties of BNKLT88 ceramics sintered at 1100°C.
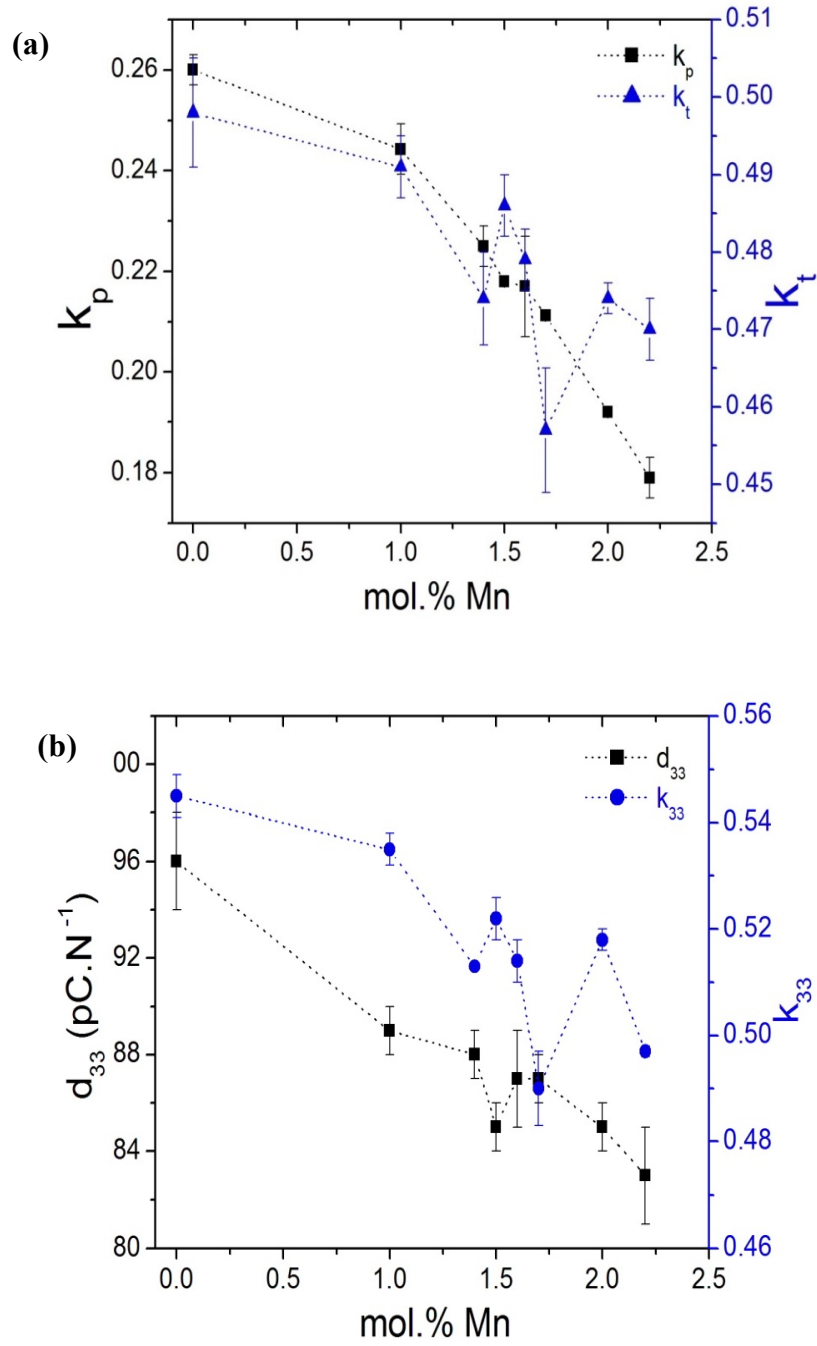
Figure 4. 5. Effect of Mn doping on (a) planar and thickness coupling coefficients and (b) piezoelectric charge coefficient and longitudinal coupling coefficient of BNKLT88 ceramics sintered at 1100°C.

Figures 4.5 (a) and (b) show the effect of Mn doping on piezoelectric and coupling coefficients. Mn doping decreased the planar and thickness coupling coefficients of BNKLT88 ceramics. The longitudinal piezoelectric constant and electromechanical coefficients were also reduced with increasing the concentration of the acceptor dopant. The decrease in piezoactivity of the ceramics with Mn content originates from domain wall pinning by oxygen vacancies, as explained previously.

Figure 4.6 shows the effect of sintering temperature on the density of 1.5 mol% Mn-doped ceramics. Other ceramics doped with different amounts of Mn, showed a similar dependency on the sintering temperature (see Table 4.1). The highest density of 5.84 g/cm3 was obtained at 1100°C. Increasing the sintering temperature caused reduction in density, due to the accelerated bismuth loss at higher temperatures. The bismuth loss at 1100°C and 1150°C was 0.5 and 0.7 wt%, respectively.
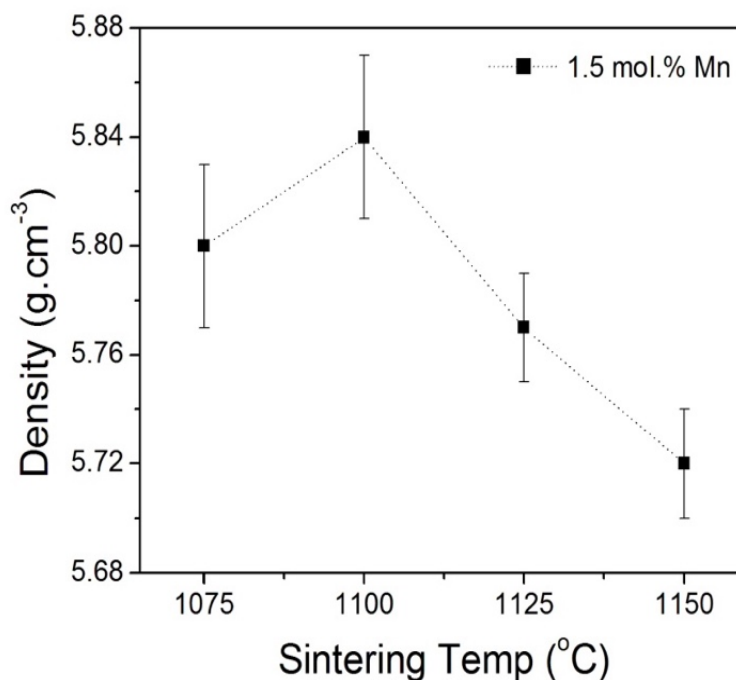
Figure 4. 6. Effect of sintering temperature on density of 1.5 mol% Mn- doped BNKLT88 ceramics.

Accordingly, the highest Q_m was also achieved at 1100°C, which was the optimum sintering temperature for 1.5% Mn-doped ceramic [Fig. 4.7 (a)]. The reduced density and probable grain growth caused the Q_m to decrease at sintering temperatures higher than 1100°C. The influence of sintering temperature on the dielectric properties of Mn-doped ceramics is depicted in Fig. 7(b). As expected from the variation trend of the density and Q_m with the sintering temperature, the lowest dielectric loss was obtained at 1100°C. The dielectric constant showed a minimum at this temperature as well. The planar and thickness coupling coefficients also decreased with increasing sintering temperature. The optimum sintering temperature for 1%, 1.5%, and 2% Mn-doped ceramics was 1125°C, 1100°C, and 1075°C, respectively. Increasing the dopant concentration decreased the optimum sintering temperature of BNKLT88 ceramics. Oxygen vacancies induced by acceptor dopants can accelerate the diffusion process at high temperatures and hence, decrease the sintering temperature [5], [22].
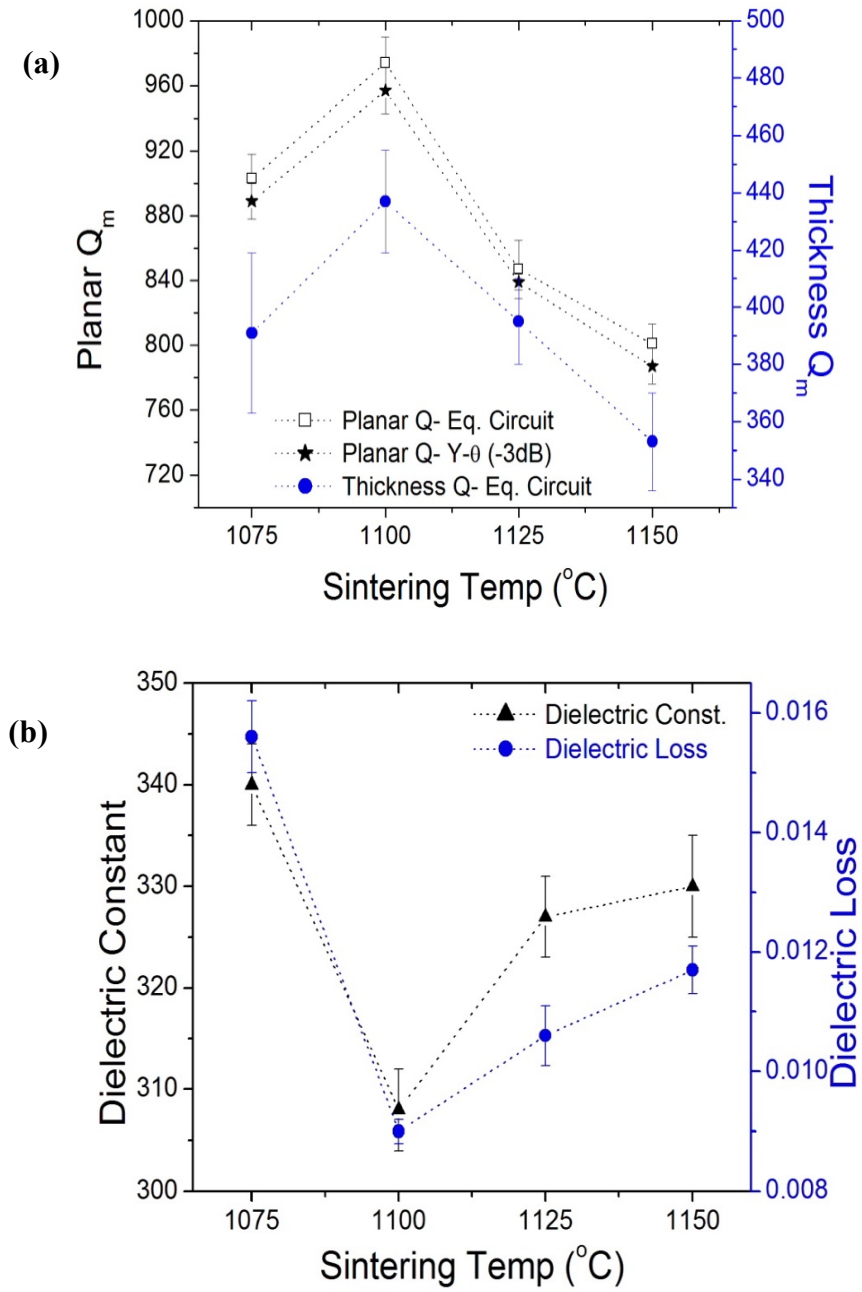
Figure 4. 7. Effect of sintering temperature on (a) planar and thickness mechanical quality factor and (b) dielectric properties of 1.5 mol% Mn-doped BNKLT88 ceramics.

4.3.2   Fe-Doped Ceramic

All Fe-doped ceramics were sintered at 1100°C. Figure 4.8 (a) shows the effects

of Fe doping on planar and thickness Q_m of BNKLT88 ceramics. Variation in dielectric

properties with Fe concentration is also depicted in Fig. 4.8 (b). The highest planar and

thickness Q_m (900 and 350, respectively) were obtained in 1.5 mol% Fe-doped ceramics.

This composition also showed the lowest dielectric loss (tanδ ~ 0.90) and dielectric

constant (ε_r ~ 300). Fe doping decreased the d_{33} and k_p in a similar manner to Mn doping.

These properties in 1.5 mol% Fe-doped samples were 81 pC/N and 0.20, respectively.
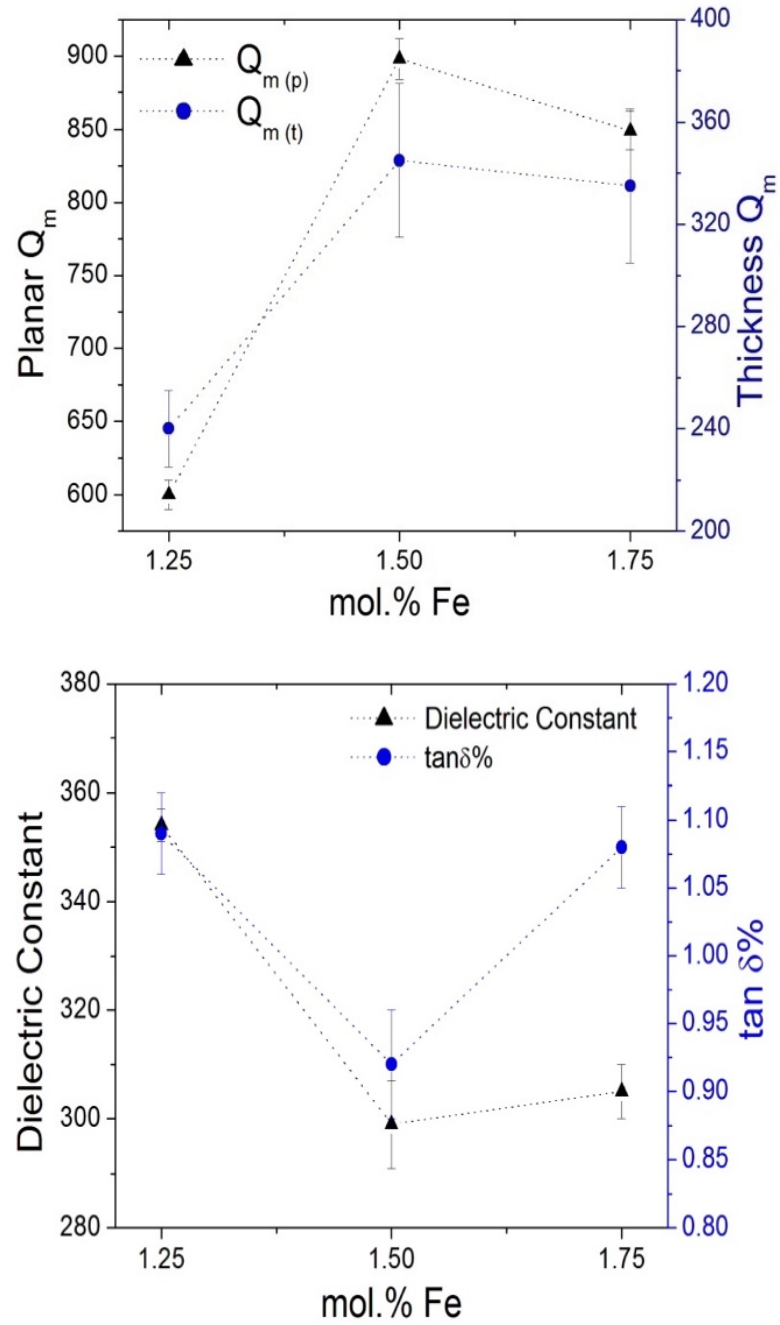
Figure 4. 8. Effect of Fe doping on (a) the planar and thickness mechanical quality factor and (b) dielectric properties of BNKLT88 ceramics sintered at 1100°C.

Fe-doped ceramics were subjected to a color change during the poling step. The color of the as-sintered ceramics was light yellow, which turned black after poling. Magnetite ($FeO.Fe_2O_3$) is extensively used as a black pigment in the dye industry. The observed color change was possibly due to the valence change in Fe^{3+} cations under application of an electric field. This electrocoloration effect has been observed in other materials such as Fe-doped $SrTiO_3$ [26].Compared with the Mn-doped ceramics, Fe-doped samples had a lower resistivity and needed to be poled at a lower temperature (85°C).

Figure 4.9 illustrates the P–E hysteresis loops of undoped, 1.5% Mn and 1.5% Fdoped BNKL88 ceramics aged for 48h at room temperature. Acceptor dopants slightly decreased the remanent and saturation polarizations (4%– 8%), and increased the coercive field (by 9%–10%) as well as the internal bias field (E_i). The internal bias is developed due to the alignment of the defect dipoles (e.g., $V_O^{\bullet\bullet} - Mn_{Ti}''$) in the direction of the spontaneous polarization [4], [6]. The internal bias field in undoped, Fe-doped, and Mn-doped BNKLT88 ceramics was measured to be about 0.7, 2.5, and 3 kV/cm, respectively.
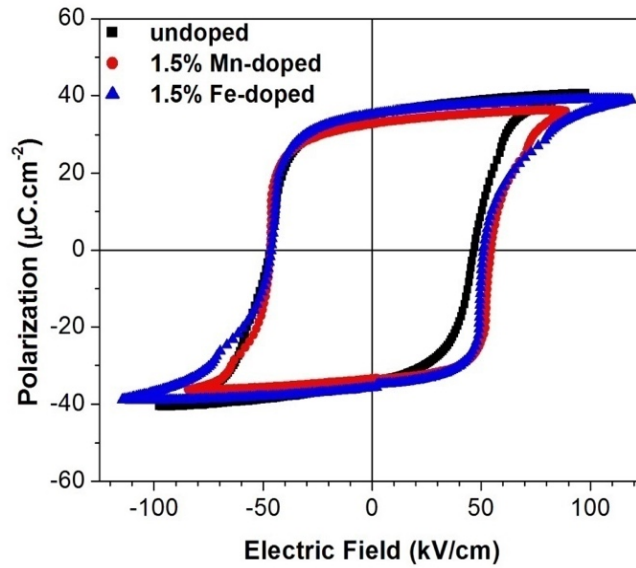
Figure 4. 9. P–E hysteresis loops of undoped, 1.5% Mn, and 1.5% Fe-doped BNKL88 ceramics

Table 4.2 compares the properties of commercial hard PZT (PZT4 and PZT8) and lead-free BNT-based ceramics developed in this research. The data for PZT ceramics were obtained from different sources [4], [27]–[31]. The crucial material properties for high power applications (Q_m, tanδ and T_C) as well as k_t, in undoped and Mn-doped BNKLT88 ceramics are comparable to PZT4 and PZT8, respectively. Lead-based materials exhibit a considerably higher d_{33}, ε_r, and k_p. Concerning the high power applications and in terms of the ferroelectric domains stability, the main advantage of BNT- based ceramics is their higher coercive field (E_c ~5 kV/mm) compared with commercial PZT (E_c ~ 1.4–2 kV/mm) [2]. Due to their higher coercive field, Mn-doped BNKLT88 ceramics are expected to show a superior performance (higher mechanical quality factor and less heat dissipations) under application of an electric field compared with PZT4 and PZT8.

Table 4. 2. Properties of Commercial Hard PZTs and Lead-Free BNT-Based Ceramics

Property	PZT4	PZT8	BNKLT88	BNKLT88 +1.5 Mn	BNKLT88 +1.5Fe
d_{33} (pC/N)	290	225	95	85	81
$\varepsilon^T_{33}/\varepsilon_0$	1300	1000	380	310	300
Tanδ %	0.5	0.4	1.1	0.85	0.90
k_t %	51	48	49	48	46
k_p %	58-64	51-60	26	22	20
Q_m	500	1000	400	970	900
T_c (ºC)	325	300	330	305	---
E_c (kV.cm^{-1})	14	20	47.2	52.2	51.7
E_i (kV.cm^{-1})~	3	3	0.7	3	2.5

4.4 Summary

In this study, the effect of acceptor dopants (Mn and Fe) and sintering temperature on the electromechanical properties of lead-free $(BiNa_{0.88}K_{0.08}Li_{0.04})_{0.5}TiO_3$ ceramics were investigated. The sintering temperature was optimized to obtain the highest density and mechanical quality factor. Acceptor dopants slightly decreased the optimum sintering temperature of BNKLT88 ceramics. Mn or Fe doping resulted in decreasing dielectric loss and considerable enhancement of the mechanical quality factor. Acceptor dopants also decreased the planar coupling coefficient and dielectric constant due to the domain wall pinning effect of oxygen vacancies. The Q_m, d_{33}, k_p, ε_r, and $\tan\delta$ values for 1.5 mol% Mn-doped ceramics sintered at 1100°C were 970, 87 pC/N, 0.218, 310, and 0.009, respectively. Although it was more difficult to pole Fe-doped ceramics due to their higher conductivity compared with Mn-doped samples, a careful control of poling conditions yielded high values of mechanical quality factor. The Q_m, d_{33}, k_p, ε_r, and $\tan\delta$ values for 1.5 mol% Fe-doped sample were measured to be 900, 81 pC/N, 0.198, 295, and 0.009, respectively. The internal bias as well as coercive field of BNT-based lead-free ceramics was increased by acceptor dopants. 1.5 mol% Mn-doped BNKLT88 ceramics sintered at 1100°C showed the lowest dielectric and mechanical losses and the highest coercive field among the studied compositions. These lead-free ceramics, which also possess a high Curie temperature, are promising materials for replacement of lead-based piezoelectrics used in high power applications.

Acknowledgments

4.5 References

[1] K. Uchino, "Piezoelectric ultrasonic motors: overview," *Smart Mater. Struct.*, vol. 7, no. 3, p. 273, 1998.

[2] H. J. Lee, S. O. Ural, L. Chen, K. Uchino, and S. Zhang, "High Power Characteristics of Lead-Free Piezoelectric Ceramics," *J. Am. Ceram. Soc.*, vol. 95, no. 11, pp. 3383–3386, Nov. 2012.

[3] L.-X. He, M. Gao, C.-E. Li, W.-M. Zhu, and H.-X. Yan, "Effects of Cr2O3 addition on the piezoelectric properties and microstructure of PbZrxTiy(Mg1/3Nb2/3)1−x−yO3 ceramics," *Journal of the European Ceramic Society*, vol. 21, no. 6, pp. 703−709, Jun. 2001.

[4] S. Zhang, J. B. Lim, H. J. Lee, and T. R. Shrout, "Characterization of Hard Piezoelectric Lead-Free Ceramics," *IEEE Transactions on Ultrasonics, Ferroelectrics, and Frequency Control*, vol. 56, no. 8, pp. 1523–1527, Aug. 2009.

[5] Y. Gao, Y.-H. Chen, J. Ryu, K. Uchino, and D. Viehland, "Eu and Yb Substituent Effects on the Properties of Pb(Zr $_{0.52}$ Ti $_{0.48}$)O $_3$ −Pb(Mn $_{1/3}$ Sb $_{2/3}$)O $_3$ Ceramics: Development of a New High-Power Piezoelectric with Enhanced Vibrational Velocity," *Japanese Journal of Applied Physics*, vol. 40, no. Part 1, No. 2A, pp. 687–693, Feb. 2001.

[6] K. Uchino *et al.*, "Loss mechanisms and high power piezoelectrics," *Journal of Materials Science*, vol. 41, no. 1, pp. 217–228, Jan. 2006.

[7] Y. Gao, K. Uchino, and D. Viehland, "Time Dependence of the Mechanical Quality Factor in 'Hard' Lead Zirconate Titanate Ceramics: Development of an Internal Dipolar Field and High Power Origin," *Japanese Journal of Applied Physics*, vol. 45, no. 12, pp. 9119–9124, Dec. 2006.

[8] J. B. Lim, S. Zhang, J.-H. Jeon, and T. R. Shrout, "(K,Na)NbO3-Based Ceramics for Piezoelectric 'Hard' Lead-Free Materials," *Journal of the American Ceramic Society*, vol. 93, no. 5, pp. 1218–1220, May 2010.

[9] E. Li, H. Kakemoto, S. Wada, and T. Tsurumi, "Enhancement of Q(m) by co-doping of Li and Cu to potassium sodium niobate lead-free ceramics," *IEEE Trans Ultrason Ferroelectr Freq Control*, vol. 55, no. 5, pp. 980–987, May 2008.

[10] U. Robels, J. H. Calderwood, and G. Arlt, "Shift and deformation of the hysteresis curve of ferroelectrics by defects: An electrostatic model," *Journal of Applied Physics*, vol. 77, no. 8, pp. 4002–4008, Apr. 1995.

[11] B. Li, G. Li, S. Zhao, L. Zhang, and A. Ding, "Characterization of the high-power piezoelectric properties of PMnN–PZT ceramics using constant voltage and pulse drive methods," *Journal of Physics D: Applied Physics*, vol. 38, no. 13, pp. 2265–2270, Jul. 2005.

[12] H.-Y. Park *et al.*, "Effect of MnO2 on the Piezoelectric Properties of the 0.75Pb(Zr0.47Ti0.53)O3–0.25Pb(Zn1/3Nb2/3)O3 Ceramics," *Journal of the American Ceramic Society*, vol. 93, no. 9, pp. 2537–2540, 2010.

[13] C. Galassi, E. Roncari, C. Capiani, and F. Craciun, "Processing and characterization of high Qm ferroelectric ceramics," *Journal of the European Ceramic Society*, vol. 19, no. 6–7, pp. 1237–1241, Jun. 1999.

[14]   Y. Gao, K. Uchino, and D. Viehland, "Domain wall release in 'hard' piezoelectric under continuous large amplitude ac excitation," *Journal of Applied Physics*, vol. 101, no. 11, p. 114110, Jun. 2007.

[15]   K. Uchino, "'Piezoelectric Transformers'; p. 176," in *Ferroelectric Devices*, Marcel Deker Inc., New York, NY, 2000.

[16]   H. Nagata, K. Takai, Y. Nomura, S. Sato, Y. Hiruma, and T. Takenaka, "Vibration velocities under high-power driving on perovskite-type lead-free ferroelectric ceramics," in *2010 IEEE International Symposium on the Applications of Ferroelectrics (ISAF)*, 2010, pp. 1–4.

[17]   M. Matsubara, K. Kikuta, and S. Hirano, "Piezoelectric properties of (K0.5Na0.5)(Nb1−xTax)O3−K5.4CuTa10O29 ceramics," *Journal of Applied Physics*, vol. 97, no. 11, p. 114105, May 2005.

[18]   Y. Hiruma, H. Nagata, and T. Takenaka, "Phase Transition Temperatures and Piezoelectric Properties of (Bi$_{1/2}$ Na$_{1/2}$)TiO$_3$ –(Bi$_{1/2}$ K$_{1/2}$)TiO$_3$ –BaTiO$_3$ Lead-Free Piezoelectric Ceramics," *Japanese Journal of Applied Physics*, vol. 45, no. 9B, pp. 7409–7412, Sep. 2006.

[19]   T. Tou, Y. Hamaguti, Y. Maida, H. Yamamori, K. Takahashi, and Y. Terashima, "Properties of (Bi$_{0.5}$ Na$_{0.5}$)TiO$_3$ –BaTiO$_3$ –(Bi$_{0.5}$ Na$_{0.5}$)(Mn$_{1/3}$ Nb$_{2/3}$)O$_3$ Lead-Free Piezoelectric Ceramics and Its Application to Ultrasonic Cleaner," *Japanese Journal of Applied Physics*, vol. 48, no. 7, p. 07GM03, Jul. 2009.

[20]   T. Takenaka, H. Nagata, and Y. Hiruma, "Phase Transition Temperatures and Piezoelectric Properties of (Bi1/2Na1/2)TiO3-and (Bi1/2K1/2)TiO3-Based Bismuth Perovskite Lead-Free Ferroelectric Ceramics," *IEEE Transactions on Ultrasonics, Ferroelectrics, and Frequency Control*, vol. 56, no. 8, pp. 1595–1612, Aug. 2009.

[21]   K. Uchino, Y. Zhuang, and S. O. Ural, "Loss determination methodology for a piezoelectric ceramic: new phenomenological theory and experimental proposals," *J. Adv. Dielect.*, vol. 01, no. 01, pp. 17–31, Jan. 2011.

[22]   H.-Q. Wang, Y.-J. Dai, and X.-W. Zhang, "Microstructure and Hardening Mechanism of K0.5Na0.5NbO3 Lead-Free Ceramics with CuO Doping Sintered in Different Atmospheres," *Journal of the American Ceramic Society*, vol. 95, no. 4, pp. 1182–1184, 2012.

[23]   G. Fan, W. Lu, X. Wang, and F. Liang, "Effects of manganese additive on piezoelectric properties of (Bi1/2Na1/2)TiO3–BaTiO3 ferroelectric ceramics," *J Mater Sci*, vol. 42, no. 2, pp. 472–476, Jan. 2007.

[24]   J. Yao *et al.*, "The influence of Mn substitution on the local structure of Na0.5Bi0.5TiO3 crystals: Increased ferroelectric ordering and coexisting octahedral tilts," *Journal of Applied Physics*, vol. 111, no. 6, p. 064109, Mar. 2012.

[25]   D. Y. Wang, N. Y. Chan, S. Li, S. H. Choy, H. Y. Tian, and H. L. W. Chan, "Enhanced ferroelectric and piezoelectric properties in doped lead-free (Bi0.5Na0.5)0.94Ba0.06TiO3 thin films," *Appl. Phys. Lett.*, vol. 97, no. 21, p. 212901, Nov. 2010.

[26]   C. Lenser *et al.*, "Spectroscopic study of the electric field induced valence change of Fe-defect centers in SrTiO3," *Phys. Chem. Chem. Phys.*, vol. 13, no. 46, pp. 20779–20786, Nov. 2011.

[27]   M. W. Hooker, "Properties of PZT-Based Piezoelectric Ceramics Between -150 and 250 C," Sep. 1998.

[28]   "Piezomaterial Data, Specific Parameters of Standard Materials. PI Ceram- ics Co., Lederhose, Germany." .

[29]   "Piezoelectric Materials Datasheet. Piezopower, CTS Electronic Compo- nents Co., Albuquerque, NM." .

[30]   "Piezoelectric Ceramics Datasheet, Morgan Advanced Materials, Berkshire, UK." .

[31]   D. Berlincourt and C. Near, "PROPERTIES OF MORGAN ELECTRO CERAMIC CERAMICS," p. 12.

Effect of Powder Particle Size on Properties of $(BiNa_{0.88}K_{0.08}Li_{0.04})_{0.5}Ti_{0.985}Mn_{0.015}O_3$

(BNKLT88-1.5Mn)

This chapter is complementary study on processing property relation of hard BNKLT88-1.5Mn and has not been submitted/published

5 Effect of Powder Particle Size on The Properties of $(BiNa_{0.88}K_{0.08}Li_{0.04})_{0.5}Ti_{0.985}Mn_{0.015}O_3$ (BNKLT88-1.5Mn)

In this chapter the effect of calcined powder particle size as well as sintering temperature on the dielectric and ferroelectric properties of BNKLT88-1.5Mn ceramics have been investigated.

5.1 Experimental Procedure

The $(BiNa_{0.88}K_{0.08}Li_{0.04})_{0.5}Ti_{0.985}Mn_{0.015}O_3$ composition was synthesized by conventional mixed oxide method with the same steps of procedure as explained in chapter 3 and 4. Different batches of powder were prepared at different mixing and milling time according to Table 5.1

Table 5. 1. Milling Conditions

Initial Milling (Mixing)	After Calcination	Abbreviation
12 h RM[1]	24 h RM	M12-M24
24 h RM	12 h RM	M24-M12
24 h RM	12 h RM +24h RM	M24-M36
24 h RM	12 h RM + 20 min PM[2]	M24-PM

[1]RM: Roller Milling

[2]PM: Planetary Milling, which was accomplished at 5 cycle of 4 min milling

with 300 rpms speed and 2 min pause between each cycle

8 wt% PVA solution (10 wt% PVA in water) was used as a binder. After sieving via 100-micron mesh, the powder was pressed to 12.9 mm circular disk-shape pellet, using uniaxial press under 150 MPa pressure. The binder removal accomplished at 550 °C for 2 h with heating and cooling rate of $2°C.min^{-1}$, followed by sintering at temperature of 1125-980 °C and duration of 2 h. After polishing the top and bottom surfaces of the pellets, the high temperature silver past (PELCO®, Ted Pella, CA) diluted in n-Butyl Acetate was applied on both sides followed by heat treatment at 550 °C for 20 min. Polling was carried out under an applied electric field of $4.5 \ kV.mm^{-1}$, at 95 °C for 15 min. Impedance analyzer HP4194A with an oscillation level of 1 volt was used to evaluate the dielectric and electromechanical properties as explained in Chapter 3.

The powder particle size was measured by a laser particle size analyzer (Zetasizer, Nano ZS, Malvern Instruments, UK). The morphology of powder was studied by Phenom Pro SEM.

EBSD scans were carried out in a TESCAN MIRA3 field emission gun scanning electron microscope at 20 kV. Samples were prepared using standard metallography protocols. This involved grinding with silicon carbide papers down to grade 4000, and polishing sequentially with diamond suspensions of 3 μm, 1 μm, and OPS colloidal silica suspension. A large scan of $500 \times 500 \ \mu m^2$ with 1μm resolution was collected on all samples. The collected raw data was post-analyzed using TSL OIM$^©$ software to extract grain size distribution.

5.2   Results and Discussion

5.2.1   Calcined Powder

Fig 5.1 illustrates the SEM-micrograph of BNKLT88-1.5Mn prepared at different milling conditions. Disregard the time and type of milling, all the powder showed irregular shape. Increasing the time to 36 h and higher led to initiation of soft agglomerates. The volume distribution of different batch of powder prepared at different milling conditions is shown in Fig. 5.2. The median particle size of the powder was decreased as a function of milling time. The presence of the soft agglomerate powder in M24-M36 condition confirmed via bimodal distribution of powder particle size. On the other side, more uniformity accompany with smaller median particle size (d_{50} = 535 nm) was observed in the M24-PM powder (Table 5.2).
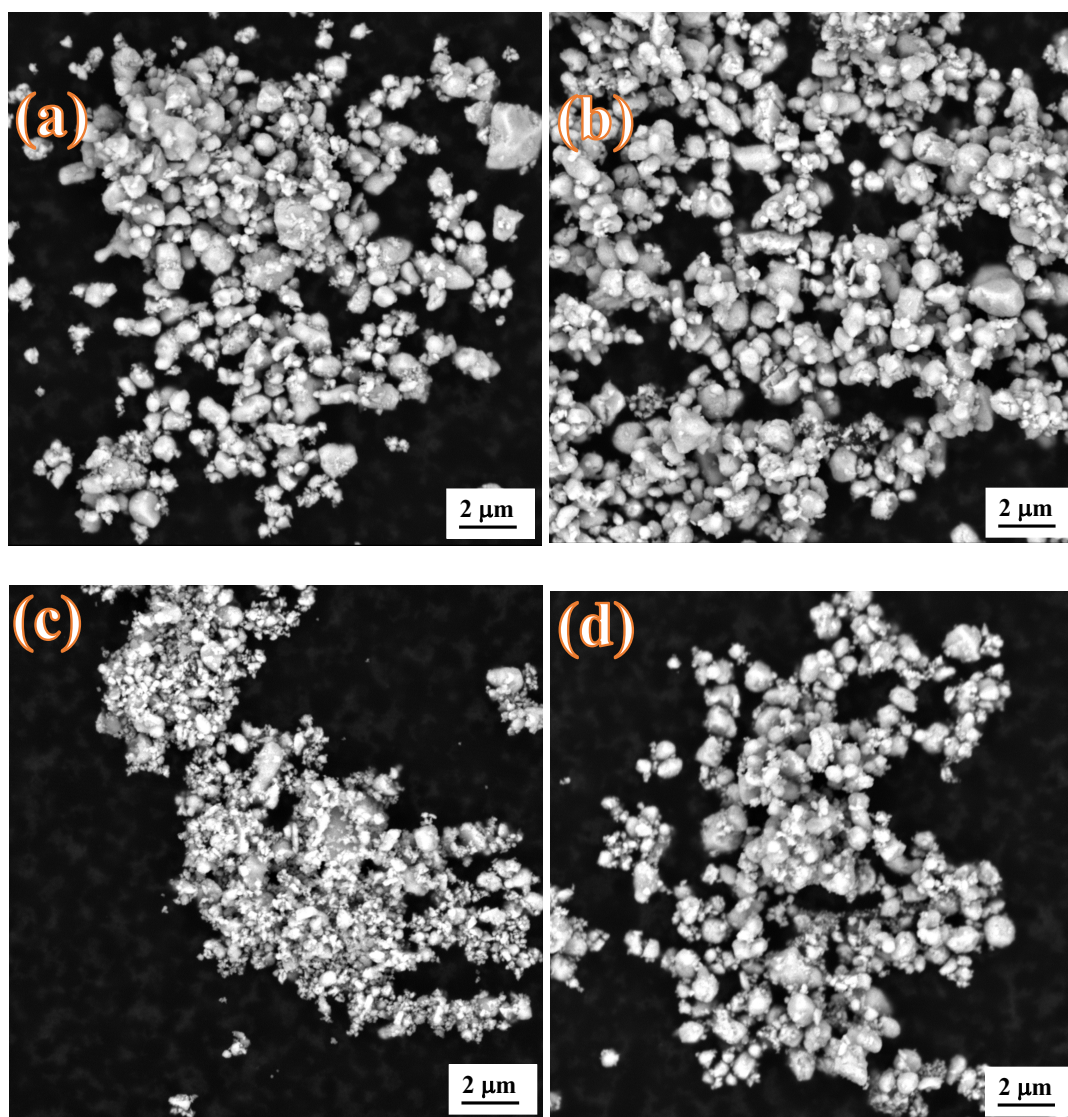
Figure 5. 1. SEM micrograph of BNKLT88-1.5Mn on (a) M12-M24 (b)M24-M12 (c)M24-M36 (d) M24-PM
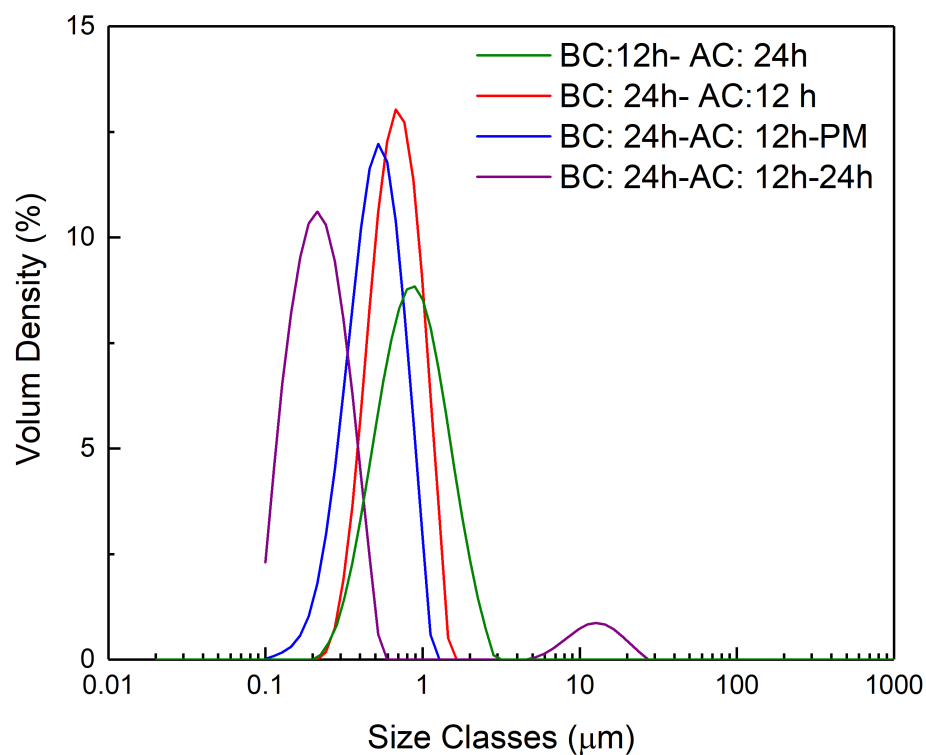
Figure 5. 2. The particle size distribution of BNKLT88-1.5 Mn powder prepared at different milling time

Table 5. 2. Numerical count particle size distribution of BNKLT88-1.5Mn powder

	D_{10} (nm)	D_{50} (nm)	D_{90} (nm)
M12-M24	470	900	1690
M24-M12	435	720	1130
M24-M36	137	235	454
M24-PM	300	535	865

5.2.2 BNKLT88-1.5Mn Ceramic

The effect of the calcined powder particle size accompany with the effect of sintering temperature on the density of the BNKLT88-1.5 Mn is illustrated in Fig. 5.3. The maximum density of about 5.77, 5.79, 5.78 g.cm^{-3} was measured in powder with D_{50} of 720 nm, 535 nm , 235 were achieved at temperatures of 1055 °C, 1010 °C, and 1020 °C, respectively. The required temperature to obtain maximum density shifted to lower temperature by decreasing the powder particle size. Finer powder has larger surface area which lead to higher the surface energy. Additionally, finer powder has higher defect energy due to the higher concentration of defects such as vacancies and local stress compared to larger powder. Consequently, the powder with smaller particle size has higher driving force for sintering. Consequently, the optimum sintering temperature shifts to lower temperture [2].
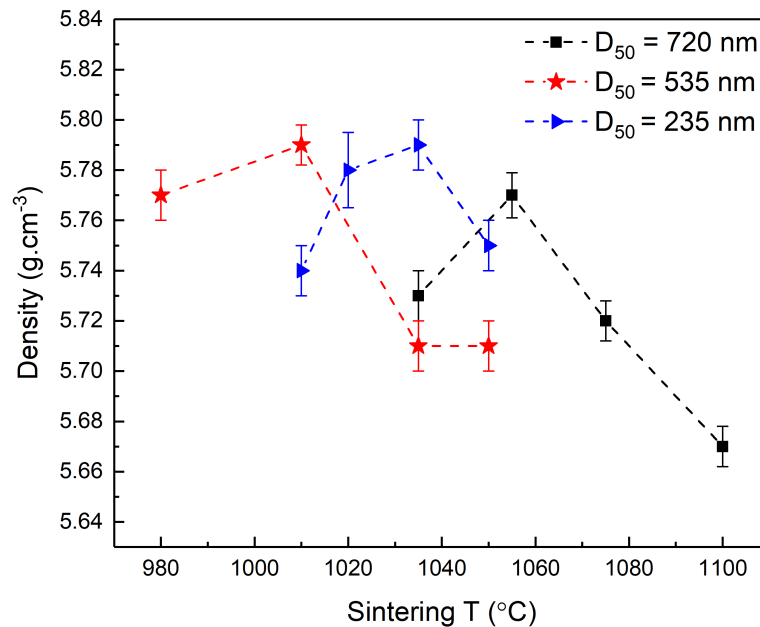
Figure 5. 3. Effect of particle size of the calcined powder and the sintering temperature on density of BNKLT88-1.5 Mn

The dependence of the dielectric and mechanical loss accompany with the effect of sintering temperature and calcined powder particle size are shown in figure 5.4 (a-b). The mechanical quality factor enhanced as a function of initial calcined powder particle size. Accordingly, the highest mechanical quality of 1200 with the lowest dielectric loss of about 1% was obtained from the powder with the median size of 535 nm at the sintering temperature of 1010 °C. Nerveless to say that, increasing the milling time before calcination effectively enhanced the dielectric and piezoelectric properties. The variation of planar and longitudinal coupling coefficient (k_p and k_{33}, respectively) as a function of initial powder particle size at the optimum sintering temperature is shown in Fig 5.5. The highest value of k_p and k_{33} was obtained on the calcined powder with the median size of 535 nm.
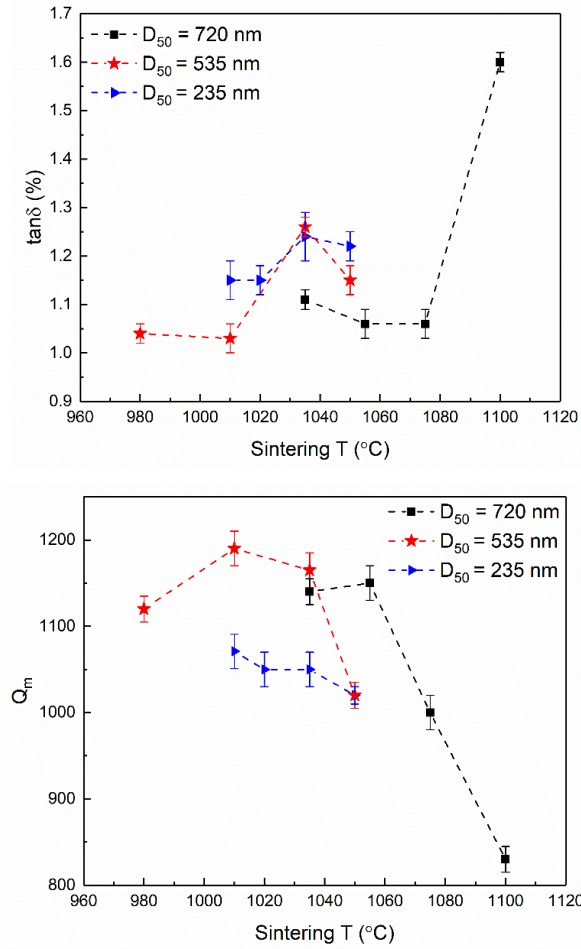
Figure 5. 4. Effect of the calcined powder particle size and sintering temperature on (a) dielectric loss and (b) and mechanical quality
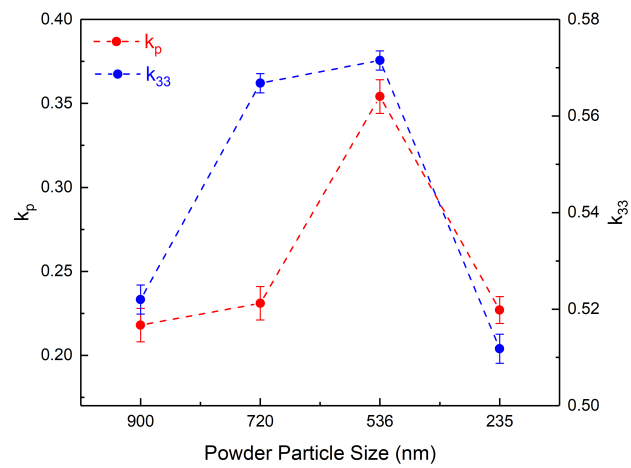
Figure 5. 5. Effect of powder particle size on the planar coupling coefficient and longitudinal coupling coefficient of BNKLT88-1.5Mn sintered at their optimum sintering temperature.

Fig. 5.6 (a-c) illustrate the microstructure of M24-M12, M24-MP, and M24-M36 ceramics sintered at 1050 °C, 1010 °C, and 1020 °C for 2h. It is apparent from the SEM images that the porosity was decreased by decreasing the calcined particle size. The smaller initial powder particle size provides a higher surface area for diffusion during sintering, which results to lower the sintering temperature and smaller grain size. Accordingly, the electron backscatter microscopy (EBSD) has been done on the samples to systematically evaluate the grain size of the specimen. The EBSD, can also, provides information about the possible texture or preferred crystal orientation in the specimen. The acquired orientation imaging microscopy (OIM) maps are shown in Fig 5.7 (a-c). Each color in this map represents a different orientation. As expected, there was not any preferred orientation direction or texture in the samples. The area fraction of grains was estimated by the circles which have exactly the same area as grains. The final analysis is summarized in Fig. 5.8. It is apparent from this data that the M12-PM samples had smaller and narrower grain size distribution.
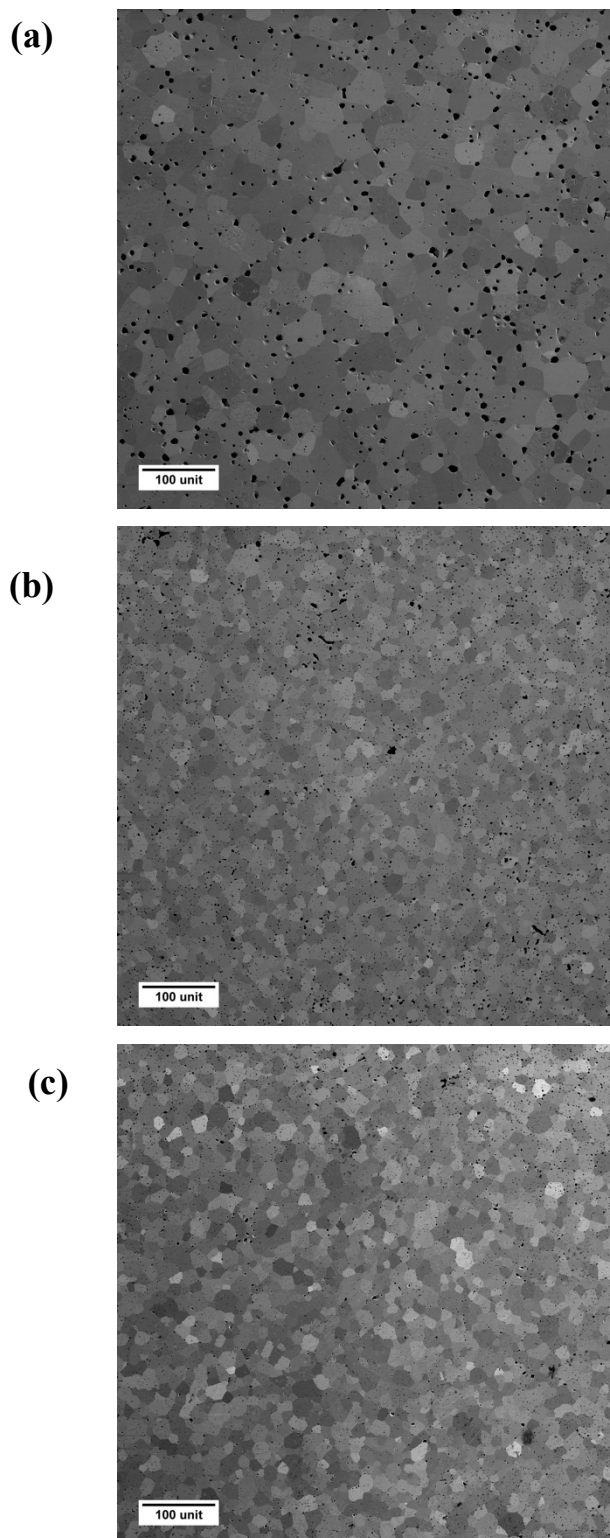
Figure 5. 6. SEM image of BNKLT88-1.5Mn (a) M12-M24, with initial powder particle size of 720 μm , sintered at 1050 °C (b) M12-PM,with initial powder particle size of 535 μm , sintered at 1010 °C (c) M12-36, with initial powder particle size of 535 μm , sintered at 1020 °C
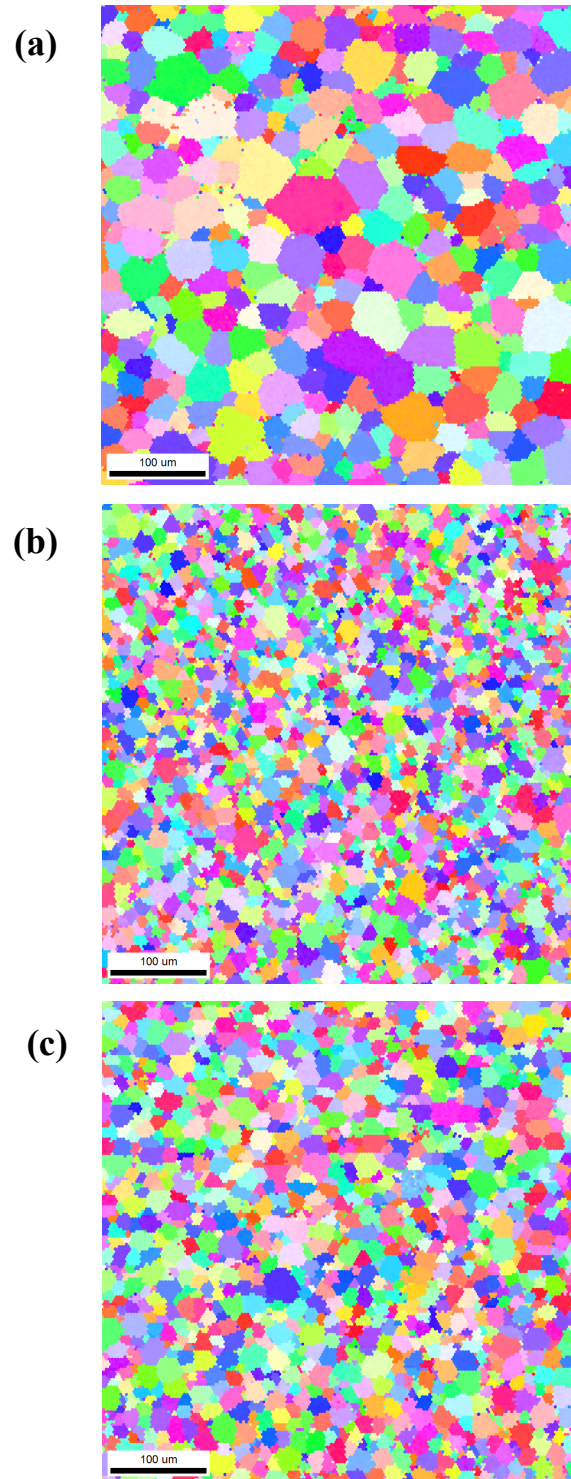
Figure 5. 7. EBSD images to measure the grain size of BNKLT88-1.5Mn (a) M12-M24, with initial powder particle size of 720 μm, sintered at 1050 °C (b) M12-PM, with initial powder particle size of 535 μm , sintered at 1010 °C (c) M12-36, with initial powder particle size of 535 μm , sintered at 1020 °C
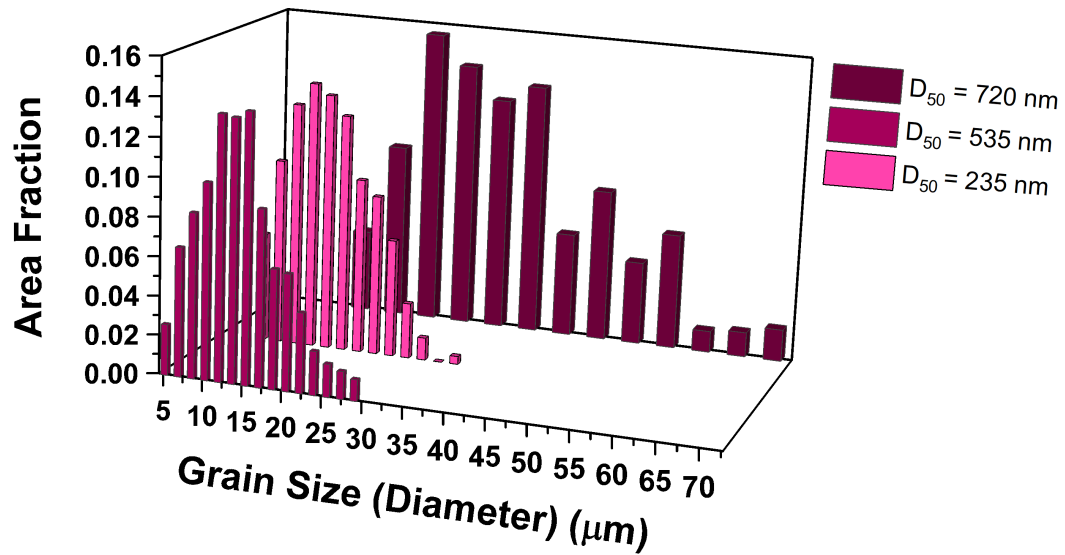
Figure 5. 8. Grain size distribution of BNKLT88-1.5Mn for calcined powder particle size of 720 nm (M24-M12), 535 nm (M24-M36), and 235 nm (M24-PM) sintered at 1050 °C, 1020 °C, and 1010 °C

5.3 Conclusion

The effects of different milling time and sintering temperature on the piezoelectric and dielectric properties of BNKLT88-1.5 Mn synthesized via solid state reaction method summarized in Table 5.3. Smaller particle size led to lowering the optimum sintering temperature due to higher surface energy and rate of diffusivity. However, the soft agglomerated was observed in powder milled at 36 h.

Higher surface energy and rate of diffusion at smaller powder particle size led to lowering sintering temperature, smaller grain size and porosity in the specimens.

Table 5. 3. Electromechanical properties of BNKLT88-1.5Mn

Sample ID	D_{50} (µm)	Sintering temperature (°C)	Density (g.cm^{-3})	ε_r	tanδ %	k_p	k_{33}	Planar Q_m
M12-M24	900	1075	5.83	340	1.56	0.235	0.538	904
		1100	5.88	308	0.99	0.218	0.523	974
		1125	5.77	327	1.06	0.216	0.519	847
M24-M12	720	1100	5.67	326	1.6	0.189	0.474	830
		1075	5.72	309	1.06	0.203	0.487	1000
		1055	5.77	294	1.06	0.191	0.567	1150
		1035	5.73	323	1.11	0.219	0.533	1140
M24-M36	Bimodal (235)	1050	5.75	342	1.22	0.209	0.545	1020
		1035	5.79	355	1.24	0.214	0.488	1050
		1020	5.78	343	1.15	0.227	0.512	1050
		1010	5.74	335	1.15	0.226	0.539	1071
M24-PM	535	1050	5.71	295	1.15	0.191	0.474	1020
		1035	5.71	316	1.26	0.204	0.402	1165
		1010	5.79	326	1.03	0.354	0.572	1190
		980	5.77	331	1.04	0.223	0.522	1120

5.1. References

[1] B. Jaffe, *Piezoelectric ceramics*. London, New York: R.A.N. Publishers, 1990.

[2] Q. Yin, B. Zhu, and H. Zeng, *Microstructure, Property and Processing of Functional Ceramics*. Berlin Heidelberg: Springer-Verlag, 2010.

High Power Performance of Manganese-Doped BNT-Based Pb-Free Piezoelectric Ceramic

Mehdi Hejazi[‡] , Elaheh Taghaddos[‡], Erkan Gurdal[§], Kenji Uchino[§],and

Ahmad Safari[‡]

[‡]Glenn Howatt Electroceramics Laboratories, Department of Materials Science and

Engineering, Rutgers, The State University of New Jersey, Piscataway, New Jersey

08854

[§]International Center for Actuators and Transducers, The Pennsylvania State University,

University Park, State College, Pennsylvania 16802

6 High Power Performance of Manganese-Doped BNT-Based Pb-Free Piezoelectric Ceramic

Abstract

Electromechanical properties and high power characteristics of Pb-free hard piezoelectric ceramics in the $(BiNa_{0.88}K_{0.08}Li_{0.04})_{0.5}(Ti_{1-x}Mn_x)O_3$ (x = 0, 0.014, 0.015, and 0.016) system were studied. Mn doping resulted in a considerable enhancement of mechanical quality factor Q_m and vibration velocity. The lowest mechanical and dielectric losses were achieved in 1.5 mol% Mn-doped ceramics with a planar Q_m of about 970 and tanδ of 0.89%. The heat dissipation and resonance frequency shift under high drive condition were remarkably suppressed upon Mn doping. The maximum vibration velocity was increased from 0.28 m.s^{-1} in undoped ceramic to 0.6 m.s^{-1} in 1.5 mol% Mn-doped composition. The results of this study revealed that Mn-doped BNT-based piezoelectrics exhibited a superior high power performance compared to their lead-based counterparts such as PZT4 and PZT8 ceramics.

6.1   Introduction

Hard piezoelectric ceramics are characterized by their high mechanical quality factor, low dielectric loss, and high Curie temperature [1], [2]. These materials are integrated in high power devices such as ultrasonic motors, piezoelectric transformers, and high intensity focused ultrasound where minimum heat dissipation and maximum output power are demanded [1], [2]. The ferroelectric domain wall motion is the main source of loss and heat generation in piezoelectric materials. Therefore, the efficiency of high power piezodevices is affected by stability of the domain configuration. According to the Eq. (6.1), the power loss per unit volume (w) is inversely proportional to the mechanical quality factor [3]

$$w = \frac{1}{2} \omega s^E T^2 Q_m^{-1} \tag{6. 1}$$

where ω is angular resonance frequency, T is stress, and s^E is elastic compliance.

To enhance the Q_m of piezoelectric ceramics, acceptor dopants such as $Mn^{2+,3+}$, $Fe^{2+,3+}$, and Cr^{3+} are incorporated into the B-site of the perovskite structure[4]–[6]. Upon addition of acceptor dopants, positively charged oxygen vacancies ($V_O^{\bullet\bullet}$) are created to maintain the charge neutrality[6], [7]. Oxygen vacancies combined with negatively charged acceptor sites (such as Mn'_{Ti} or Mn''_{Ti}) form oriented defect dipoles. The defect dipoles pin the ferroelectric domain walls and increase the mechanical quality factor as well as the coercive field of piezoelectrics [3], [6]–[10].

The Q_m values of piezoceramics reported in the literature are usually measured under low drive condition (~1 V). However, loss mechanisms under high electric fields are different than those of low drive condition. The figure of merit for high power applications

is the vibration velocity which is proportional to the product of mechanical quality factor and electromechanical coefficient. The vibration velocity (v_o) is defined as the product of angular resonance frequency (ω) and the root mean square (rms) of maximum vibration amplitude ϵ_m [3], [6], [8], [9], [11]:

$$v_o = \frac{1}{\sqrt{2}}\omega\epsilon_m = \frac{4}{\pi}\sqrt{\frac{\varepsilon_{33}^T}{\rho}}\,(k_{31}.Q_m).E \tag{6.2}$$

where ρ is the density, ε_{33}^T is the relative permittivity, k_{31} is the transverse coupling coefficient, and E is the driving electric field.

Materials with a low mechanical and dielectric losses (high Q_m and low tanδ), high coercive field E_c, and high k_{ij} values are promising candidates for high power devices. PZT4 and PZT8 are well-known acceptor-doped lead-based hard piezoelectrics which are frequently used in high power devices. These ceramics were chosen for comparison with lead-free compositions developed in this research. It is vital for a hard piezoceramic to maintain its high Q_m and low tanδ at high vibration velocities, that is, under application of a high electric field. It is known that the Q_m of Piezoelectric ceramics abruptly decreases as the vibration velocity surpasses a critical value [6].

In general, there are three types of losses in piezoelectrics: mechanical (elastic), dielectric, and piezoelectric (electromechanical) losses [11], [12]. In ferroelectric ceramics, the losses mainly originate from the internal friction caused by hysteretic effects of domain wall motion [7], [9], [11], [13].In these materials, under low drive conditions, mechanical loss is the dominant loss mechanism. This type of loss is basically originated from the motion of non-180° domain walls. On the other hand, the dielectric loss becomes prevailing at high drive condition [11]. The movement of 180° domain walls is accountable for

dielectric loss [9], [11]. Therefore, suppression of the ferroelectric domain wall motion by addition of acceptor dopants is an essential key in development of hard piezoelectrics for high power devices [2], [14], [15]. Despite recent development of hard BNT-based ceramics with Q_m values of 500–800, there are very few studies which investigate the high power performance of these lead-free materials[3], [5], [16]–[19].

In this article, electromechanical properties and high power characteristics of undoped and Mn-doped 0.88 $[Bi_{0.5}Na_{0.5}TiO_3]$–$0.08[Bi_{0.5}K_{0.5}TiO_3]$–$0.04[Bi_{0.5}Li_{0.5}TiO_3]$ lead- free piezoelectric ceramics (abbreviated to BNKLT88) prepared by mixed-oxide route were systematically studied. The resonance frequency shift, mechanical quality factor, heat generation, and input power of BNT-based transducers were measured under high drive condition. The performance of these Pb-free compositions was compared to their lead- based counterparts such as PZT4 and PZT8 which have similar mechanical quality factor to undoped and Mn-doped BNKLT88 ceramics.

6.2   Experimental Procedure

The conventional mixed-oxide method was used to prepare $(BiNa_{0.88}K_{0.08}Li_{0.04})_{0.5}(Ti_{1-x}Mn_x)O_3$ (x = 0, 0.014, 0.015, and 0.016) ceramics. Raw materials including high purity oxides and carbonate powders (>99.9%) with appropriate molar ratios were milled in acetone with zirconia balls for 12 h. The mixed powder was calcined at 800°C for 3 h and then was ball-milled for 12 h. 8 wt% Polyvinyl Alcohol solution was added as a binder before pressing. Disk-shaped samples of 14 mm in diameter and about 2 mm in thickness were uniaxially pressed at 150 MPa. Pressed pellets were sintered at 1100°C after binder removal. Fired-on silver electrodes were applied on samples for measurement of electrical properties. The ceramics were poled in silicon oil bath at

95°C for 15 min under an electric field of 50 kV.cm^{-1}. The density of ceramics was calculated based on the dimensions and weight of each sample.

The dielectric constant (ε_{33}^T) and dielectric loss (tanδ) were measured at 1kHz by an impedance analyzer (HP4194a; Hewlett Packard, Tokyo, Japan). A Berlincourt piezometer was used to measure the longitudinal piezoelectric charge coefficient (d$_{33}$) at 100 Hz. Piezoelectric planar and thickness coupling coefficients (k$_p$ and k$_t$, respectively) were calculated from the resonance and antiresonance frequencies of the impedance traces, based on the IEEE standards, as explained in Ref. [20] The experimental setup and details of high power measurements can be found in Refs. [3], [12]. Disk-shaped transducers with thickness of 1 mm and diameter of about 12 mm were used for low power as well as high power measurements. The frequency sweep was performed with a step size of 50 Hz per step. A sinusoidal signal was generated by a function generator (HP 33120A; Hewlett-Packard, Palo Alto, CA) and amplified by a power amplifier (NF 4010; NF Corporation, Yokohanma, Japan). The sample current was detected by a clamp-on AC current sensor (TCP 305; Tektronix, Beaverton, OR). Vibration amplitudes (v_{rms}) on the edges of the piezoelectric disks were measured using laser interferometer (Polytec PI, Model OFV-511; Polytec Inc., Irvine, CA). The voltage, current, and displacement waveforms of the piezoelectric disks were monitored by two digitizing oscilloscopes (TDS 3014B, Tektronix). The temperature on the surface of the sample was monitored by an IR thermometer (Hioki 3445, Nagano, Japan) and observed by an IR thermal camera (FLIR Systems Therma- CAM S40; FLIR Systems, Boston, MA). The driving voltage and current were automatically adjusted using a LabVIEW controlled computer to maintain a constant vibration velocity over the whole range of frequencies. The planar mechanical quality

factor (Q_m) at the resonance and antiresonance frequencies were measured from the impedance curves at each vibration velocity by using 3 dB up/down method [12].

6.3 Results and discussion

6.3.1 Low Drive Performance

Table 6.1 shows the density and electromechanical properties of undoped and Mn-doped ceramics sintered at 1100°C extracted from our recent publication [20]. Increasing the Mn concentration up to 1.5 mol%, remarkably enhanced the planar Q_m. Further increase in the dopant concentration resulted in a reduction of the Q_m. The maximum planar Q_m and minimum dielectric loss of 1.5 mol% Mn-doped ceramics were measured to be about 970% and 0.89%, respectively. The mechanical quality factor of BNT-based ceramics was higher than Mn-doped BNKLT88 and potassium niobate (KN) ceramics reported by Nagata et al. (Q_m of 730 and 820, respectively) [16]. A comprehensive study on the effects of acceptor dopants and sintering temperature on electromechanical properties of Pb-free BNT-based ceramics can be found in Ref. [20].

Table 6. 1. The Density and Electromechanical Properties of Undoped and Mn-Doped BNKLT88 Ceramics Sintered at 1100°C [20].

Mn mol.%	Density (g.cm^{-3})	d_{33} (pC.N^{-1})	K	tanδ%	k_p	k_t	Planar Q_m
0	5.78±0.05	96±1	374±4	1.21±0.04	0.260±0.003	0.498±0.005	402±8
1.4	5.78±0.02	88±1	324±3	0.97±0.03	0.224±0.003	0.474±0.006	868±12
1.5	5.88±0.03	85±1	308±4	0.89±0.03	0.218±0.001	0.487±0.004	974±17
1.6	5.76±0.01	87±1	320±5	1.01±0.05	0.217±0.01	0.479±0.004	886±26

Table 6.2 compares the electromechanical properties of commercial hard PZTs (PZT4 and PZT8) and BNKLT88 ceramics [20]. The data for Pb-based electroceramics were obtained from Refs. [5], [21]–[25] The mechanical quality factor, dielectric loss, and Curie temperature of undoped and Mn-doped Pb-free ceramics are comparable to those of PZT4 and PZT8, respectively. Lead-based materials exhibit a considerably higher planar coupling coefficient and dielectric constant. The main advantage of BNT-based ceramics for high power applications is their high coercive field ($E_c \sim 50$ kV.cm^{-1}) compared to commercial PZT's ($E_c \sim 14$– 20 kV.cm^{-1}) [3]. As will be discussed in the next section, due to their higher coercive field, BNKLT88 ceramics show superior performance at high vibration velocities.

Table 6. 2. Properties of Commercial Hard PZTs and Pb-Free BNT-Based Ceramics [5], [20]–[25]

Property	PZT4	PZT8	BNKLT88	1.5Mn-BNKLT88
d_{33} (pC/N)	290	225	95	85
ε^T_{33}	1300	1000	380	310
Tanδ %	0.5	0.4	1.1	0.85
k_t %	51	48	49	48
k_p %	58-64	51-60	26	22
Q_m	500	1000	400	970
T_c (ºC)	325	300	330	305
E_c (kV.cm^{-1})	14	20	47.2	52.2
E_i (kV.cm^{-1})~	3	3	0.7	3

6.3.2 High Drive Performance

Fig. 6.1 shows the variations of the resonance frequency (f_r) as a function of the vibration velocity in undoped and Mn- doped BNT-based compositions. The resonance frequency of all transducers decreased with increasing the vibration velocity. The decrease in resonance frequency was due to the softening phenomenon as a result of evolution of domain walls, and hysteretic effects at high electric fields which results in energy dissipation and heat generation [2], [3], [7], [9], [16], [26]. A similar trend has been observed in other hard Pb-free and Pb-based ceramics [3], [26]. As depicted in Fig. 6.1, the frequency shift was considerably suppressed upon Mn-doping. Ceramics doped with 1.5 mol% Mn showed the lowest resonance and antiresonance frequency shift due to their stabilized domain configuration. For example, at a vibration velocity of 0.4 m.s^{-1}, the resonance frequency shift was decreased by 75% through Mn-doping.
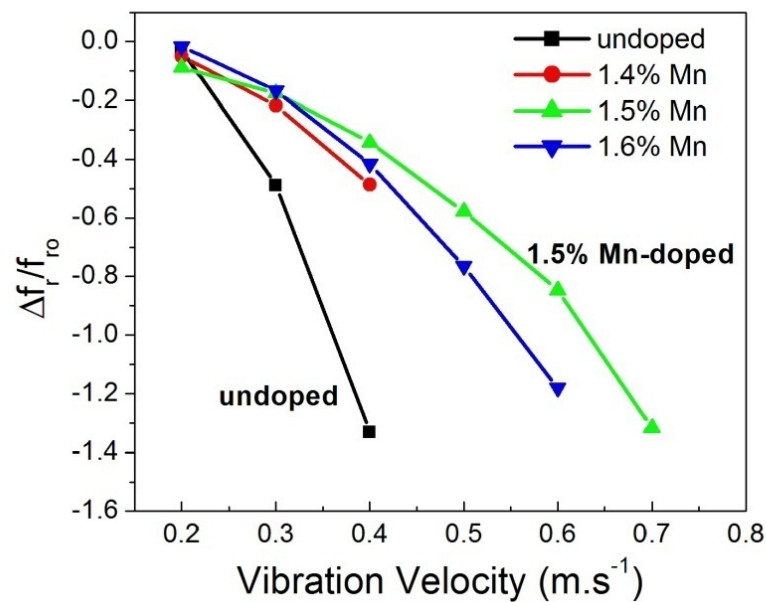
Figure 6. 1. The resonance frequency shift with vibration velocity in undoped and Mn-doped BNT-based transducers.

The heat generation in undoped and Mn-doped Pb-free transducers was also measured as a function of vibration velocity and the results are illustrated in Fig. 6.2. Mn-doping effectively reduced the heat dissipation in BNT-based ceramics. The minimum temperature rise was observed in 1.5 mol % Mn-doped BNKLT88 composition. At a vibration velocity of 0.3 m.s^{-1}, the temperature rise in undoped, 1.5% Mn- doped, and 1.6% Mn-doped transducers were 26°C, 5°C, and 9°C, respectively.
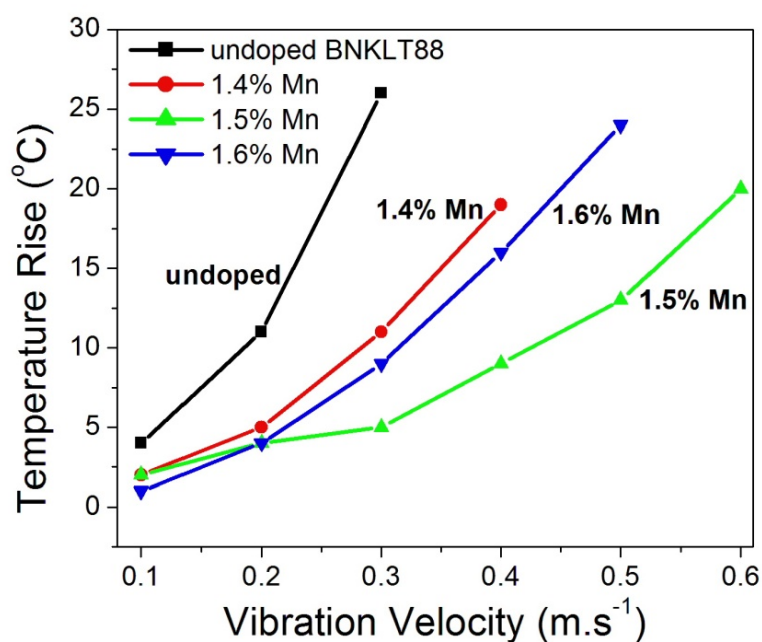
Figure 6. 2. The heat dissipation under high power condition in undoped and Mn-doped BNT-based transducers.

Figure 6.3 depicts the effect of vibration velocity on mechanical quality factor of undoped and Mn-doped transducers. The data for PZT4 and PZT8 ceramics were obtained from Ref. [3].

It is noticeable that the Q_m of 1.5% and 1.6% Mn-doped BNT-based transducers almost remained constant up to a vibration velocity of 0.4 $m.s^{-1}$. The Q_m values of these compositions at a vibration velocity of 0.5 $m.s^{-1}$ were 738 and 534, respectively. On the other hand, the Q_m of PZT8 transducer sharply dropped at vibration velocities of higher than 0.2 $m.s^{-1}$. Similarly, the performance of the undoped BNKLT88 transducer was greater than PZT4. Although the PZT4 sample possessed a higher Q_m at low vibration velocities (less than 0.15 $m.s^{-1}$), its Q_m decreased faster than that of BNKLT88. At a vibration velocity of 0.2 $m.s^{-1}$, the Q_m values of PZT4 and undoped BNKLT88 were 250 and 295, respectively. The maximum vibration velocity is defined as the v_{rms} at a temperature rise of 20°C. The undoped, 1.5% Mn-doped, and 1.6% Mn-doped Pb-free ceramics showed a maximum vibration velocity of 0.28, 0.6, and 0.48 $m.s^{-1}$, respectively. The maximum vibration velocity for hard commercial PZTs falls in range of 0.3–0.5 $m.s^{-1}$ [6], [27]. Therefore, the maximum vibration velocity of Mn-doped BNT-based ceramics was higher than that of commercial PZT-based piezoelectric ceramics. Hard BNT-based ceramics developed in this work (1.5 mol% Mn-doped composition) also showed better high power characteristics compared to other Pb-free ceramics such as Cu-doped $(Na_{0.5}K_{0.5})(Nb_{0.97}Sb_{0.03})O_3$, Co-doped $BaTiO_3$ and Co-doped 0.83BNT–0.084BKT–0.03BLT–0.056BT ceramics. The mechanical quality factors of these materials at a vibration velocity of 0.2 $m.s^{-1}$ were reported to be around 800, 480, and 800, respectively. In addition, the heat generation and frequency shift with increasing the vibration velocity

was inferior to Mn-doped BNT-based ceramics. High power performance of $(Na_{0.5}K_{0.5})NbO_3$, $BaTiO_3$, and BNT-based ceramics in Refs. [3], [26] have only been measured up to a vibration velocity of 0.25 and 0.4 $m.s^{-1}$, respectively.
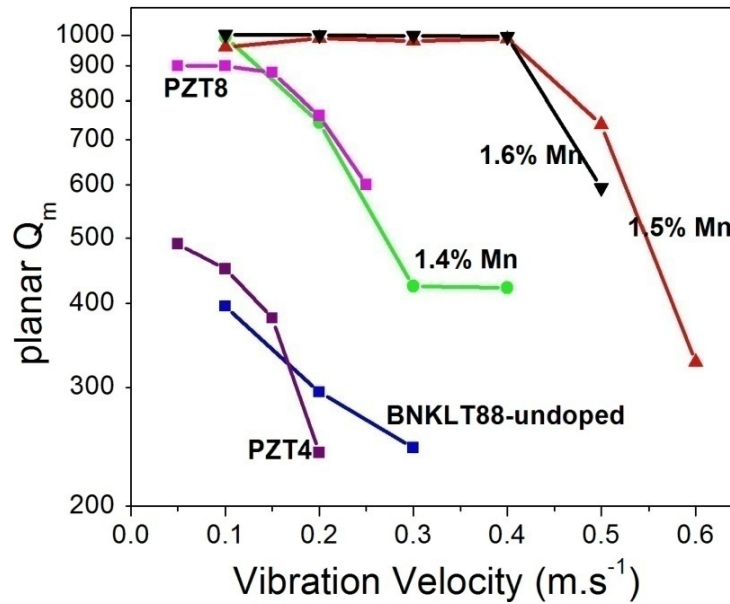
Figure 6. 3. The mechanical quality factor of undoped and Mn-doped BNT-based ceramics versus vibration velocity. The PZT4 and PZT8 data are shown for a comparison.3 Qm values are shown on a logarithmic scale.

Superior high power performance of BNT-based ceramics compared to PZTs, can be attributed to their higher coercive field [3]. As shown in Table 6.2, the coercive field in hard PZTs falls in a range of 14–20 $kV.cm^{-1}$. However, in BNT-based ceramics, the coercive field is as high as 52 $kV.cm^{-1}$. Materials with a high coercive field have a more stable domain configuration and due to the difficulty of polarization reversal are more resistant to depoling. As pointed out earlier, the major part of the loss in ferroelectric ceramics is resulted by destabilization of ferroelectric domains. The diminished domain

wall mobility in Mn-doped BNT-based ceramics decreased the overall loss and heat generation under high drive conditions. On the contrary, the performance of hard PZTs is degraded at high electric fields because of their lower coercive field. These results are in agreement with high power performance of Co-doped and Mn-doped BNT ceramics reported by other researchers [3], [16].

Piezoelectric resonators are usually designed to operate at the resonance frequency. Recent studies on Pb-based ceramics have shown that operation of some piezoelectric devices at antiresonance frequency results in a higher efficiency [12]. IEEE standards assume that the Q_m at the resonance and antiresonance frequencies have the same values [28]. However, there might be a considerable difference between Q_m values measured at these two frequencies. Figures 6.4 (a)–(c) compare the performance of undoped, 1.5% Mn-doped, and 1.6% Mn-doped BNKLT88 piezoelectric ceramics at the resonance and antiresonance modes. The Q_m values measured at resonance and antiresonance frequencies are shown by Q_{mA} and Q_{mB}, respectively. In undoped composition, similar to hard PZTs, [12] a higher efficiency was achieved at the antiresonance frequency compared to the resonance frequency ($Q_{mB} > Q_{mA}$ and $\Delta T_B < \Delta T_A$). On the contrary, Mn-doped transducers showed a higher efficiency at the resonance frequency ($Q_{mB} \leq Q_{mA}$ and $\Delta T_B \geq \Delta T_A$). The origins of the discrepancy between Q_{mA} and Q_{mB} are not clear yet. However, phenomenological theories correlate the observed differences to the relative values of the dielectric, mechanical, and piezoelectric losses. For 31-mode, following equations have been developed [12]:

$$Q_{mA=\frac{1}{tan\phi'_{11}}} \tag{6.3}$$

$$\frac{1}{Q_{mB}} = \frac{1}{Q_{mA}} - \frac{2}{1+\left(\frac{1}{k_{31}}-k_{31}\right)^2 \Omega_{B,31}^2}(2tan\,\theta'_{31} - tan\,\delta'_{33} - tan\,\phi'_{11}) \tag{6.4}$$

where tan δ', tan ϕ', and tan θ' are intensive dielectric, mechanical, and piezoelectric loss factors, $\Omega_{B,31} = \frac{2\pi f_a L}{2\vartheta_{11}^E}$, and v^E_{11} is the longitudinal sound velocity under constant E. By considering these equations, it is clear that $Q_{mB} > Q_{mA}$ if 2tanθ'>(tanϕ'+tanδ') and $Q_{mB} < Q_{mA}$ if 2tanθ'<(tanϕ'+tanδ'). The piezoelectric loss is the factor that determines whether Q_{mB} is larger than Q_{mA}, although it was previously neglected by most researchers and electroceramic manufacturers. Recently, it has been confirmed that the magnitude of the piezoelectric loss is comparable to dielectric and mechanical losses [12]. There are various domain reversal possibilities in a crystal, which contribute to dielectric, mechanical, and piezoelectric losses [7]. The dielectric loss is originated from the hysteresis during the 180° polarization reversal under an applied electric field. The mechanical loss comes from reorientation of 90° domain walls under application of an external stress. The piezoelectric loss is believed to originate from 90° polarization reversal under application of an electric field [7]. It appears that the domain wall clamping effect of Mn as an acceptor dopant, effectively decreased the piezoelectric loss in a way that 2tanθ'<(tanϕ'+tanδ') condition was met, and therefore, the efficiency of the Mn-doped transducer at the resonance frequency became higher than the antiresonance frequency.
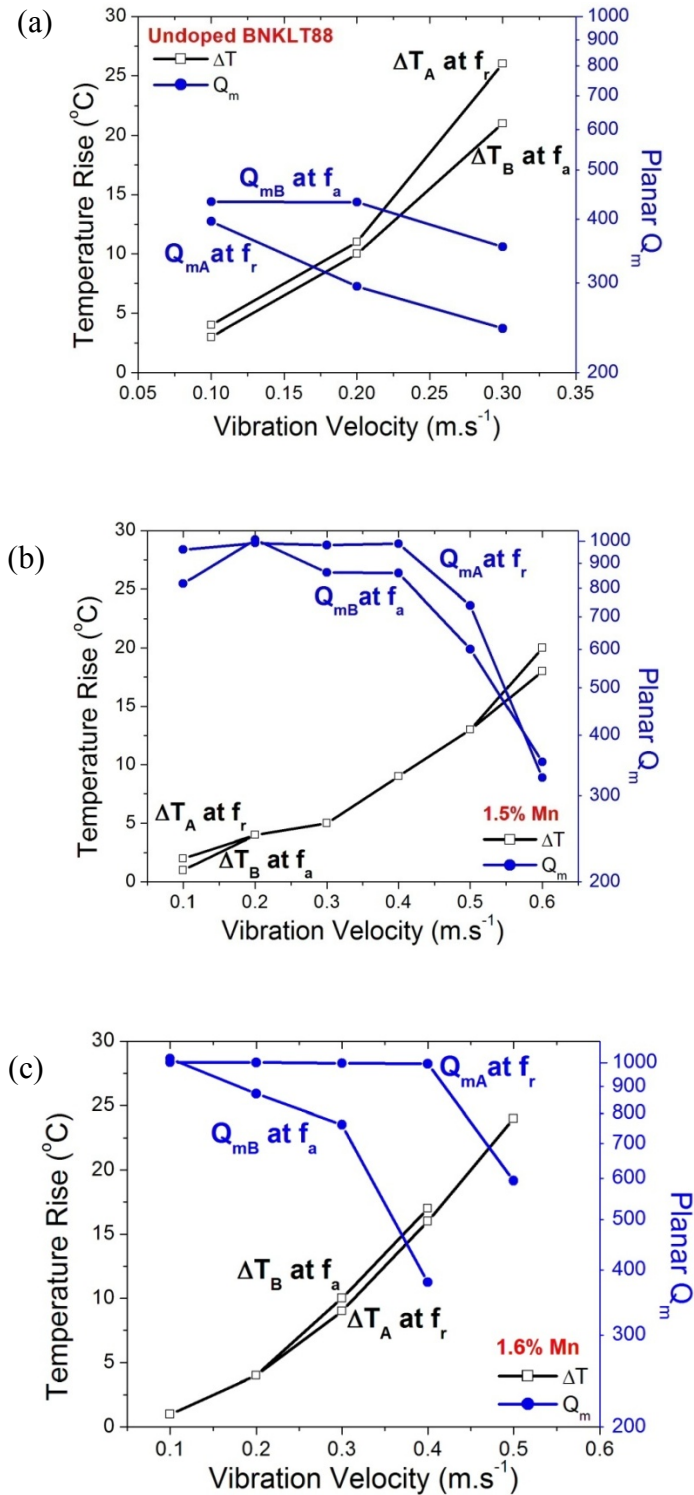
Figure 6. 4. Effects of vibration velocity on the heat dissipation and mechanical quality factor of (a) undoped (b) 1.5% Mn-doped (c) 1.6% Mn-doped BNKLT88 transducers measured at resonance and antiresonance frequencies. Qm values are shown on a logarithmic scale.

Figure 6.5(a) demonstrates the driving voltage and current in 1.5 mol% Mn-doped BNKLT88 ceramics at different vibration velocities. The lowest voltage and current were obtained at the resonance and antiresonance frequencies, respectively. The main difference between the transducers response at the resonance and antiresonance frequencies was the driving impedance/admittance [12]. While a low driving voltage and high driving current were required at the resonance frequency, the opposite was observed at the antiresonance frequency. With increasing the vibration velocity, the driving voltage and current increased as expected. The input driving power in the vicinity of fundamental resonances in undoped and Mn-doped ceramics is shown in Fig. 6.5 (b). The minimum input powers in these graphs correspond to the resonance and antiresonance frequencies. The input power of transducers at the resonance frequency was decreased by about 70%–75% through Mn doping. In undoped transducers, the input power at f_a was less than f_r which again confirms the higher efficiency of the transducer at antiresonance frequency. On the other hand, in 1.5 mol% Mn-doped transducers, the input power at antiresonance frequency was higher than that of resonance frequency which is in agreement with the data shown in Fig. 6.4. Increasing the vibration velocity led to increasing the input power. It also resulted in shifting and broadening the resonance and antiresonance peaks. This was caused by heat dissipation and a reduced mechanical quality factor at high vibration velocities as discussed throughout the study.
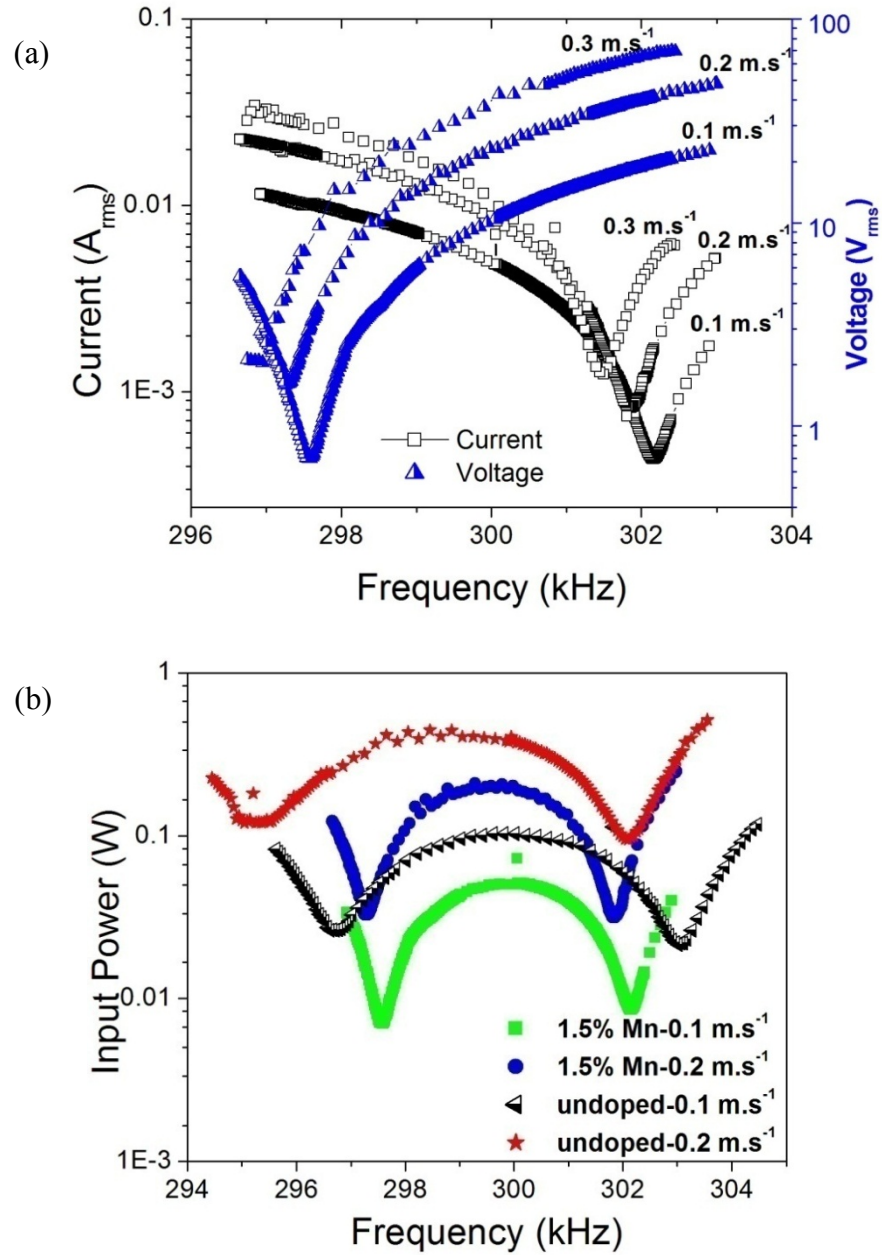
Figure 6. 5. (a) The driving voltage and current in 1.5 mol% Mn-doped BNKLT88 transducers at different vibration velocities (b) input power across the resonance and antiresonance frequencies in undoped and 1.5 mol% Mn-doped BNKLT88 transducers.

6.4   Conclusion

The electromechanical properties and high power performance of undoped and Mn-doped $(BiNa_{0.88}K_{0.08}Li_{0.04})_{0.5}(Ti_{1-x}Mn_x)O_3$ (x = 0, 0.014, 0.015, and 0.016) piezoelectric ceramics were studied. It was shown that Mn doping considerably decreased the mechanical, dielectric, and piezoelectric losses. The Q_m and tanδ values for 1.5 mol% Mn-doped ceramic were 970 and 0.89%, respectively. Mn doping effectively reduced the heat dissipation and input power of BNT-based transducers and resulted in a higher vibration velocity. The BNKLT88 ceramics doped with 1.5 mol% Mn exhibited an outstanding high power performance with a maximum vibration velocity of 0.6 m/s which was higher than that of PZT8 and PZT4. High mechanical quality factor coupled with a high coercive field contributed to the enhanced high power performance of Mn-doped BNT-based transducers.

Acknowledgment

6.5   References

[1] K. Uchino, "Piezoelectric ultrasonic motors: overview," *Smart Mater. Struct.*, vol. 7, no. 3, p. 273, 1998.

[2] Y. Gao, K. Uchino, and D. Viehland, "Domain wall release in 'hard' piezoelectric under continuous large amplitude ac excitation," *Journal of Applied Physics*, vol. 101, no. 11, p. 114110, Jun. 2007.

[3] H. J. Lee, S. O. Ural, L. Chen, K. Uchino, and S. Zhang, "High Power Characteristics of Lead-Free Piezoelectric Ceramics," *J. Am. Ceram. Soc.*, vol. 95, no. 11, pp. 3383–3386, Nov. 2012.

[4] L.-X. He, M. Gao, C.-E. Li, W.-M. Zhu, and H.-X. Yan, "Effects of Cr2O3 addition on the piezoelectric properties and microstructure of PbZrxTiy(Mg1/3Nb2/3)1−x−yO3 ceramics," *Journal of the European Ceramic Society*, vol. 21, no. 6, pp. 703–709, Jun. 2001.

[5] S. Zhang, J. B. Lim, H. J. Lee, and T. R. Shrout, "Characterization of Hard Piezoelectric Lead-Free Ceramics," *IEEE Transactions on Ultrasonics, Ferroelectrics, and Frequency Control*, vol. 56, no. 8, pp. 1523–1527, Aug. 2009.

[6] Y. Gao, Y.-H. Chen, J. Ryu, K. Uchino, and D. Viehland, "Eu and Yb Substituent Effects on the Properties of $Pb(Zr_{0.52}Ti_{0.48})O_3$ –$Pb(Mn_{1/3}Sb_{2/3})O_3$ Ceramics: Development of a New High-Power Piezoelectric with Enhanced Vibrational Velocity," *Japanese Journal of Applied Physics*, vol. 40, no. Part 1, No. 2A, pp. 687–693, Feb. 2001.

[7] K. Uchino *et al.*, "Loss mechanisms and high power piezoelectrics," *Journal of Materials Science*, vol. 41, no. 1, pp. 217–228, Jan. 2006.

[8] Y. Gao, K. Uchino, and D. Viehland, "Time Dependence of the Mechanical Quality Factor in 'Hard' Lead Zirconate Titanate Ceramics: Development of an Internal Dipolar Field and High Power Origin," *Japanese Journal of Applied Physics*, vol. 45, no. 12, pp. 9119–9124, Dec. 2006.

[9] K. Uchino, *Ferroelectric Devices*. CRC Press, 2000.

[10]   U. Robels, J. H. Calderwood, and G. Arlt, "Shift and deformation of the hysteresis curve of ferroelectrics by defects: An electrostatic model," *Journal of Applied Physics*, vol. 77, no. 8, pp. 4002–4008, Apr. 1995.

[11]   K. Uchino and S. Hirose, "Loss mechanisms in piezoelectrics: how to measure different losses separately," *IEEE Transactions on Ultrasonics, Ferroelectrics, and Frequency Control*, vol. 48, no. 1, pp. 307–321, Jan. 2001.

[12]   K. Uchino, Y. Zhuang, and S. O. Ural, "Loss determination methodology for a piezoelectric ceramic: new phenomenological theory and experimental proposals," *J. Adv. Dielect.*, vol. 01, no. 01, pp. 17–31, Jan. 2011.

[13]   B. Li, G. Li, S. Zhao, L. Zhang, and A. Ding, "Characterization of the high-power piezoelectric properties of PMnN–PZT ceramics using constant voltage and pulse drive methods," *Journal of Physics D: Applied Physics*, vol. 38, no. 13, pp. 2265–2270, Jul. 2005.

[14]   H.-Y. Park *et al.*, "Effect of MnO2 on the Piezoelectric Properties of the 0.75Pb(Zr0.47Ti0.53)O3–0.25Pb(Zn1/3Nb2/3)O3 Ceramics," *Journal of the American Ceramic Society*, vol. 93, no. 9, pp. 2537–2540, 2010.

[15]   C. Galassi, E. Roncari, C. Capiani, and F. Craciun, "Processing and characterization of high Qm ferroelectric ceramics," *Journal of the European Ceramic Society*, vol. 19, no. 6–7, pp. 1237–1241, Jun. 1999.

[16]   H. Nagata, K. Takai, Y. Nomura, S. Sato, Y. Hiruma, and T. Takenaka, "Vibration velocities under high-power driving on perovskite-type lead-free ferroelectric ceramics," in *2010 IEEE International Symposium on the Applications of Ferroelectrics (ISAF)*, 2010, pp. 1–4.

[17]   T. Tou, Y. Hamaguti, Y. Maida, H. Yamamori, K. Takahashi, and Y. Terashima, "Properties of (Bi $_{0.5}$ Na $_{0.5}$)TiO $_3$ –BaTiO $_3$ –(Bi $_{0.5}$ Na $_{0.5}$)(Mn $_{1/3}$ Nb $_{2/3}$)O $_3$ Lead-Free Piezoelectric Ceramics and Its Application to Ultrasonic Cleaner," *Japanese Journal of Applied Physics*, vol. 48, no. 7, p. 07GM03, Jul. 2009.

[18]   T. Takenaka, H. Nagata, and Y. Hiruma, "Phase Transition Temperatures and Piezoelectric Properties of (Bi1/2Na1/2)TiO3-and (Bi1/2K1/2)TiO3-Based Bismuth Perovskite Lead-Free Ferroelectric Ceramics," *IEEE Transactions on Ultrasonics, Ferroelectrics, and Frequency Control*, vol. 56, no. 8, pp. 1595–1612, Aug. 2009.

[19]   Y. Hiruma, H. Nagata, and T. Takenaka, "Phase-transition temperatures and piezoelectric properties of (Bi1/2Na1/2)TiO3- (Bi1/2Li1/2)TiO3-(Bi1/2K1/2)TiO3 lead-free ferroelectric ceramics," *IEEE Transactions on Ultrasonics, Ferroelectrics, and Frequency Control*, vol. 54, no. 12, pp. 2493–2499, Dec. 2007.

[20]   E. Taghaddos, M. Hejazi, and A. Safari, "Electromechanical Properties of Acceptor-Doped Lead-Free Piezoelectric Ceramics," *J. Am. Ceram. Soc.*, vol. 97, no. 6, pp. 1756–1762, Jun. 2014.

[21]   M. W. Hooker, "Properties of PZT-Based Piezoelectric Ceramics Between -150 and 250 C," Sep. 1998.

[22]   "Piezomaterial Data, Specific Parameters of Standard Materials. PI Ceram- ics Co., Lederhose, Germany." .

[23]   "Piezoelectric Materials Datasheet. Piezopower, CTS Electronic Compo- nents Co., Albuquerque, NM." .

[24]   "Piezoelectric Ceramics Datasheet, Morgan Advanced Materials, Berkshire, UK." .

[25]   D. Berlincourt and C. Near, "PROPERTIES OF MORGAN ELECTRO CERAMIC CERAMICS," p. 12.

[26]   E. A. Gurdal, S. O. Ural, H.-Y. Park, S. Nahm, and K. Uchino, "High Power (Na0.5K0.5)NbO3-Based Lead-Free Piezoelectric Transformer," *Jpn. J. Appl. Phys.*, vol. 50, no. 2R, p. 027101, Feb. 2011.

[27]   "Comparison of Power Density Characteristics among Disk and Plate Shaped Piezoelectric Devices," *Jpn. J. Appl. Phys.*, vol. 49, no. 2R, p. 021502, Feb. 2010.

[28]   "Publication and Proposed Revision of ANSI/IEEE Standard 176-1987 'ANSI/IEEE Standard on Piezoelectricity,'" *IEEE Transactions on Ultrasonics, Ferroelectrics, and Frequency Control*, vol. 43, no. 5, pp. 717-, Sep. 1996.

Effect of Acceptor Dopant on the Electrical Properties and Conductivity of BNT-Based Piezoelectric Ceramic

Elaheh Taghaddos, Ahmad Safari

7 Effect of Acceptor Dopant on The Electrical Properties and Conductivity of BNT-Based Piezoelectric Ceramic

Abstract

The effect of Mn and Fe dopants on the electromechanical and electrochemical properties of $0.88[Bi_{0.5}Na_{0.5}]TiO_3$-$0.08[Bi_{0.5}K_{0.5}]TiO_3$-$0.04[Bi_{0.5}Li_{0.5}]TiO_3$ piezoceramic are investigated with particular emphasis on the complex impedance in the temperature range from 450 to 600 °C. The impedance spectra have been simulated with equivalent circuits in order to extract bulk and grain boundary characteristics and to determine activation energies of conduction. Mn and Fe dopants considerably enhance the mechanical quality factor and decrease the dielectric loss compared to the undoped composition. Mn-doping leads to dramatically higher resistivity in the bulk and modest increase in the grain boundaries activation energy. On the other hand, conductivity increases dramatically via Fe-doping with a significant lowering of the activation energy in the bulk and corresponding raising of the activation energy at the grain boundaries in comparison to Mn-doped and undoped ceramic. The bulk conductivity of Fe-doped piezoceramic reaches as high as 0.01 S.cm^{-1} at 600 °C.

7.1 Introduction

Piezoelectric and ferroelectric materials are widely applied in civil, military, and energy applications as major components of high-tech devices. Piezoelectric materials are used as tunable high-dielectric materials for high-frequency applications such as nonlinear optical devices, ferroelectric memories, vibration damping, artificial muscles, airbag sensors, fuel atomizers, inject printers, disposable patient monitors, and ultrasonic imaging [1]–[3].

While lead-based piezoelectric materials dominate the market of piezoelectric devices, there are growing calls for safer materials that are lead-free. Discovered by Smolenskii and Agranovkava, et al. in 1960, $(Bi_{0.5}Na_{0.5})TiO_3$ (BNT) is one of the most promising lead-free piezoelectric materials [4]. This composition has perovskite structure, large remnant polarization ($P_r = 38$ $\mu C.cm^{-2}$) and high Curie temperature ($T_c = 320$ °C). Over that past few decades, a considerable amount of research has been carried out on BNT and its solid solution with other ferroelectric materials [5]–[9]. Compositional engineering has been used to improve piezoelectric properties. In the perovskite structure the substitution of the A-site ions with donor dopants of higher valency creates A-site vacancies and randomly distributed point defects, which induce soft piezoelectric characteristics.

On the other hand, substitution at the A- or B-site with acceptor dopants, i.e. lower valence ions, creates oxygen vacancies in order to maintain charge neutrality. The positively charged oxygen vacancies can diffuse to the domain wall through octahedral sites of the perovskite structure and form oriented dipoles with negatively charged acceptor sites [10], [11]. Substitution on the Ti-site of BNT-based compositions with Mn or Fe

results in a pinning effect of the domain wall, decreasing dielectric loss and enhancing the mechanical quality factor (Q_m). Acceptor doped BNT-based ceramics with high Curie temperature (T_c), coercive field (E_c), and Q_m are suitable alternatives to lead-based hard PZT compositions for high power applications. Despite the comprehensive investigation in compositional engineering to enhance the electromechanical properties of the lead-free ceramics, there is limited information about the defect chemistry of the different compositions. This information is essential in order to tune the ferroelectric and dielectric properties of ceramics. For example, Li, et al. reported a new application for a non-stoichiometric and acceptor-doped $(Bi_{0.5}Na_{0.5})TiO_3$ composition as an oxygen ion conductor in electrochemical devices such as solid oxide fuel cells [12], [13]. The ionic conductivity can change by orders of magnitude as a result of minor changes in the defect chemistry. As a result, it is essential to study the conduction mechanism and to identify the contribution of microscopic elements such as interior grain (bulk), grain boundary, and interface to the dielectric response and to the conductivity of polycrystalline materials. Complex impedance spectroscopy (CIS) is a powerful technique used to systematically measure the electrical properties of electroceramics and to study the kinetics of ionic movement in solids for a wide range of frequencies. By fitting the impedance spectra to equivalent circuit models, detailed information about the electrical properties of bulk, grain boundaries, and interfaces can be determined [14].

Generally, ceramic materials exhibit some form of parallel resistor-capacitor (R//C) circuit behavior corresponding to the bulk crystal, grain boundaries, and ceramic-electrode interface. A departure from a perfect R//C circuit model is apparent when a depressed semicircular arc in the complex impedance is observed due to non-Debye

behavior [15], [16], whereby a single time constant is replaced by a distribution of time constants due to the presence of diffusion, surface defects, local charge inhomogeneities, two or three phase regions, and variation in compositions, or other factors, causing dispersion from ideal behavior [17]. This dispersion results in a decoupling of the phase angle between applied voltage and induced current during sweeps of the AC frequency. The aforementioned behavior is modeled with a constant phase element (CPE) in place of a capacitor [18].

In this study electromechanical properties, electrical conductivity and impedance relaxation of $(BiNa_{0.88}K_{0.08}Li_{0.04})_{0.5}TiO_3$ (BNKLT88) has been systematically studied. The effect of Mn and Fe acceptor dopants on impedance relaxation and electrical conductivity has been investigated and compared to the undoped ceramic.

7.2 Experimental Procedure

The conventional mixed oxide route was used to prepare $(BiNa_{0.88}K_{0.08}Li_{0.04})_{0.5}TiO_3$ (BNKLT88) and $(BiNa_{0.88}K_{0.08}Li_{0.04})_{0.5}Ti_{0.995}A_{0.015}O_3$ (A = Mn, Fe) ceramics. Raw materials, including high-purity oxides and carbonate powders, were dried overnight at 120 °C. The powders were mixed in a Nalgene bottle with appropriate molar ratios and were milled with zirconia balls in acetone for 12 h. The mixed powder was dried to a slurry at 120 °C and calcined at 800 °C for 3 hours. The calcined powders were ball milled again for 12 hours to break up hard agglomerates. After binder addition of 8 wt% Polyvinyl Alcohol in solution, 14 mm diameter disk-shaped samples were uniaxially pressed at 150 MPa in a stainless steel die. Upon binder removal at 550 °C

for 20 min, pellets were sintered at temperatures 1075–1125 °C for 2 h. Detailed sample preparations and electromechanical characterization has been described elsewhere [19].

The ThermoFisher K-Alpha X-Ray Photoelectron Spectroscopy (XPS) with 1486.7keV x-ray photon energy and 400 μm step size used to study the samples chemistry. First the survey scan has been done over the 1350-0 eV range with 1 eV step size. Then, the specific range of 740-700 eV, 660-632 eV, and 474,448 eV were scanned in details to explore the oxidation state of Fe, Mn, and Fe, respectively.

The impedance spectra were measured with a Gamry Reference 600+ Potentiostat with frequency range of $1\text{-}10^6$ Hz and 1000 mV applied voltage. The complex impedance was measured at the temperature range of 450-600 °C with 25 °C step size. The impedance data (Z^*) was converted to resistivity (ρ^*) by accounting for the geometrical parameters of the specimen (Eq.7.1)

$$\rho^* = \rho' - j\rho'' = {Z^*}/{L},$$ (7. 1)

with complex impedance,

$$Z^* = Z' - jZ''$$ (7. 2)

where $L = {H}/{A}$ represents the geometrical factor, A is electrode area, and H is the thickness of the sample (electrode separation). All ceramics had comparable geometrical factors, A ≅ 0.93-0.92 cm ^{2} and H ≅ 0.1-0.085 cm. Zview2 software, ver. 3.5d Scribner Associate, Inc., was used to fit the measured impedance data with an equivalent electrical circuit. The ac conductivity was extracted from the fitted impedance data.

7.3   Result and Discussion

7.3.1   Electromechanical Properties and XRD Analysis

The XRD patterns of undoped, Mn-doped and Fe-doped BNKLT88 are illustrated in Fig. 7.1. Mn-doped and Fe-doped BNKLT88 show similar XRD patterns to undoped BNKLT88, with pure perovskite structure suggesting that Mn and Fe cations successfully substituted the Ti^{4+} ions.
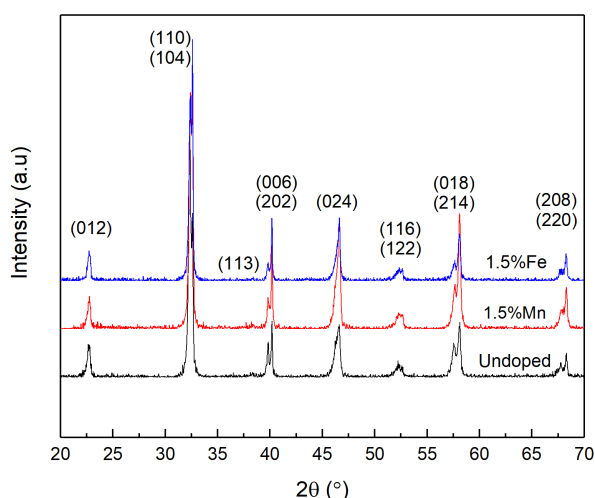
Figure 7. 1. XRD patterns of undoped, Mn-doped and Fe-doped BNKLT88 ceramic showing pure perovskite structure.

The oxidation state of Ti, Mn and Fe in both Mn-doped and Fe-doped BNKLT88 composition were investigated via XPS and the representative spectra are illustrated in Fig 7.2. The Mn 2p spectrum of Mn-doped ceramic shown in Fig 7.2-b. The presence of divalent manganese cation confirmed via observed peak at binding energy of 640.8 eV accompany with a satellite Mn $2p_{3/2}$ peak located at 645 eV. On the other side, the binding energy and consequently the Mn peak position for different oxidation states are very close to each other (MnO: 641.4 eV, Mn_2O_3: 641.4 eV, and MnO_2: 641.8), which makes it

difficult to indicate the exact position for each valence state. The peak broadening of satellite Mn $2p_{3/2}$ reveals the coexistence of Mn^{2+} with higher valence cations of Mn^{3+}. In the case of BNKLT88-1.5Fe composition, the observed Fe $2p_{3/2}$ at binding energy of 709.7 eV along with Fe (II) satellite peak at 712.9 eV in the Fe 2p spectrum (Fig 7.2 d) verified the presence of Fe^{+2}. The broadening peak of Fe $2p_{3/2}$ and its satellite reveals the coexistence of Fe^{+3} and Fe^{+2}. Mn^{+2} with ionic radius of $r \sim 0.67$ Å low spin, $r \sim 0.83$ Å high spin, Mn^{+3} with ionic radius of $r \sim 0.58$ Å low spin, $r \sim 0.64$ Å high spin, Fe^{+2} with ionic radius of $r \sim 0.61$ Å low spin, $r \sim 0.78$ Å high spin, Fe^{+3} with ionic radius of $r \sim 0.55$ Å low spin, $r \sim 0.64$ Å high spin would preferably sitting on the Ti^{+4} site with ionic radios of 0.68 Å. Nerveless to say that the exitance of Ti^{+4} for both compositions were verified via 2p XPS spectrum of Ti (Fig 2a and 2c).
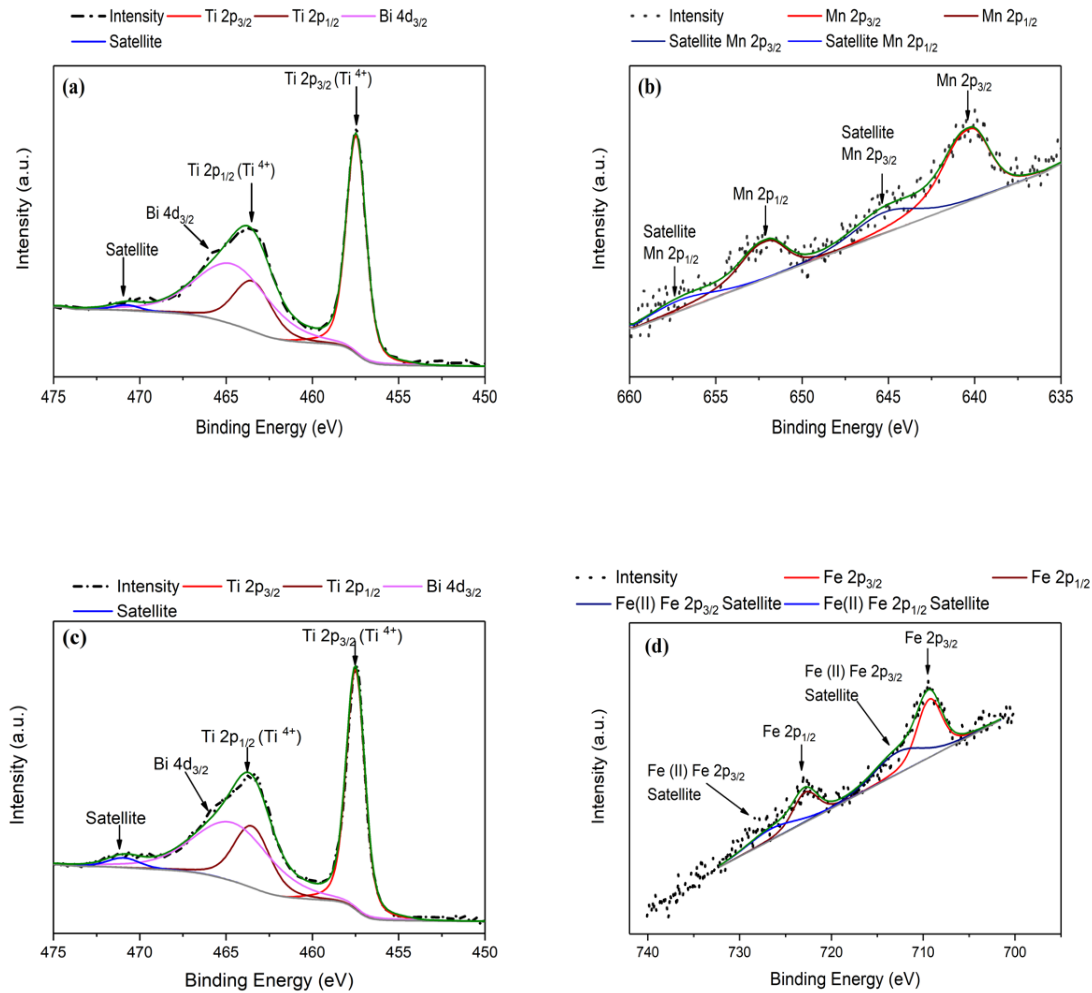
Figure 7. 2 Ti 2p XPS spectrum (a) Mn 2P XPS spectrum for BNKLT88-1.5Mn composition, Ti 2p XPS spectrum (b), and Fe 2p XPS spectrum for BNKLT88-1.5Fe composition

Table 7.1 summarizes the density and electromechanical properties of undoped, Mn-doped and Fe-doped BNKLT88 extracted from a recent publication by this group [19]. Mn and Fe as acceptor dopants remarkably enhanced the mechanical quality factor and decreased dielectric loss. Mn and Fe-doped BNKLT88 also showed smaller planar coupling coefficients and dielectric constant as well as larger coercive field (E_c) and internal bias field (E_i) due to the domain wall pinning effect of oxygen vacancies.

Table 7. 1. Electromechanical properties of undoped, Mn-doped and Fe-doped BNKLT88 ceramics [19].

Properties	Density (g/cm³)	d_{33} (pC/N)	$\varepsilon^T_{33}/\varepsilon_0$	tanδ (%)	k_t (%)	k_p (%)	Q_m	E_c (kV.cm⁻¹)	E_i (kV.cm⁻¹)
BNKLT88	5.78	95	380	1.1	49	26	400	47.2	0.7
BNKLT88-1.5Mn	5.88	85	310	0.85	48	22	970	52.2	3
BNKLT88-1.5Fe	5.78	81	300	0.9	46	20	900	51.7	2.5

As previously reported [19], the Fe-doped BNKLT88 underwent a color change during the poling. The pale yellow color of the as-sintered ceramic turned black after poling. The valance change in Fe^{3+} cations under application of an electric field may cause the observed color change, referred to as an electrocoloration effect. This phenomenon has also been reported in other materials such as Fe-doped $SrTiO_3$ [20]. Compared to Mn-doped ceramics, Fe-doped samples required lower temperature and voltage to be poled, which can be attributed to lower resistivity of Fe-doped samples. The

7.3.2 Impedance Spectroscopy

The electrical resistivity of Mn[21] , MnO [22], Mn_2O_3 [23], [24] at room temperature are in the range of ~1.44 × 10^{-7} kΩ.cm, ~10^6 kΩ.cm, and ~10^2 kΩ.cm respectively. Additionally, the electrical resistivity of Fe, and Fe_3O_4 ($Fe^{+2}Fe^{+3}_2O_4$)[25] at room temperature are ~10^{-7} kΩ.cm and ~ 4.9 × 10^{-6} kΩ.cm. The conductivity of Mn and Fe increased as a function of temperature, while the resistivity of oxide decreased. By

comparison of these number, one can see that the conductivity of manganese oxide is much higher than iron oxide.

The temperature dependence of the complex impedance of undoped, Fe-doped and Mn-doped BNKLT88 ceramics are illustrated as Nyquist plots in Fig. 7.3-7.5. In all cases, the center of the semicircles did not lie on the real axis (Z′), necessitating the usage of a constant phase element (CPE) in place of a capacitor. Moreover, the radii of the semicircles and their intercept with Z′ decreased with increasing the temperature. This indicates that temperature is inversely proportional to AC resistivity for both bulk and grain boundary components, a typical behavior of semiconductors. Fitting of undoped, Fe-doped and Mn-doped BNKLT88 ceramics yielded fitting parameters given in Supplementary Tables S7.1-S7.3, for reference.

The Nyquist plots of the undoped BNKLT88 ceramic were accurately fit with three R//CPE sub-circuits and an inductor in series (Fig. 7.3(a)) at the measured temperature range (450 - 600 °C). The first and second R//CPE sub-circuits are assigned to interior grain (bulk) and grain boundary responses, respectively, at high frequencies. The third sub-circuit is assigned to the low frequency response of the silver electrode interface with the ceramic. The inductor, L is assigned to the self-inductance of the measuring system. The R//CPE element with the larger resistance dominates the complex impedance response while the R//CPE element with the smaller capacitance dominates the electrical modulus response [14]. Moreover, the contribution of interior grain and grain boundary can be evaluated from the fitting of the impedance spectra. It can be seen from the data in Table S7.1 that the resistivity of the grain boundary (R_{gb}) is always larger than resistivity of bulk

(R_b). In other words, the grain boundary impedance is the dominant resistive component in the undoped BNKLT88 ceramic.
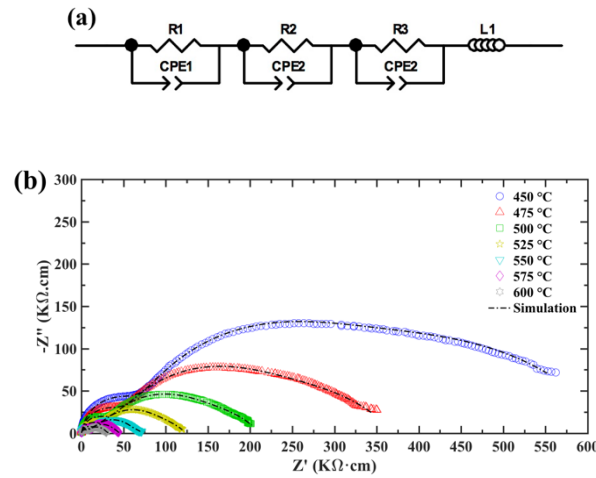
Figure 7. 3. An equivalent circuit used in the analysis of the impedance data of BNKLT88 (a) and the Nyquist plot for experimental and simulated data (b).

The Nyquist plots of 1.5Mn-doped BNKLT88 ceramic are modeled with two R//CPE sub-circuits in series with a CPE and an inductance (Fig. 7.4 (a)). The first two R//CPE correspond to interior grain and grain boundary terms while the individual CPE roughly corresponds to the electrode-interface response. It is apparent from Fig. 7.4(b) that the magnitude of R_b is always larger than R_{gb}, which indicates that the interior grain impedance is the dominant resistive component in the 1.5Mn-doped samples. As a result of Mn doping the resistivity of the bulk has been increased and becomes the dominant component in the impedance.
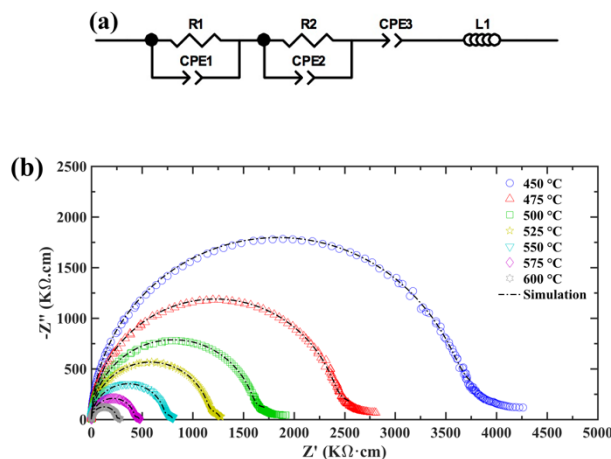
Figure 7. 4. An equivalent circuit used in the analysis of the impedance data of
BNKLT88-1.5Mn (a) and the Nyquist plot for experimental and simulated data (b).

The Fe-doped composition has lower impedance values compared to undoped,
which can be attributed to higher conductivity in this material. The equivalent circuit
includes two standard R//CPE, an inductance, and a Randles circuit with Warburg element
connected in series (Fig. 7.5(a)). The value of the resistance in all three regimes (R_b, R_{gb},
R_e) decreases as a function of temperature while the resistivity of interior grain is larger
than R_{gb}. This trend suggests that similar to the Mn-doped composition the dominant
resistance comes from the interior grains.
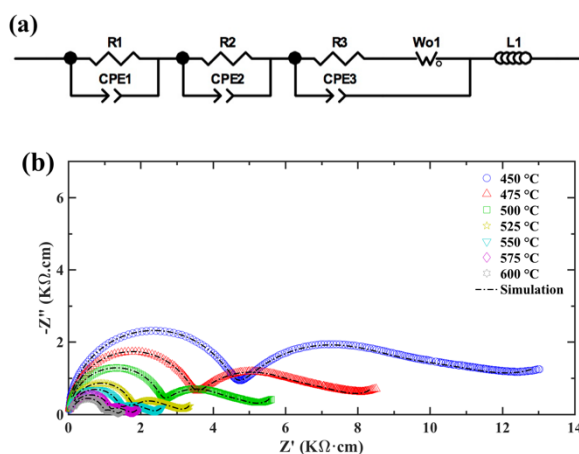
Figure 7. 5. An equivalent circuit used in the analysis of the impedance data of
BNKLT88-1.5Fe (a) and the Nyquist plot for experimental and simulated data (b).

Impedance spectroscopy is a useful tool to analyze the resistivity and conductivity when long-range conduction dominates and it gives information on the element with larger resistance. On the other hand, if the localized relaxation dominates then modulus spectroscopy function is more suitable, as it provides information about elements with lower capacitance [14]. As a result, it is necessary to analyze the data in both terms in order to obtain comprehensive information about the physical process taking place in the material.

The complex impedance data is converted to complex modulus data using the following relation,

$$M^* = M' + jM'' = j\omega C_0 Z^* \tag{7.3}$$

where M* is the complex modulus, M′ and M″ are the real and imaginary components of the modulus, ω is the AC angular frequency, C_0 is the vacuum capacitance, and Z* is the complex impedance.

The complex electrical modulus of BNKLT88, BNKLT88-1.5Mn, BNKLT88-1.5Fe are shown in Fig. 7.6. The magnitude of the modulus spectra increase proportionally with temperature, demonstrating the temperature dependence of capacitance in BNT-based compositions, which is typical behavior of ferroelectric materials at temperatures above the Curie temperature.

Modulus spectra of undoped BNKLT88 ceramic contain two irregular semicircles related to bulk and grain boundary. On the other hand, the modulus plot of Mn-doped and Fe-doped ceramics both contain a single semicircle attributed to the bulk with its smaller capacitance. Nevertheless, the capacitance of the bulk is on the order of 10^{-2} - 10^{-3} times smaller than the capacitance of the grain boundaries, which can result in one visible semicircle in the complex modulus plot.
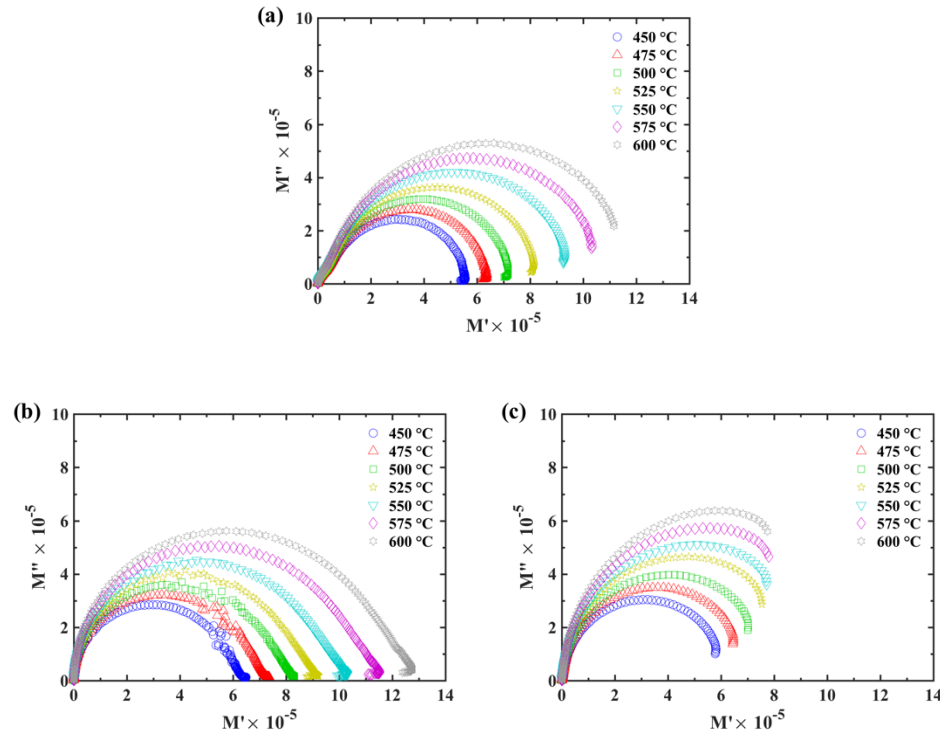
Figure 7. 6. The complex electrical modulus at varying temperatures of (a) BNKLT88 (b)BNKLT88-1.5Mn (c) BNKLT88-1.5Fe.

The variation of the real part of the impedance (Z′) as a function of frequency at different temperatures is shown in Fig. 7.7, with clear differences between the different dopants. Frequency dependence of the real impedance of the undoped and 1.5Fe doped ceramic show double sigmoidal behavior, while the 1.5 Mn-doped sample shows single sigmoidal behavior. In all three cases, the real impedance became saturated at higher frequencies, indicating the presence of a mixed nature of polarization behavior in the material [26]. Also, the value of the real impedance at low frequencies decreased with increasing temperature, indicating the presence of a negative temperature coefficient of resistance (NTCR) in the material in the low-frequency regime. On the other hand, the magnitude of the real impedance merges for all temperatures at high frequencies which can

be attributed to elevation of ac conductivity (σ_{ac}) and caused by the release of the space charge and lowering in the barrier properties of the material [27], [28]. In the perovskite structure it is possible that the contribution of defects like oxygen vacancies is more dominant in the high-frequency regime and gives rise to higher ac conductivity [14], [29].
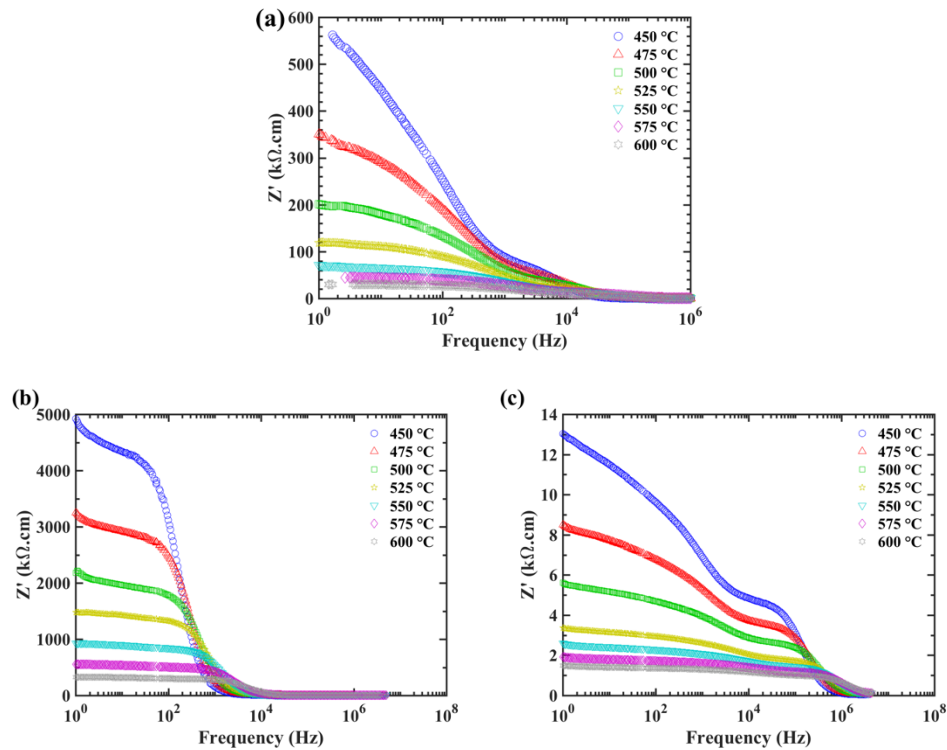
Figure 7. 7. Variation of the real part of the Impedance of (a)BNKLT88, (b)BNKLT88-1.5Mn and (c) BNKLT88-1.5Fe with frequency at different temperatures.

Fig. 7.8 presents the variation of the imaginary part of the impedance (Z'') as a function of frequency in the temperature range of 450-600 °C. The information on the type and strength of the dielectric relaxation phenomenon can be obtained from the appearance of a peak at a characteristic angular frequency, ω_{max} ($= 2\pi f_{max}$) [26]. Undoped and Fe-doped compositions show two peaks referring to two relaxation phenomena in these materials.
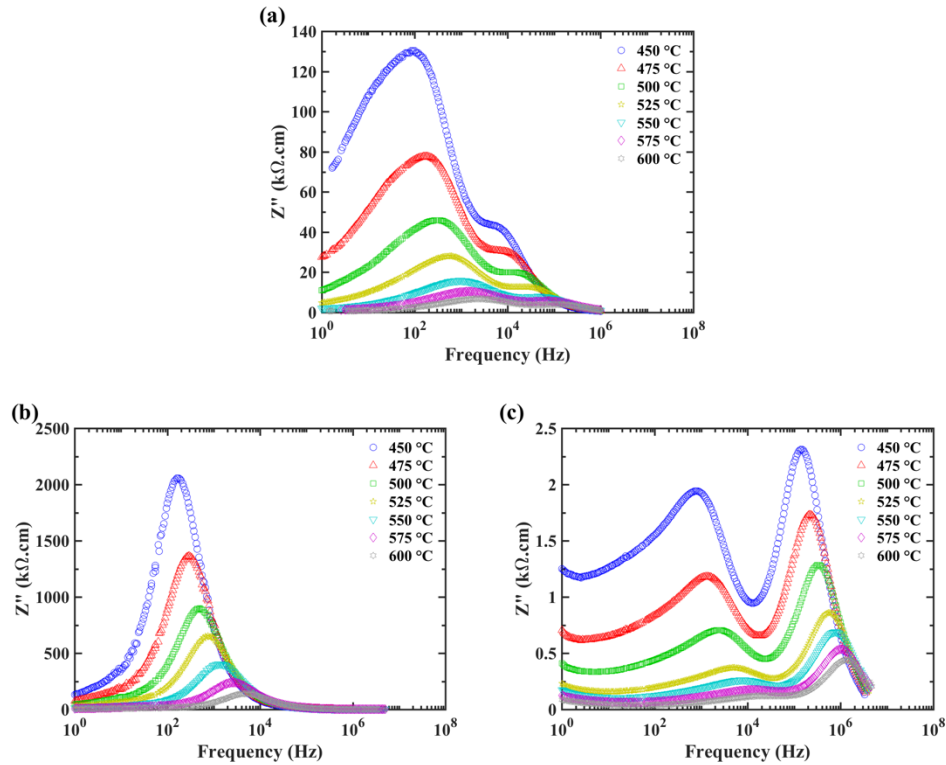
Figure 7. 8. Variation of the imaginary part of the Impedance with frequency at different temperatures for BNKLT88, (b)BNKLT88-1.5Mn, and (c) BNKLT88-1.5Fe.

In contrast, Mn-doped samples show one peak at all measured temperatures. The magnitude of the peaks in all three compositions decreases inversely with the temperature. Additionally, the peak position shifts toward higher frequencies, which suggests the existence of a temperature dependent electrical relaxation phenomenon in the material. The broadening of the peak width at higher temperatures indicates that there is a temperature dependent broadening of the relaxation time. The merging of the imaginary impedance curves in the high frequency regime could be the result of reduction of the space charge polarization at higher frequency. The observed relaxation process may be described with immobile species at low temperatures and defects at high temperatures [30], [31].
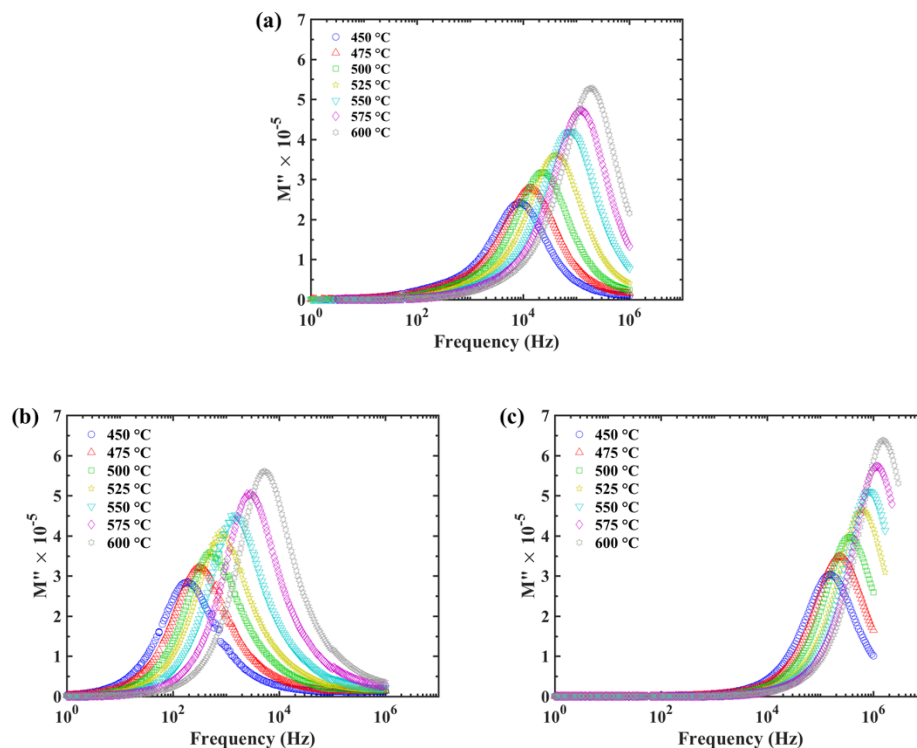
Figure 7. 9. Variation of the imaginary part of electrical modulus as a function of frequency for (a) BNKLT88 (b) BNKLT88-1.5Mn (c) BNKLT88-1.5Fe.

Fig. 7.9 shows the variation of the imaginary part of the electrical modulus (M″) as a function of frequency in the temperature range of 450-600 °C. The value of the imaginary modulus increases inversely with frequency, reaching a maximum value at a particular frequency and then decreasing at lower frequencies. Raising the temperature causes the maximum imaginary modulus to increase in magnitude and shift to higher frequencies. The appearance of this peak points to the transition from long range to short range mobility. Ions are capable of moving long distances via vacancy hopping given an applied field of low enough frequency. However, at higher frequencies, to the right of the peak maximum, the mobility of ions is limited to their potential well and consequently only experience localized motion. Furthermore, the long-range conduction region decreases with Mn-

doping and increases with Fe-doping.
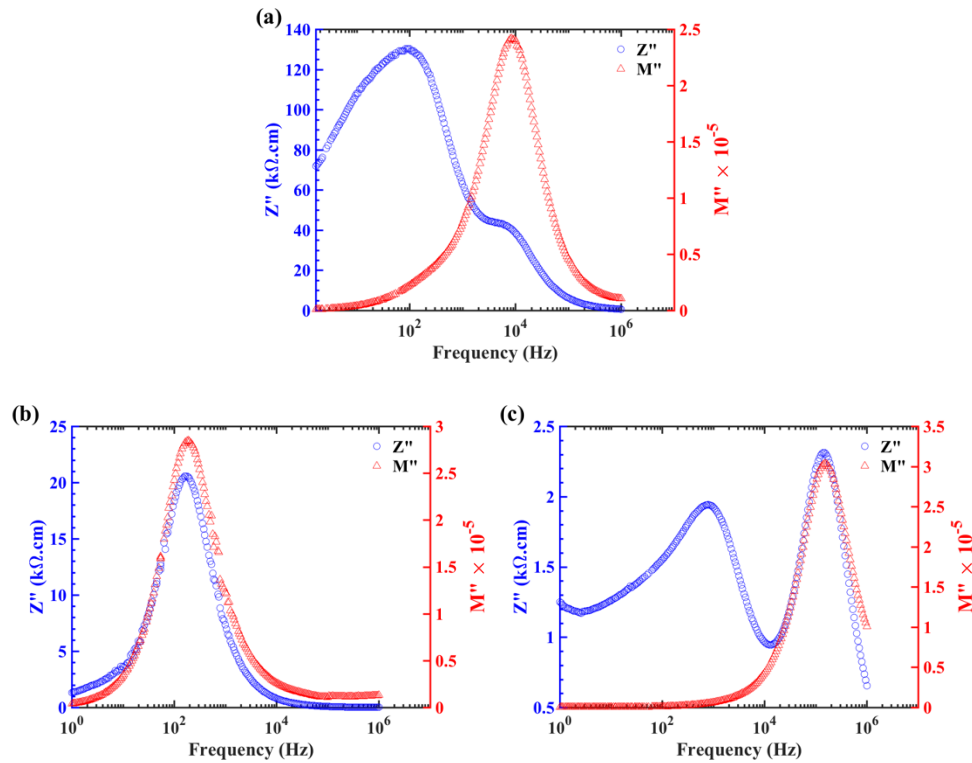
Figure 7. 10. The imaginary parts of the impedance Z″ and electrical modulus M″ as a function of frequency at 450 °C for (a) BNKLT88 (b) BNKLT88-1.5Mn (c) BNKLT88-1.5Fe.

A simultaneous plot of Z″ and M″ versus frequency (Fig. 7.10) provides useful information about the relaxation process. The coincidence of Z″ and M″ peaks at roughly the same frequency indicates long-range movement of charge carriers while the occurrence of Z″ and M″ peaks at different frequencies indicates short-range movement of charge carriers [30], [32]. Undoped and Fe-doped BNKLT88 samples show significant mismatch between Z″ and M″ peaks which indicates a localized process and departure from ideal Debye-like behavior. However, while the Mn-doped sample exhibits smaller mismatch between Z″ and M″ peaks, it still shows slight deviation from ideal Debye behavior. Non-Debye relaxation processes justify the existence of constant phase elements (CPE), which

have been used to model and interpret the electrical behavior of materials [30], [32].
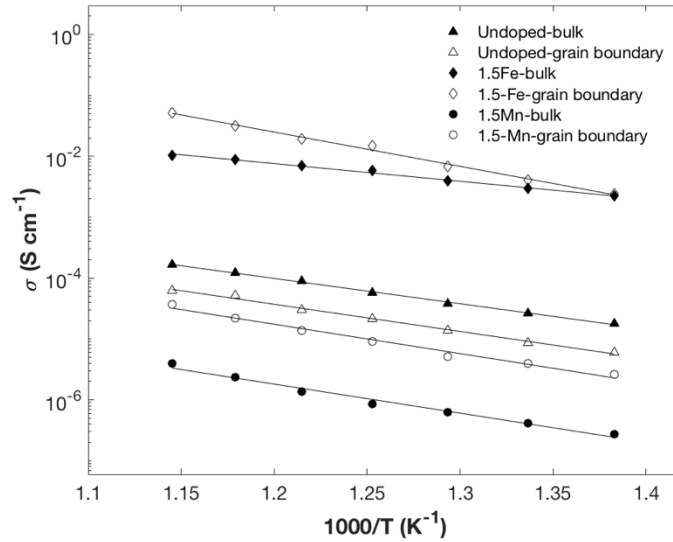
Figure 7. 11. Arrhenius plots of interior grain and grain boundary conductivity for BNKLT88, BNKLT88-1.5Mn, and BNKLT88-1.5Fe.

The temperature dependence of the bulk and grain boundary conductivity for BNKLT88, BNKLT88-1.5Mn and BNKLT88-1.5Fe is illustrated in Fig. 7.11 as an Arrhenius plot. The electrical conductivity of both bulk and grain boundary constituents follow the Arrhenius-type behavior, indicating a thermally activated process and again showing the negative temperature coefficient of resistance (NTCR) behavior in BNT-based compositions. Fe-doped samples have higher bulk and grain boundary conductivity compared to the undoped and Mn-doped samples. The conductivity of the Fe-doped ceramic was as high as 0.0103 S.cm^{-1} at 600 °C.

Considering the Arrhenius behavior of conductivity, the activation energies were calculated according to

$$\sigma = \sigma_0 \exp\left(-\frac{E_a}{kT}\right),$$ (7. 4)

where σ is the conductivity, σ_0 is a pre-exponential factor, E_a is the activation energy, k is Boltzmann's constant $(1.38\times10^{-23}$ J.K^{-1} or 8.617×10^{-5} eV.K$^{-1})$, and T is the absolute temperature (K).

The dominant conduction process depends on the nature of the charge carriers, such as electrons/holes, cations/anions, or oxygen vacancies, and can switch from one conduction mechanism to another by altering the temperature [33]. The ionic conductivity in perovskite oxides results from the migration of oxygen vacancies $(V_O^{\bullet\bullet})$ in the structure, which leads to high sample-electrode capacitance (1-10 µF), large sample-electrode resistance, and a spike in the low frequency region of the Nyquist plot [34]–[36].

Acceptor dopants not only generate oxygen vacancies $(V_O^{\bullet\bullet})$ but also can trap them and lead to complex defects,

$$2Mn_{Ti}^{''} + V_O^{\bullet\bullet} \leftrightarrow \left\{Mn_{Ti}^{''}V_O^{\bullet\bullet}\right\}^x \tag{7.5}$$

and

$$2Fe_{Ti}^{''} + V_O^{\bullet\bullet} \leftrightarrow \left\{Fe_{Ti}^{''}V_O^{\bullet\bullet}\right\}^x \tag{7.6}$$
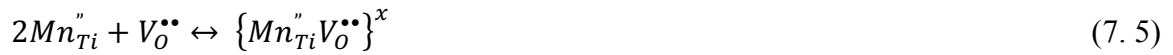
The complex defects have higher migration enthalpies (0.9-1.13eV) compared to free oxygen vacancies (0.62-0.60 eV) [37], [38]. As a result, the ionic conductivity depends not only on the total concentration of oxygen vacancies $([V_O^{\bullet\bullet}]_{tot})$ but also concentration of free vacancies $([V_O^{\bullet\bullet}]_f)$. In other words, the ionic conductivity is enhanced as a result of increasing $[V_O^{\bullet\bullet}]_f$, which is temperature dependent.

The activation energies, proportional to the slopes of the Arrhenius plots of conductivity, are given in Table 7.2. The lower bulk activation energy of the Fe-doped composition may result from higher $[V_O^{\bullet\bullet}]_f$, which results in higher ionic conductivity. The existence of ionic

conductivity in Fe-doped ceramic is confirmed by the spike in low frequency region of the Nyquist plot and the existence of a Warburg element in the electrical circuit (Fig. 7.4). On the other hand, the activation energy of the Mn-doped composition suggests the existence of complex defects rather than free oxygen vacancies, which results in lower ionic conductivity. In order to identify the contribution of ionic and electronic conductivity and provide adequate evaluation of all other contributors, further studies are required. The ionic contribution can be evaluated with oxygen tracer diffusion experiments.

Table 7. 2. Summary of activation energies for bulk and grain boundary of BNKLT88, BNKLT88-1.5Mn, and BNKLT88-1.5Fe. Activation energies are calculated from the slope of the Arrhenius plots of conductivity.

Composition	$E_{a\text{-bulk}}$ (eV)	$E_{a\text{-grain boundary}}$ (eV)
BNKLT88	0.98	0.92
BNKLT88-1.5Mn	0.95	0.97
BNKLT88-1.5Fe	0.58	1.12

7.4   Conclusion

Impedance spectroscopy and electromechanical studies were undertaken on $(BiNa_{0.88}K_{0.08}Li_{0.04})_{0.5}Ti_{0.995}A_{0.015}O_3$ (A = Mn, Fe) piezoceramic which were synthesized through conventional solid-state reaction technique. Mn and Fe-doped compositions both showed similar electromechanical hardening behavior with respect to higher mechanical quality factor, smaller dielectric loss and lower coupling coefficient compared to the undoped ceramic.

The negative temperature coefficient of resistance (NTCR) in all compositions was verified by inverse relationship of resistivity and temperature. For the case of Mn-doping,

the conductivity was found to decrease in comparison to undoped BNKLT88, which is suggested to result from high concentration of trapped oxygen vacancies in the structure and makes this composition a promising candidate for high power applications.

In contrast, the impedance of the Fe-doped composition was reduced and ionic conductivity was increased, which makes this composition a potential candidate for intermediate temperature SOFC applications. The conductivity of the Fe-doped sample reached 0.01 S.cm^{-1} at 600 °C in air. The activation energy suggests that higher conductivity in the Fe-doped sample is mainly due to the high concentration of free oxygen vacancies at the studied temperature range.

Acknowledgements

7.5 Supplementary Information

Table S7. 1. Impedance parameters of BNKLT88 at different temperatures.

T	R_b (Ω)	Y_{0b} (nF)	α_b	R_{gb} (Ω)	Y_{0gb} (nF)	α_{gb}	R_{el} (Ω)	Y_{0el} (μF)	α_{el}
450	5213	3.83	1	19,740	0.153	0.836	34,620	2.37	0.595
475	3561	3.50	1	14,550	0.243	0.774	16,840	4.67	0.548
500	2501	2.94	1	9,247	0.268	0.768	8,213	6.91	0.551
525	1657	2.56	1	6,047	0.313	0.757	3,986	12.9	0.522
550	1050	2.18	1	4,559	0.513	0.7	1,228	87.1	0.500
575	774.2	1.94	1	2,586	0.475	0.729	921	40.9	0.472
600	563.1	1.78	1	2,217	0.698	0.685	376	741	0.359

Table S7. 2. Impedance parameter of BNKLT88-1.5Mn at different temperatures.

T	R_b (Ω)	Y_{0b} (nF)	α_b	R_{gb} (Ω)	Y_{0gb} (μF)	α_{gb}
450	397,750	2.55	0.983	41,667	0.811	0.919
475	264,190	2.29	0.982	27,207	0.107	0.895
500	174,950	2.09	0.980	21,214	0.107	0.891
525	126,740	1.95	0.978	12,002	0.121	0.899
550	79,202	1.81	0.975	7,847	1.80	0.858
575	46,667	1.65	0.974	4,914	2.48	0.829
600	27,724	1.52	0.973	2,968	4.82	0.799

Table S7. 3. Impedance parameter of BNKLT88-1.5Fe at different temperatures.

T	R_b (Ω)	Y_{0b} (nF)	α_b	R_{gb} (Ω)	Y_{0gb} (μF)	α_{gb}	R_3 (Ω)	Y_{0el} (μF)	α_{el}
450	336.6	3.436	0.994	309	2.8744	0.801	242	886.67	0.650
475	253.8	3.026	0.993	183	3.1605	0.802	152	125.99	0.616
500	189.6	2.684	0.993	110	3.6044	0.798	90	190.23	0.589
525	128.8	2.345	0.992	50	3.7631	0.813	54	222.58	0.549
550	105.4	2.214	0.989	39	4.6664	0.789	27	183.59	0.607
575	84.8	2.06	0.987	24	4.3497	0.805	17	149.54	0.622
600	72.43	1.937	0.984	14	3.919	0.822	12	107.07	0.650

7.6   References

[1] J. Rödel, K. G. Webber, R. Dittmer, W. Jo, M. Kimura, and D. Damjanovic, "Transferring lead-free piezoelectric ceramics into application," *J. Eur. Ceram. Soc.*, vol. 35, no. 6, pp. 1659–1681, Jun. 2015.

[2] "PZT to Lead Free Piezo Ceramics: A Review: Ferroelectrics: Vol 474, No 1." [Online]. Available: https://www.tandfonline.com/doi/abs/10.1080/00150193.2015.997146?journalCode= gfer20. [Accessed: 09-Oct-2018].

[3] G. H. Haertling, "Ferroelectric Ceramics: History and Technology," *J. Am. Ceram. Soc.*, vol. 82, no. 4, pp. 797–818, Apr. 1999.

[4] T. Takenaka and H. Nagata, "Current status and prospects of lead-free piezoelectric ceramics," *J. Eur. Ceram. Soc.*, vol. 25, no. 12, pp. 2693–2700, 2005.

[5] J. Rödel, W. Jo, K. T. P. Seifert, E.-M. Anton, T. Granzow, and D. Damjanovic, "Perspective on the Development of Lead-free Piezoceramics," *J. Am. Ceram. Soc.*, vol. 92, no. 6, pp. 1153–1177, Jun. 2009.

[6] T. Takenaka, K. Maruyama, and K. Sakata, "(Bi1/2Na1/2)TiO3-BaTiO3 System for Lead-Free Piezoelectric Ceramics," *Jpn. J. Appl. Phys.*, vol. 30, no. 9S, p. 2236, Sep. 1991.

[7] D. Lin, D. Xiao, J. Zhu, and P. Yu, "Piezoelectric and ferroelectric properties of [Bi0.5(Na1−x−yKxLiy)0.5]TiO3 lead-free piezoelectric ceramics," *Appl. Phys. Lett.*, vol. 88, no. 6, p. 062901, Feb. 2006.

[8] K. Y. Yuji Hiruma, "Phase transition temperature and electrical properties of (Bi1/2Na1/2)TiO3–(Bi1/2A1/2)TiO3 (A=Li and K) lead-free ferroelectric ceramics," *J. Appl. Phys.*, no. 8, pp. 084121-084121–7, 2008.

[9] T. Takenaka, H. Nagata, and Y. Hiruma, "Phase Transition Temperatures and Piezoelectric Properties of (Bi1/2Na1/2)TiO3-and (Bi1/2K1/2)TiO3-Based Bismuth Perovskite Lead-Free Ferroelectric Ceramics," *IEEE Trans. Ultrason. Ferroelectr. Freq. Control*, vol. 56, no. 8, pp. 1595–1612, Aug. 2009.

[10]   Y. Gao, Y.-H. Chen, J. Ryu, K. Uchino, and D. Viehland, "Eu and Yb Substituent Effects on the Properties of Pb(Zr $_{0.52}$ Ti $_{0.48}$)O $_3$ –Pb(Mn $_{1/3}$ Sb $_{2/3}$)O $_3$ Ceramics: Development of a New High-Power Piezoelectric with Enhanced Vibrational Velocity," *Jpn. J. Appl. Phys.*, vol. 40, no. Part 1, No. 2A, pp. 687–693, Feb. 2001.

[11]   K. Uchino *et al.*, "Loss mechanisms and high power piezoelectrics," in *Frontiers of Ferroelectricity*, Springer US, 2006, pp. 217–228.

[12]   M. Li *et al.*, "A family of oxide ion conductors based on the ferroelectric perovskite Na$_{0.5}$Bi$_{0.5}$TiO$_3$," *Nat. Mater.*, vol. 13, no. 1, pp. 31–35, Jan. 2014.

[13]   M. Li *et al.*, "Dramatic Influence of A-Site Nonstoichiometry on the Electrical Conductivity and Conduction Mechanisms in the Perovskite Oxide Na0.5Bi0.5TiO3," *Chem. Mater.*, vol. 27, no. 2, pp. 629–634, Jan. 2015.

[14]   D. C. Sinclair and A. R. West, "Impedance and modulus spectroscopy of semiconducting BaTiO3 showing positive temperature coefficient of resistance," *J. Appl. Phys.*, vol. 66, no. 8, pp. 3850–3856, Oct. 1989.

[15]   B. K. Barick, K. K. Mishra, A. K. Arora, R. N. P. Choudhary, and D. K. Pradhan, "Impedance and Raman spectroscopic studies of (Na 0.5 Bi 0.5)TiO 3," *J. Phys. Appl. Phys.*, vol. 44, no. 35, p. 355402, 2011.

[16] Q. Xu *et al.*, "Dielectric behavior and impedance spectroscopy in lead-free BNT–BT–NBN perovskite ceramics for energy storage," *Ceram. Int.*, vol. 42, no. 8, pp. 9728–9736, Jun. 2016.

[17] E. Barsoukov and J. R. Macdonald, *Impedance Spectroscopy: Theory, Experiment, and Applications*. Hoboken, UNITED STATES: John Wiley & Sons, Incorporated, 2005.

[18] S. Pandey, D. Kumar, O. Parkash, and L. Pandey, "Equivalent circuit models using CPE for impedance spectroscopy of electronic ceramics," *Integr. Ferroelectr.*, vol. 183, no. 1, pp. 141–162, Sep. 2017.

[19] E. Taghaddos, M. Hejazi, and A. Safari, "Electromechanical Properties of Acceptor-Doped Lead-Free Piezoelectric Ceramics," *J. Am. Ceram. Soc.*, vol. 97, no. 6, pp. 1756–1762, Jun. 2014.

[20] C. Lenser *et al.*, "Spectroscopic study of the electric field induced valence change of Fe-defect centers in SrTiO3," *Phys. Chem. Chem. Phys.*, vol. 13, no. 46, pp. 20779–20786, Nov. 2011.

[21] P. D. Desai, H. M. James, and C. Y. Ho, "Electrical Resistivity of Aluminum and Manganese," *J. Phys. Chem. Ref. Data*, vol. 13, no. 4, pp. 1131–1172, Oct. 1984.

[22] V. G. Bhide and R. H. Dani, "Electrical conductivity in oxides of manganese and related compounds," *Physica*, vol. 27, no. 9, pp. 821–826, Sep. 1961.

[23] F. Hong, B. Yue, N. Hirao, Z. Liu, and B. Chen, "Significant improvement in Mn2O3 transition metal oxide electrical conductivity via high pressure," *Sci. Rep.*, vol. 7, no. 1, Dec. 2017.

[24] P. H. Klose, "Electrical Properties of Manganese Dioxide and Manganese Sesquioxide," *J. Electrochem. Soc.*, vol. 117, no. 7, pp. 854–858, Jul. 1970.

[25] N. M. Botrous El Badramany, E. F. Mina, H. D. Merchant, S. Arafa, and R. P. Poplawsky, "Electrical Resistivity of Magnetite and Nickel Ferrous Ferrite Above 300°K," *J. Am. Ceram. Soc.*, vol. 62, no. 3–4, pp. 113–116, Mar. 1979.

[26] R. N. P. Choudhary, D. K. Pradhan, C. M. Tirado, G. E. Bonilla, and R. S. Katiyar, "Impedance characteristics of Pb(Fe2/3W1/3)O3–BiFeO3 composites," *Phys. Status Solidi B*, vol. 244, no. 6, pp. 2254–2266, Jun. 2007.

[27] J. Suchanicz, "The low-frequency dielectric relaxation Na0.5Bi0.5TiO3 ceramics," *Mater. Sci. Eng. B*, vol. 55, no. 1, pp. 114–118, Aug. 1998.

[28] S. Sen and R. N. P. Choudhary, "Impedance studies of Sr modified BaZr0.05Ti0.95O3 ceramics," *Mater. Chem. Phys.*, vol. 87, no. 2, pp. 256–263, Oct. 2004.

[29] M. A. Rafiq, M. N. Rafiq, and K. Venkata Saravanan, "Dielectric and impedance spectroscopic studies of lead-free barium-calcium-zirconium-titanium oxide ceramics," *Ceram. Int.*, vol. 41, no. 9, Part A, pp. 11436–11444, Nov. 2015.

[30] S. Sen, R. N. P. Choudhary, and P. Pramanik, "Structural and electrical properties of Ca2+-modified PZT electroceramics," *Phys. B Condens. Matter*, vol. 387, no. 1, pp. 56–62, Jan. 2007.

[31] R. Rai, I. Coondoo, R. Rani, I. Bdikin, S. Sharma, and A. L. Kholkin, "Impedance spectroscopy and piezoresponse force microscopy analysis of lead-free $(1 - x)$ K0.5Na0.5NbO3 − xLiNbO3 ceramics," *Curr. Appl. Phys.*, vol. 13, no. 2, pp. 430–440, Mar. 2013.

[32]   D. K. Pradhan, R. N. P. Choudhary, C. Rinaldi, and R. S. Katiyar, "Effect of Mn substitution on electrical and magnetic properties of Bi0.9La0.1FeO3," *J. Appl. Phys.*, vol. 106, no. 2, p. 024102, Jul. 2009.

[33]   P. Dhak, D. Dhak, M. Das, K. Pramanik, and P. Pramanik, "Impedance spectroscopy study of LaMnO3 modified BaTiO3 ceramics," *Mater. Sci. Eng. B*, vol. 164, no. 3, pp. 165–171, Oct. 2009.

[34]   M. V. Raymond and D. M. Smyth, "Defects and charge transport in perovskite ferroelectrics," *J. Phys. Chem. Solids*, vol. 57, no. 10, pp. 1507–1511, Oct. 1996.

[35]   W. M. Zhu and Z.-G. Ye, "Effects of chemical modification on the electrical properties of 0.67BiFeO3−0.33PbTiO3 ferroelectric ceramics," *Ceram. Int.*, vol. 30, no. 7, pp. 1435–1442, Jan. 2004.

[36]   A. Perejón, E. Gil-González, P. E. Sánchez-Jiménez, A. R. West, and L. A. Pérez-Maqueda, "Electrical properties of bismuth ferrites: Bi2Fe4O9 and Bi25FeO39," *J. Eur. Ceram. Soc.*, Sep. 2018.

[37]   F. Cordero, "Hopping and clustering of oxygen vacancies in SrTiO3 by anelastic relaxation," *Phys. Rev. B*, vol. 76, no. 17, Nov. 2007.

[38]   A. Hackmann and O. Kanert, "NMR investigation of defect properties in single crystal SrTiO3," *Radiat. Eff. Defects Solids*, vol. 119–121, no. 2, pp. 651–656, Nov. 1991.

Electromechanical Properties of Flash Sintered BNT-Based Piezoelectric Ceramic

Elaheh Taghaddos[1], Harry Charalambous[1], Thomas Tsakalakos[1], Ahmed Safari[1]

Rutgers University, Department of Materials Science and Engineering, Piscataway, NJ 08854, United States

8   Electromechanical Properties of Flash Sintered BNT-Based Piezoelectric Ceramic

Abstract

Lead-free, $(BiNa_{0.88}K_{0.08}Li_{0.04})_{0.5}Ti_{0.995}Mn_{0.015}O_3$ piezoceramic has been successfully densified by a novel electrical current applied technique known as flash sintering (FS) at 880 °C. The effect of alternating and direct current, current density limit and holding time on the densification, crystal structure, electromechanical and electrical properties have been investigated. The optimum flash condition was obtained with a 1 KHz alternating current, 100 V·cm^{-1} initial electric field and preset maximum current limit of 1.5 A·cm^{-2}. The flash sintered specimen is characterized with finer grain size (10-15 µm), slightly higher electromechanical properties and higher symmetry butterfly shape strain hysteresis loop compared to conventional sintering. Under both sintering conditions uniform distribution of elements and pure rhombohedral structure were observed. Flash sintering also results in lower resistivity and more significant grain boundaries contributions in the conduction mechanism.

8.1   Introduction

Since the first publication by Cologna, et al. [1], the flash sintering has been used to densify a wide variety of binary and ternary oxide ceramics such as oxygen-ion conductors [2]–[8], semiconductors [9]–[14] , dielectrics [15], [16], and piezoelectrics [17]–[20]. The extension of the flash sintering technique to complex oxides is an important area of future study as these materials have a wide variety of uses in industry such as transducers, capacitors, actuators, among other applications. Lead-based piezoceramics such as lead zirconate titanate (PZT) have outstanding ferroelectric and piezoelectric properties and, as a result, the market of piezoelectric devices and commercial products is dominated by these compositions. However, lead is a toxic element and can directly, through inhalation, or indirectly, via contamination of food, rain, etc., be absorbed into the body. The hazardous nature of lead has driven numerous studies to develop a replacement for lead-based piezoceramics. In this regard, BNT-based piezoelectric materials are the most promising candidates for many applications such as high-frequency ultrasound [21], ultrasonic cleaners [22], and high intensity focus transducers [23].

Numerous studies have been performed to optimize the properties of BNT-based piezoceramics and to lower the sintering temperature through binary/ternary solid solution or by adding sintering aids. In this regard, $Bi_{0.5}K_{0.5}TiO_3$ (BKT) and $Bi_{0.5}Li_{0.5}TiO_3$ (BLT) are two of the most widely used additives to BNT in order to enhance the electromechanical properties [24]. Furthermore, the value of the K^+, Li^+ ratio is a key determining factor in obtaining optimal electrical properties of BNT-BKT-BLT compositions. The highest mechanical quality factor, Q_m=430, was achieved with 0.88BNT-0.08BKT-0.04BLT (BNKLT88) [25]. Substitution of the B-site in the perovskite structure (ABO_3) with an

acceptor dopant such as $Mn^{2+, 3+}$, $Fe^{2+, 3+}$, and Cr^{3+} has resulted in a hard piezoelectric composition with high mechanical quality factor and coercive field which makes this a promising candidate for high power applications [24], [26]–[28].

Recently, considerable efforts have been given to utilize newly developed sintering procedures in order to achieve dense ceramics at low temperatures such as spark plasma sintering [29], [30], cold sintering [31], [32], two step sintering [33]–[37] and flash sintering [19], [20], [38], [39]. A series of in-situ flash sintering studies have demonstrated that the flash effect requires comparable sintering temperatures to conventional, pressureless heating [12], [14], [40], but requires shorter dwell time, often resulting in finer microstructure. The lowering of the sintering duration is a critical parameter allowing the production of pristine, high purity BNT-based compositions by avoiding bismuth and alkali loss during sintering [41]–[43].

Furthermore, complex impedance spectroscopy has been developed as a useful tool to study changes in chemical composition and microstructure via their effect on the AC phase shift of a materials electrical response. The non-Debye behavior of this system has been modeled with a series of R//CPE combined elements [44], [45] in order to simulate and deconvolute the contributions of bulk, grain boundary, and electrode-interface components. Impedance spectroscopy has been successfully used in analysis of the properties of flash sintered 3YSZ [46], GDC [38], LSGM [47], BiFeO3 [48], ZnO [13], and Li-NMC [49].

This work aims to establish flash sintering of $(BiNa_{0.88}K_{0.08}Li_{0.04})_{0.5}Ti_{0.995}Mn_{0.015}O_3$ (Mn-doped BNKLT88) piezoceramic. The effect of alternating current (AC) and direction current (DC) electric field, maximum current limit (J_{max}) and dwell time under

current control have been investigated. A detailed comparison of the microstructural, electrical and electromechanical properties of flash sintered (FS) and conventionally sintered (CS) BNKLT88 is provided.

8.2 Experimental Procedure

The conventional mixed oxide route was used to prepare $(BiNa_{0.88}K_{0.08}Li_{0.04})_{0.5}Ti_{0.995}$ $Mn_{0.015}$ O_3 ceramics (BNKLT88-1.5Mn). Raw materials, including high-purity oxides and carbonate powders, were dried overnight at 200 °C. The powders were then weighted to stoichiometry, mixed in a Nalgene bottle with appropriate molar ratios and milled in acetone with zirconia balls for 12 h. The mixed powder was dried at 90 °C and calcined at 800 °C for 3 h. After a repeated milling process, 8 wt% polyvinyl alcohol solution was added to the calcined powder. Green compacts were pressed in a 6.35 mm die under 150 MPa uniaxial load.

For the CS experiments, specimens were heated at a rate of 5 °C·min⁻¹ to 1020 °C and held for 2 h. For the FS experiments, the specimens were loaded onto a stage with platinum electrodes attached to both ends. The top platinum electrode is placed between the specimen and an alumina rod, with a wire connection to outside the furnace. The alumina rod is pressed with a small weight (0.6 kg) in order to provide sufficient and uniform contact between the electrode and sample surface. The uniform contact is essential to avoid channeling. The bottom electrode sits on a flat alumina stage with platinum wire connection to outside the furnace. Direct current (DC) and alternating current (AC, 1 KHz) electric fields with 100 V·cm⁻¹ magnitude was applied in separate experiments while the furnace was heated at a rate of 10 °C·min⁻¹ to a temperature of 880 °C. A linear rise in the

current (Stage I) eventually led to runaway Joule heating and a nonlinear rise in the current (Stage II). Upon reaching the preset maximum current limit, J_{max} = 1, 1.5 and 2 A·cm^{-2}, the power supply was switched to current control and the furnace was held at 880 °C while the current limit was maintained for 5, 10, 20 and 30 min at a steady state (Stage III). The specimens were then annealed by maintaining the same furnace temperature for 1 h. This had the effect of enhancing the dielectric properties of the ceramic as flash sintering of titanium-based oxides was found to result in oxygen ion transport and slight reduction [14], [50], [51].

In order to measure the electromechanical properties, the sintered ceramics were lapped down to 650 μm and then electroded using fired-on silver paint, followed by heat treatment at 550 °C for 20 min. The electroded ceramics were poled in a silicon oil bath at 95 °C under an applied electric field of 45 kV·cm^{-1} for 15 min.

The dielectric constant ($\varepsilon_r = \varepsilon^T{}_{33}/\varepsilon_0$) and dielectric loss (tan δ) were measured at 1 kHz using an impedance analyzer (HP4194a; Hewlett Packard, Tokyo, Japan). A Berlincourt piezometer was used to measure the longitudinal piezoelectric charge coefficient (d_{33}) at 100 Hz. Piezoelectric planar coupling coefficients (k_p) were calculated based on the resonance and antiresonance frequencies of the impedance traces using the IEEE standards [52], [53],

$$\frac{k_p^2}{1-k_p^2} = \frac{\Delta f}{f_r} \cdot \frac{(\sigma^p)^2 + \eta^2 - 1}{1 + \sigma^p} \qquad (8.1)$$

$$\Delta f = f_a - f_r \qquad (8.2)$$

where f_r and f_a are the resonance and anti-resonance frequency, σ^p is Poisson's ratio and η is the frequency constant of a disk resonator.

A Sawyer-Tower circuit (Radiant Technology Inc., Albuquerque, NM) at a pulse width of

1000 ms (1 Hz frequency) with triangular wave signal was used to measure room temperature polarization-field (P-E) hysteresis loops.

Temperature dependence of the dielectric constant was characterized with an Agilent 4284A Precision LCR Meter. The MTI-2000 photonic sensor (MTI Instruments, Albany, NY) in conjunction with a 10 kV DC power supply (Trek model 610C from Radiant Technologies Inc., Albuquerque, NM) and a special displacement fixture (Radiant Technologies Inc., Albuquerque, NM) was used to determine the axial displacement of the ceramics. Measurements were carried out under DC bipolar modes with an electric field of 8 kV·cm^{-1}.

Impedance spectroscopy was performed using a Gamry 600+ potentiostat at frequency range of 1 Hz – 1 MHz, 1000 mV applied voltage, and 450 – 600 °C temperature range with 25 °C step size. The impedance data (Z^*) was converted to resistivity (ρ^*) by accounting for the geometrical parameters of the specimen,

$$\rho^* = \rho' - j\rho'' = {Z^*}/{L} \tag{8.3}$$

where $L = {H}/{A}$ represents the geometrical factor, A is the electrode area, and H is the thickness of the sample (electrode separation).

Data were fit to equivalent circuits using an open-source Zfit MATLAB program and the resulting fitting parameters were used to calculate Arrhenius temperature dependence of the conductivity.

A series of parallel-circuit resistor and constant phase element (R//CPE) combined elements were used to simulate the bulk, grain boundary, and electrode-interface complex impedance according to the procedure outlined by Pandey, et al. [54]. Using this model, the combined complex impedance in the parallel circuit was determined such that

$$\frac{1}{Z_{R//CPE}} = \frac{1}{Z_R} + \frac{1}{Z_{CPE}} = \frac{1}{R} + Y_0(j\omega)^{\alpha} \tag{8.4}$$

and

$$Z_{R//CPE} = \frac{R}{1+(j\omega)^{\alpha}\tau} \tag{8.5}$$

The fitting parameters were defined as resistance parameter, R, and CPE parameters, Y_0 and α such that $0<\alpha<1$. In the case of ideal capacitor behavior the relaxation time constant, $\tau = (RY_0)^{1/\alpha}$, reduces to an RC circuit, $\tau = RC$, where the capacitance, $C=Y_0$ and $\alpha=1$. The conductivity (σ) were determined independently from each R//CPE circuit using the following relations:

$$\sigma = Re\left(\frac{1+Y_0R(j\omega)^{\alpha}}{LR}\right) \tag{8.6}$$

After electrical characterization, specimens were mechanically polished and thermally etched at 850 °C for 30 min. Micrographs were collected using a Phenom Pro SEM with 10 kV electron gun. ImageJ software was used to estimate grain and pore sizes while specimen density was determined from Archimedes method. Furthermore, chemical analysis was performed using energy-dispersive spectroscopy (EDS) with a Zeiss Sigma Field Emission SEM.

Powder diffraction was performed using a Philips X'Pert Pro on a zero background silicon base. The data were collected over a 2θ range of 20-70° with 0.01° step size and 80 s acquisition time per step. Intensity profiles were normalized with respect to the highest intensity peak.

8.3   Results and Discussion

The electrical data and linear strain during flash with AC electric field are summarized in Fig. 8.1. The temperature ramp induces the beginning of linear shrinkage, which enhances the conductivity of the specimen at high temperatures and allows the

beginning of current flow, which rises exponentially. The furnace is held constant at the onset of current control to avoid specimen melting during extended hold times.
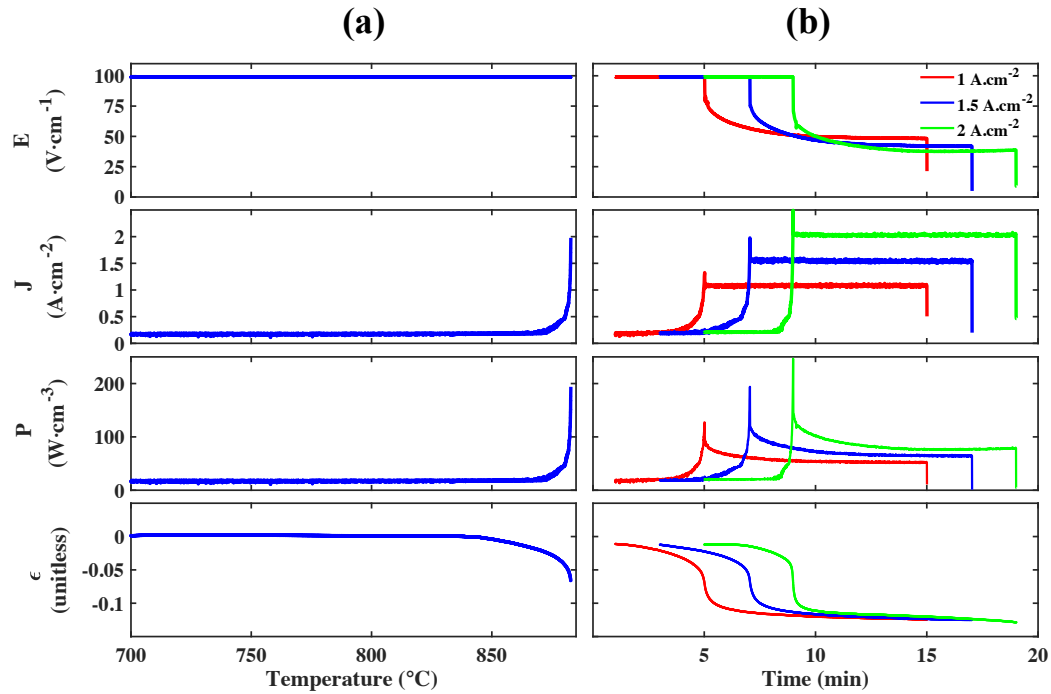
Figure 8. 1 . Analysis of electric field (E), Current density (J), power density(P), and linear strain (ϵ). (a)The non-isothermal ramp of the temperature at a rate of 10 °C·min^{-1} corresponds to stage I and II of flash after which (b) the furnace temperature is held constant at the power spike and stage III is allowed to proceed for 10 min. Three select current density limits are indicated in subplot (b).

X-ray diffraction patterns (Fig. 8.2) indicate pure perovskite structure with rhombohedral symmetry under conventional and AC flash sintering conditions. However, samples prepared using DC electric field show initiation of secondary phases. Three potential reasons are considered for this effect. First, there may be current localization under DC electric field as observed in BiFeO$_3$ [55], which causes locally much higher temperatures and sample decomposition. On the other hand, no channeling effects were

directly observed in the sample, which otherwise cause the formation of visible pinholes in the sample. BNKLT88-1.5Mn contains three different alkali metals in the composition and the application of DC field may cause alkali ion diffusion in one direction for extended time, eventually compromising the single phase perovskite structure. Finally, flash sintering under DC field has been demonstrated to cause a Peltier effect [56], resulting in temperature variation across the thickness of the sample [50], with some regions of fine microstructure and some other regions with heating above the thermodynamic stability of this composition. Thus, DC electric field is not suited to sintering of BNT-based compositions.
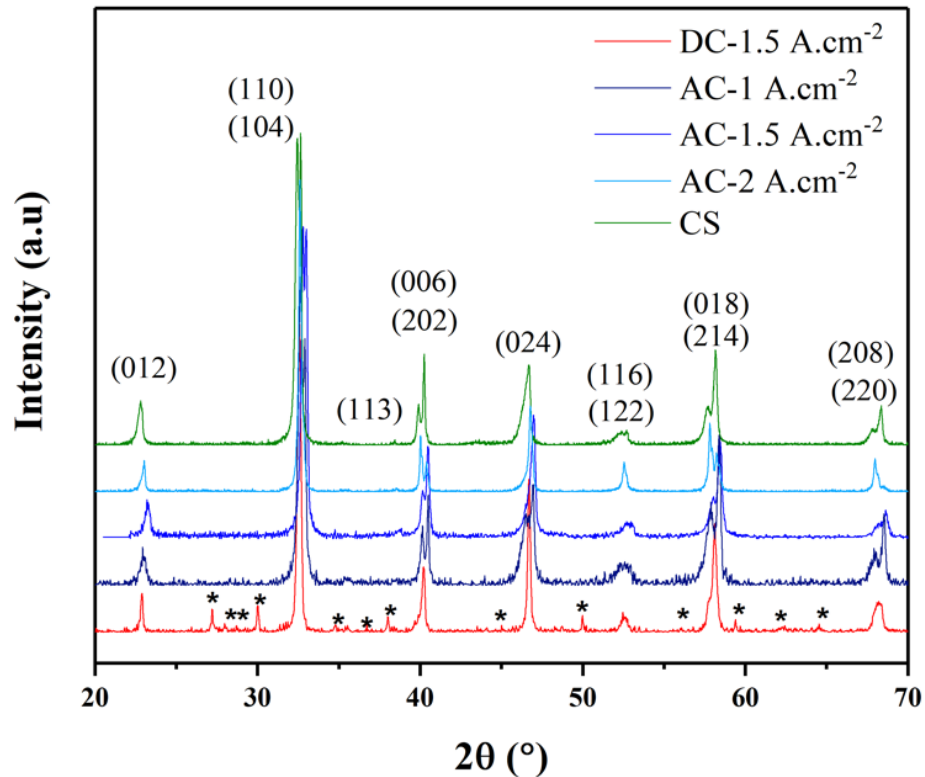
Figure 8. 2. X-ray diffraction patterns for conventional sintering (CS), AC and DC flash sintering (FS).

The density and electromechanical properties of the BNKLT88-1.5Mn flash sintered ceramics at varying maximum current densities and hold times are summarized in Table 8.1 and Table 8.2, respectively. The electromechanical properties are sensitive to the current limit. The highest density, piezoelectric charge coefficient and mechanical quality factor were obtained with J_{max}=1.5 A·cm^{-1} so this limit was chosen as the condition to investigate the effect of stage III hold time.

The effect of hold time, summarized in Table 8.2, indicates moderate improvement, up to 20 min hold, including slightly higher dielectric constant (ε_r =356), piezoelectric charge coefficient (d_{33}=89), planar coupling coefficient (k_p = 0.224), and lower dielectric loss ($\tan\delta$ = 0.84 %). The reason for these improved properties may be related to the rapid heating, with heating rates up to 100 °C·s^{-1} [3] whereas the conventional heating process was much slower, at 5 °C·min^{-1}, resulting in much shorter duration at elevated temperatures. This may result in lower bismuth segregation or alkali metal evaporation, both of which are temporal, thermally activated processes. The remainder of the elemental and electrical characterization (Fig.8.3) comparing FS to CS use the specimen flashed under J_{max}=1.5 A·cm^{-1} and 10 min holding time.

However, the mechanical quality factor of the CS ceramic is higher (Q_m = 980) compared to the best FS ceramic (Q_m = 650). High mechanical quality factor in the CS ceramic is attributed to the creation of oxygen vacancies and dipole defects due to Mn doping. The extrinsic ferroelectric contributions are minimized as a result of a domain wall pinning effect of oxygen vacancies, point defects and dipole defects [22], [26], [27], [57]. Higher temperature and longer dwell time increases the population of defects. Consequently, the CS samples may have higher concentration of complex defects and

defect dipoles compared to samples prepared using the flash technique. Migration of defects to domain boundaries and grain boundaries pins the domain wall, limits domain switching during poling, and decreases the extrinsic contribution, which leads to lower piezoelectric charge coefficient and higher mechanical quality factor. However, in the case of flash sintering the migration of defects to their stable configuration is prevented as a result of rapid quenching after removal of the electric field. Consequently, the disordered defects are frozen and, thus, domain wall mobility can be increased which may result in lower mechanical quality factor as well as moderately higher dielectric and piezoelectric properties [58]. The alternating current used for FS may also de-pin the domain wall and consequently decrease the mechanical quality factor.

Table 8. 1. Electromechanical properties of BNKLT88-1.5Mn flash sintered at different J_{max} with 10 min hold and 1 h annealing at 880 °C.

J_{max} (A·cm^{-2})	Density (g·cm^{-3})	d_{33} (pC·N^{-1})	$\varepsilon^T_{33}/\varepsilon_0$	tanδ (%)	k_p	Planar Q_m
1	5.58	89	392	0.88	0.217	470
1.5	5.72	92	334	1.44	0.212	530
2	5.6	70	343	1.35	0.216	500

Table 8. 2. Electromechanical properties of BNKLT88-1.5Mn flash sintered with different hold times at J_{max} = 1.5 A·cm^{-2} and 1 h post anneal time at 880°C. Conventional sintering results included for reference.

Sintering Technique	t_{hold} (min)	Density (g·cm^{-3})	d_{33} (pC·N^{-1})	$\varepsilon^T_{33}/\varepsilon_0$	tanδ (%)	k_p	Planar Q_m
FS	5	5.7 ± 0.03	92	384	1.24	0.215	410
	10	5.72 ± 0.02	92	334	1.44	0.212	530
	20	5.74 ± 0.01	89	356	0.84	0.224	650
	30	5.75 ± 0.02	85	369	0.75	0.210	365
CS	1020/2h	5.68 ± 0.02	85	300	0.97	0.212	980

The micrographs shown in Fig.8.3 indicate reduced grain size for the FS sample (10-15 μm) compared to the CS sample (30-40 μm). A potential explanation for the dielectric and piezoelectric enhancement in FS ceramic may be the result of finer grain size [59]. The average pore size of the flash sintered ceramic (1.4 μm) was 50% smaller compared to the conventionally sintered ceramic (2.6 μm). Total porosity volume is similar in both cases as flash sintering is still a pressureless sintering technique, which makes full density a difficult proposition, and higher temperature and longer dwell time would simply result in pore consolidation through Oswald ripening [60].
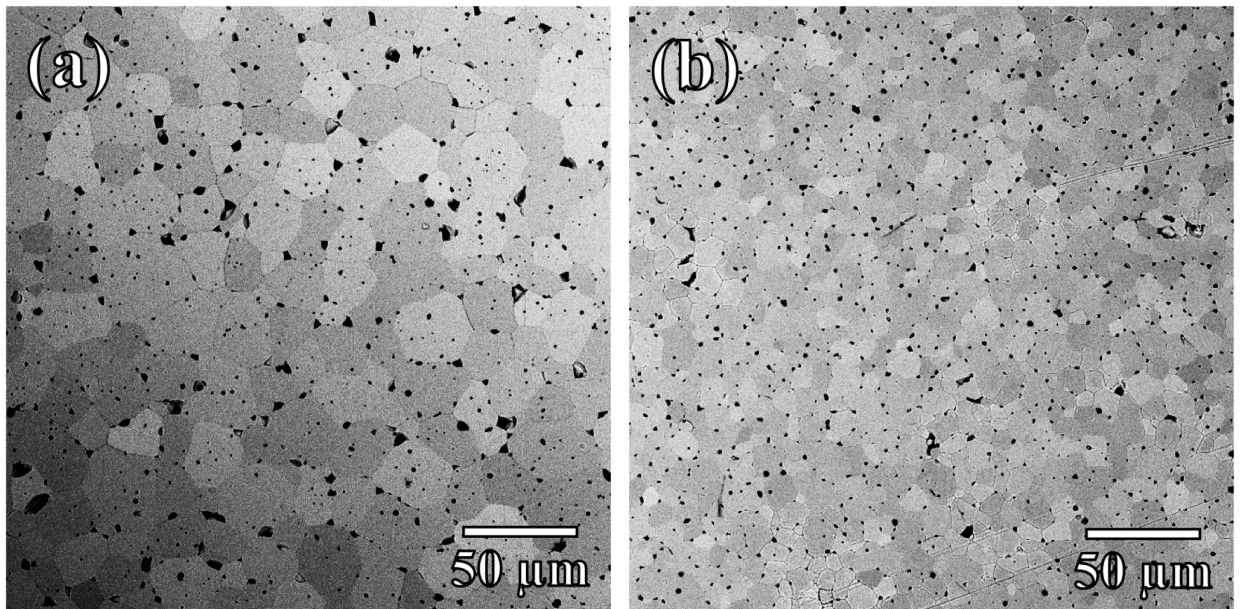
Figure 8. 3. Comparative micrographs of BNKLT88-1.5Mn sintered under (a) conventional and (b) flash conditions.

Elemental mapping of FS and CS BNKLT88-1.5Mn ceramic is shown in Fig. 8.4 (a-b). The EDS mapping confirms uniform distribution of elements within grains and indicates no discernable inhomogeneity in the chemical composition or core-ring structures as observed in KNN [19].
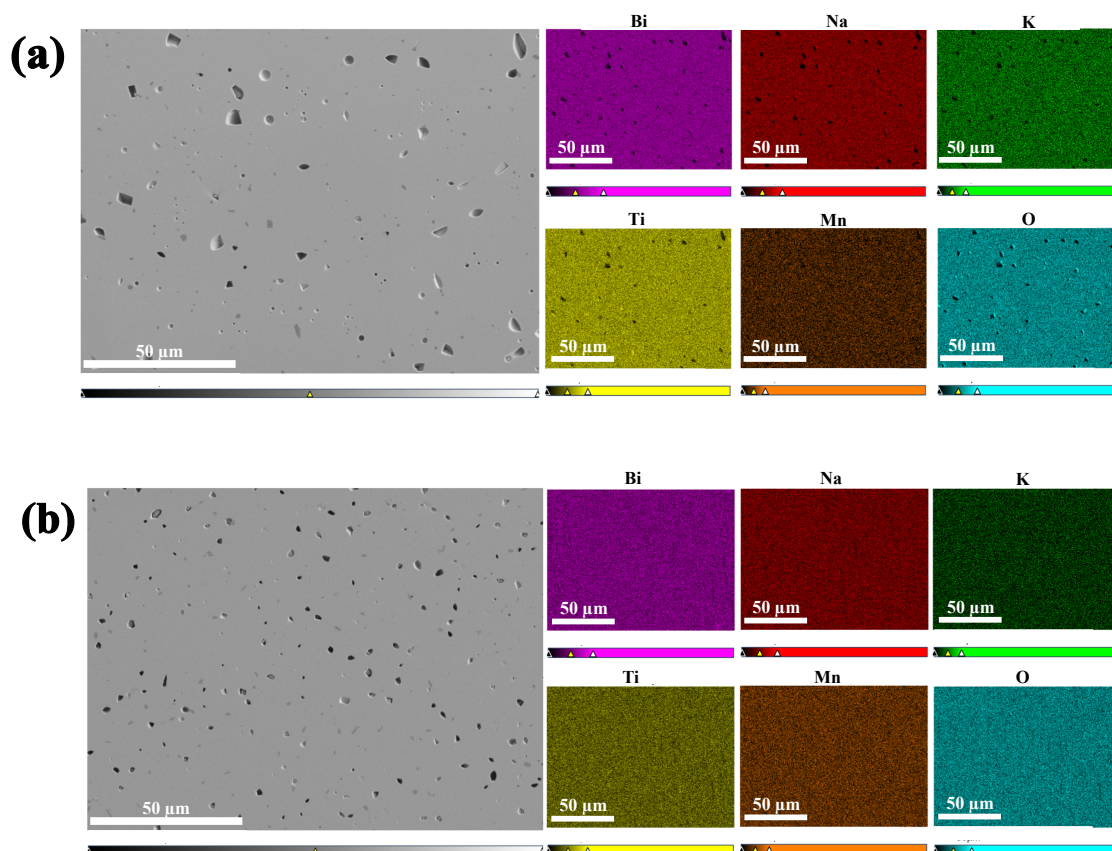
Figure 8. 4. Elemental mapping of (a) conventional (b) flash sintered ceramic

The temperature dependence of the dielectric constant and loss tangent (tanδ) is shown in Fig. 8.5 (a-b) for poled FS and CS samples at 1 and 10 KHz. The depolarization temperature (T_d), which is defined by the first observed peak in the heating cycle of tanδ, is 202 °C and 205 °C for the FS and CS ceramic, respectively. The rhombohedral to tetragonal phase transition (T_{R-T}) of the FS ceramic is shifted to slightly lower temperature (210 °C) compared to the CS ceramic (220°C). The dielectric maximum temperature (T_m) is 265 °C for both sintering conditions.
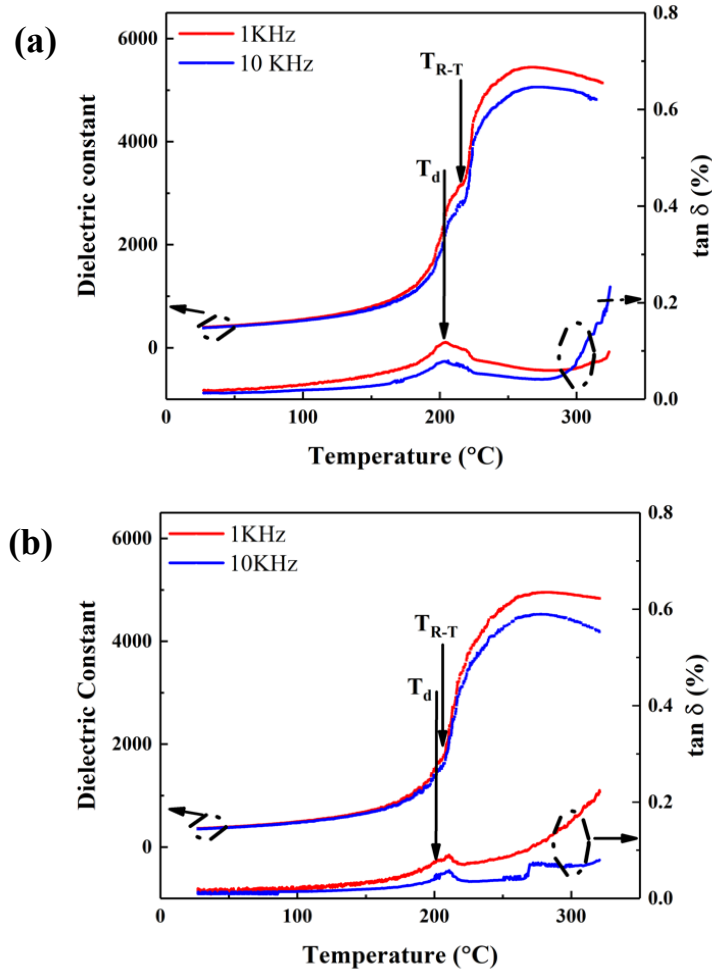
Figure 8. 5. (a) Temperature dependence of the dielectric constant and loss tangent, tanδ (%), of BNKLT88-1.5Mn conventionally sintered in a previous work [23]. (b) As a comparison the same data is measured for the flash sintered ceramic.

The P-E and S-E hysteresis loops of CS and FS BNKLT88-1.5Mn are illustrated in Fig. 8.6 (a) and (b), respectively. Flash sintered ceramics show 7% higher remnant polarization (P_r =37 $\mu C \cdot cm^{-2}$) and saturation polarization (P_s = 41$\mu C \cdot cm^{-2}$) compared to conventionally sintered ceramics. However, the same coercive field ($E_c \cong 54\ kV \cdot cm^{-1}$) was obtained for both sintering conditions. Increasing remnant polarization in flash sintered samples, as explain previously, can be attributed to higher mobility of the domain wall and less complex defects in the structure [58]. FS ceramics exhibit a classic "butterfly"-shaped strain with higher symmetry compared to CS samples, which have a more asymmetric loop. The presence of significant defects in CS ceramic is verified by the asymmetric S-E loop [59].
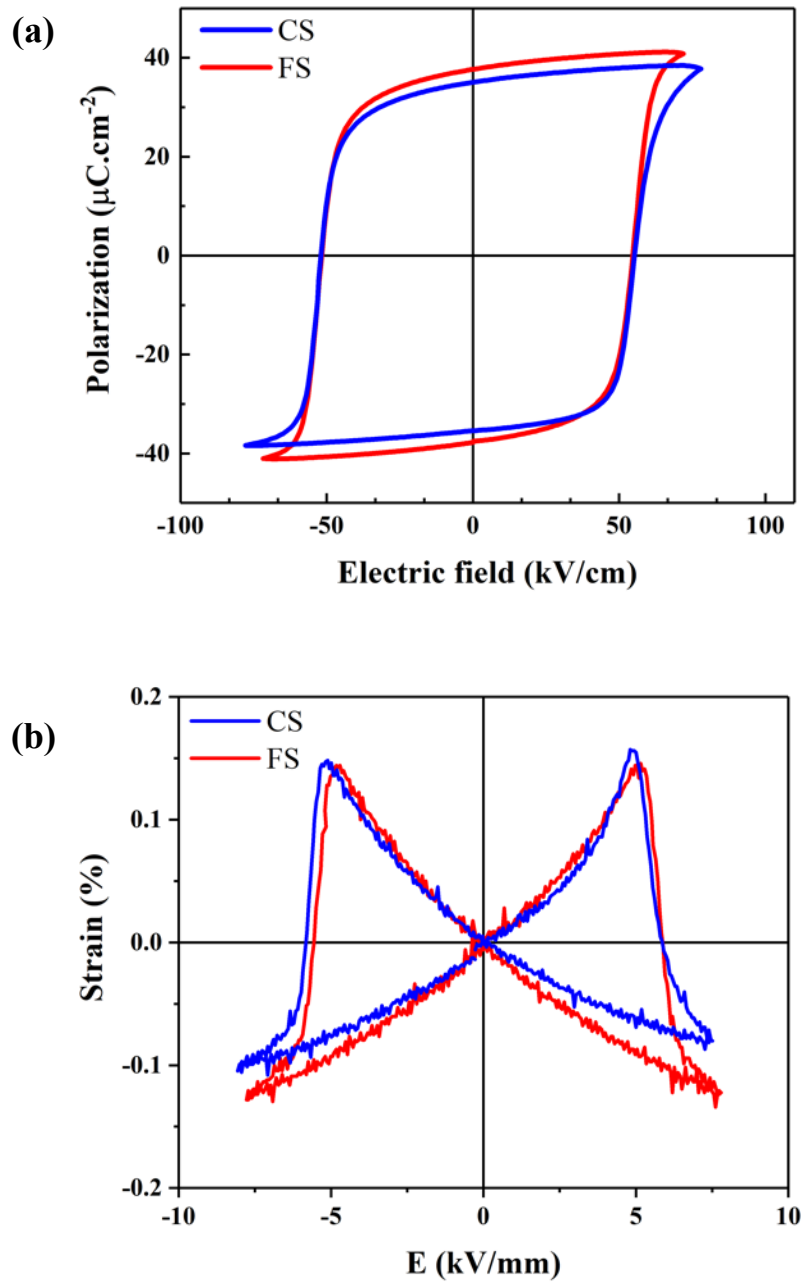
Figure 8. 6 (a) P-E hysteresis loops, and (b) strain versus electric field, S-E, curves for conventional sintered (CS) and flash sintered (FS) BNKLT88-1.5Mn.

The complex impedance plot of the FS sample is shown in fig 8.7a and compared with impedance spectrum of CS ceramic in fig 8.7b. Based on the shape of the plots, 3 R\\CPE elements in series with inductance is required to simulate FS sample spectrum while the CS is required 2 R\\CPE elements in series with a CPE and an inductance. The FS sample contains a high frequency (bulk) semicircular arc with CPE exponent ranging from 0.88-0.92 and medium frequency (grain boundary) semicircular arc with CPE exponent ranging from 0.73-0.77. The grain boundaries are found to have high dispersion, which may be related to rapid grain boundary movement during the flash and rapid quenching when the electric field is turned off. Additionally, the resistivity of the bulk component was slightly higher than grain boundary component. The conventionally sintered sample has a large, near perfect circular arc at higher frequency corresponding to the bulk, resulting in constant phase element close to the ideal capacitor, 0.97-0.98. A small arc at low frequency corresponds to grain boundaries with CPE exponent ranging from 0.80-0.92.
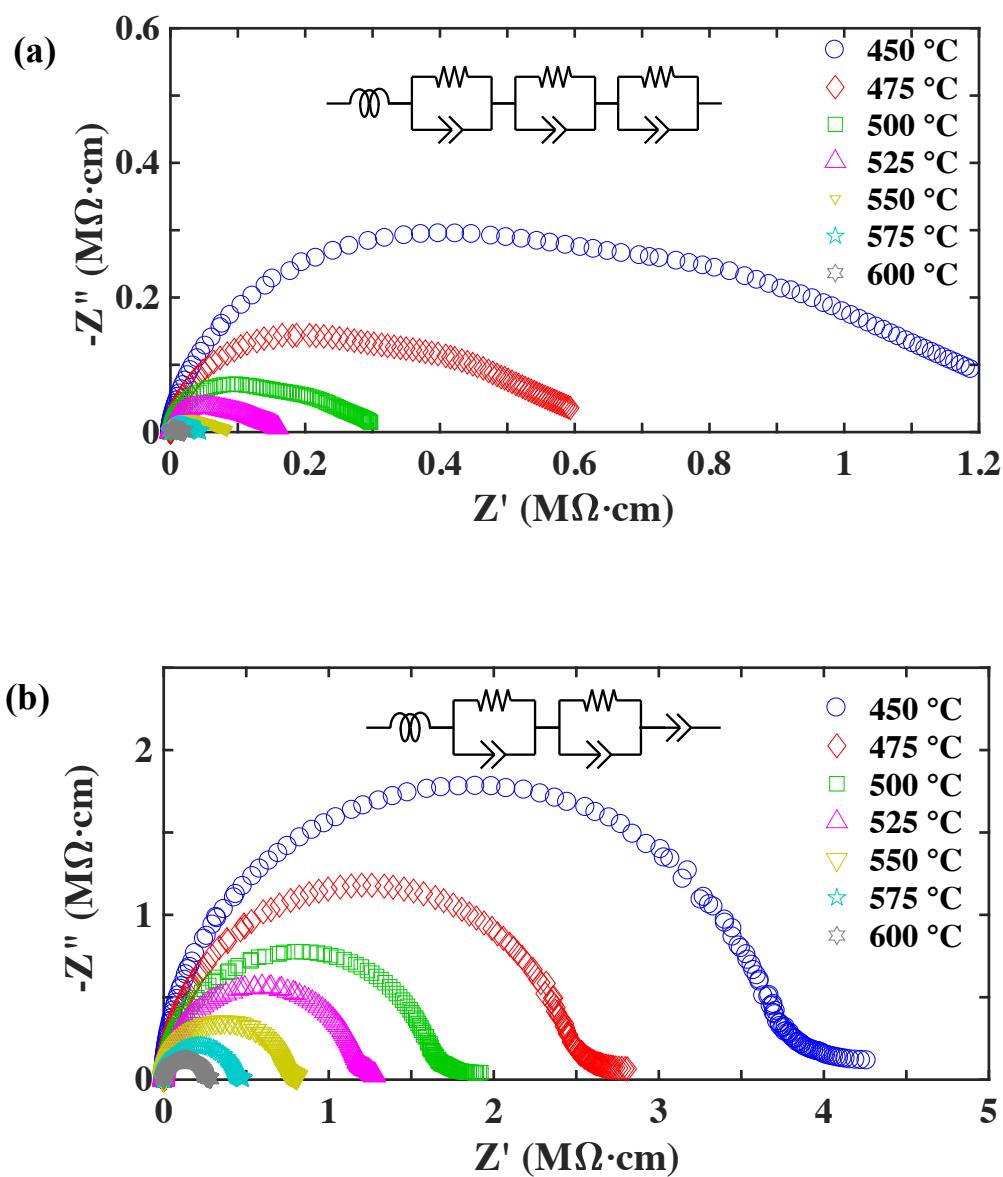
Figure 8. 7. Comparison of complex impedance for (a) FS and (b) CS along with equivalent circuits used to model the electrical behavior.

The log-log plots of conductivity versus inverse temperature is shown in Fig. 8.8. The bulk and grain boundary conductivity of the flash sintered samples are initially similar in magnitude, but diverge at higher temperatures. In the case of conventional sintering, the conductivity of the grain boundary component is larger than the bulk over the entire studied temperature range, which can be attributed to higher concentration of defects at the grain boundaries. The most likely causes of lower bulk conductivity of CS ceramic is the creation of complex defects due to the sintering method along with Mn-doping.

As shown in Table 8.3, the activation energy for electrical conductivity at the grain boundaries, determined from the slope of the AC conductivity plot is 15% and 6% greater than for the bulk in the FS and CS ceramics, respectively. In addition, the activation energy is 40% higher for the flash sintered ceramic compared to the conventionally sintered ceramic.
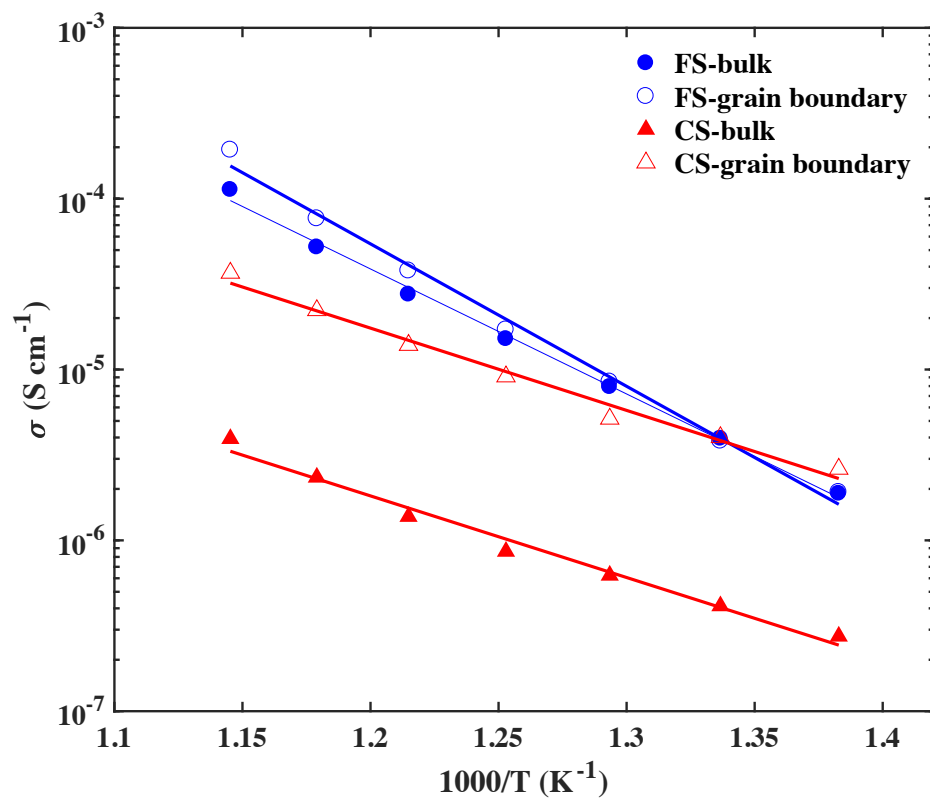
Figure 8. 8. Arrhenius plots of bulk and grain boundary conductivity for flash sintered (FS) and conventionally sintered (CS) BNKLT88-1.5Mn ceramic.

Table 8. 3. Bulk and grain boundary activation energies derived from temperature dependence of the ac conductivity

Sintering conditions	$E_{a,bulk}$ (eV)	$E_{a,gb}$ (eV)
Conventional sintering	0.95	1.01
Flash sintering	1.45	1.65

8.4 Summary

$(BiNa_{0.88}K_{0.08}Li_{0.04})_{0.5}Ti_{0.995}$ $Mn_{0.015}$ O_3 ferroelectric ceramics have been successfully consolidated via flash sintering at 880 °C and properties have been compared by the conventional sintered sample at 1020 °C. An AC field is required to obtain pure perovskite phase with uniform distribution of elements. The flash parameters of a 1 KHz AC electric field with 100 V·cm^{-1} initial electric field and preset maximum current limit of 1.5 A·cm^{-2} were optimum sintering parameters. The average grain size of the FS ceramic was 10-15 μm which is three times finer than conventionally sintered (30-40 μm). As compared to CS ceramic, the FS samples show slightly higher piezoelectric charge coefficient, dielectric permittivity, coupling coefficient, and smaller dielectric. Improved properties may be attributed to rapid heating and lower time at elevated temperature, avoiding alkali or bismuth loss, or to finer microstructure. The alternating current and fast cooling may be considered as major factors in lowering of the mechanical quality factor in these samples. The dielectric maximum temperature of the FS ceramic was the same as CS (T_m =265 °C), while T_{R-T} shifts to 10 °C lower temperature (220°C to 210 °C). The electrical study shows that the conductivity of bulk and grain boundaries is larger in FS ceramic than in CS sample while the activation energy is increased.

Acknowledgements

8.5   References

[1] M. Cologna, B. Rashkova, and R. Raj, "Flash Sintering of Nanograin Zirconia in <5 s at 850°C," *Journal of the American Ceramic Society*, vol. 93, no. 11, pp. 3556–3559, Nov. 2010.

[2] Jha S. K., Terauds K., Lebrun J.-M., and Raj R., "Beyond flash sintering in 3 mol % yttria stabilized zirconia," *J. Ceram. Soc. Japan*, vol. 124, no. 4, pp. 283–288, Apr. 2016.

[3] W. Ji, B. Parker, S. Falco, J. Y. Zhang, Z. Y. Fu, and R. I. Todd, "Ultra-fast firing: Effect of heating rate on sintering of 3YSZ, with and without an electric field," *Journal of the European Ceramic Society*, vol. 37, no. 6, pp. 2547–2551, Jun. 2017.

[4] M. Cologna, A. L. G. Prette, and R. Raj, "Flash-Sintering of Cubic Yttria-Stabilized Zirconia at 750°C for Possible Use in SOFC Manufacturing," *Journal of the American Ceramic Society*, vol. 94, no. 2, pp. 316–319, Feb. 2011.

[5] R. Muccillo and E. N. S. Muccillo, "Shrinkage control of yttria-stabilized zirconia during ac electric field-assisted sintering," *Journal of the European Ceramic Society*, vol. 34, no. 15, pp. 3871–3877, Dec. 2014.

[6] X. Hao, Y. Liu, Z. Wang, J. Qiao, and K. Sun, "A novel sintering method to obtain fully dense gadolinia doped ceria by applying a direct current," *Journal of Power Sources*, vol. 210, pp. 86–91, Jul. 2012.

[7] L. Spiridigliozzi, *Doped-Ceria Electrolytes: Synthesis, Sintering and Characterization*. Springer International Publishing, 2018.

[8] H. Charalambous, S. K. Jha, J. Okasinski, and T. Tsakalakos, "Spectral analysis and temperature measurement during flash sintering under AC electric field," *Materialia*, vol. 6, p. 100273, Jun. 2019.

[9] S. K. Jha and R. Raj, "The Effect of Electric Field on Sintering and Electrical Conductivity of Titania," *Journal of the American Ceramic Society*, vol. 97, no. 2, pp. 527–534, Feb. 2014.

[10] S. K. Jha, J. M. Lebrun, K. C. Seymour, W. M. Kriven, and R. Raj, "Electric field induced texture in titania during experiments related to flash sintering," *Journal of the European Ceramic Society*, vol. 36, no. 1, pp. 257–261, Jan. 2016.

[11] Y. Zhang, J.-I. Jung, and J. Luo, "Thermal runaway, flash sintering and asymmetrical microstructural development of ZnO and ZnO–Bi2O3 under direct currents," *Acta Materialia*, vol. 94, pp. 87–100, Aug. 2015.

[12] H. Charalambous, S. K. Jha, R. T. Lay, A. Cabales, J. Okasinski, and T. Tsakalakos, "Investigation of temperature approximation methods during flash sintering of ZnO," *Ceramics International*, vol. 44, no. 6, pp. 6162–6169, Apr. 2018.

[13] H. Charalambous, S. K. Jha, K. H. Christian, R. T. Lay, and T. Tsakalakos, "Flash Sintering using Controlled Current Ramp," *Journal of the European Ceramic Society*, vol. 38, no. 10, pp. 3689–3693, Aug. 2018.

[14] H. Charalambous *et al.*, "In situ measurement of temperature and reduction of rutile titania using energy dispersive x-ray diffraction," *Journal of the European Ceramic Society*, vol. 38, no. 16, pp. 5503–5511, Dec. 2018.

[15] M. Cologna, J. S. C. Francis, and R. Raj, "Field assisted and flash sintering of alumina and its relationship to conductivity and MgO-doping," *Journal of the European Ceramic Society*, vol. 31, no. 15, pp. 2827–2837, Dec. 2011.

[16] H. Yoshida, Y. Sakka, T. Yamamoto, J.-M. Lebrun, and R. Raj, "Densification behaviour and microstructural development in undoped yttria prepared by flash-sintering," *Journal of the European Ceramic Society*, vol. 34, no. 4, pp. 991–1000, Apr. 2014.

[17] J.-C. M'Peko, J. S. C. Francis, and R. Raj, "Field-assisted sintering of undoped BaTiO3: Microstructure evolution and dielectric permittivity," *Journal of the European Ceramic Society*, vol. 34, no. 15, pp. 3655–3660, Dec. 2014.

[18] L. A. Perez-Maqueda *et al.*, "Insight into the BiFeO3 flash sintering process by in-situ energy dispersive X-ray diffraction (ED-XRD)," *Ceramics International*, Aug. 2018.

[19] Corapcioglu G., Gulgun M. A., Kisslinger K., Sturm S., Jha S. K., and Raj R., "Microstructure and microchemistry of flash sintered K0.5Na0.5NbO3," *J. Ceram. Soc. Japan*, vol. 124, no. 4, pp. 321–328, Apr. 2016.

[20] X. Su *et al.*, "Flash sintering of lead zirconate titanate (PZT) ceramics: Influence of electrical field and current limit on densification and grain growth," *Journal of the European Ceramic Society*, vol. 38, no. 10, pp. 3489–3497, Aug. 2018.

[21] M. M. Hejazi, B. Jadidian, and A. Safari, "Fabrication and evaluation of a single-element Bi0.5Na0.5TiO3-based ultrasonic transducer," *IEEE Transactions on Ultrasonics, Ferroelectrics, and Frequency Control*, vol. 59, no. 8, pp. 1840–1847, Aug. 2012.

[22] T. Tou, Y. Hamaguti, Y. Maida, H. Yamamori, K. Takahashi, and Y. Terashima, "Properties of (Bi $_{0.5}$ Na $_{0.5}$)TiO $_3$ –BaTiO $_3$ –(Bi $_{0.5}$ Na $_{0.5}$)(Mn $_{1/3}$ Nb $_{2/3}$)O $_3$ Lead-Free Piezoelectric Ceramics and Its Application to Ultrasonic Cleaner," *Japanese Journal of Applied Physics*, vol. 48, no. 7, p. 07GM03, Jul. 2009.

[23] E. Taghaddos, T. Ma, H. Zhong, Q. Zhou, M. X. Wan, and A. Safari, "Fabrication and Characterization of Single-Aperture 3.5-MHz BNT-Based Ultrasonic Transducer for Therapeutic Application," *IEEE Transactions on Ultrasonics, Ferroelectrics, and Frequency Control*, vol. 65, no. 4, pp. 582–588, Apr. 2018.

[24] Y. Hiruma, T. Watanabe, H. Nagata, and T. Takenaka, "Piezoelectric Properties of (Bi1/2Na1/2)TiO3-Based Solid Solution for Lead-Free High-Power Applications," *Jpn. J. Appl. Phys.*, vol. 47, no. 9S, p. 7659, Sep. 2008.

[25] Y. Hiruma, H. Nagata, and T. Takenaka, "Phase-transition temperatures and piezoelectric properties of (Bi1/2Na1/2)TiO3- (Bi1/2Li1/2)TiO3-(Bi1/2K1/2)TiO3 lead-free ferroelectric ceramics," *IEEE Transactions on Ultrasonics, Ferroelectrics, and Frequency Control*, vol. 54, no. 12, pp. 2493–2499, Dec. 2007.

[26] E. Taghaddos, M. Hejazi, and A. Safari, "Electromechanical Properties of Acceptor-Doped Lead-Free Piezoelectric Ceramics," *J. Am. Ceram. Soc.*, vol. 97, no. 6, pp. 1756–1762, Jun. 2014.

[27] M. Hejazi, E. Taghaddos, E. Gurdal, K. Uchino, and A. Safari, "High Power Performance of Manganese-Doped BNT-Based Pb-Free Piezoelectric Ceramics," *J. Am. Ceram. Soc.*, vol. 97, no. 10, pp. 3192–3196, Oct. 2014.

[28] N. M. Hagh, B. Jadidian, and A. Safari, "Property-processing relationship in lead-free (K, Na, Li) NbO3-solid solution system," *J Electroceram*, vol. 18, no. 3–4, pp. 339–346, Jun. 2007.

[29]   T. Hungría, J. Galy, and A. Castro, "Spark Plasma Sintering as a Useful Technique to the Nanostructuration of Piezo-Ferroelectric Materials," *Advanced Engineering Materials*, vol. 11, no. 8, pp. 615–631, Aug. 2009.

[30]   Y. J. Wu, N. Uekawa, K. Kakegawa, and Y. Sasaki, "Compositional fluctuation and dielectric properties of Pb(Zr0.3Ti0.7)O3 ceramics prepared by spark plasma sintering," *Materials Letters*, vol. 57, no. 3, pp. 771–775, Dec. 2002.

[31]   H. Guo, A. Baker, J. Guo, and C. A. Randall, "Cold Sintering Process: A Novel Technique for Low-Temperature Ceramic Processing of Ferroelectrics," *Journal of the American Ceramic Society*, vol. 99, no. 11, pp. 3489–3507, Nov. 2016.

[32]   H. Guo, A. Baker, J. Guo, and C. A. Randall, "Protocol for Ultralow-Temperature Ceramic Sintering: An Integration of Nanotechnology and the Cold Sintering Process," *ACS Nano*, vol. 10, no. 11, pp. 10606–10614, Nov. 2016.

[33]   I.-W. Chen and X.-H. Wang, "Sintering dense nanocrystalline ceramics without final-stage grain growth," *Nature*, vol. 404, no. 6774, pp. 168–171, Mar. 2000.

[34]   S. Wada *et al.*, "Preparation of barium titanate–potassium niobate ceramics using interface engineering and their piezoelectric properties," *Journal of the Ceramic Society of Japan*, vol. 118, no. 1380, pp. 691–695, 2010.

[35]   X.-H. Wang, I.-W. Chen, X.-Y. Deng, Y.-D. Wang, and L.-T. Li, "New progress in development of ferroelectric and piezoelectric nanoceramics," *Journal of Advanced Ceramics*, vol. 4, no. 1, pp. 1–21, Mar. 2015.

[36]   T. Karaki, K. Yan, T. Miyamoto, and M. Adachi, "Lead-Free Piezoelectric Ceramics with Large Dielectric and Piezoelectric Constants Manufactured from BaTiO 3 Nano-Powder," *Japanese Journal of Applied Physics*, vol. 46, no. No. 4, pp. L97–L98, Jan. 2007.

[37]   N. J. Lóh, L. Simão, C. A. Faller, A. De Noni, and O. R. K. Montedo, "A review of two-step sintering for ceramics," *Ceramics International*, vol. 42, no. 11, pp. 12556–12572, Aug. 2016.

[38]   T. Jiang *et al.*, "Understanding the Flash Sintering of Rare-Earth-Doped Ceria for Solid Oxide Fuel Cell," *Journal of the American Ceramic Society*, vol. 98, no. 6, pp. 1717–1723, Jun. 2015.

[39]   M. Yu, S. Grasso, R. Mckinnon, T. Saunders, and M. J. Reece, "Review of flash sintering: materials, mechanisms and modelling," *Advances in Applied Ceramics*, vol. 116, no. 1, pp. 24–60, Jan. 2017.

[40]   S. K. Jha *et al.*, "In-situ observation of oxygen mobility and abnormal lattice expansion in ceria during flash sintering," *Ceramics International*, vol. 44, no. 13, pp. 15362–15369, Sep. 2018.

[41]   B. Malič, A. Benčan, T. Rojac, and M. Kosec, "Lead-free Piezoelectrics Based on Alkaline Niobates: Synthesis, Sintering and Microstructure," *Acta Chimica Slovenica*, vol. 55, no. 4, pp. 719–726, Dec. 2008.

[42]   T. Takenaka, H. Nagata, and Y. Hiruma, "Current Developments and Prospective of Lead-Free Piezoelectric Ceramics," *Jpn. J. Appl. Phys.*, vol. 47, no. 5S, p. 3787, May 2008.

[43]   K. Wang and J.-F. Li, "(K, Na)NbO3-based lead-free piezoceramics: Phase transition, sintering and property enhancement," *J Adv Ceram*, vol. 1, no. 1, pp. 24–37, Mar. 2012.

[44]   B. K. Barick, K. K. Mishra, A. K. Arora, R. N. P. Choudhary, and D. K. Pradhan, "Impedance and Raman spectroscopic studies of (Na 0.5 Bi 0.5)TiO 3," *J. Phys. D: Appl. Phys.*, vol. 44, no. 35, p. 355402, 2011.

[45]   Q. Xu *et al.*, "Dielectric behavior and impedance spectroscopy in lead-free BNT–BT–NBN perovskite ceramics for energy storage," *Ceramics International*, vol. 42, no. 8, pp. 9728–9736, Jun. 2016.

[46]   J.-C. M'Peko, J. S. C. Francis, and R. Raj, "Impedance Spectroscopy and Dielectric Properties of Flash Versus Conventionally Sintered Yttria-Doped Zirconia Electroceramics Viewed at the Microstructural Level," *Journal of the American Ceramic Society*, vol. 96, no. 12, pp. 3760–3767, Dec. 2013.

[47]   K. Sun *et al.*, "Flash-Sintering and Characterization of La0.8Sr0.2Ga0.8Mg0.2O3-δ Electrolytes for Solid Oxide Fuel Cells," *Electrochimica Acta*, vol. 196, pp. 487–495, Apr. 2016.

[48]   L. A. Perez-Maqueda, E. Gil-Gonzalez, A. Perejon, J.-M. Lebrun, P. E. Sanchez-Jimenez, and R. Raj, "Flash sintering of highly insulating nanostructured phase-pure BiFeO3," *Journal of the American Ceramic Society*, vol. 100, no. 8, pp. 3365–3369, Aug. 2017.

[49]   P. Shi, G. Qu, S. Cai, Y. Kang, T. Fa, and C. Xu, "An ultrafast synthesis method of LiNi1/3Co1/3Mn1/3O2 cathodes by flash/field-assisted sintering," *Journal of the American Ceramic Society*, vol. 101, no. 9, pp. 4076–4083, Sep. 2018.

[50]   H. Charalambous, S. K. Jha, H. Wang, X. L. Phuah, H. Wang, and T. Tsakalakos, "Inhomogeneous reduction and its relation to grain growth of titania during flash sintering," *Scripta Materialia*, vol. 155, pp. 37–40, Oct. 2018.

[51]   B. Yoon *et al.*, "Measurement of O and Ti atom displacements in TiO2 during flash sintering experiments," *Journal of the American Ceramic Society*, vol. 101, no. 5, pp. 1811–1817, May 2018.

[52]   "Publication and Proposed Revision of ANSI/IEEE Standard 176-1987 'ANSI/IEEE Standard on Piezoelectricity,'" *IEEE Transactions on Ultrasonics, Ferroelectrics, and Frequency Control*, vol. 43, no. 5, pp. 717-, Sep. 1996.

[53]   "IRE Standards on Piezoelectric Crystals: Measurements of Piezoelectric Ceramics, 1961," *Proceedings of the IRE*, vol. 49, no. 7, pp. 1161–1169, Jul. 1961.

[54]   S. Pandey, D. Kumar, O. Parkash, and L. Pandey, "Equivalent circuit models using CPE for impedance spectroscopy of electronic ceramics," *Integrated Ferroelectrics*, vol. 183, no. 1, pp. 141–162, Sep. 2017.

[55]   M. S. Bernardo, T. Jardiel, A. C. Caballero, M. Bram, J. Gonzalez-Julian, and M. Peiteado, "Electric current activated sintering (ECAS) of undoped and titanium-doped BiFeO3 bulk ceramics with homogeneous microstructure," *Journal of the European Ceramic Society*, vol. 39, no. 6, pp. 2042–2049, Jun. 2019.

[56]   H. J. Goldsmid, *The physics of thermoelectric energy conversion*. San Rafael, CA : Bristol, UK: Morgan & Claypool Publishers ; IOP Publishing, 2017.

[57]   H. Nagata, K. Takai, Y. Nomura, S. Sato, Y. Hiruma, and T. Takenaka, "Vibration velocities under high-power driving on perovskite-type lead-free ferroelectric ceramics," in *2010 IEEE International Symposium on the Applications of Ferroelectrics (ISAF)*, 2010, pp. 1–4.

[58]   T. Rojac, M. Kosec, B. Budic, N. Setter, and D. Damjanovic, "Strong ferroelectric domain-wall pinning in BiFeO3 ceramics," *Journal of Applied Physics*, vol. 108, no. 7, p. 074107, Oct. 2010.

[59]   Y. Tan *et al.*, "Unfolding grain size effects in barium titanate ferroelectric ceramics," *Scientific Reports*, vol. 5, p. 9953, May 2015.

[60]   J. Schmelzer, J. Möller, and V. V. slezov, "Ostwald ripening in porous materials: The case of arbitrary pore size distributions," *Journal of Physics and Chemistry of Solids*, vol. 56, no. 8, pp. 1013–1022, Aug. 1995.

Fabrication and Characterization of Single-Aperture 3.5 MHz BNT-based Ultrasonic Transducer for Therapeutic Application

E. TAghaddos[1] , T. Ma[2], H. Zhong[3], Q. Zhou[4], M. X. Wan[3], A. Safari[1]

[1] Glenn Howatt Electroceramic Laboratory, Department of Materials Science and Engineering, Rutgers University

[2] Institute of Biomedical and Health Engineering, Shenzhen Institute of Advanced Technology, Chinese Academy of Science.

[3] Biomedical Engineering Department, Xi'an Jiaotong University, No.28, Xianning West Road, Xi'an, China.

[4] Department of Biomedical Engineering and the National Institutes of Health (NIH) Resource Center for Medical Ultrasonic Transducer Technology, University of Southern California, Losangeles, CA

Published in:

9   Fabrication and Characterization of Single-Aperture 3.5 MHz BNT-Based Ultrasonic Transducer for Therapeutic Application

Abstract

This paper discusses the fabrication and characterization of 3.5 MHz single-element transducers for therapeutic applications in which the active elements are made of hard lead-free BNT-based and hard commercial PZT (PZT-841) piezoceramics. Composition of $(BiNa_{0.88} K_{0.08}Li_{0.04})_{0.5}(Ti_{0.985}Mn_{0.015})O_3$ (BNKLT88-1.5Mn) was used to develop lead-free piezoelectric ceramic. Mn-doped samples exhibited high mechanical quality factor (Q_m) of 970, thickness coupling coefficient (k_t) of 0.48, a dielectric constant (ε^T_{33}) of 310 (at 1kHz), depolarization temperature (T_d) of 200 °C, and coercive field (E_c) of 52.5 kV/cm. Two different unfocused single element transducers using BNKLT88-1.5Mn and PZT-841 with the same center frequency of 3.5 MHz and similar aperture size of 10.7 mm and 10.5 mm were fabricated. Pulse-echo response, acoustic frequency spectrum, acoustic pressure field, and acoustic intensity field of transducers were characterized. The BNT-based transducer shows linear response up to the peak to peak voltage of 105 V in which the maximum rarefactional acoustic pressure of 1.1 MPa, and acoustic intensity of 43 W.cm^{-2} were achieved. Natural focal point of this transducer was at 60 mm from the surface of the transducer.

9.1 Introduction

The high intensity focused ultrasound (HIFU) transducers, with frequencies in a range of 0.5 to 8 MHz, have been widely used for non-invasive therapeutic procedures such as treatment of benign prostate hyperplasia (BPH) [1], [2], prostate cancer [3]–[7], breast tumor[8], [9], uterine fibroids [10], [11], liver cancer [12] renal tumor[13], pancreatic cancer [14], and bone metastases [15].

The optimal choice of therapeutic ultrasound (US) frequency is application-specific and represents a compromise between treatment depth and the desired rate of heating. Lower frequency transducers are used for deep treatment (e.g. transcranial application) and heat deposition applications, while higher frequency transducers are used for superficial treatments such as prostatic applications [16], [17].

Piezoelectric ceramics with high depolarization temperature, high mechanical quality factor, low dielectric loss, and relatively high coercive field are required for high power devices such as HIFU transducers. Additionally, higher power transmission of ultrasound is desirable which is obtained by using low dielectric and mechanical loss materials. It is critical for hard piezoceramics to maintain its low dielectric and mechanical loss at a high vibration velocity under the application of high electric field. Until now, only lead-based piezoelectric compositions such PZT4 and PZT8 have been commercially employed as active elements of HIFU transducers. However, lead is a toxic element which can cause severe health issues for human beings. Therefore, researchers have been trying to develop and characterize hard lead-free composition for high power applications to protect the environment and public health [18]–[20]. It is reported that the BNT-based ceramics with rhombohedral structure exhibit promising performance under high drive

conditions [21]–[24]. Specifically, substitution of B-site (Ti) with Mn in $0.88[Bi_{0.5}Na_{0.5}TiO_3]$-$0.08[Bi_{0.5}K_{0.5}TiO_3]$-$0.04[Bi_{0.5}Li_{0.5}TiO_3]$ (BNKLT88) ceramic resulted in decreasing dielectric loss, the planar coupling coefficient, and dielectric constant. Acceptor dopant ($Mn^{+2,+3}$) considerably enhanced the mechanical quality factor caused by the domain wall pinning effect of oxygen vacancies [19]–[21]. It has been demonstrated that the BNKLT88 ceramics doped with 1.5 mol.% Mn (BNKLT88-1.5Mn) show outstanding high power performance. Acceptor dopant ($Mn^{+2,+3}$) significantly increased the vibration velocity and suppressed the heat dissipation under high drive condition. Hard Mn-doped lead-free piezoceramics with a maximum vibration velocity (v_{rms}) of 0.6 m.s^{-1} exhibited superior high power performance compared to hard commercial PZTs (v_{rms} = 0.3-0.5 m.s^{-1})[22], [25], [26].

This study investigates the performance of hard BNKLT88-1.5Mn piezoceramics for high intensity focused ultrasound transducer (HIFU). Here, unfocused lead-free single element transducer with a center frequency of 3.5 MHz have been prototyped. Pulse-echo response and the acoustic properties of the transducer such as the frequency spectrum, the acoustic pressure field, and the acoustic intensity field were characterized and compared to the PZT-based transducer with similar frequency and aperture size. The experimental results demonstrate that BNKLT88-1.5Mn composition is a promising candidate for HIFU transducer applications.

9.2   Experimental procedures

9.2.1   Preparation and Characterization of the BNT-Based Ceramics

Hard lead-free and lead-based ferroelectric ceramics were used in this study. The lead-free $(BiNa_{0.88}K_{0.08}Li_{0.04})_{0.5}(Ti_{0.985}Mn_{0.015})O_3$ composition (abbreviated to BNKLT88-1.5Mn) was prepared in the laboratory setting while the PZT-841 was purchased from APC International, Ltd.

The conventional mixed-oxide method was used to prepare BNKLT88-1.5Mn. High purity precursor ($\geq$ 99.9%) including oxides and carbonates powders were dried overnight at 120 °C. Then, dried powders were mixed and milled in acetone and yttrium-stabilized zirconium balls for 12 hours followed by calcination at 800°C for 3 hours. The procedure continued by milling the calcined powder for 12 hours and adding binder (8 wt% Polyvinyl Alcohol solution) to prepare a disk-shaped specimen under 150 MPa uniaxial pressure. Upon binder removal at 550°C, pellets were sintered at 1100°C for 2 hours. Sintered ceramics were lapped down and then were electroded using high-temperature silver paste. Electroded ceramics were poled in a silicone oil bath at 95°C under an applied electric field of 45 kV.cm^{-1} for 15 min. The hard PZT ceramics (PZT 841) has been provided by APC International, Ltd.

The density was calculated based on the dimensions and weight of each sample. The dielectric constant ($\varepsilon^T_{33}/\varepsilon_o$) and dielectric loss (tanδ) were measured at 1kHz at room temperature by an impedance analyzer (HP4194a; Hewlett Packard, Tokyo, Japan). A Berlincourt piezometer was used to measure the longitudinal piezoelectric charge coefficient (d_{33}) at 100 Hz. IEEE standards method, resonance and anti-resonance frequencies of the impedance traces, has been used to calculate the piezoelectric planar and

thickness coupling coefficients (k_p and k_t, respectively) [20], [21], [27]. The longitudinal coupling coefficient, k_{33}, was estimated from the thickness and planar coupling coefficients according to (9.1) [28], [29].

$$k_{33}^2 = k_p^2 + k_t^2 - k_p^2 k_t^2 \tag{9.1}$$

The clamped relative permittivity ($\varepsilon^s_{33}/\varepsilon_0$) was calculated by (9.2) [30]

$$\varepsilon_{33}^S/\varepsilon_0 = (\varepsilon_{33}^T/\varepsilon_0)\left[(1-k_p^2)(1-k_t^2)\right] \tag{9.2}$$

The mechanical quality factor (Q_m) was obtained by (9.3) [30]

$$Q_m = \frac{1}{R}\sqrt{\frac{L}{C_a}} \tag{9.3}$$

where R, L, and C_a are the resistance, inductance, and capacitance of the Van Dyke equivalent circuit of a piezoelectric resonator at the resonance frequency.

The room temperature polarization-field (P-E) hysteresis loops were measured using a Sawyer-Tower circuit (Radiant Technology Inc., Albuquerque, NM) at a pulse width of 1000 ms (1 Hz frequency) using a triangular wave signal. The dielectric-temperature behavior of the samples was characterized during the heating ramp, within the temperature range of 30-320°C, by Agilent 4284A Precision LCR Meter.

9.2.2 Fabrication and Characterization of Ultrasonic Transducers

A PiezoCAD software (Sonic Concepts Inc., Woodinville, WA) was used to design and predict acoustic performance. In this experiment, we intend to evaluate the performance of unfocused single element 3.5 MHz BNT-based transducer and compare it to the lead-based transducer with the same frequency and aperture size.

Fig. 9.1 shows the schematic of the structure of a plain transducer. The BNKLT88-1.5 Mn and PZT-841 ceramics with a diameter of 10.7 and 10.5 mm were lapped down to a thickness of 665 and 485 μm, respectively, to achieve the desired resonance frequency of 3.5 MHz. A gold electrode with a thickness of 1000 Å was sputtered on one side of the ceramic to function as the bottom electrode. After attaching the 200-μm- wire to the bottom electrode using silver epoxy, the sample was placed inside a brass tube housing. Then the brass tube was filled with Epotek-301 epoxy (Epoxy Technology Inc., Billerica, MA) and was cured at room temperature for 24 hours. In order to connect the ceramic to the brass tube, the front side of the transducer was covered by a gold electrode. It should be noted that there were no matching circuit, backing layer, and matching layer on the design of these transducers.
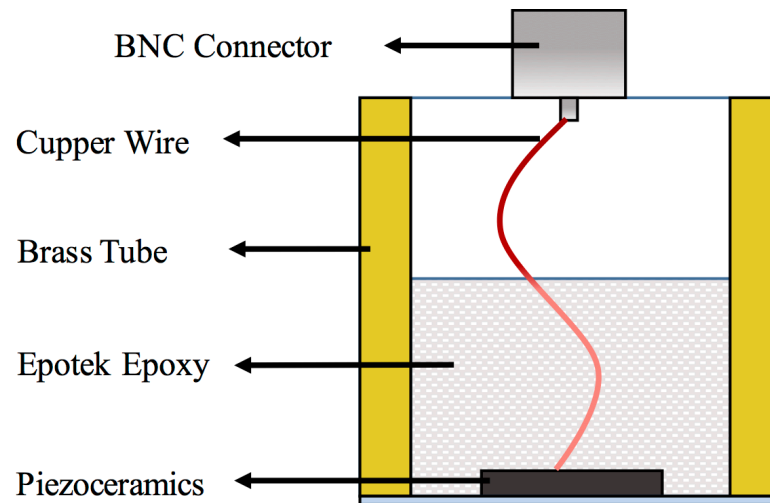
Figure 9. 1. Schematic illustration of the unfocused ultrasonic transducer

A conventional pulse-echo method in a water tank at room temperature was used to analyze the pulse-echo responses. The transducer was mounted in a tank filled with degassed water and was connected to a variable attenuator and the pulser-receiver (Model 5072R, Panametrics). One cycle of a unipolar signal covering a broadband, 0.5-60 MHz, was used to drive the signal, while a transducer-target distance was set to 55-60 mm from the x-cut quartz target. The bandwidth (BW) of the transducer was calculated by

$$BW = \frac{f_H - f_L}{f_C} \times 100 \tag{9.4}$$

where f_c is the center frequency, f_L and f_H are low and high frequencies, respectively, at the -6dB points of the frequency response spectrum.

Acoustic characterization set-up is shown in Fig. 9.2. An electric sine-wave pulse with 20 cycles (n= 20) generated by Pulse/Receiver PRP4000 (Ritec Inc. Warwick, R.I. USA) provided the transmit waveform to the transducer. The acoustic field was calibrated by a hydrophone-plane-scan method using Multiscan system (C329S, Panametrics Inc., Waltham, MA, USA) with needle hydrophone (0.5 mm diameter; Precision Acoustic Ltd, Dorchester, UK). Hydrophone sensitivity was 1109 mV/MPa at 3.5 MHz. The hydrophone scanned the emission field to measure the acoustic pressure and intensity of the transducers in zy-plane (Plane in z and y directions). The pulse repetition frequency (PRF) of 100 Hz and frequency of 3.5 MHz were used for all of the acoustic characterizations.
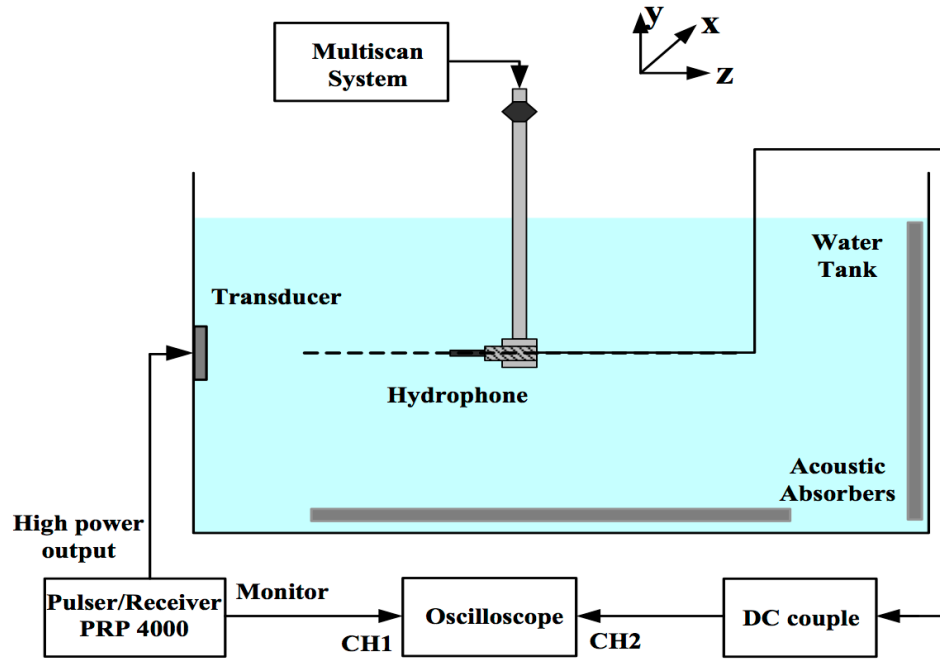
Figure 9. 2. High power characterization set up

Spatial peak pulse average intensity (I_{sppa}) and spatial peak temporal average intensity (I_{spta}) calculated by [31]–[33]

$$I_{sppa} = P^2/2\rho_0\, c_0 \qquad (9.5)$$

$$I_{spta} = I_{sppa} \times PD \times PRF \qquad (9.6)$$

$$PD = \frac{n}{f} \qquad (9.7)$$

where P is pressure amplitude in-situ, ρ_0 is density (ambient density of the medium), c_0 (ambient sound speed), PD is the pulse duration, n is the number of cycles in the pulse, and f is the operating frequency of the transducer.

Output power of the transducer (w_o) and the -6dB pulse-echo beam diameter (BD-6dB) can be evaluated by (9.8) and (9.9)

$$w_o = \frac{\pi BD^2_{-6dB}}{4} I_{spta} \tag{9.8}$$

$$BD_{-6dB} = 1.02\, Fc/fD \tag{9.9}$$

in which F is the focal length, c is the material sound velocity, f is the frequency, and D is the diameter of the transducer (active element).

9.3 Result and Discussion

BNKLT88-1.5Mn has rhombohedral structure at room temperature with complicated phase transitions. The temperature dependence of dielectric constant and loss tangent (*tanδ*) of poled BNKLT88-1.5 Mn at 0.1, 1 and 10 kHz are demonstrated in Fig. 9.3. Three recognizable anomalies were observed which were related to the depolarization temperature (T_d) close to 205°C, rhombohedral to tetragonal phase transition at 220°C, and dielectric maximum temperature (T_m) at 265°C. The depolarization temperature has been determined by the first peak of temperature-dependent tanδ on heating the poled sample. Deterioration of piezoelectric properties of BNT-based composition occur at T_d and the operating temperature range should be restricted to temperatures lower than T_d. It worth mentioning that the operating temperature range of lead-based ceramic is limited to Curie temperature (300-320°C) [34]–[36]. In practice, the surface temperature of the transducer does not reach 50°C which is much lower than T_d of BNT-based ceramic.
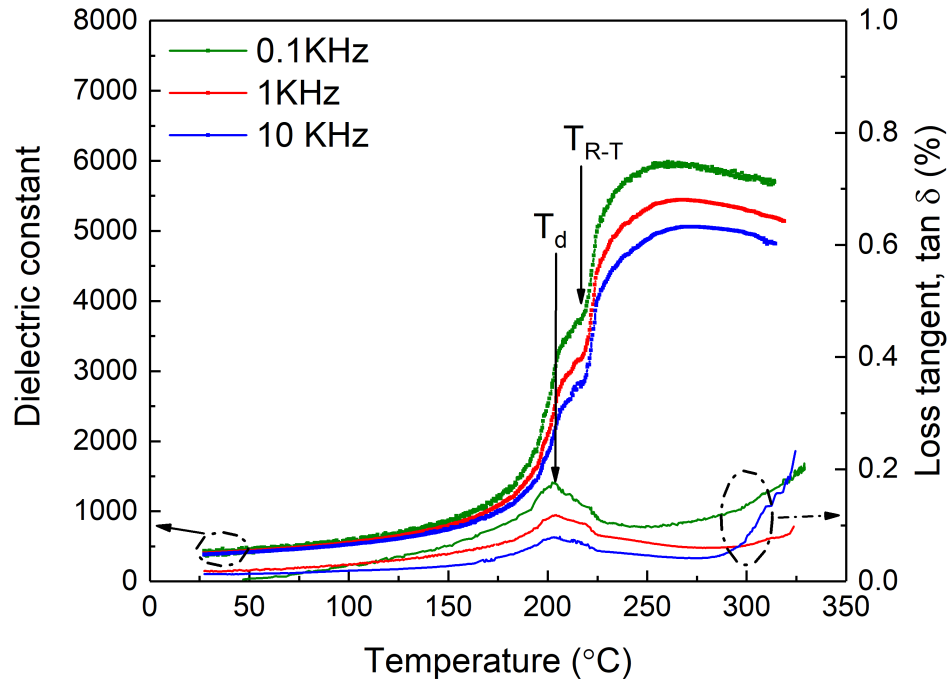
Figure 9. 3. Temperature dependence of dielectric constant and loss tangent, tan δ (%) of BNKLT88-1.5Mn for poled samples

Fig. 9.4 shows the polarization-field (P-E) plots for un-doped and 1.5 Mn-doped BNKLT88 ceramic. The remanent and saturation polarizations slightly decrease through the acceptor dopant, while the coercive field and the internal bias field (E_i) increase. The alignment of the defect dipoles (e.g., $V_O^{\bullet\bullet}$—Mn_{Ti}'') in the direction of spontaneous polarization results in the development of internal bias field. The undoped and 1.5% Mn-Doped BNKLT88 ceramics show E_i of 0.7 and 3 kV/cm, respectively. Dielectric and piezoelectric properties of BNKLT88-1.5 Mn ceramic are summarized and compared to hard PZT in Table 9.1. The properties of commercial hard PZT were obtained from references [19], [37]–[42]. BNKLT88-1.5Mn exhibited a mechanical quality factor and dielectric loss comparable with hard PZT. Although, the BNT-based composition shows considerably lower planar coupling coefficient and dielectric constant, its higher coercive

field (E_c=52 kV.cm^{-1}) makes it an excellent candidate for high power applications. The piezoceramic with a higher coercive field shows higher depolarization field and better performance at higher vibration velocity. High power performance of Mn-doped BNKLT88 composition has been comprehensively studied and can be found in references [22]–[24], [27].
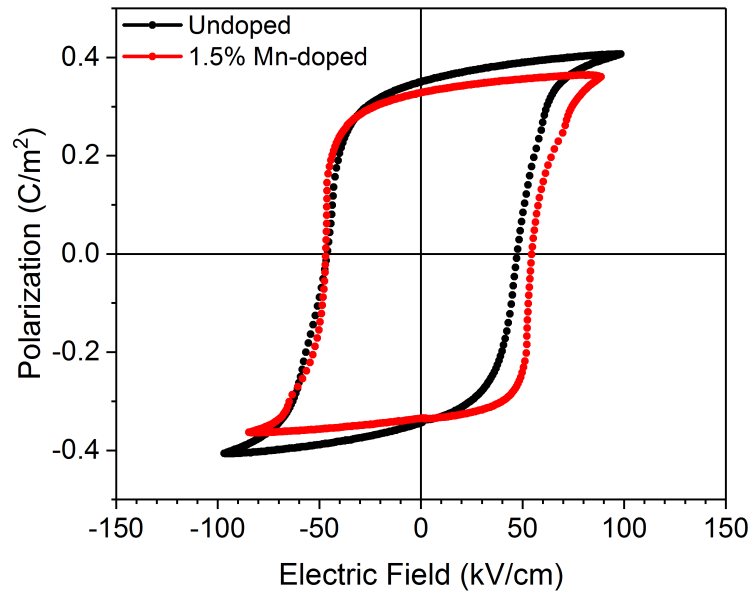
Figure 9. 4. The polarization-field behavior of undoped and 1.5%Mn doped BNKLT88 Ceramics

The time-echo responses, frequency spectra, and PiezoCAD results of the unfocused transducers are shown in Fig. 9.5. The BNT-based transducer (Fig. 9.5a and 9.5c) exhibited center frequency (f_c) of 3.6 MHz, and -6 dB bandwidth of 19.9%. Evaluation of the pulse-echo waveform of the PZT-based transducer (Fig. 9.5b and 9.5d) exhibited center frequency (f_c) of 3.9 MHz, and -6 dB bandwidth of 17.95%. Fig. 5 shows a good agreement between simulation and experiment results for both transducers.
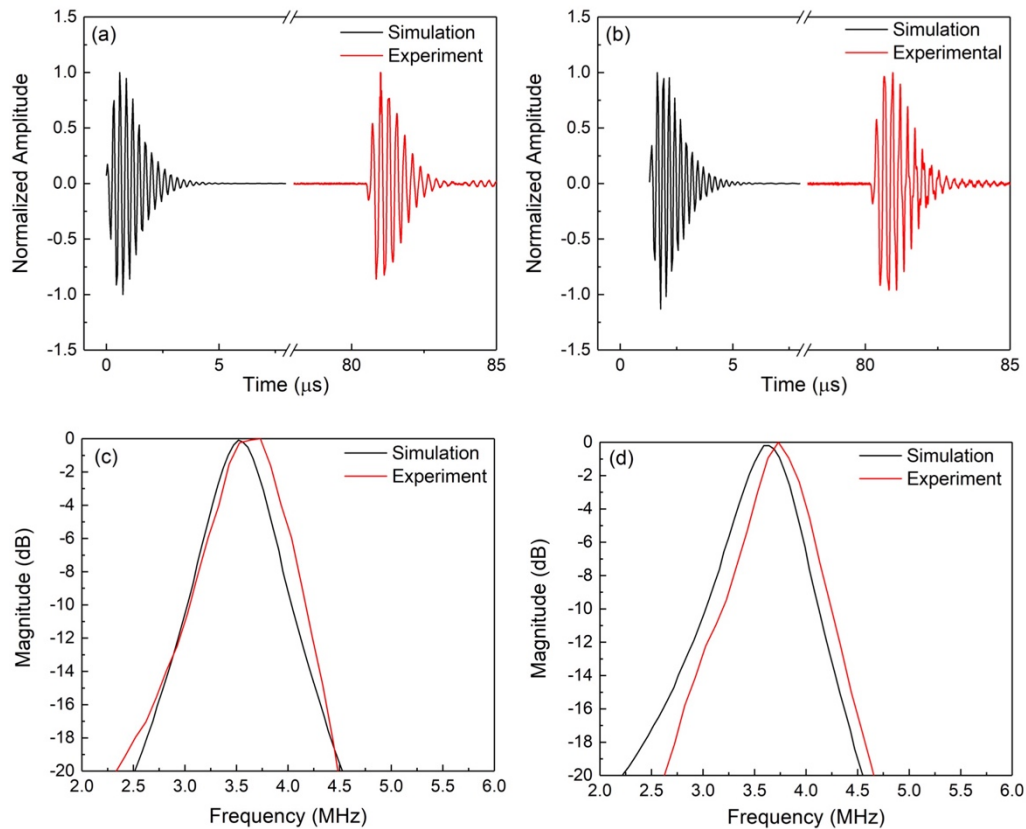
Figure 9. 5. The time and frequency domain spectrum of the unfocused BNKLT88-1.5Mn (a)-(d) and PZT-841 (b),(c). The simulation results have also been illustrated for comparison with experimental data

Table 9. 1. Properties of commercial hard PZTs and lead-free BNT-based ceramics [21], [37]–[41]

Property	PZT4	PZT8	PZT 841	BNKLT88	BNKLT88-1.5Mn
d_{33} (pC/N)	290	225	300	95	85
ε^T_{33}	1300	1000	1375	380	310
tanδ %	0.5	0.4	0.4	1.1	0.85
k_t %	51	48	---	49	48
k_p %	58-64	51-60	60	26	22
Q_m	500	1000	1400	400	970
E_c (kV.cm^{-1})	14	20	---	47.2	52.2
E_i (kV.cm^{-1})	3	3	---	0.7	3
T_c (°C)	328	300	320	~275 (T_m)	265 (T_m)
T_d (°C)	---	---	---	~220	205
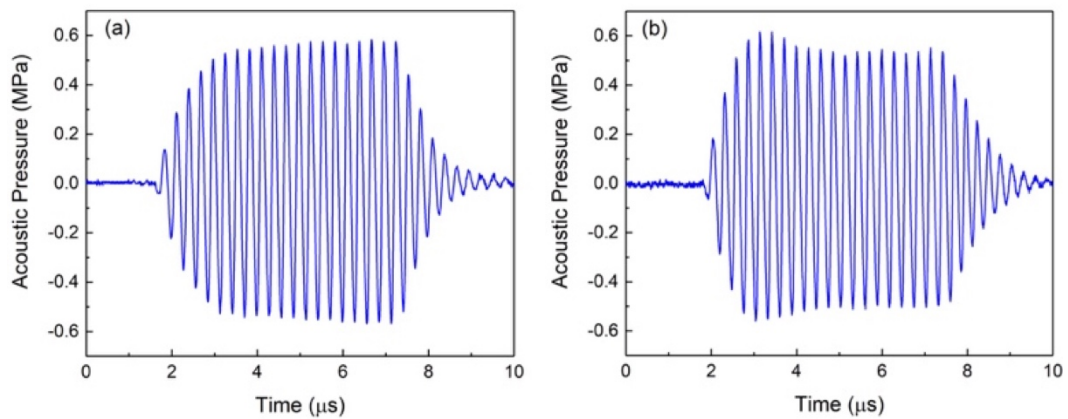
Figure 9. 6. Acoustic pressure spectrum of (a) BNT-based transducer and (b) PZT-based transducer at the 20 burst count (n=20)

The acoustic pressure waveform of both transducers at 20 burst count reached to stable value after 4 or 5 cycles as shown in Fig. 9. 6.

Fig. 9.7 shows the acoustic pressure vs. peak-to-peak voltage (V_{pp}) behavior of the transducers. The linear and quadratic regression of rarefactional acoustic (Negative Acoustic) pressure has been used to obtain the starting point of nonlinearity. The rarefactional acoustic pressure of BNT-based transducer shows linear response up to 105 V where the acoustic pressure was measured to be about 1.13 MPa. The PZT transducer shows nonlinearity after 70 V with an acoustic pressure of 1.01 MPa. Using (9.5), the acoustic intensities corresponding to the maximum rarefactional pressure of BNT-based and PZT-based transducer was calculated to be 43 $W.cm^{-2}$ and 34 $W.cm^{-2}$ respectively. One can conclude that the peak rarefaction pressure of the BNT-based transducer can reach a higher value than the PZT-based transducer.
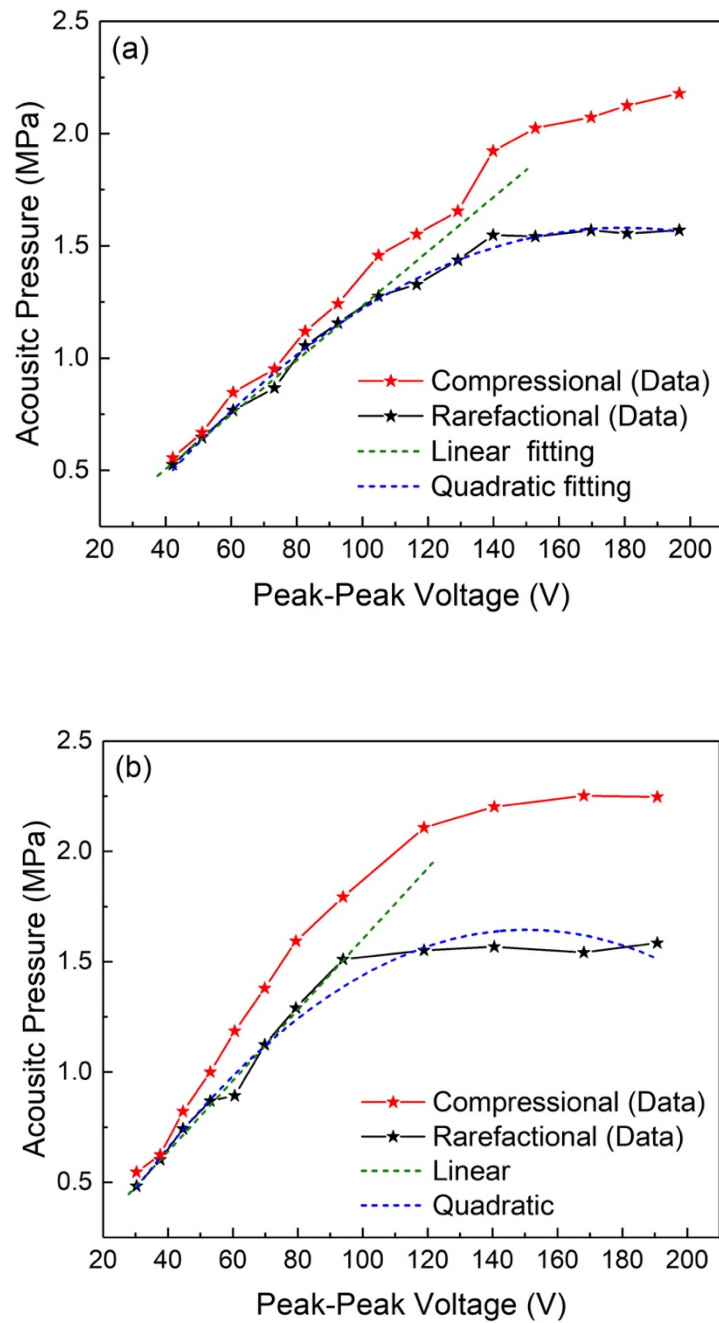
Figure 9. 7. Compressional and rarefactional acoustic pressure vs. peak to peak voltage of 3.5 MHz (a)BNT-based transducer (b) PZT-based transducer

The probability and threshold for inertial cavitation defines through the concept of the Mechanical Index (MI)

$$MI = \frac{P_{r,derated}}{\sqrt{f}_c} \qquad (9.\,10)$$

in which the $P_{r,derated}$ is the derated peak rarefactional pressure (MPa) at the location of the maximum peak intensity integral and f is the frequency (MHz). Food and Drug Administration (FDA) mandates the mechanical index to be less than 1.9 for diagnostic transducers. The high value of MI (>0.7) is needed for significant cavitation activity and bioeffects [43]. Considering the saturation of rarefactional pressure of BNT-based transducer at V_{pp} of approximately 105V with the pressure of 1.13 Mpa, the mechanical index (MI) can reach to 0.6, depending on the peak to peak voltage. In the same way, the mechanical index of the PZT-based transducer can reach to 0.58 at V_{pp} of 70V. This result suggests that the potential of the BNT-based transducer for inertial cavitation is comparable with the PZT-based transducer.

Fig. 9.8 (a-c) shows the 2-dimensional distribution of acoustic pressure and acoustic intensity along Z-axis of the BNT-based transducer measured at the peak-to-peak voltage of 57V. This transducer illustrates maximum rarefactional pressure of 0.52 MPa at about 60 mm from the transducer surface. The near field and far field regions of the ultrasound beam can be determined from these results (Fig. 9.8a). The maximum acoustic pressure corresponds to the natural focal point, the transition point from the near field to the far field regions, of a flat transducer. The spatial peak pulse average intensity of BNT-based transducer was measured 9.57 W.cm^{-2} (Fig. 9.8c) and is calculated by (5) as 9.03 W.cm^{-2}. The spatial peak temporal average (I_{spta}) and output power of BNT-based transducer were 5.4×10^{-3} W.cm^{-2} and 3.2 mW respectively.

Acoustic pressure and intensity field of the PZT-based transducer at the peak to peak voltage of 45V is presented in Fig. 9.8 (d-f). The maximum rarefaction pressure of 0.58 MPa, the spatial peak pulse average of 14.9 $W.cm^{-2}$, calculated spatial peak temporal average of 8.6×10^{-3} $W.cm^{-2}$, and the output power of 0.35 mW were obtained at 55 mm distance from the surface of the transducer.

The nonlinearity of the BNT-based transducer occurs at higher V_{pp} compared to PZT-transducer. The BNT-based transducer has higher depolarization field which allows imposing higher operating field. This results in obtaining higher acoustic pressure, acoustic intensity and output power compared to PZT-transducer. Table 9.2 summarizes the acoustic output exposure level of the transducers.
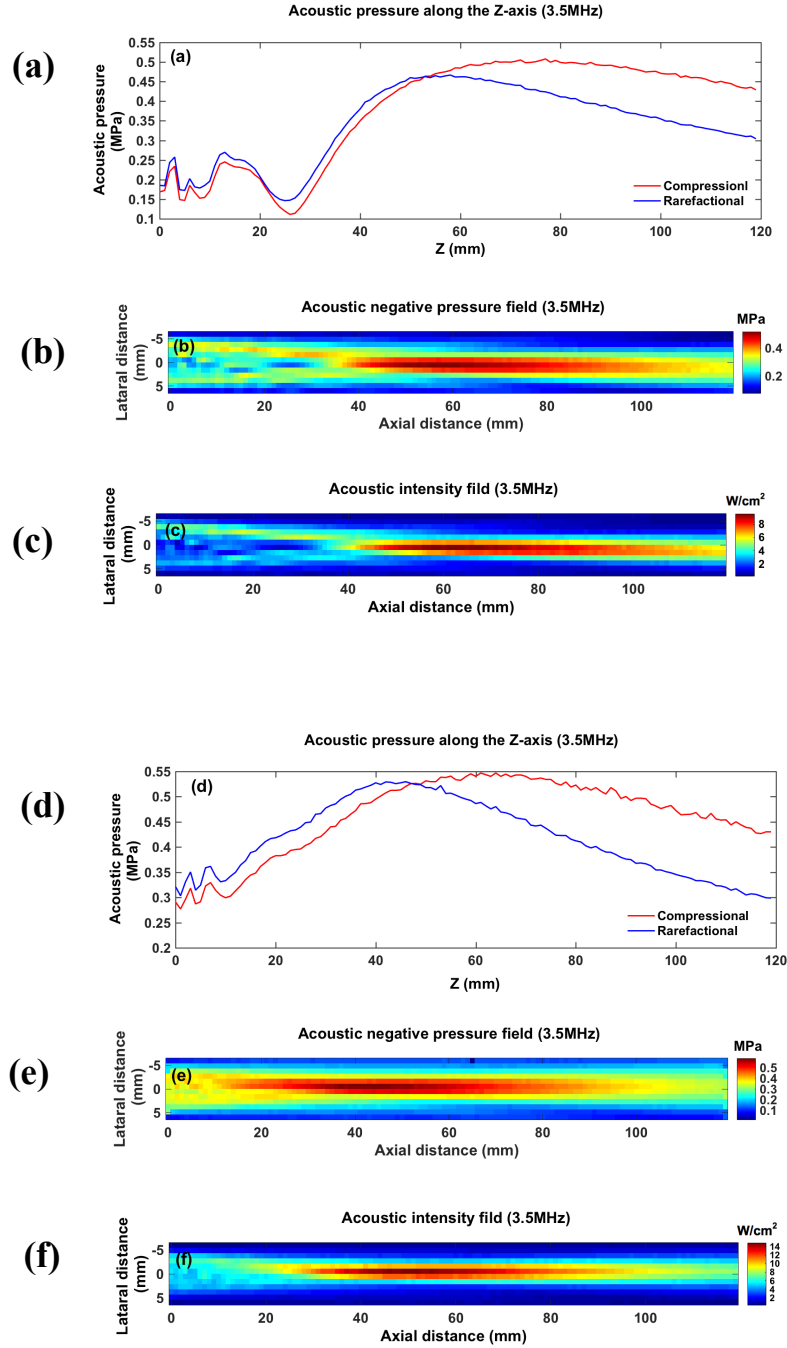
Figure 9. 8. (a) Acoustic pressure along the z-axis of BNT-based transducer, (b) &(c) 2D distribution of rarefaction acoustic pressure and acoustic intensity of BNT-based transducer, (d) Acoustic pressure along the z-axis of PZT-based transducer (e)&(f) 2D distribution of rarefaction acoustic pressure and acoustic intensity of PZT-based transducer

Table 9. 2. Acoustic Output Exposure levels

| | V_{pp} (V) | $P_{r,max}$ (MPa) | I_{sppa} (W/cm^2) | | I_{spta} (W/cm^2) (Eq.6) | | MI | W_o (mW) |
			Exp.	Eq. 5	Exp. I_{sppa}	I_{sppa} from Eq. 5		
BNKLT88-1.5Mn	57	0.52	9.6	9.03	5.5×10^{-3}	5.2×10^{-3}	0.28	0.24
	105	1.13	---	42	---	24.4×10^{-3}	0.60	~1.1
PZT 841	45	0.6	14	12.2	8.6×10^{-3}	7×10^{-3}	0.32	0.35
	70	1.01	---	34	---	19.5×10^{-3}	0.58	~ 0.8

9.4   Conclusion

In this study, the electromechanical properties at room temperature, temperature dependence of dielectric constant, and loss tangent of BNKLT88-1.5Mn have been studied. T_d, T_{R-T}, and T_m of this lead-free BNT-based composition were 205 °C, 220°C, and 265 °C respectively. Two different unfocused single-element transducers with a center frequency of 3.5 MHz were fabricated using BNKLT88-1.5Mn and PZT841 ceramics. BNT-based transducer showed -6 dB bandwidth of 20% which is similar to -6 dB bandwidth of PZT841 transducer (~18%). $P_{r,max}$, I_{sppa}, $I_{spta,}$ and w_o values of the BNT-based transducer measured at the peak to peak voltage of 57V were 0.52 MPa, 9.6 W/cm^2, 5.5×10^{-3} W/cm^2, and 0.24 mW, respectively. Additionally, the rarefaction pressure, acoustic intensity, spatial peak temporal average intensity and output power of lead-free transducer can reach to 1.1 MPa, 42 W/cm^2, 24×10-3 W/cm^2 and 1 mW at higher V_{pp}. In the same way, $P_{r,max}$, I_{sppa}, I_{spta} and w_o values of PZT-based transducer evaluated at the peak to peak voltage of 45V were 0.58 MPa, 14.9 W/cm^2, 8.6×10^{-3} W/cm^2, and 0.35 mW, respectively. The results of this study showed that the performance of BNT-based transducer was comparable with PZT-based one.

9.5 References

[1] L. d. Sullivan, M. g. McLoughlin, L. g. Goldenberg, M. e. Gleave, and K. w. Marich, "Early experience with high-intensity focused ultrasound for the treatment of benign prostatic hypertrophy," *Br. J. Urol.*, vol. 79, no. 2, pp. 172–176, Feb. 1997.

[2] T. Uchida, M. Muramoto, H. Kyunou, M. Iwamura, S. Egawa, and K. Koshiba, "Clinical outcome of high-intensity focused ultrasound for treating benign prostatic hyperplasia: preliminary report," *Urology*, vol. 52, no. 1, pp. 66–71, Jul. 1998.

[3] C. Chaussy and S. Thüroff, "The status of high-intensity focused ultrasound in the treatment of localized prostate cancer and the impact of a combined resection," *Curr. Urol. Rep.*, vol. 4, no. 3, pp. 248–252, May 2003.

[4] S. Thüroff *et al.*, "High-intensity focused ultrasound and localized prostate cancer: efficacy results from the European multicentric study," *J. Endourol. Endourol. Soc.*, vol. 17, no. 8, pp. 673–677, Oct. 2003.

[5] C. Chaussy and S. Thüroff, "High-intensity focused ultrasound in prostate cancer: results after 3 years," *Mol. Urol.*, vol. 4, no. 3, pp. 179–182, 2000.

[6] T. Uchida *et al.*, "Five years experience of transrectal high-intensity focused ultrasound using the Sonablate device in the treatment of localized prostate cancer," *Int. J. Urol.*, vol. 13, no. 3, pp. 228–233, Mar. 2006.

[7] A. Blana, B. Walter, S. Rogenhofer, and W. F. Wieland, "High-intensity focused ultrasound for the treatment of localized prostate cancer: 5-year experience," *Urology*, vol. 63, no. 2, pp. 297–300, Feb. 2004.

[8] H. Furusawa *et al.*, "The evolving non-surgical ablation of breast cancer: Mr Guided focused ultrasound (MRgFUS)," *Breast Cancer*, vol. 14, no. 1, pp. 55–58, Jan. 2007.

[9] F. Wu *et al.*, "Extracorporeal high intensity focused ultrasound treatment for patients with breast cancer," *Breast Cancer Res. Treat.*, vol. 92, no. 1, pp. 51–60.

[10] S. D. LeBlang, K. Hoctor, and F. L. Steinberg, "Leiomyoma Shrinkage After MRI-Guided Focused Ultrasound Treatment: Report of 80 Patients," *Am. J. Roentgenol.*, vol. 194, no. 1, pp. 274–280, Jan. 2010.

[11] K. Funaki, H. Fukunishi, and K. Sawada, "Clinical outcomes of magnetic resonance-guided focused ultrasound surgery for uterine myomas: 24-month follow-up," *Ultrasound Obstet. Gynecol.*, vol. 34, no. 5, pp. 584–589, Nov. 2009.

[12] C.-X. Li *et al.*, "Analysis of clinical effect of high-intensity focused ultrasound on liver cancer," *World J. Gastroenterol.*, vol. 10, no. 15, pp. 2201–2204, Aug. 2004.

[13] F. WU, Z.-B. WANG, W.-Z. CHEN, J. BAI, H. ZHU, and T.-Y. QIAO, "Preliminary Experience Using High Intensity Focused Ultrasound for the Treatment of Patients With Advanced Stage Renal Malignancy," *J. Urol.*, vol. 170, no. 6, Part 1, pp. 2237–2240, Dec. 2003.

[14] F. Wu *et al.*, "Feasibility of US-guided High-Intensity Focused Ultrasound Treatment in Patients with Advanced Pancreatic Cancer: Initial Experience," *Radiology*, vol. 236, no. 3, pp. 1034–1040, Sep. 2005.

[15] B. Liberman *et al.*, "Pain Palliation in Patients with Bone Metastases Using MR-Guided Focused Ultrasound Surgery: A Multicenter Study," *Ann. Surg. Oncol.*, vol. 16, no. 1, pp. 140–146, Nov. 2008.

[16] Y.-F. Zhou, "High intensity focused ultrasound in clinical tumor ablation," *World J. Clin. Oncol.*, vol. 2, no. 1, pp. 8–27, Jan. 2011.

[17]   D. >Gail ter Haar and C. Coussios, "High intensity focused ultrasound: Physical principles and devices," *Int. J. Hyperthermia*, vol. 23, no. 2, pp. 89–104, Jan. 2007.

[18]   H. J. Lee, S. O. Ural, L. Chen, K. Uchino, and S. Zhang, "High Power Characteristics of Lead-Free Piezoelectric Ceramics," *J. Am. Ceram. Soc.*, vol. 95, no. 11, pp. 3383–3386, Nov. 2012.

[19]   S. Zhang, J. B. Lim, H. J. Lee, and T. R. Shrout, "Characterization of Hard Piezoelectric Lead-Free Ceramics," *IEEE Trans. Ultrason. Ferroelectr. Freq. Control*, vol. 56, no. 8, pp. 1523–1527, Aug. 2009.

[20]   T. Tou, Y. Hamaguti, Y. Maida, H. Yamamori, K. Takahashi, and Y. Terashima, "Properties of (Bi $_{0.5}$ Na $_{0.5}$)TiO $_3$ –BaTiO $_3$ –(Bi $_{0.5}$ Na $_{0.5}$)(Mn $_{1/3}$ Nb $_{2/3}$)O $_3$ Lead-Free Piezoelectric Ceramics and Its Application to Ultrasonic Cleaner," *Jpn. J. Appl. Phys.*, vol. 48, no. 7, p. 07GM03, Jul. 2009.

[21]   E. Taghaddos, M. Hejazi, and A. Safari, "Electromechanical Properties of Acceptor-Doped Lead-Free Piezoelectric Ceramics," *J. Am. Ceram. Soc.*, vol. 97, no. 6, pp. 1756–1762, Jun. 2014.

[22]   M. Hejazi, E. Taghaddos, E. Gurdal, K. Uchino, and A. Safari, "High Power Performance of Manganese-Doped BNT-Based Pb-Free Piezoelectric Ceramics," *J. Am. Ceram. Soc.*, vol. 97, no. 10, pp. 3192–3196, Oct. 2014.

[23]   H. Nagata, K. Takai, Y. Nomura, S. Sato, Y. Hiruma, and T. Takenaka, "Vibration velocities under high-power driving on perovskite-type lead-free ferroelectric ceramics," in *2010 IEEE International Symposium on the Applications of Ferroelectrics (ISAF)*, 2010, pp. 1–4.

[24]   Y. Hiruma, H. Nagata, and T. Takenaka, "Phase-transition temperatures and piezoelectric properties of (Bi1/2Na1/2)TiO3- (Bi1/2Li1/2)TiO3-(Bi1/2K1/2)TiO3 lead-free ferroelectric ceramics," *IEEE Trans. Ultrason. Ferroelectr. Freq. Control*, vol. 54, no. 12, pp. 2493–2499, Dec. 2007.

[25]   Y. Gao, Y.-H. Chen, J. Ryu, K. Uchino, and D. Viehland, "Eu and Yb Substituent Effects on the Properties of Pb(Zr $_{0.52}$ Ti $_{0.48}$)O $_3$ –Pb(Mn $_{1/3}$ Sb $_{2/3}$)O $_3$ Ceramics: Development of a New High-Power Piezoelectric with Enhanced Vibrational Velocity," *Jpn. J. Appl. Phys.*, vol. 40, no. Part 1, No. 2A, pp. 687–693, Feb. 2001.

[26]   "Comparison of Power Density Characteristics among Disk and Plate Shaped Piezoelectric Devices," *Jpn. J. Appl. Phys.*, vol. 49, no. 2R, p. 021502, Feb. 2010.

[27]   T. Takenaka, H. Nagata, and Y. Hiruma, "Phase Transition Temperatures and Piezoelectric Properties of (Bi1/2Na1/2)TiO3-and (Bi1/2K1/2)TiO3-Based Bismuth Perovskite Lead-Free Ferroelectric Ceramics," *IEEE Trans. Ultrason. Ferroelectr. Freq. Control*, vol. 56, no. 8, pp. 1595–1612, Aug. 2009.

[28]   Z.-Y. Shen, J.-F. Li, R. Chen, Q. Zhou, and K. K. Shung, "Microscale 1–3-Type (Na,K)NbO3-Based Pb-Free Piezocomposites for High-Frequency Ultrasonic Transducer Applications," *J. Am. Ceram. Soc. Am. Ceram. Soc.*, vol. 94, no. 5, pp. 1346–1349, May 2011.

[29]   M. M. Hejazi, B. Jadidian, and A. Safari, "Fabrication and evaluation of a single-element Bi0.5Na0.5TiO3-based ultrasonic transducer," *IEEE Trans. Ultrason. Ferroelectr. Freq. Control*, vol. 59, no. 8, pp. 1840–1847, Aug. 2012.

[30]   "Publication and Proposed Revision of ANSI/IEEE Standard 176-1987 'ANSI/IEEE Standard on Piezoelectricity,'" *IEEE Trans. Ultrason. Ferroelectr. Freq. Control*, vol. 43, no. 5, p. 717–, Sep. 1996.

[31]   M. S. Canney, M. R. Bailey, L. A. Crum, V. A. Khokhlova, and O. A. Sapozhnikov, "Acoustic characterization of high intensity focused ultrasound fields: A combined measurement and modeling approach," *J. Acoust. Soc. Am.*, vol. 124, no. 4, pp. 2406–2420, Oct. 2008.

[32]   C. R. Hill, "Optimum acoustic frequency for focused ultrasound surgery," *Ultrasound Med. Biol.*, vol. 20, no. 3, pp. 271–277, Jan. 1994.

[33]   S. B. Barnett and G. Kossoff, "Temporal peak intensity as a critical parameter in ultrasound dosimetry," *J. Ultrasound Med. Off. J. Am. Inst. Ultrasound Med.*, vol. 3, no. 9, pp. 385–389, Sep. 1984.

[34]   Y. Hiruma, H. Nagata, and T. Takenaka, "Phase Transition Temperatures and Piezoelectric Properties of $(Bi_{1/2} Na_{1/2})TiO_3 – (Bi_{1/2} K_{1/2})TiO_3 – BaTiO_3$ Lead-Free Piezoelectric Ceramics," *Jpn. J. Appl. Phys.*, vol. 45, no. 9B, pp. 7409–7412, Sep. 2006.

[35]   Y. Hiruma, H. Nagata, and T. Takenaka, "Phase Transition Temperatures and Piezoelectric Properties of (Bi1/2Na1/2)TiO3–(Bi1/2K1/2)TiO3–BaTiO3 Lead-Free Piezoelectric Ceramics," *Jpn. J. Appl. Phys.*, vol. 45, no. 9S, p. 7409, Sep. 2006.

[36]   E.-M. Anton, W. Jo, D. Damjanovic, and J. Rödel, "Determination of depolarization temperature of (Bi1/2Na1/2)TiO3-based lead-free piezoceramics," *J. Appl. Phys.*, vol. 110, no. 9, p. 094108, Nov. 2011.

[37]   T. R. Shrout and S. J. Zhang, "Lead-free piezoelectric ceramics: Alternatives for PZT?," *J. Electroceramics*, vol. 19, no. 1, pp. 113–126, Feb. 2007.

[38]   M. W. Hooker, "Properties of PZT-Based Piezoelectric Ceramics Between -150 and 250 C," Sep. 1998.

[39]   "Piezoelectric Materials Datasheet. Piezopower, CTS Electronic Compo- nents Co., Albuquerque, NM." .

[40]   "Piezomaterial Data, Specific Parameters of Standard Materials. PI Ceram- ics Co., Lederhose, Germany." .

[41]   "Piezoelectric Ceramics Datasheet, Morgan Advanced Materials, Berkshire, UK." .

[42]   "Physical and Piezoelectric Properties of APC Materials, APC Internationla, Ltd,United State & Canada." .

[43]   Center for Devices and Radiological Health, "Guidance for Industry and FDA Staff - Information for Manufacturers Seeking Marketing Clearance of Diagnostic Ultrasound Systems and Transducers." Rockville, MD, 09-Sep-2008.

SUMMARY AND CONCLUSION

In this thesis development, processing properties relationship including the effect of calcined particle size on transition temperature and electromechanical properties, as well as conductivity behavior of lead-free $(BiNa_{0.88} K_{0.08}Li_{0.04})_{0.5}Ti_{1-x}A_x O_3$ (A=Fe or Mn, x=1-2.2 mol%) composition, were comprehensively explored. Samples were sintered by conventional and flash methods. The functionality of composition was evaluated and compared by prototyping of low-frequency BNKLT88 and PZT transducers for high power application. The numerous experiments led to the significant conclusions which are presented as he following sections:

A) Acceptor-Doped Lead-Free BNKLT88 Ceramics by Conventional Sintering

The specimens powder was synthesized via conventional mixed oxide method. The raw materials including carbonates and oxides were weighted stichometry, mixed via roller milling and then calcined at 800 °C for 3 h. Green pellets were pressed at 150 MPa and then sintered at different temperatures for the duration of 2 h to achieve the highest density and optimum dielectric and piezoelectric properties. Electromechanical properties were evaluated based on IEEE standard. It was concluded that

1) A significant enhancement of planar and thickness Q_m was obtained with Mn or Fe-doping. The optimum concentration of dopants were at 1.5 mol% of Mn or Fe wherein the highest Q_m of 970 and 900 and the lowest dielectric loss of 0.88% and 0.9% were achieved, respectively.

2) The dielectric, dissipation factor, piezoelectric and coupling coefficient were decreased with increasing the Mn concentration.

3) The calcined powder with a median particle size of 535 nm sintered at 1020 °C revealed finer grain size and narrower distribution of grains and highest Q_m of 1200.

4) XPS evaluation of the oxidation state of Mn and Fe revealed coexistence of Mn^{2+}/Mn^{3+} or Fe^{2+}/Fe^{3+}.

B) High Power Performance of Hard BNT-Based Compositions

The high power performance of conventional sintered BNKLT88 + xMn (x = 0, 1.4, 1.5, and 1.6%) ceramics was studied under constant vibration velocity mode in which the following results were established:

5) Mn-doping (1.5 mol %) considerably improved the high power characteristic of BNKLT88 ceramic with improved maximum vibration velocity.

6) Mn-doping resulted in suppression of heat generation and reduction of resonance frequency shift. Minimum input power and the best efficiency was obtained in BNKLT88-1.5 Mn samples.

7) Mn-doped ceramics exhibited better efficiency with higher Q_m and lower heat generation at antiresonance frequency than the resonance frequency.

8) BNT-based transducers with E_C of 52.2 kV.cm^{-1} showed superior high power performance compare to hard commercial PZT8 and PZT4.

9) The input power required to operate the transducer was increased as a function of vibration velocity and decreased by Mn-doping. The large displacement of ceramic at resonance and antiresonance frequency resulted in the minimum input power at these fundamental frequencies.

C) Electrical Properties of Acceptor-Doped BNKLT88 Composition

The electrical conductivity and impedance relaxation of conventional sintered BNKLT88, in a temperature range from 450-600 °C were comprehensively studied using impedance spectroscopy. The effect of 1.5 mol% Mn and Fe acceptor dopants on the conductivity and impedance relaxation have been thoroughly explored. The impedance spectra have been simulated to the equivalent circuits and the following conclusions were drawn:

10) The negative temperature coefficient of resistance (NTCR) was observed in undoped, 1.5 mol% Mn and 1.5 mol% Fe-doped compositions.

11) Mn-doping considerably increased the bulk resistivity which might be attributed to the higher concentration of complex defect in the system. The grain boundary activation energy modestly increased while the bulk activation energy decreased.

12) The conductivity remarkably enhanced via Fe-doping and reached to 0.01 S.cm^{-1} at 600 °C. The lower impedance in Fe-doped samples might be explained by a higher concentration of free oxygen vacancies in the system which confirmed by a lower bulk activation energy.

13) Fe-doped composition with high ionic conductivity is a potential candidate for Solid Oxide Fuel Cell (SOFC) applications.

D) Electromechanical Properties of Flash Sintered BNT-Based Piezoceramics

Sintering behavior of BNKLT88-1.5Mn composition under electrical current has been explored. The effect of flash parameters including alternating current, direct current, current density limit and holding time on the densification, microstructure,

electromechanical and electrical properties has been reported. The initial electric field was kept constant at 100 V.cm^{-1} for all the conditions and heat treatment at 880 °C for 1 h has been performed on all flashed samples.

14) The presence of secondary phases in XRD pattern of samples developed under DC current has been detected. Three possible explanation might be current localization under DC electric filed, different diffusion rate and direction of alkaline elements under DC electric filed or Peltier effect

15) XRD pattern of samples sintered under AC electric field showed pure perovskite structure with Rhombohedral symmetry while the uniform distribution of elements confirmed by EDS analysis.

16) The optimum applied current density was 1.5 A.cm^{-2} in which the highest density, piezoelectric coefficient, and mechanical quality factor were obtained.

17) The optimum flash parameters were obtained at 1 KHz AC electric field, preset maximum current limit of 1.5 A.cm^{-2} and holding time of 20 min, wherein smaller average grain size, smaller dielectric loss and slightly higher piezoelectric charge coefficient, dielectric permittivity and coupling coefficient were obtained compared to conventionally sintered samples.

18) Alternative current, shorter sintering time, and rapid quenching after removing the electric field might be considered as major factors in lowering the mechanical quality factor in flash sintered specimens. The rhombohedral to the tetragonal phase transition of flash sintered samples shifted to lower temperature by 10 °C while the maximum dielectric temperature remained unchanged.

E) Single Aperture 3.5 MHz Transducers

BNKLT88-1.5 Mn with high mechanical quality factor, a high coercive field, low dielectric loss, outstanding high power performance, and high vibration velocity is a promising candidate for hard PZT counterpart. The functionality of hard BNT-based composition was evaluated by the prototyping of low frequency transducer for high intensity focused ultrasound transducer (HIFU) applications. For this aim, two single element ultrasonic transducers with the same center frequency of 3.5 MHz and similar aperture size of 10.7 mm and 10.5 mm were designed and fabricated based on hard BNKLT88-1.5Mn and hard commercial PZT (PZT-841), respectively. The characterization of developed transducers revealed that

19) There was a good agreement between simulation and experimental for both BNT-based and PZT-based transducers.

20) -6dB bandwidth of BNT-based and PZT-based transducers was measured to be 18% and 20%, respectively.

21) BNT-based and PZT-based transducer showed linear respond up to peak to peak voltage (V_{pp}) of 105 and 70 V in which maximum rarefaction pressure ($P_{r,max}$) of 1.13 and 1.01 Mpa were obtained while the acoustic intensity was calculated to be 43 W.cm^{-2} and 34 W.cm^{-2}, respectively.

22) It has been found that the potential of BNT-based transducer for inertial cavitation was comparable with PZT-transducer.

23) Evaluation of 2-dimension distribution of acoustics intensity and acoustic pressure of BNT-based at V_{pp} of 57 V showed spatial peak pulse average (I_{sppa}) of 9.6 W.cm^{-2} and spatial peak temporal average (I_{spta}) of 5.5×10^{-3} W.cm^{-2}.

24) I_{sppa} of 14 W.cm^{-2} and I_{spta} of 8.6×10^{-3} W.cm^{-2} were obtained in PZT-based transducer under an operating field of 45 V.

25) Considering the higher depolarization field of BNT-based transducer, it is possible to apply higher operating field on this device which might result in obtaining higher I_{sppa} and I_{spta}. The results of this research confirmed that the performance of BNT-based and PZT-based were comparable.